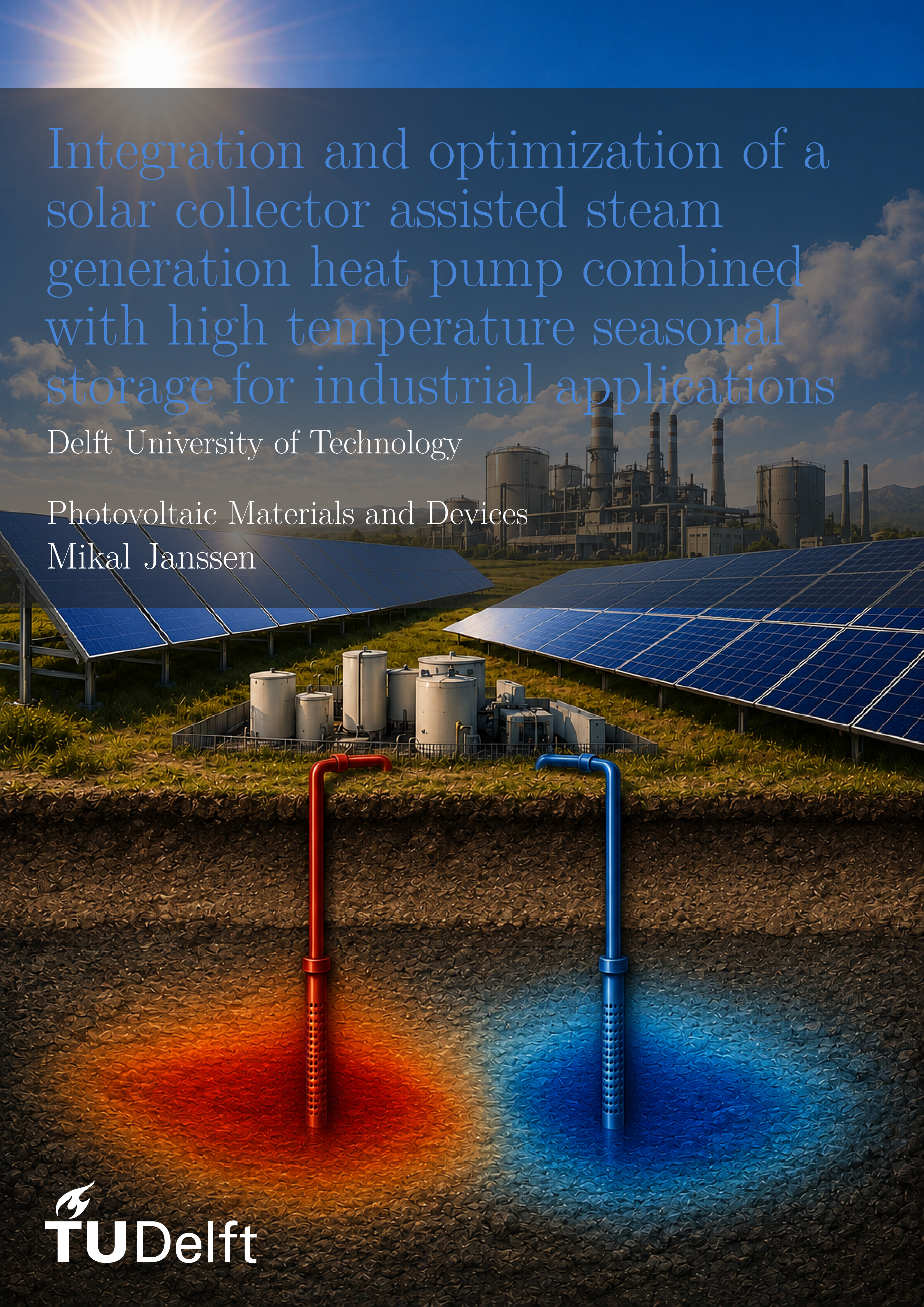

Integration and optimization of a solar collector assisted steam generation heat pump combined with high temperature seasonal storage for industrial applications

Delft University of Technology

Photovoltaic Materials and Devices
Mikal Janssen

TU Delft

Integration and optimization of a solar collector assisted steam generation heat pump combined with high temperature seasonal storage for industrial applications

Thesis report

by

Mikal Janssen

To obtain the degree of Master of Science at the Delft University of Technology.
To be defended publicly on: 8$^{\text{th}}$ July, 2026.

Student number:	5089239	
Thesis committee	Prof.dr.ir. O. Isabella	TU Delft, Committee chair
	Dr.ir. R. Santbergen	TU Delft, Supervisor
	Dr. E. Zanetti	TU Delft, External Committee member
	Dr. Z. Ul-Abdin	TU Delft, Daily Supervisor
Project Duration:	November, 2025	July, 2026
Faculty:	Faculty of Electrical Engineering, Mathematics and Computer Science	TU Delft

Abstract

This thesis addresses the urgent challenge of decarbonizing large-scale industrial process heating with limited available electricity grid capacity. An integrated energy system is developed combining solar heat generation with thermal storage coupled to a high-temperature heat pump for industrial process heating up to 150 °C. This work involves the development of individual component models capable of high temperature (100–150 °C) operation and the integration of these components into a numerical energy system model. The model is evaluated for two industrial sectors, Food & Beverage (130 °C) and Paper & Pulp (150 °C), under northern and southern European climate conditions. The developed integrated model is added to the PVMD Toolbox, an advanced modeling tool developed by the Photovoltaic Materials and Devices research group at TU Delft.

Through dynamic hourly simulations over a full year, the theoretical feasibility of the integrated energy system has been demonstrated. The thermal efficiency of the solar thermal collectors averages 40% and 50% in Delft and Seville respectively. Significant reductions in peak electricity grid consumption of 70% and 100% can be achieved for northern and southern European climates respectively. Solar thermal collector count is the most important performance variable over all scenarios and seasonal heat storage is essential for peak load reductions in northern European climates. The system can be economically competitive compared to a natural gas boiler reference (80 €/MWh) in Seville, achieving a minimum LCOH of 66 €/MWh. For Delft the lowest LCOH is 119 €/MWh, not yet competitive under current gas prices but considerably less exposed to fossil fuel price volatility.

Acknowledgments

I would like to thank my TU Delft supervisors, Rudi Santbergen and Zain Ul-Abdin, for their support, guidance, and constructive feedback during my thesis. Their support has been integral to both the direction and quality of this work.

I am also grateful to Emanuele Zanetti for his valuable input in the design of the integrated industrial energy system, and to Martin Bloemendal and Stijn Beernink for their time and expertise during our meetings concerning the aquifer thermal energy storage modeling. I would like to thank Annalisa Di Napoli for sharing her expertise of high temperature PVT modeling. My thanks also go to the wider PVMD group for their feedback and support throughout the project.

Finally, I wish express my heartfelt gratitude to my family, friends, and girlfriend for their companionship, encouragement and patience during this thesis project. Their love and reassurance have been invaluable to my well-being and motivation during these last 8 months.

Use of large language models

During the preparation of this thesis, the author used Claude (Anthropic) to assist with academic language editing, grammar correction, brainstorming, plotting, and Matlab code debugging. All technical content, results, analysis, and conclusions are the author's own.

Contents

Abstract **i**

Acknowledgments **ii**

List of Symbols **v**

Acronyms **viii**

List of Figures **viii**

List of Tables **xii**

1 Introduction **1**
1.1 Industrial heating demand and net congestion . . . 1
1.2 Solar energy . . . 2
1.2.1 Photovoltaic systems . . . 3
1.2.2 Solar thermal . . . 3
1.2.3 Photovoltaic thermal . . . 4
1.2.4 Concentrated solar energy . . . 5
1.3 Heat pumps . . . 6
1.4 Thermal energy storage . . . 7
1.5 System models . . . 8
1.5.1 Solar energy for industry . . . 9
1.5.2 Solar energy and seasonal storage . . . 11
1.6 Research gap . . . 12
1.7 Research objectives . . . 14
1.8 Thesis outline . . . 14

2 Overview of the numerical component models **15**
2.1 PVMD toolbox . . . 15
2.2 Solar collectors and thermal buffer storage . . . 16
2.2.1 Photovoltaic module - existing model . . . 17
2.2.2 Solar thermal - existing model . . . 17
2.2.3 Solar thermal - modified model . . . 18
2.2.4 Photovoltaic Thermal - newly developed model . . . 19
2.2.5 Water tank - newly developed model . . . 20
2.3 Heat pump - newly developed model . . . 20
2.3.1 Coolprop . . . 22
2.4 Heat exchangers - newly developed model . . . 22
2.5 Aquifer thermal energy storage - existing . . . 24
2.5.1 Aquifer thermal energy storage - modified model . . . 24
2.6 Hydraulic Pumps ATES - newly developed model . . . 27
2.7 Electrical battery - newly developed model . . . 28
2.8 Conclusion . . . 29

3 Integrated system **30**
3.1 System configurations . . . 31
3.2 Operational modes . . . 32
3.2.1 Mode I: Balanced operation . . . 33
3.2.2 Mode II: Surplus . . . 34
3.2.3 Mode III: Shortage . . . 36
3.2.4 Heat exchanger temperature . . . 38
3.2.5 Electrical energy . . . 41
3.2.6 Control strategy . . . 42
3.3 Model inputs . . . 43
3.3.1 Industry demand . . . 43
3.3.2 Weather data . . . 44
3.4 Validation of the model . . . 45
3.4.1 Solar collector validation . . . 46
3.4.2 ATES validation . . . 47
3.4.3 HP system validation . . . 48
3.5 Conclusion . . . 49

4 Results and Discussion **51**
4.1 System performance . . . 51
4.1.1 Configurations 1 to 6 comparison . . . 51
4.1.2 Simulation highlights . . . 53
4.1.3 Main takeaways system performance . . . 66
4.2 Optimization . . . 67
4.2.1 Optimal ST/PV ratio . . . 67
4.2.2 Component quantity optimization . . . 68
4.2.3 System size heatmap . . . 70
4.2.4 Main takeaways optimization . . . 73
4.3 Economic analysis . . . 74
4.3.1 Optimal configuration economically . . . 76
4.3.2 Main takeaways economic analysis . . . 79
4.4 Conclusion . . . 80

5 Conclusion **81**
5.1 Summary of key findings . . . 81
5.2 Final conclusion . . . 82

6 Recommendations **83**

A Chapter 2 **94**
A.1 Phase change material storage . . . 94
A.1.1 Simulation results . . . 95
A.1.2 Detailed simulation results . . . 96
A.2 Heat Exchanger Area Estimation . . . 101

B Chapter 3 **103**
B.1 Heat Loss through horizontal transport . . . 103
B.1.1 Heat Loss Model . . . 103
B.1.2 Hydraulic Pressure Loss Model . . . 104
B.1.3 Impact on System COP . . . 104

C Chapter 4 **107**
C.1 PVT performance . . . 107
C.2 PVT optimum . . . 112

List of Symbols

Symbol	Definition	Unit
General parameters		
C_w	Specifc heat capacity of water	$\mathrm{J\,kg^{-1}\,K^{-1}}$
Photovoltaic model		
P_pv	Electrical power generated by PV module	W
P_S	Available solar power on module	W
η_pv	Electrical efficiency of PV module	–
$\eta_\mathrm{pv,ref}$	Reference PV module efficiency at STC	–
G	Plane of array irradiance	$\mathrm{W\,m^{-2}}$
G_ref	Reference irradiance at STC	$\mathrm{W\,m^{-2}}$
G_NOCT	Irradiance under NOCT conditions	$\mathrm{W\,m^{-2}}$
A_mod	PV module area	$\mathrm{m^2}$
β	Temperature coefficient of PV efficiency	$\%\,\mathrm{K^{-1}}$
δ	Irradiance coefficient of PV efficiency	–
T_pv	Actual PV cell temperature	°C
$T_\mathrm{pv,ref}$	Reference PV cell temperature at STC	°C
T_am	Ambient temperature	°C
$NOCT$	Nominal operating cell temperature	°C
Solar thermal / PVT collector model		
η_th	Thermal efficiency of ST/PVT collector	–
η_th^0	Initial guess thermal efficiency of PVT collector	–
η_0	Zero loss efficiency of ST/PVT collector	–
η_el	Electrical efficiency of PVT module	–
T_in	Inlet temperature of ST/PVT collector	°C
T_out	Outlet temperature of ST/PVT collector	°C
T_a	Ambient outside temperature	°C
T_m	Mean temperature of ST/PVT collector	°C
T_m^0	Initial guess mean temperature of ST/PVT collector	°C
T_red	Reduced temperature of ST/PVT collector	$\mathrm{m^2\,K\,W^{-1}}$
a_1	First order heat loss coefficient of ST/PVT	$\mathrm{W\,m^{-2}\,K^{-1}}$
a_2	Second order heat loss coefficient of ST/PVT	$\mathrm{W\,m^{-2}\,K^{-2}}$
A_c	Surface area of the ST/PVT collector	$\mathrm{m^2}$
N_ST	Number of ST collectors	–
Buffer storage model		
ΔT	Temperature change of buffer storage	K
Q_in	Heat flow inserted into buffer storage	W
Q_out	Heat flow extracted from buffer storage	W
M_w	Water mass in buffer tank	kg
T_wt	Temperature of buffer storage	°C
$T_\mathrm{wt,max}$	Maximum temperature of buffer storage	°C

Symbol	**Definition**	**Unit**
Heat pump model		
COP	Coefficient of performance of heat pump	–
COP_{carnot}	Theoretical Carnot coefficient of performance	–
COP_{system}	System COP including ATES pumping losses	–
ΔT_{HP}	Temperature lift of heat pump	K
T_{source}	Source temperature of heat pump	°C
T_{sink}	Sink temperature of heat pump	°C
A	Temperature-lift coefficient dependent on demand temperature	K
Heat exchanger model		
ΔT_{hex}	Temperature change of fluid across heat exchanger	K
T_{pinch}	Pinch point temperature difference	K
h_{hex}	Specific enthalpy of water leaving heat exchanger	$\mathrm{J\,kg^{-1}}$
h_{vb}	Specific enthalpy of water in vacuum boiler	$\mathrm{J\,kg^{-1}}$
x_{evap}	Mass fraction of water flashed to steam	–
Q_{red}	Reduction in buffer heat demand due to flash evap.	J
Q_{source}	Heat transferred per unit mass of ATES water	$\mathrm{J\,kg^{-1}}$
$Q_{\text{delivered}}$	Total thermal energy delivered per unit mass	$\mathrm{J\,kg^{-1}}$
W_{pump}	Pumping power per unit mass of ATES water	$\mathrm{J\,kg^{-1}}$
M_{ATES}	Mass flow rate of water between ATES wells	$\mathrm{kg\,s^{-1}}$
ATES model		
R	Annual recovery efficiency of ATES	–
R_{th}	Thermal radius of aquifer	m
Ra^*	Modified Rayleigh number for ATES	–
A_{ates}	Curve fitting coefficient for ATES recovery	–
B_{ates}	Curve fitting coefficient for ATES recovery	–
H_{a}	Screen length of ATES well	m
k_a^h	Horizontal permeability of aquifer	$\mathrm{m^2}$
k_a^v	Vertical permeability of aquifer	$\mathrm{m^2}$
μ	Dynamic viscosity of water	Pa s
V_{in}	Annual injected volume of water into ATES	$\mathrm{m^3}$
ρ_{w}	Density of water	$\mathrm{kg\,m^{-3}}$
ΔT_{aq}	Temperature change of aquifer	K
C_{ates}	Thermal capacity of aquifer	$\mathrm{J\,K^{-1}}$
n	Number of ATES well pairs	–
V_{ates}	Volume of ATES	$\mathrm{m^3}$
V_{in}	Annual injected volume into ATES	$\mathrm{m^3}$
C_{w}^{w}	Specific heat capacity of water at warm well temp.	$\mathrm{J\,kg^{-1}\,K^{-1}}$
C_{w}^{c}	Specific heat capacity of water at cold well temp.	$\mathrm{J\,kg^{-1}\,K^{-1}}$
C_r	Specific heat capacity of aquifer rock	$\mathrm{J\,kg^{-1}\,K^{-1}}$
ρ_r	Density of aquifer rock	$\mathrm{kg\,m^{-3}}$
ϕ	Porosity of aquifer	–
T_{aquifer}	Temperature of aquifer	°C
T_{aq}^{w}	Temperature of warm ATES well	°C
$T_{\text{aq,max}}^{\text{c}}$	Maximum permissible temperature of warm ATES well	°C
T_{aq}^{c}	Temperature of cold ATES well	°C
ATES hydraulic model		
D	Inner pipe diameter	m
$\dot{Q}$	Volumetric flow rate per well	$\mathrm{m^3\,s^{-1}}$
V	Flow velocity in pipe	$\mathrm{m\,s^{-1}}$
W_P	Total pumping power	W
η_{pump}	Pump efficiency	–
$\Delta P_{\text{hydraulic}}$	Hydrostatic pressure contribution	Pa

Symbol	**Definition**	**Unit**
$\Delta P_{\text{friction}}$	Frictional pressure drop in pipe	Pa
ΔP_{total}	Total pressure drop in ATES pipe	Pa
g	Gravitational acceleration	$\mathrm{m\,s^{-2}}$
L_{ates}	Depth of aquifer	m
Re	Reynolds number	–
f_D	Darcy friction factor	–
ϵ	Pipe wall roughness	m
Battery storage model		
SOC	State of charge of battery storage	–
ΔSOC	Change in state of charge of battery	–
η_{bat}	Charge and discharge efficiency of battery	–
E_{in}	Energy flow into battery storage	J
E_{out}	Energy flow out of battery storage	J
C_{bat}	Battery capacity	J
System energy balance		
T_{D}	Required industrial process temperature	°C
Q_{D}	Industrial heat demand	J
Q_{HP}	Heat extracted by heat pump	J
Q_{ST}	Thermal energy generated by ST collectors	J
Q_{surplus}	Surplus thermal energy available for ATES charging	J
W_{backup}	Electrical work supplied by backup resistive heater	J
W_{HP}	Electrical work done by HP compressors	J
W_{P}	Electrical work done by ATES hydraulic pumps	J
W_{el}	Total electrical power demand of system	J
W_{grid}	Net electricity consumption from grid	J
W_{PV}	Total electrical energy generated by PV collectors	J
ΔQ	Hourly net thermal energy balance of system	J
M_{steam}	Mass of steam generated by heat pump	kg
x_{evap}	Fraction of mass evaporated in valve	–
D	Constant dependent on demand temperature	°C
M_{ates}	Mass flow rate between ATES wells	kg
L_w	Latent heat of vaporization of water	$\mathrm{J\,kg^{-1}}$
Economic model		
E_{heat}	Discounted total heat delivered to industry	GJ
N	System lifetime	years
$r_{\text{O\&M}}$	Annual O&M cost as fraction of CAPEX	–
DR	Discount rate	–
E_{grid}	Annual grid electricity consumption	MWh
P_{elec}	Industrial electricity price	€/MWh
Q_{industry}	Heat delivered to industry in first year	GJ
SD	Annual degradation rate of solar collectors	–

Acronyms

Acronym	**Definition**
ATES	aquifer thermal energy storage.
CAPEX	capital expenditure.
COP	coefficient of performance.
CPVT	concentrated photovoltaic thermal.
DNI	direct normal irradiation.
ETC	evacuated tube collector.
ETS	Emissions Trading System.
EU	European Union.
FPC	flat plate collector.
HEX	heat exchanger.
HP	heat pump.
HT	high temperature.
LCOH	levelized cost of heat.
OPEX	operational expenditure.
PCM	phase change material.
PV	photovoltaic.
PVMD	Photovoltaic Materials and Devices.
PVT	photovoltaic-thermal.
ST	solar thermal.
STC	standard test conditions.
TES	thermal energy storage.
TTES	tank thermal energy storage.

List of Figures

1.1 Heating demand Europe for different industry sectors adapted from [1]. 2
1.2 Reduced temperature curves for a variation of solar thermal (ST) collectors adapted from [2]. 3
1.3 Flat plate collector on the left and evacuated tube collector on the right[3]. 4
1.4 Illustration of different layers in a glazed photovoltaic-thermal (PVT) module [4]. 5
1.5 Schematic of a vapor compression cycle heat pump highlighting the main components [5]. 6
1.6 Illustration of aquifer thermal energy storage (ATES) and Tank thermal energy storage (tank thermal energy storage (TTES)). 8
1.7 Solar-assisted process heating for industry system model [6]. 10
1.8 Model including solar energy, seasonal storage, and heat pump for residential use [7]. . . 11
1.9 A simplified overview of the components of the energy model. The figure shows how the heat and electricity generation are integrated with storage and a heat pump to provide high-temperature (130–150 °C) steam to industry. The aquifer thermal energy storage (ATES) is used as both the source and sink of the heat pump (HP) depending on the season. 13

2.1 Simplified schematic showing how the ST modules on the left are integrated with the thermal buffer storage on the right. 16
2.2 Flow chart of ST and PVT modeling showing the iterative process which determines the performance. The left loop is used for the solar thermal collector and the photovoltaic thermal collector makes use of both loops to determine the electrical and thermal efficiency of the collector. 19
2.3 High vacuum insulated flat plate ST collector. 20
2.4 High vacuum insulated flat plate PVT collector. 20
2.5 Simplified HP schematic highlighting the main components of the TNO and Standard Fasel prototype. Adapted from Ramirez et al. [8]. 21
2.6 The COP characteristics of the numerical HP model (orange) are compared against the COP_{carnot} characteristics (blue). The actual prototype performance (yellow). 22
2.7 Temperature of heat exchanger integrated with the ATES in two scenarios: Surplus operation where cold water is pumped from the cold to the warm well and heated through steam condensation and shortage operation where the ATES is delivering heat to the HP by pumping water from the warm to the cold well. The reference warm and cold well temperatures are also presented. 23
2.8 ATES operation in summer (left) and winter (right) showing the temperature ranges and important well parameters. Adapted from Bloemendal et al. [9]. 24
2.9 Illustration of water moving up through an ATES pipe on the left and a cross section of the pipe on the right. 27
2.10 Illustration of the individual components into an integrated industrial system. 29

3.1 Schematic diagram of an industrial heating system comprising out of solar collectors (ST, PVT, and photovoltaic (PV)), an ATES system, heat exchangers, a buffer storage tank, and a HP 30
3.2 Configuration 1 (reference): Resistive heater heat generation. 31

3.3 Configuration 2 (reference): ST heat generation with HP. . . . 31
3.4 Configuration 3 (reference): ATES seasonal storage. . . . 32
3.5 Configuration 4 (reference): PV electricity generation. . . . 32
3.6 Configuration 5 (main): Battery energy storage system. . . . 32
3.7 Configuration 6 (main): PVT heat and electricity generation. . . . 32
3.8 Illustration of operational Mode I: Balanced operation. System relies on buffer storage tank to supply heat and no surplus generation takes place, with buffers storage operating temperatures constrained by $80 \leq T_{\mathrm{wt}} \leq 120$ °C, while $T_{\mathrm{D}} \in \{130, 150\}$ °C. . . . 34
3.9 Illustration of operational Mode IIA: Charging of ATES. Surplus heat from the ST collectors is used to charge the ATES, with ATES operating temperatures constrained by $90 \leq T^{\mathrm{w}}_{\mathrm{aq}} \leq 150$ °C, $40 \leq T^{\mathrm{c}}_{\mathrm{aq}} \leq 100$ °C. . . . 35
3.10 Illustration of operational Mode IIB: Curtailment ST. Excess heat generation in the ST collectors is curtailed, where $T_D \in \{130, 150\}$ °C. . . . 36
3.11 Illustration of operational Mode IIIA: Discharge ATES. The ATES warm well supplies heat to the HP, with ATES operating temperatures constrained by $90 \leq T^{\mathrm{w}}_{\mathrm{aq}} \leq 150$ °C, $40 \leq T^{\mathrm{c}}_{\mathrm{aq}} \leq 100$ °C, while $T_D \in \{130, 150\}$ °C. . . . 37
3.12 Illustration of operational Mode IIIB: Backup electrical boiler. Shortage of heat requires a backup electrical boiler to be used for heat generation, where $T_{\mathrm{D}} \in \{130, 150\}$ °C. . . . 38
3.13 Illustrative example of HP compressor and hydraulic pump power consumption during Mode IIIA operation for $T_{\mathrm{ATES}} = 120$ °C and $T_{\mathrm{D}} = 130$ °C. The compressor power increases and the pumping power decreases with increased HP temperature lift. . . . 39
3.14 coefficient of performance (COP) of a heat pump including hydraulic pumping power from the ATES. The dotted line shows the COP without hydraulic pumping power. $T_{\mathrm{D}} = 130$ °C, depth = 400 m. Optimum temperature lifts for varying ATES temperatures are included. . . . 40
3.15 COP of a heat pump including hydraulic pumping power from the ATES. The dotted line shows the COP without hydraulic pumping power. $T_{\mathrm{D}} = 150$ °C, depth = 400 m. Optimum temperature lifts for varying ATES temperatures are included. . . . 41
3.16 Flow chart depicting the control strategy used in this thesis. A clear distinction is made between the default, surplus, and shortage modes. . . . 42
3.17 The steam demand for the paper & pulp, and food & beverage industries for three days 44
3.18 Monthly weather data Delft. . . . 45
3.19 Monthly weather data Seville. . . . 45
3.20 Hourly weather data Delft for three weeks. . . . 45
3.21 Hourly weather data Seville for three weeks. . . . 45
3.22 PV yield simulation results compared against Solargis data. . . . 46
3.23 Annual ST collector efficiency results compared against literature. . . . 46
3.24 Thermal and electrical efficiency of the PVT collectors for Delft. . . . 47
3.25 Thermal and electrical efficiency of the PVT collectors for Seville. . . . 47
3.26 Development of ATES temperatures for three ST collector quantities over a five year period. . . . 48
3.27 Monthly COP distribution of the HP for the 100,000 ST module scenario using the Paper & Pulp heating demand profile, and Delft weather data. . . . 49

4.1 Annual grid electricity consumption for different system configurations. Config. 1: Resistive heater, Config. 2: ST with HP, Config. 3: ATES, Config. 4: PV. Config. 5: Battery, Config. 6: PVT. . . . 52
4.2 Annual peak grid electricity consumption for different system configurations. Config. 1: Resistive heater, Config. 2: ST with HP, Config. 3: ATES, Config. 4: PV. Config. 5: Battery, Config. 6: PVT. . . . 53
4.3 Thermal and electrical efficiency of ST and PV respectively for the Delft Food & Beverage scenario. . . . 54
4.4 Activation of operational modes for the Delft Food & Beverage scenario. . . . 55
4.5 Temperature of the buffer storage and warm ATES well for the Delft Food & Beverage scenario. . . . 55
4.6 System COP for the Delft Food & Beverage scenario. . . . 56

4.7 Electricity consumption of Mode I, Mode II, and Mode III for the Delft Food & Beverage scenario. . . . 57
4.8 Electricity demand, generation and grid consumption in the Delft Food & Beverage scenario. . . . 57
4.9 Temperature of the buffer storage and warm ATES well for the Delft Paper & Pulp scenario. 58
4.10 System COP for the Delft Paper & Pulp scenario. . . . 59
4.11 Electricity demand, generation and grid consumption in the Delft Paper & Pulp scenario. 60
4.12 Thermal and electrical efficiency of ST and PV respectively for the Seville Food & Beverage scenario. . . . 61
4.13 Activation of operational modes for the Seville Food & Beverage scenario. . . . 61
4.14 Temperature of the buffer storage and warm ATES well for the Seville Food & Beverage scenario. . . . 62
4.15 System COP for the Seville Food & Beverage scenario. . . . 63
4.16 Electricity consumption of Mode I, Mode IIA, and Mode IIIA for the Seville Food & Beverage scenario. . . . 63
4.17 Electricity demand, generation and grid consumption in the Seville Food & Beverage scenario. . . . 64
4.18 System COP for the Seville Paper & Pulp scenario. . . . 65
4.19 Electricity demand, generation and grid consumption in the Seville Paper & Pulp scenario. 66
4.20 Optimal performing ST fraction for different scenarios. . . . 68
4.21 System performance for varying collector quantities and scenarios. . . . 68
4.22 System performance for varying ATES well pair quantities and scenarios. . . . 69
4.23 System performance for varying battery quantities and scenarios. . . . 70
4.24 Heatmap Delft Food & Beverage total consumption. . . . 71
4.25 Heatmap Delft Food & Beverage peak load. . . . 72
4.26 Heatmap Seville Food & Beverage total consumption. . . . 72
4.27 Heatmap Seville Food & Beverage peak load. . . . 73
4.28 Heatmap presenting the levelized cost of heat (LCOH) of the Delft Food & Beverage scenario for varying system sizes. . . . 76
4.29 capital expenditure (CAPEX) Delft Food & Beverage scenario. . . . 77
4.30 LCOH as function of discount rate for the Delft Food & Beverage scenario. . . . 77
4.31 Heatmap presenting the LCOH of the Seville Food & Beverage scenario for varying system sizes. . . . 77
4.32 CAPEX Seville Food & Beverage scenario. . . . 78
4.33 LCOH as function of discount rate for the Seville Food & Beverage scenario. . . . 78
4.34 CAPEX Seville Food & Beverage scenario 100% grid independence. . . . 78
4.35 LCOH as function of discount rate for the Seville Food & Beverage scenario 100% independence. . . . 78

A.1 Annual grid electricity consumption for water tank and phase change material (PCM) thermal buffer storage technologies. . . . 95
A.2 Annual peak grid electricity consumption for water tank and PCM thermal buffer storage technologies. . . . 96
A.3 Weekly and annual storage temperatures for the PCM buffer of 83 °C using the Delft Food & Beverage scenario. . . . 97
A.4 Weekly and annual storage temperatures for the PCM buffer of 117 °C using the Delft Food & Beverage scenario. . . . 97
A.5 Annual COP comparison for two PCM phase change temperatures using the Delft Food & Beverage scenario. . . . 98
A.6 Annual electrical power consumption comparison for two PCM phase change temperatures using the Delft Food & Beverage scenario. . . . 98
A.7 Weekly and annual storage temperatures for the PCM buffer of 83 °C using the Seville Paper & Pulp scenario. . . . 99
A.8 Three week storage temperature comparison for two PCM phase change temperatures using the Seville Paper & Pulp scenario. . . . 99

A.9 Three week COP comparison for two PCM phase change temperatures using the Delft Food & Beverage scenario. 100
A.10 Annual comparison of electrical demand and grid consumption for two phase change temperatures. 101

B.1 Thermal losses due to horizontal transport of water through pipes. 104
B.2 Fraction of hydrostatic and friction pressure losses for horizontal transport through pipes. 104
B.3 COP of a heat pump including pumping losses and heat loss for long horizontal transport distances. The dotted line shows the COP without hydraulic pumping power. $T_{\mathrm{D}} = 130$ °C, depth = 400 m, $T^{\mathrm{w}}_{\mathrm{aq}} = 120$ °C 105
B.4 COP of a heat pump including pumping losses and heat loss for long horizontal transport distances. The dotted line shows the COP without hydraulic pumping power. $T_{\mathrm{D}} = 150$ °C, depth = 400 m, , $T^{\mathrm{w}}_{\mathrm{aq}} = 120$ °C 106

C.1 Thermal and electrical efficiency of PVT modules for the Delft Food & Beverage scenario. 107
C.2 Electricity demand, generation and grid consumption in the Delft Food & Beverage scenario with PVT. 108
C.3 Temperature of the buffer storage and warm ATES well for the Delft Food & Beverage scenario with PVT. 109
C.4 Electricity demand, generation and grid consumption in the Delft Paper & Pulp scenario with PVT. 109
C.5 Temperature of the buffer storage and warm ATES well for the Delft Paper & Pulp scenario with PVT. 110
C.6 Thermal and electrical efficiency of PVT modules for the Seville Food & Beverage scenario. 110
C.7 Temperature of the buffer storage and warm ATES well for the Seville Food & Beverage scenario with PVT. 111
C.8 Electricity demand, generation and grid consumption in the Seville Paper & Pulp scenario with PVT. 112
C.9 System performance for varying PVT collector quantities. 113
C.10 System performance for varying PVT and ST quantities and ratios. 113

List of Tables

1.1 LCOH for solar-assisted industrial heating scenarios in literature. 10

2.1 Parameters flat plate ST collectors 18
2.2 Aquifer thermal energy storage parameters 26

4.1 System performance study parameters 52
4.2 Economic parameters used in the LCOH assessment. 75
4.3 LCOH and CAPEX contributions for three different scenarios. 79

A.1 Parameters for phase change material heat storage [10] 95
A.2 Estimated heat exchanger areas at peak design duty. 102

Chapter 1

Introduction

1.1. Industrial heating demand and net congestion

The European Union (EU) has set the ambitious goal to be the first climate-neutral continent by 2050 [11]. One of the key challenges in achieving climate neutrality is the decarbonization of industrial process heating. Industry represented 24.6% of the final energy consumption in the EU in 2023 [12]. Two thirds of industrial energy consumption comes from industrial heating [13]. Consequently, decarbonization of industrial heating is a significant step towards a renewable future, as it accounts for around 16.4% of the final energy consumption in the EU. The need for alternatives to fossil fuel energy carriers for industry is further reinforced by the price volatility of imported energy carriers such as natural gas. Following the Russian invasion of Ukraine in 2022, European gas prices increased by more than 200% [14], resulting in significant increases in operational cost for industry. Furthermore, European dependence on imported fossil fuels raises strategic concerns about energy security [15]. Transitioning industrial heating away from natural gas therefore serves two purposes: reducing carbon emissions and securing European energy autonomy.

One of the most promising technologies for generating industrial heat is the industrial heat pump (HP). When powered with renewable electricity, the carbon footprint of these HPs is negligible. One of the main advantages of using a HP is the high efficiency that can be reached. Industrial HPs typically operate at a coefficient of performance (COP) in the range of 2–5 [16]. This corresponds to the delivery of 2–5 J of thermal energy per joule of electrical energy consumption. Current industrial HPs are capable of reaching 150 °C, and HPs that can reach up to 200 °C are currently in development [17].

Figure 1.1 shows the heat demand, within the temperature range accessible by heat pump technology, of different industrial sectors in Europe [1]. The total heat consumption within the 100–150 °C range adds up to 192.36 TWh/year, while heat consumption within the 150–200 °C range adds up to 80.11 TWh/year. When combined these add up to approximately 20% of total industrial heating demand in Europe, indicating a substantial potential market for industrial heat supplied by HP technologies. The food and beverage industry is especially interesting since there is substantial heating demand using temperatures within the accessible range for industrial HPs. The paper, pulp, and print industry is also a potentially interesting sector, since a large fraction of heat in this sector is at temperatures slightly higher than 150 °C which is close to currently available industrial heat pumps. Additionally, HPs are able to reach progressively higher temperatures as advances in compressor design and working fluids are realized. A small selection of the processes that make use of heat between 100 to 200 °C are drying, distillation, and cooking [18].

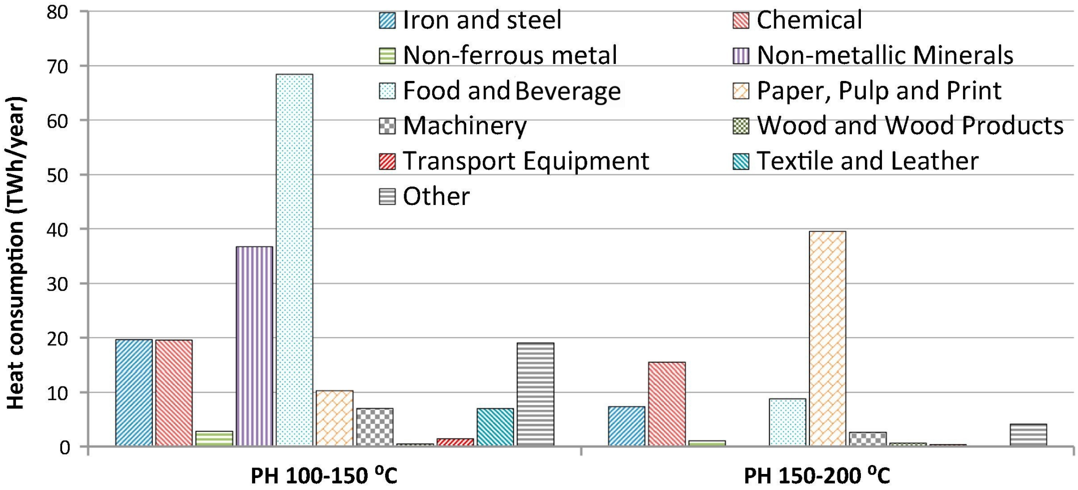

Figure 1.1. Heating demand Europe for different industry sectors adapted from [1].

When industry switches from fossil fuel use to electric HPs, a high-capacity electrical grid connection is required to meet the increased power demand. Although industrial heat pumps offer substantial efficiency and emissions benefits, their large-scale deployment introduces significant challenges for electricity infrastructure. The additional electricity demand can be difficult to realize in countries where the electrical grid is already used maximally. The Netherlands is already facing significant grid congestion challenges and more European countries are following. The additional electrical demand of heating, industry, and transport which are switching away from fossil fuels, in combination with the intermittent generation of electricity from solar and wind energy are difficult to integrate in the current electrical grid [19]. According to the International Energy Agency (IEA) there are ten thousand large consumers waiting for a connection to the electrical grid of the Netherlands at this moment [20]. Grid congestion issues represent a major bottleneck for the large-scale implementation of low emission heating technologies in industry. To enable large industrial parties to switch to renewable energy, alternative strategies have to be considered.

One potential strategy to address these challenges is to make industry (partly) self-sufficient. This entails that industrial facilities generate their own energy locally. This can be achieved by solar energy, which is characterized by low levelized costs of energy and wide availability [21]. Both heat and electricity can be harvested, which could be used for industrial processes [22]. Annual solar irradiance depends on the geographic location of the solar system. A large fraction of European industry is located at higher latitudes which are characterized by lower annual irradiation and significant seasonal irradiance imbalance. Most industries operate year round to achieve maximal production output using the available equipment. Consequently, seasonal energy storage is required to mitigate excessive demand-side management, which is associated with lower industrial efficiency and additional costs [23]. Through the combination of solar energy generation and seasonal storage, industry will potentially be able to switch to renewable energy without being restricted by electricity grid congestion.

Solar energy generation technologies, including solar thermal, photovoltaic thermal, and photovoltaic are discussed in Section 1.2. In Section 1.3, HPs are discussed, which are used to bring water to higher temperatures according to industry demand. Section 1.4 covers the thermal energy storage that is needed for the year-round supply of process heat. Finally, previous research on integrated heating systems are discussed in Section 1.5.

1.2. Solar energy

As discussed in Section 1.1, solar energy offers the capability to supply both electrical and thermal energy to industrial applications. However, the suitability of solar heat strongly depends on the required temperature for industrial process heating. Multiple technologies can be used to supply industrial heating, offering specific advantages and disadvantages. Solar energy conversion technologies relevant to industrial applications can be broadly categorized into photovoltaic (PV), solar thermal (ST), and a combination of both photovoltaic-thermal (PVT). For higher temperature outputs concentrated PVT/ST can be utilized, which is discussed in Section 1.2.4.

1.2.1. Photovoltaic systems

PV is a mature technology in which incident photons are converted into electron-hole pairs, which are subsequently separated and collected at the contacts. Through this process an electric current is generated. This electricity can be used in HPs to provide heating for industry. Currently, most commercial PV modules are made using monocrystalline silicon PERC cells which operate at around 22–23% conversion efficiency under standard test conditions [24]. Continued research efforts into PV technology result in significant efficiency increases year by year. New PV technologies such as TOPCon and tandem cells provide significant potential efficiency improvements in the future, to eventually reach module efficiencies of more than 35% [25].

PV technology is currently one of the most promising technologies for generating renewable energy. PV module prices have seen a sharp decline over the last decades [26], making PV a cheap option in many places around the world. Although the electric efficiency of PV technologies is consistently improving [27], photovoltaics still experience high intrinsic losses. Up to 75% of incident solar radiation is converted into heat instead of usable electricity [28]. Consequently the operating temperature of the cell increases, which reduces the electrical solar cell performance [29].

1.2.2. Solar thermal

ST collectors generate heat directly by absorbing solar radiation and converting it into thermal energy. The performance of ST depends on the ambient temperature, irradiance and the temperature of the working fluid. The thermal efficiency of a ST collector can be described using the steady state method, as presented by Obstawski et al. [30]. In this method the efficiency is a function of the zero loss coefficient, the reduced temperature, and two coefficients which can be experimentally determined or retrieved from physical model simulations. The equation and coefficients are further discussed in Section 2.2.2. As a general rule, the efficiency decreases with increasing working fluid temperature or decreasing irradiance, as illustrated in Figure 1.2.

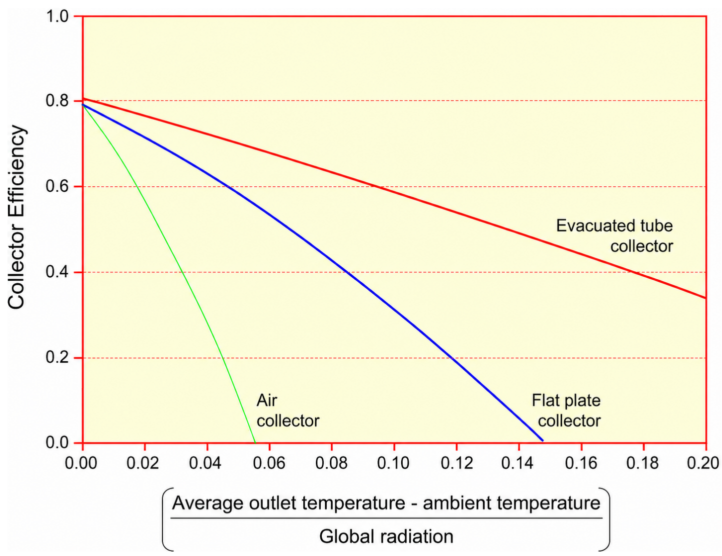

Figure 1.2. Reduced temperature curves for a variation of ST collectors adapted from [2].

The two most common ST technologies are displayed in Figure 1.3, flat plate collector (FPC) and evacuated tube collector (ETC). This study focuses on liquid-based ST collectors, since air-based ST collector efficiency decreases rapidly under elevated temperatures, as illustrated in Figure 1.2.Flat plate collectors (FPCs) consist of a dark absorber plate coupled to fluid carrying tubes that extract heat from the absorber plate. This is encapsulated by insulating layers to prevent heat loss to the environment. Due to insulation, FPCs operate at higher temperatures than regular PV modules. FPCs generally operate at temperatures from 30 to 80 °C [18] but can reach temperatures of up to 200 °C with high-vacuum insulation [31]. The efficiency of FPCs is strongly dependent on ambient conditions and the flow rate of the working fluid. In general, 50–70% thermal efficiency can be assumed as a reasonable reference under test conditions [32].

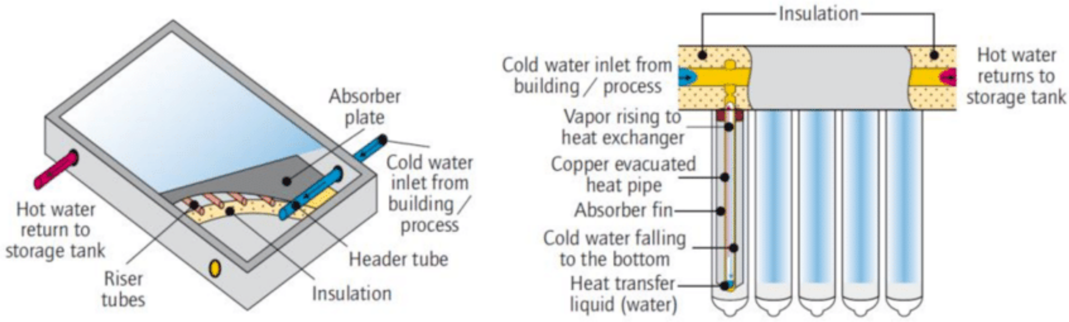

Figure 1.3. Flat plate collector on the left and evacuated tube collector on the right[3].

ETC collectors consist of a series of glass tubes. A vacuum is created within these tubes that minimizes heat losses through convection and conduction. Within these glass tubes an absorber is located which captures solar radiation. The heat is collected using a circulating fluid. Due to the very high insulation, evacuated tube collectors (ETCs) can reach significantly higher temperatures in the range of 50–200 °C. ETC generally perform better than flat plate collectors at the same conditions [33]. This is illustrated by the much steeper reduced temperature slope of the FPC in Figure 1.2. Under favorable test conditions ETC are able to reach efficiencies close to 90% [34]. In general, better insulation leads to higher performance due to a decrease in thermal losses to the ambient air.

1.2.3. Photovoltaic thermal

A third option are PVT collectors. These are a combination of PV and ST technologies, able to generate electric current as well as heat. This sets them apart from ST and PV modules, allowing them to achieve higher overall efficiencies. According to a study by Santbergen et al. [35], the thermal efficiency of PVT systems is up to 19% lower than that of a ST system and the electrical efficiency is up to 14% lower compared to pure PV systems. Although the individual thermal and electrical efficiency of PVT collectors is lower than that of dedicated ST and PV collectors, the combined output of two PVT collectors is generally higher than that of one ST collector next to one PV module. Consequently, PVT systems typically require a smaller total collector area than an equivalent ST plus PV installation [36]. Under certain circumstances the electrical performance of PVT can exceed that of pure PV. When very low temperature output is required the PVT module will be colder than that of a regular PV module. This results in a higher electrical efficiency at the cost of a lower output temperature. PVT modules can generally be divided into two main categories: Air-based PVT and liquid-based PVT for which the most common working fluid is water. Water-based modules are more efficient than air-based PVT modules due to the better thermo-physical properties of water compared to air [37]. This study focuses on water-based PVT, since this technology is more suitable for industry utilization. Another subdivision that can be made is the distinction between glazed and unglazed PVT panels. Glazed PVT modules have an additional insulation layer at the front which prevents heat losses, as illustrated in Figure 1.4. This enables glazed PVT to reach higher temperatures and thermal efficiency. One downside of these panels is that the electrical performance of these modules is lower compared to unglazed or regular PV modules since they generally operate at higher temperatures [38]. Unglazed PVT systems operate at significantly lower temperatures and are therefore not suitable for industrial use [22]. For this reason this thesis will focus on glazed PVT modules.

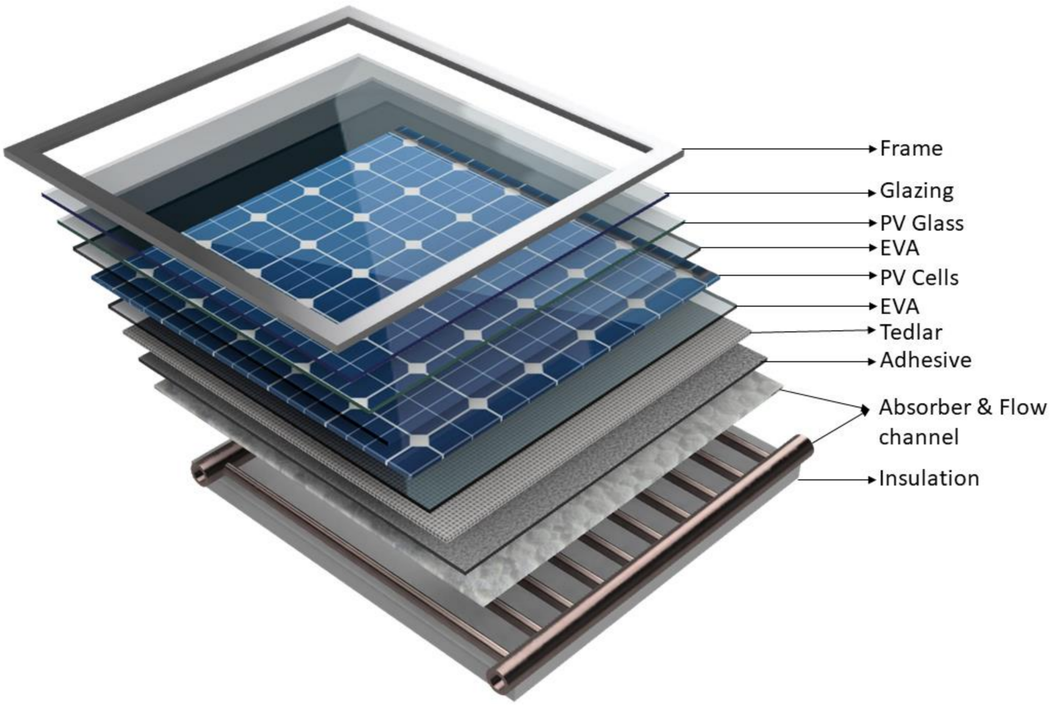

Figure 1.4. Illustration of different layers in a glazed PVT module [4].

According to a review study by Lamnatou et al. [39], thermal efficiency of water-based PVT ranges between 50–85% while the electrical efficiency is in the range of 12–15%, based on systems using c-Si cells with a rated efficiency of approximately 15% at standard test conditions (STC). The relatively low electrical efficiency is attributable to optical losses from the front glazing, increased reflection from low-emissivity coatings, and elevated operating temperatures, which together reduce efficiency by approximately 7% [40]. Modern high-efficiency c-Si cells (20–23% at STC) would yield correspondingly higher electrical output when integrated into PVT collectors. The reviewed systems operated at 50–60 °C under Chinese and European climate conditions, with the majority employing glazed collectors. The thermal and electrical performance depend substantially on the working fluid temperature, the flow rate, the received irradiance, and the ambient temperature.

1.2.4. Concentrated solar energy

Concentrated solar energy can be useful in industrial processes when higher temperatures are needed. The basic principle of concentrated solar energy is that light is focused onto a collector which results very high local irradiance. Concentrated systems exist for PV, ST, and PVT but the focus is on the latter two in this research. There are multiple common ways to concentrate the light as presented by Kumar et al. [18].

Concentrated ST and PVT are able to reach very high temperatures. This can be very useful for industrial applications which generally need higher temperatures than that which can be generated using unconcentrated PVT and ST. Some concentrated ST technologies such as heliostat field reflectors are able to reach temperatures up to 2000 °C [18]. Most concentrated ST systems operate at substantially lower working temperatures.

Parabolic through collectors can reach temperatures of up to 400 °C, far beyond medium temperature heat requirements considered in this thesis. On top of that parabolic through collectors are a relatively simple technology, requiring only one axis of movement. concentrated photovoltaic thermal (CPVT) operates at slightly lower temperatures of around 100 to 250 °C [39]. In return, it is able to generate electricity which can be used to power HPs. Many concentrated photovoltaic thermal (CPVT) systems designs utilize high efficiency PV cells such as triple junction cells. This allows CPVT systems to reach higher electrical efficiency (20% to 30%) than unconcentrated PVT. In return, the thermal efficiency is slightly lower since part of the incoming radiation is transferred into electrical energy.

It should be noted that, unlike unconcentrated solar collectors, concentrated collectors are not able to use diffuse irradiance effectively [41]. The fraction of diffuse irradiance can be high in some locations, which greatly impacts the performance of concentrated solar collectors. Especially in the regions at high latitude the diffuse irradiance fraction can be large, in the Netherlands approximately 50% of incoming irradiance is diffuse [42]. Consequently, high latitude regions might be unsuitable for concentrated solar systems.

Although industry relevant temperatures of 150 °C can be reached directly by some solar thermal collectors, a higher thermal efficiency may be obtained if the ST collector generates somewhat lower temperature heat (100 °C). This heat can then be upgraded to 150 °C by a heat pump. Depending on the climate multiple different collector types can be used to provide 100 °C, from FPC to parabolic through collectors which all have distinct advantages and disadvantages. For this reason care has to be taken when selecting the type of solar collector, since system performance can be affected significantly.

1.3. Heat pumps

Heat pumps use electrical energy to upgrade heat from a lower temperature source to a higher temperature sink, typically through a vapor compression cycle [43]. However, other HP designs are available, such as semi-open type steam compression heat pumps which generate steam directly [44]. A prototype of such HP design, which can generate 160 °C steam for industry, has been developed by Standard Fasel and TNO [8]. HPs are an attractive option for industry to provide process heating with a low carbon footprint since they primarily consume electricity. A schematic of a vapor compression HP is shown in Figure 1.5. Heat pumps utilize refrigerant as a working fluid. The choice of refrigerant is constrained by the required source and sink temperatures, pressure levels, thermodynamic performance and environmental considerations such as global warming potential [45].

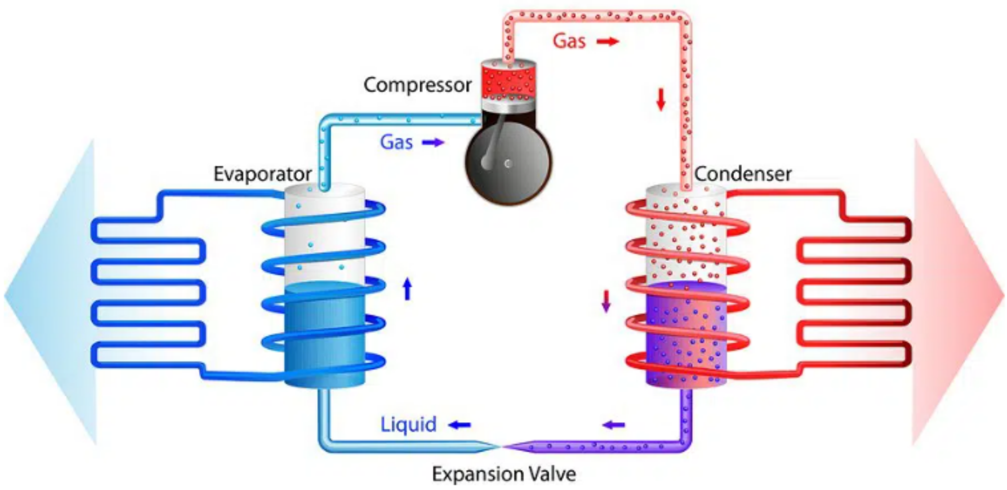

Figure 1.5. Schematic of a vapor compression cycle heat pump highlighting the main components [5].

Vapor compression HPs consist of 4 main components which are listed below.

1. Evaporator: The evaporator extracts heat from a low temperature region. This causes the refrigerant to evaporate into a gas.
2. Compressor: The compressor uses electricity to compress the gas. The compression of the gas increases the temperature.
3. Condenser: In the condenser, heat is extracted from the gas. This causes the gas to condense into a liquid.
4. Expansion valve: In the expansion valve the pressure of the refrigerant drops.

HPs can be divided into conventional HPs which have heat sink temperatures of up to 80 °C, high temperature (HT)-HPs that supply heat of up to 100 °C, and very HT-HPs for which the heat sink temperatures are above 100 °C [46]. Very HT-HPs are mainly used in industry because delivered temperatures are beyond what is necessary for domestic heating. This study focuses on very high temperature heat pumps suitable for industrial process heating applications. These HPs can upgrade water from the ST/PVT collectors when output temperatures are not high enough for direct industrial consumption.

The performance of a HP can be described using the COP value. The thermodynamic (theoretical) maximum COP can be described using Equation 1.1, where T_{sink} and T_{source} describe the output and input temperature in Kelvin respectively.

$$\text{COP}_{\text{carnot}} = \frac{T_{\text{sink}}}{T_{\text{sink}} - T_{\text{source}}} \tag{1.1}$$

HPs generally operate at a fraction of the thermodynamic maximum COP. For a heat pump which delivers heat at 150 °C and has a heat source of 80 °C, the COP_{carnot} is 6.0. In practice, industrial HPs generally operate at a COP between 40–60% of COP_{carnot} [47]. As presented in an experimental study of a HP by Ramirez et al. [8], the input temperature has a significant impact on the performance of a HP. When integrating HPs into a system with (intermittent) solar heat generation, T_{source} can vary greatly. Therefore, it is important to use accurate input temperatures per hour instead of describing the HP performance using a single COP value [48]. The temperature lift, defined as the difference between sink and source temperatures, is a primary determinant of HP performance.

1.4. Thermal energy storage

Solar energy is an intermittent energy resource. There are both daily as well as seasonal fluctuations in the availability of solar energy. Consequently, thermal energy storage (TES) is required to balance solar heat supply and industrial demand. The temperature of the thermal energy storage (TES) should be high enough for the HP to be able to operate effectively. As a result, the required temperature of the seasonal storage is largely dependent on the specific temperature demand from industry in combination the operational range of the HP. For this thesis, storage mediums capable of delivering heat at temperatures between 80 and 150 °C are considered. This thesis proposes three key criteria for assessing the suitability of a TES system for industrial applications: the heat has to be able to be stored seasonally without significant losses, the temperature of the storage has to be high enough to be useful for industry and the system has to be financially competitive.

TES can be divided into three categories: sensible heat storage, latent heat storage and thermo-chemical heat storage [49]. Sensible heat storage is the most mature and works through fluctuating the temperature of the storage system. Water tank thermal energy storage (TTES) is the most widely deployed technology for sensible industrial heat storage [50]. Although this technology is mature and available at low cost, it is not as suitable for seasonal thermal energy storage in industry, as impractically large storage volumes are required for seasonal storage [51].

One of the most promising sensible TES technologies for seasonal storage is aquifer thermal energy storage (ATES), illustrated in Figure 1.6. ATES systems can store large volumes of heated water, up to 1,000,000 m^3 per year [52]. Low-temperature systems operating below 25 °C are widely deployed in the Netherlands, commonly at depths of 20–150 m [53]. Medium-temperature systems operating between 25–90 °C have been demonstrated at research scale, including a recent TU Delft project investigating ATES up to 90 °C at depths of approximately 200 m [54]. High temperature ATES (HT-ATES), operating above 90 °C, as required for industrial heating are still in an early development stage and currently no large-scale systems are operational. However, numerical modeling results have been promising with HT-ATES (up to 300 °C) achieving up to 85% recovery efficiency under favorable geological conditions [55].

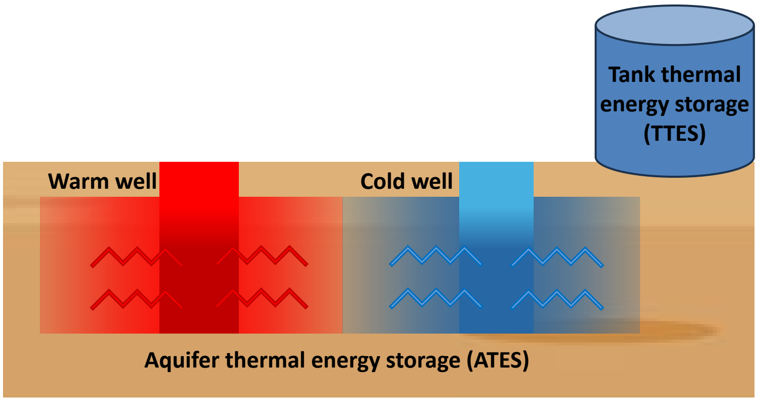

Figure 1.6. Illustration of aquifer thermal energy storage (ATES) and Tank thermal energy storage (TTES).

Although HT-ATES systems have some significant advantages compared to other storage mediums, there are also a number of potential risks associated with these systems. Elevated temperatures increase the risk of clogging and corrosion in the ATES infrastructure [56]. High temperature systems also have an increased risk for geochemical reactions to take place in the aquifer and precaution is needed to prevent thermal contamination of the shallow ground water reserves [57].

In addition, HT-ATES systems require specific geological formations such as a porous aquifer deep underground with an insulating layer on top to prevent groundwater contamination. For temperatures beyond 100 °C, care has to be taken to not exceed the boiling point of water. Since boiling point increases with pressure and pressure increases with depth, HT-ATES systems have to be placed deeper underground (beyond 400 meter) to maintain water in liquid form [55, 57]. High temperatures (beyond 100 °C) and deep geological placement make HT-ATES systems similar to those used for geothermal energy generation. It should be noted that the technologies serve fundamentally different purposes. Where geothermal systems extract heat from the earth as an energy source, ATES systems store externally generated heat which can later be extracted. Nonetheless, insights from geothermal drilling and well design can inform the further development of HT-ATES systems.

Latent heat storage is a less mature technology, however, it does provide some specific advantages. Latent heat storage is based on phase change materials (PCM). The temperature of the TES is dependent on which material is chosen, a comprehensive overview of different materials with different phase change temperatures is given in research by Sarbu et al. [58]. A key advantage of latent heat storage is the stable temperature during phase change, which can be beneficial for process heat applications requiring a constant supply temperature. However, the large volumes of PCM material required for seasonal storage, combined with the high cost of suitable phase change materials compared to water, make this technology considerably more expensive than ATES systems [59].

For large-scale seasonal storage, HT-ATES emerges as the most technically and economically plausible option, given its low cost per unit of stored energy and scalability compared to tank and PCM storage [51, 59, 60]. For short-term storage cycles, water tank TES remains the most mature and widely deployed technology [50], while PCM storage is considered as an alternative for comparison in this study. Previous research on solar energy combined with seasonal storage has mainly focused on sensible heat storage [7, 61–63] but some research also involves latent and thermo-chemical storage [64, 65]. Since most of this research is focused on residential heating below 80 °C, these studies are not directly applicable to industrial heating applications requiring temperatures of 130–150 °C.

1.5. System models

This section reviews existing literature on solar systems for industrial heat supply. Firstly, system models that utilize solar heat generation for industrial applications are considered. Secondly, research which combines solar energy and seasonal storage are discussed.

1.5.1. Solar energy for industry

Previous research has demonstrated the technical potential for solar-assisted process heat generation for industrial applications [6, 66–69]. Kumar et al. [66] concludes that the most important factors for financial attractiveness of ST in industry are the type of solar collector, process temperature and pressure requirements, availability of solar radiation, and to what extent TES is utilized. The research concludes that hot water (85–95 °C) generation with flat plate collector systems can often be economically competitive, but that the concentrated collectors for steam generation (140–180 °C) have long payback times. The study does not consider the use of HPs for increasing the output temperatures reached by flat plate collectors to the industrial demand temperatures.

Silva et al. [67] have developed a model for a high temperature ST system providing heating for industry. A co-simulation model is used combining TRNSYS and Modelica software. The model has been validated using an existing ST plant in Spain. Finally, the model was applied on an industrial application in Spain requiring 150 °C steam. The system achieved an annual solar fraction of 67% without significant heat storage. This demonstrates the feasibility of ST systems, especially for locations with sufficient direct irradiation like Spain. However, the study does not consider seasonal TES or peak grid load reduction, which are essential requirements for northern European climates and congested electricity networks.

Allouhi et al. [70] studied the use of ETC for 60–90 °C temperature industry heating in Morocco. The payback period was optimized by varying the collector area and storage tank volume. The study concludes that the collector area is more important for the performance compared to the storage tank volume. However, these results are difficult to extrapolate to locations with lower solar irradiance or significant seasonal fluctuations.

Mousa et al. [68] have modeled the performance of different solar collector systems for industrial process heating of 180 °C in TRNSYS. Different collector configurations were considered, including PV, ST, coupled PVT, beam split PVT, and PV combined with ST. An important performance criterion was the direct normal irradiation (DNI) ratio at the modeled location. The performance of concentrated systems is significantly worse when the direct normal irradiation (DNI) ratio is below 50% since concentrated systems do not utilize diffuse light effectively. The highest solar fraction (84.2%) was reached by a thermally uncoupled concentrated PVT system. For locations with a low DNI ratio these systems perform poorly. The second highest solar fraction (79.1%) was reached by evacuated flat plate systems which have a high annual efficiency at process temperature. Since these systems effectively utilize the diffuse irradiance they were not affected much by a low DNI ratio and were the overall best performing technology. PV and thermally coupled PVT systems demonstrated lower solar fractions. These findings support the selection of evacuated flat plate ST collectors in this thesis, which prioritizes performance under the diffuse irradiance conditions characteristic of northern European climates. However, neither seasonal thermal energy storage nor peak grid load reduction are considered, leaving the system-level integration challenges for northern climates unaddressed.

Another study conducted by Mousa et al. [69] highlights that a mix of technologies gives the best performance in most scenarios. It also provides a methodology to decide on the best solar technology mix per location. This methodology uses financial and environmental parameters to optimize the solar mix per location. Kumar et al. [6] discusses a solar-assisted process heating setup displayed in Figure 1.7. PVT and ST are used in tandem to generate heated water around 60 °C for process heating. A model is created in TRNSYS and validated using an experimental setup. This setup is able to deliver low temperature process heating of 60 °C to industry. While the designed system gives an interesting example of integrated solar assisted industrial heating, it operates under lower temperatures and does not employ a HP.

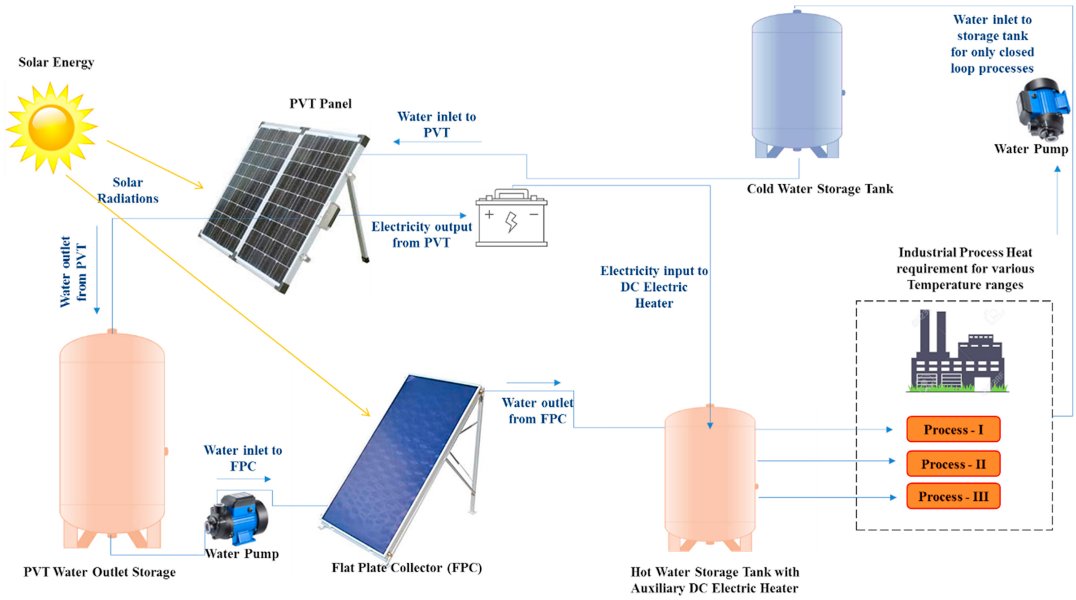

Figure 1.7. Solar-assisted process heating for industry system model [6].

For large-scale implementation of solar-assisted industry heating it is crucial that the selected mix of technologies is economically competitive in addition to being technically feasible. Table 1.1 presents the levelized cost of heat (LCOH) of solar-assisted industrial heating systems in the literature. The LCOH is expressed in €/MWh alongside a brief description of each system configuration. Considerable variation in LCOH are observed across different locations and system architectures. The reviewed literature generally does not target a 100% solar fraction, generating a part of the heat using other sources (e.g. natural gas). Furthermore, none of these studies incorporate seasonal thermal storage. For high irradiance climates such as South-East Asia and Spain, where systems only employ ST collectors and do not require high solar fractions, the LCOH can be as low as 35 €/MWh [71–73]. For western European climates such as Austria and the Netherlands, the cheapest reported results indicated LCOH values around 80 €/MWh [71, 73, 74]. For more northern European climates, LCOH can increase to 145 €/MWh, when only a 25% solar fraction is required [73]. The most important parameters for determining LCOH are the local climate, required solar fraction, and required process temperature.

Table 1.1. LCOH for solar-assisted industrial heating scenarios in literature.

Solar-assisted industry heating system description	**LCOH** (€/MWh)	**Source**
Steam 152 °C Spain	38–51	[73]
Steam 152 °C Austria	87–116	[73]
Steam 152 °C Stockholm	104–145	[73]
Steam $<$ 400 °C southern Europe	40–70	[72]
Steam 150 °C South-East Asia	35	[71]
Steam 150 °C western Europe	80	[71]
Steam 120 °C South Korea	78–110	[75]
Water 100 °C Mexico including HT-HP and storage	103	[76]
Steam 140 °C Spain including HT-HP	60	[74]
Steam 140 °C Netherlands including HT-HP	85	[74]

The key takeaway from these studies is that industrial process heat in the range of approximately 100–150 °C can be supplied using solar energy. The most important performance parameters are the total annual irradiation, the seasonal irradiation imbalance, and the DNI ratio. The technical performance of HT-ST collectors depends on these parameters. Furthermore, the LCOH of solar-assisted industry heating is largely dependent on climate, required temperature, and required solar fraction.

Under favorable conditions, a LCOH below 40 €/MWh can be achieved. For high latitudes, system cost increases significantly to as much as 145 €/MWh. Consequently, optimal system configuration can change significantly depending on the geographic location of the system, the industrial demand temperature, and the required solar fraction.

1.5.2. Solar energy and seasonal storage

As discussed in Section 1.4 the majority of research on combining solar energy and seasonal storage is focused on the residential sector. Even though the use case and required temperatures of this research do not align with the scope of this study, these studies provide valuable insights into system integration, operational strategies, and the role of seasonal storage. Furthermore, the developed system models can provide a useful starting point for the development of an industrial system model.

Several studies have investigated the integration of solar energy with seasonal TES, predominantly in residential or district heating contexts [7, 61, 64, 77]. Ul-Abdin et al. [7] have created a model which compares the performance of different solar collectors including PV, ST, and PVT in combination with an ATES system and a HP. Figure 1.8 shows how the different components are integrated into one system. Different modes of operation were developed to efficiently operate the system and utilize the different components optimally. The research concludes that for a Dutch climate unglazed PVT collectors peak at temperatures around 40 °C. Glazed ST collectors reach higher temperatures of slightly more than 50 °C. This suggests that for a Dutch climate these type of solar collectors require a substantial temperature lift using a HP to meet industrial process requirements. Other types of solar collectors might be considered for future system designs to increase the temperature of the fluid which is delivered by these collectors. Furthermore, the study showed a significant increase in HP performance when utilizing seasonal TES, which can be attributed to higher source temperatures of the HP. The operating temperatures of the solar collectors and ATES are far below that required by industry. Furthermore, the study does not consider grid congestion constraints, both of which are addressed in this thesis.

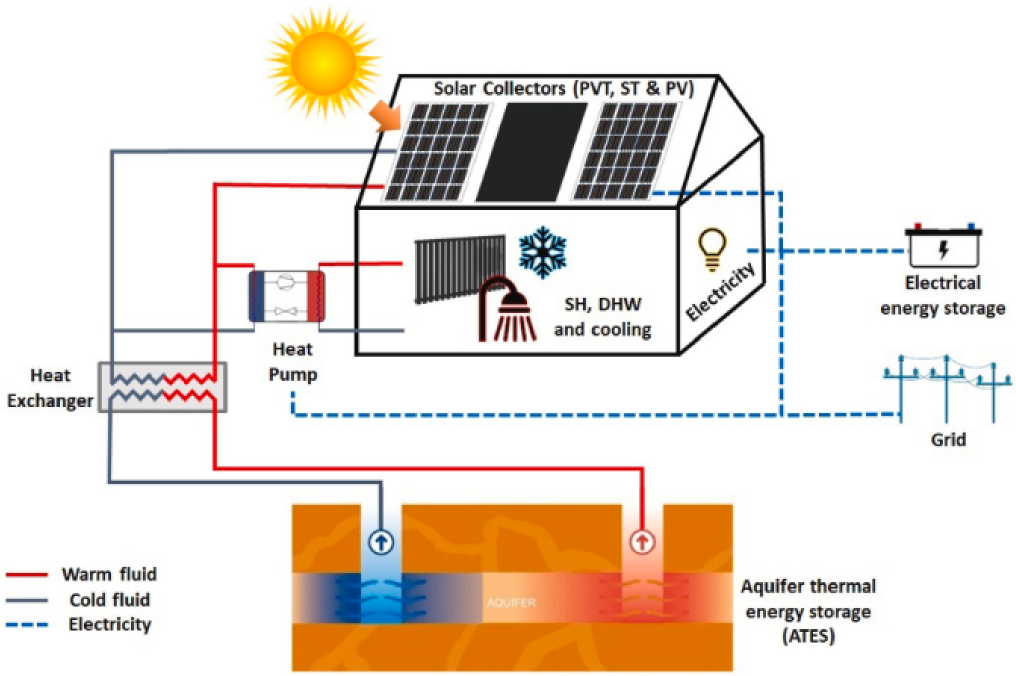

Figure 1.8. Model including solar energy, seasonal storage, and heat pump for residential use [7].

Beijneveld [61] developed an extensive PVT + ATES model for a fifth generation district heating network. The heating network operates at low temperatures between 10–20 °C but under certain conditions higher temperatures of up to 60 °C were reached. It concludes that the PVT and ATES size are crucial parameters for the performance of the system. In general larger PVT size increased the solar fraction and increased the thermal flux into the system. Increasing the size of the ATES resulted in higher thermal losses and a lower aquifer temperature. Consequently, the electrical energy required to power the HP also increased. Although this work provides valuable insights into the dynamic interaction between PVT collectors, ATES seasonal storage, and HP operation, the low operating temperatures are incompatible with industrial process heat requirements. The extension of this system concept to high-temperature operation above 100 °C, as required for industrial steam generation, has not been investigated.

An optimization model for solar district heating system including borehole TES for high latitudes is discussed by Hirvonen et al. [77]. The system integrates ST, borehole TES, and a HP to achieve a solar fraction greater than 90%. It shows that residential systems can be supplied by these kinds of systems even in high latitude countries such as Finland. However, the study does not conclude how solar assisted HT industrial steam generation performs in this climate.

Thinsurat et al. [64] developed a model to study the performance of PVT in combination with thermo-chemical storage for domestic hot water use. Thermal simulations were done using ANSYS fluent and the electrical system model was made in MATLAB. The TES effectively stored heat seasonally to provide heating in winter months. Two different PVT modules were considered, one was significantly better insulated with an air-gap. The thermal performance of the insulated module was much better for the cold climate region which was used. These results indicate that ST and PVT modules in cold climates might need additional insulation to be able to operate properly. This is especially vital for high temperature heat generation as discussed in this thesis.

The main takeaways from the aforementioned studies are that the type of solar collector used is crucial for the performance of the system. The climate plays a significant role in the viability of different solar collector technologies. Furthermore, the size of the seasonal storage is an important factor in system performance. Few models have been developed for solar assisted industrial heating including seasonal TES. This can be attributed to the high industry temperatures, which make seasonal storage difficult. Especially at reasonable prices such as those that can be reached by ATES systems operating at lower temperatures. ATES systems with temperatures higher than 100 °C are theoretically possible without significant increases in price. For these reasons, this type of TES is an interesting avenue to consider when higher storage temperatures are required.

1.6. Research gap

The reviewed literature demonstrates that solar-assisted industrial process heating is technically feasible and cost-competitive in high irradiance climates. However, several research gaps remain.

First, contemporary studies on solar-assisted industrial process heating do not consider the constraints of a congested electricity grid. Current research focuses primarily on system costs, solar fractions, and collector efficiencies. This excludes peak electricity load, the most important parameter for securing a grid connection in a congested network. This constraint introduces additional challenges, especially for winter in high latitude locations when solar irradiance is sparse.

Second, there is a lack of research on solar energy combined with seasonal storage for industrial process heat at temperatures of 130–150 °C. Literature on seasonal thermal energy storage is primarily focused on residential applications with storage temperatures below 60 °C. For industrial process heating in winter, significantly higher storage temperatures are required. For very large seasonal storage volumes, ATES is currently the only economically viable storage technology. However, HT-ATES operating at temperatures beyond 100 °C is still in an early development stage and has not yet been integrated with ST generation. In the majority of studies combining ST with HP systems, the ATES serves as a low-temperature heat source of the HP, with system operation being driven by the heating demand [7, 61]. However, in this thesis the ATES functions as both the source and sink of the HP. During periods with excess irradiation the ATES is used as the HP heat sink, while the ATES functions as a heat source during periods in which ST generation is insufficient.

Third, the individual technologies that are required for such a system are at varying levels of maturity. As mentioned previously, HT-ATES at the required temperatures is in an early development stage and there are currently no large-scale experimental projects able to demonstrate technical and economic feasibility. HT-ST collectors are a mature technology already implemented at large scale. In contrast, well-insulated PVT collectors operating at temperatures above 100 °C are a novel technology, with limited system-level integration studies available. Furthermore, high-temperature steam compression heat pumps capable of delivering 150 °C steam to industry have only recently been developed [8] and have not yet been widely deployed in combination with ST.

The combination of these high-temperature components is illustrated in Figure 1.9. The figure provides a simplified diagram that illustrates the integration of the different technologies incorporated in the industrial energy system. In this thesis, a numerical model is developed to simulate this integrated energy system, assessing its technical potential under varying conditions, including a northern and southern European climate, and two industrial sectors. Subsequently, the system is optimized by minimizing LCOH under grid congestion constraints.

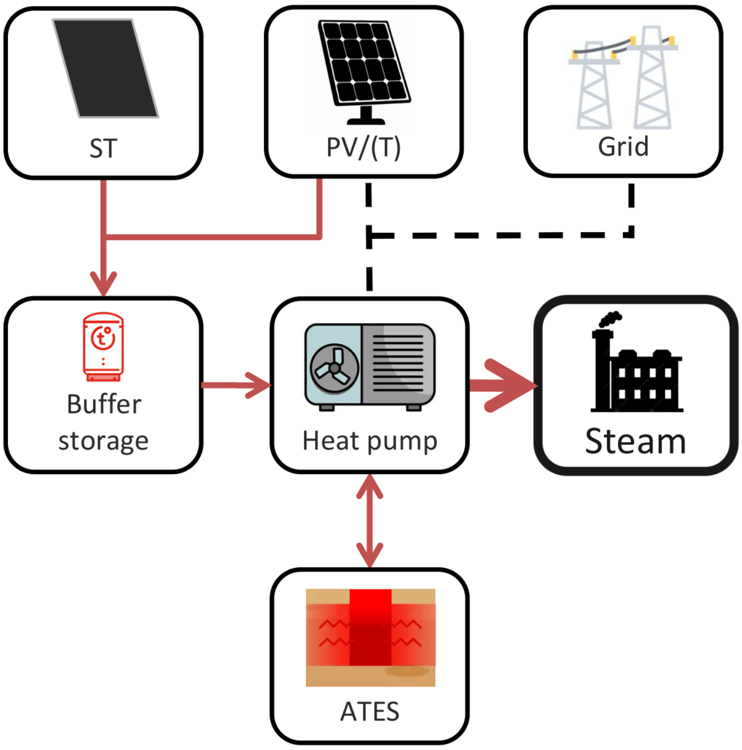

Figure 1.9. A simplified overview of the components of the energy model. The figure shows how the heat and electricity generation are integrated with storage and a heat pump to provide high-temperature (130–150 °C) steam to industry. The ATES is used as both the source and sink of the HP depending on the season.

1.7. Research objectives

This thesis addresses the question: ”To what extent can solar-assisted industrial process heating in combination with thermal energy storage reduce grid congestion problems in Europe?”. This main objective will be achieved by realizing the following objectives.

1. To develop and adapt numerical models for the individual system components required for a high-temperature heating system, including thermal energy storage, a heat pump, and solar collectors. (Chapter 2)
2. To develop an integrated energy model that combines the high-temperature components described in Chapter 2 into a complete industrial process heat supply system, with multiple operational modes and system configurations. (Chapter 3)
3. To use the integrated model under varying operating conditions to examine to what extent medium temperature (130–150 °C) industrial heat demand can be covered by solar energy generation, using high temperature solar thermal and photovoltaic collectors in combination with thermal energy storage comprising a thermal buffer storage and a seasonal high temperature aquifer thermal energy storage system. (Chapter 4)
4. To optimize the system size and perform an economic analysis on the developed industrial energy system, assessing the economic viability of the system under varying climate conditions. (Chapter 4)

1.8. Thesis outline

This thesis report is structured as follows: Chapter 2 describes the individual component models. Chapter 3 focuses on the system model that integrates the individual component models. In Chapter 4 the results are presented and discussed. The performance of the system is compared for a range of European locations. In addition, different system configurations are compared to determine which system functions optimally. Subsequently, Chapter 5 covers the conclusions, where the main findings of this study are presented. Chapter 6 presents recommendations for future work.

Chapter 2

Overview of the numerical component models

The objective of this chapter is to develop and adapt numerical models for the individual system components required for a high temperature heating system, including thermal energy storage, a heat pump, and solar collectors (Objective 1). Designing an energy system that integrates technologies ranging from solar energy generation to thermal energy storage, as seen in Figure 1.9, requires a thorough understanding of the individual numerical component models involved. Therefore, each component model is described in detail before integration into the broader Photovoltaic Materials and Devices (PVMD) toolbox framework. Particular attention is given to the assumptions underlying each model, ensuring a clear understanding of the strengths and weaknesses of the modeling approach.

Section 2.1 discusses the PVMD toolbox which is used as the foundation of the model [7]. A description of the toolbox and the relevant functions of the toolbox is provided. Secondly, the individual component models are presented in detail. The governing equations and relevant parameters are presented to provide a detailed understanding of the modeling approach. Relevant assumptions and simplifications that are made in the model will also be mentioned and explained. To provide a clear overview of the additions made in this thesis, a distinction is made between preexisting PVMD toolbox models and models that have been modified or developed as part of this thesis and will be added to the toolbox.

2.1. PVMD toolbox

This thesis uses the PVMD toolbox as its foundation for energy modeling. The PVMD toolbox is a MATLAB based software tool developed by the Photovoltaic Materials and Devices (PVMD) research group at the Delft University of Technology. The toolbox was primarily created to model the energy output of PV systems based on fundamental material parameters [78]. Since then the toolbox has been expanded to cover a wider range of applications, including PVT systems [79] and integrated systems for domestic cases[7]. In addition, new numerical models are added to the toolbox such as heat pumps (HP) and thermal energy storage [80]. Furthermore, several integrated models have been created that focus on domestic heating, hot water consumption, and electricity consumption [81, 82]. The current toolbox is focused on domestic energy consumption and does not include integrated models and components designed for temperature requirements greater than 100 °C. This thesis expands the PVMD toolbox with high temperature components and an integrated industrial process heating model capable of delivering steam at temperatures up to 160 °C.

The toolbox is structured into several sub-functions, which allow for the modeling and analysis of a variety of solar collectors. Additionally, the toolbox is able to model different scenarios with diverse system configurations, surrounding structures, and weather conditions [83]. Hourly weather data is used including: direct/diffuse irradiance, ambient temperature, and wind speed to calculate the electrical power output of PV systems, as well as the thermal output of ST systems. The relevant sub-functions which are used in this thesis are listed and explained below.

1. MODULE - performs optical simulations to determine the amount of incident light on the PV panels at module level. In this thesis, the module geometry is based on this sub function.
2. WEATHER - Used to determine the plane of array irradiance on the solar panels based on irradiance data.
3. THERMAL - Calculate the temperatures for all the cells in the module. Additionally, the thermal performance of ST and PVT modules is determined here. In addition, it includes integrated solar collector systems for domestic use and components such as thermal energy storage and HP models.

The models developed in this thesis (HT-HP, HT-ST, HT-PVT, and HT-ATES) are incorporated into the THERMAL sub-function of the PVMD toolbox, expanding existing integrated systems to be able to model high temperature applications such as industry heating. By continuous expansion and improvement of the toolbox functionality, the toolbox can provide valuable modeling data for a growing number of scenarios.

2.2. Solar collectors and thermal buffer storage

This section outlines the numerical models of various solar collectors and the thermal buffer storage connected to the ST/PVT. First, PV modules are discussed in Section 2.2.1, then the model for the ST modules is given in Section 2.2.2 and 2.2.3, after that a model for the PVT modules is explained in Section 2.2.4. Finally, the water based thermal buffer storage tank is discussed in Section 2.2.5. Additionally, a PCM based buffer storage has been considered in this thesis for which the modeling method and results can be found in Appendix A.1.

Before describing each component individually, Figure 2.1 illustrates how the solar collectors and buffer storage interact within the system. Water from the buffer storage is fed into the ST, heated by solar irradiance and returned to the buffer storage. This cycle increases the total thermal energy stored in the buffer tank. Q_{out} shows the extraction from heat from the buffer tank that is delivered to the HP.

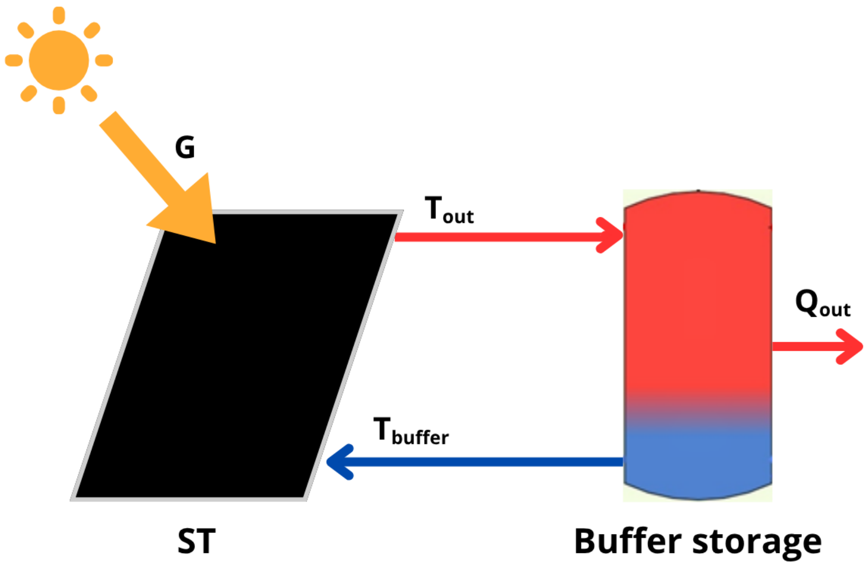

Figure 2.1. Simplified schematic showing how the ST modules on the left are integrated with the thermal buffer storage on the right.

2.2.1. Photovoltaic module - existing model

Photovoltaic modules provide electrical power to the HP and the hydraulic ATES pumps. The electric power P_{pv} generated by the PV module is calculated using the equations given below, which are based on the methodology proposed by Ul-Abdin et al. [7]. The module tilt is optimized for the latitude of the PV installation and shading losses are not considered. Furthermore, losses in transmission and conversion of electricity are neglected.

$$P_{\mathrm{pv}} = P_{\mathrm{S}} \eta_{\mathrm{pv}}, \tag{2.1}$$

where η_{pv} is the electrical efficiency of the PV module and P_S is the available solar power that can be expressed as follows:

$$P_{\mathrm{S}} = G A_{\mathrm{mod}}, \tag{2.2}$$

where G is the plane of array irradiance (W/m^2) reaching the PV module and A_{mod} (m^2) is the module area. The electrical efficiency η_{pv} is determined by Equation 2.3.

$$\eta_{\mathrm{pv}} = \eta_{\mathrm{pv,ref}}[1 + \beta(T_{\mathrm{pv}} - T_{\mathrm{pv,ref}}) + \delta \ln \frac{G}{G_{\mathrm{ref}}}], \tag{2.3}$$

where the reference PV module efficiency $\eta_{pv,ref}$ is 23% under STC ($T_{pv,ref}$ = 25 °C, G_{ref} = 1000 W/m^2, and the wind speed is 0 m/s). The reference module efficiency is 23%, consistent with current commercially available c-Si PERC modules. The temperature coefficient β = -0.25%/K and the irradiance coefficient δ = 0.052. The irradiance G is taken directly from the solar radiation inputs into the model. The actual cell temperature (T_{pv})is determined using a NOCT modeling approach:

$$T_{\mathrm{pv}} = T_{\mathrm{am}} + \frac{G}{G_{\mathrm{NOCT}}}(NOCT - 20), \tag{2.4}$$

where T_{am} is the ambient temperature and NOCT is the nominal operating cell temperature, defined under the following standard conditions. Irradiance G_{NOCT} = 800 W/m^2, ambient temperature = 20 °C, wind speed = 1 m/s, and an open backside mounting configuration. For c-Si PV modules the NOCT value is approximately 45 °C [84]. The NOCT model does not include wind speed variations and therefore overestimates cell temperatures in locations with high wind speed, resulting in an underestimation of the PV electricity yield.

2.2.2. Solar thermal - existing model

This section outlines the numerical model used to evaluate the performance of the water-based flat plate collectors. The PVMD toolbox is equipped with a dynamic model for a glazed flat plate solar thermal (ST) module developed by Ul-Abdin et al.[7] as well as simple reduced temperature models which offer a computationally efficient alternative. Since the reduced temperature models are able to provide accurate results with significantly less required computational power, this approach is taken in this thesis. It should be noted that the electricity required to pump water through the collectors and the thermal losses in the connecting pipes are neglected.

The preexisting reduced temperature models are based on the steady state method discussed in Section 1.2.2 and make use of the second order thermal efficiency approach presented below in Equation 2.5. This equation characterizes the thermal efficiency of the ST module using specific coefficients that describe the performance of the module under varying operating conditions. This approach is the industry standard and corresponding coefficients are included in ST data sheets, with representative reduced temperature curves for three commercial collector types shown in Figure 1.2.

$$\eta_{\mathrm{th}} = \eta_0 - a_1 \left(T_{\mathrm{red}}\right) - a_2\, G \left(T_{\mathrm{red}}\right)^2, \tag{2.5}$$

where the thermal efficiency of the ST collector is given by η_{th}, and a_1 and a_2 are unique coefficients that correspond to the thermal performance of a ST collector, determined through dynamic modeling or experimental data. The zero loss efficiency η_0 is the efficiency of the module when the inlet temperature of the module is equal to the outside temperature such that the net heat change to the outside is effectively zero. The aforementioned coefficients a_1, a_2, and the η_0 can be determined through experimental results or dynamic models through curve fitting. This equation is only valid when the flow rate is high and the fluid only experiences a small temperature increase between inlet and outlet of a ST module. When the temperature increase within the ST is more than a few degrees Celsius, this method underestimates the thermal losses to the outside and thereby overestimate the efficiency of the modules. T_{red} denotes the reduced temperature of the module and is expressed as follows:

$$T_{\mathrm{red}} = \frac{T_{\mathrm{in}} - T_{\mathrm{am}}}{G}. \tag{2.6}$$

where the inlet temperature of the module and the ambient outside temperature are given by T_{in} and T_{a} respectively. Incoming plane of array irradiance is denoted by G in W/m^2.

2.2.3. Solar thermal - modified model

The preexisting PVMD toolbox models are designed for ST modules which operate at temperatures between 20 °C and 70 °C. When higher temperatures are required, the modules need additional thermal insulation to prevent heat losses. This requires different types of ST collectors such as evacuated tube collectors or evacuated flat plate collectors. The coefficients for the evacuated flat plate collectors used in this thesis can be found in table 2.1. The coefficients are based on commercial evacuated flat plate collectors produced by TVP solar. The TVP solar collectors are capable of delivering water at a temperature of up to 200 °C to industry by using high vacuum insulation on their ST collectors. Experimental validation of the high temperature ST collector model was not possible within the scope of this study, as no suitable test setup was available. Furthermore, the existing dynamic models within the research group are limited to low temperature ST/PVT and therefore cannot be used as a reference model.

Table 2.1. Parameters flat plate ST collectors

Parameter	Flat plate ST collector
$\dot{m}_{\mathrm{w}}$ (kg s^{-1})	0.02
A_{c} (m^2)	2.0
T_{STC} (°C)	25
NOCT (°C)	48
G_{STC} (W m^{-2})	1000
C_w (J kg^{-1} K^{-1})	4186
a_1 (W m^{-2} K^{-1})	1.553
a_2 (W m^{-2} K^{-1})	0
η_0 (-)	0.757

To better account for thermal losses across the solar collector, T_{in} in Equation 2.5 is replaced with the mean temperature of the collector T_{m}. This equation has to be implicitly solved since T_{m} is dependent on η_{th}, as illustrated in Figure 2.2. Here, the temperature of the buffer tank is used to make an initial guess for the mean module temperature T_{m}^0.

The mean module temperature is used in combination with irradiance and ambient temperature data from the weather file to find the reduced temperature of the module. The altered Equation 2.6 is used to find the ST thermal efficiency. The thermal efficiency is used to approximate the outlet temperature of the water. Using the average of the inlet and outlet temperature, the mean module temperature T_{m} is determined. This approach is only accurate if temperature in the ST increases somewhat linearly and can therefore not be used for very low flow rates. When the difference between the initial guess T_{m}^0 and the calculated T_{m} is less than the defined tolerance, the loop is finished. The thermal efficiency η_{th}, mean temperature T_{m}, and output temperature T_{out} are delivered as output of the model. This heated water is added to the buffer storage, thereby increasing the stored thermal energy.

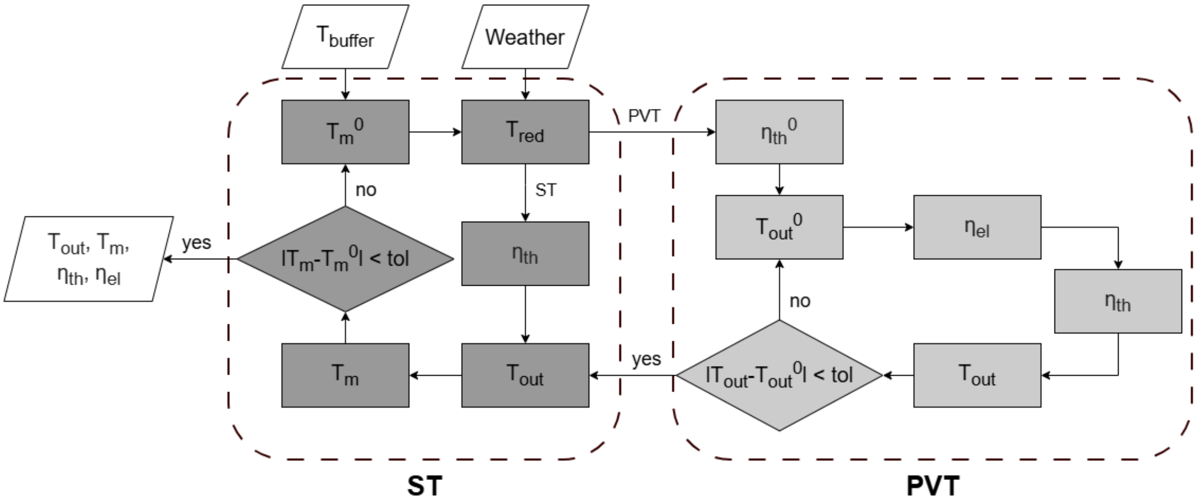

Figure 2.2. Flow chart of ST and PVT modeling showing the iterative process which determines the performance. The left loop is used for the solar thermal collector and the photovoltaic thermal collector makes use of both loops to determine the electrical and thermal efficiency of the collector.

2.2.4. Photovoltaic Thermal - newly developed model

As the PVMD toolbox does not include a high temperature PVT model, one has been developed as part of this work. The model couples a similar reduced temperature thermal efficiency approach described in Section 2.2.3 with the temperature-dependent electrical efficiency model of Section 2.2.1. Due to the relationship between the electrical efficiency η_{el}, thermal efficiency η_{th}, and the output temperature T_{out} a secondary embedded loop is required to solve the equations. Figure 2.2 illustrates how the PVT code is integrated into the ST code.

The initial guess of the mean module temperature T_{m}^{0} and the reduced temperature T_{red} are determined as explained in Section 2.2.3. The reduced temperature is used to make an initial guess for the thermal efficiency η_{th}, then a guess for the output temperature T_{out}^{0} is made based on η_{th} . The output temperature of the fluid is assumed to be equal to the temperature of the PV module T_{pv} which is integrated into the flat plate ST collector. Subsequently, the η_{el} is determined on the basis of the module temperature T_{pv}, using Equation 2.3. The thermal efficiency η_{th} is then adjusted by subtracting the PV efficiency from the previously determined thermal efficiency as function of the reduced temperature 2.7. This results in a new PVT outlet temperature. When the new outlet temperature of the PVT module is within tolerance of the initial guess, the outer loop checks whether the mean temperature has also converged. Once both conditions are satisfied, the thermal and electrical efficiencies are returned as outputs.

$$\eta_{\mathrm{th}} = \eta_{\mathrm{th}}^{0} - \eta_{\mathrm{el}}. \tag{2.7}$$

The reduced temperature curves of the ST and PVT collectors can be found in Figures 2.3 and 2.4. The Reduced temperature for the electrical efficiency has been approximated through curve fitting simulated data from a the PVT collector and have been presented for a irradiance of 1000 W/m^2 in the figure. The black cross denotes the most common operational point of the PVT collectors in the integrated system, when the temperature difference between the collectors and ambient is approximately 100 °C. At these elevated operational temperatures the electrical efficiency of the PVT reduces from 22–23% to 16–18%.

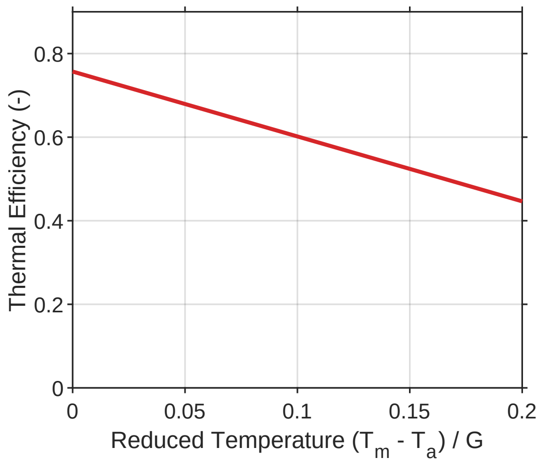

Figure 2.3. High vacuum insulated flat plate ST collector.

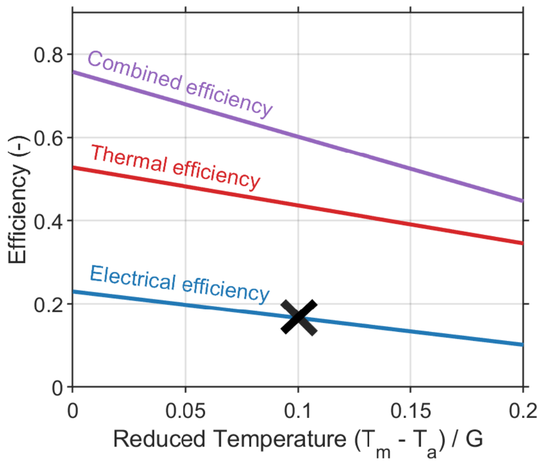

Figure 2.4. High vacuum insulated flat plate PVT collector.

2.2.5. Water tank - newly developed model

The water tank is modeled as a lumped energy sensible heat storage using a fixed volume of water. The water volume is warmed up by the ST/PVT and cooled down by extracting heat from the tank using a heat exchanger. The temperature change of the water as a result of these processes can be found in Equation 2.8.

$$\Delta T_{\mathrm{wt}} = \frac{Q_{\mathrm{in}} - Q_{\mathrm{out}}}{M_{\mathrm{wt}} C_{\mathrm{w}}}, \tag{2.8}$$

where Q_{in} and Q_{out} are the inserted and extracted heat flows. The mass of the water tank is denoted by M_{wt} and c_p is the specific heat capacity of water in the tank. The temperature of the water in the buffer tank (T_{wt}) varies between 80 and 120 °C. When the water is above 100 °C it has to be stored at pressures greater than 1 bar to avoid evaporation. The tank is assumed to be well insulated such that it has negligible thermal losses to the outside. Since the buffer storage is cycled at a much higher frequency than the ATES the thermal losses are comparatively small.

2.3. Heat pump - newly developed model

The numerical HP model is based on a study by TNO and Standard Fasel [8], which characterizes the performance of a high temperature semi-open type steam compression HP. It makes use of a steam compression cycle and delivers steam directly on the sink side. A simplified schematic of the HP can be found in Figure 2.5, showing the operating design of the prototype. A vacuum boiler operates at low pressure between 0.2–0.7 bar, enabling water to evaporate at relatively low temperatures (60–90 °C). The water is fed into the vacuum boiler and heated via a heat exchanger. The heat flux causes the water to partially evaporate, after which the steam is separated. The steam is fed into a two-stage compressor that compresses the steam, increasing its pressure and temperature. The HP is originally designed to be used in combination with industrial waste heat but can also utilize ST heat without requiring significant modifications. The HP is capable of delivering steam at sink temperatures T_{sink} between 130–160 °C, corresponding to a pressure of 2.7–5.9 bar respectively.

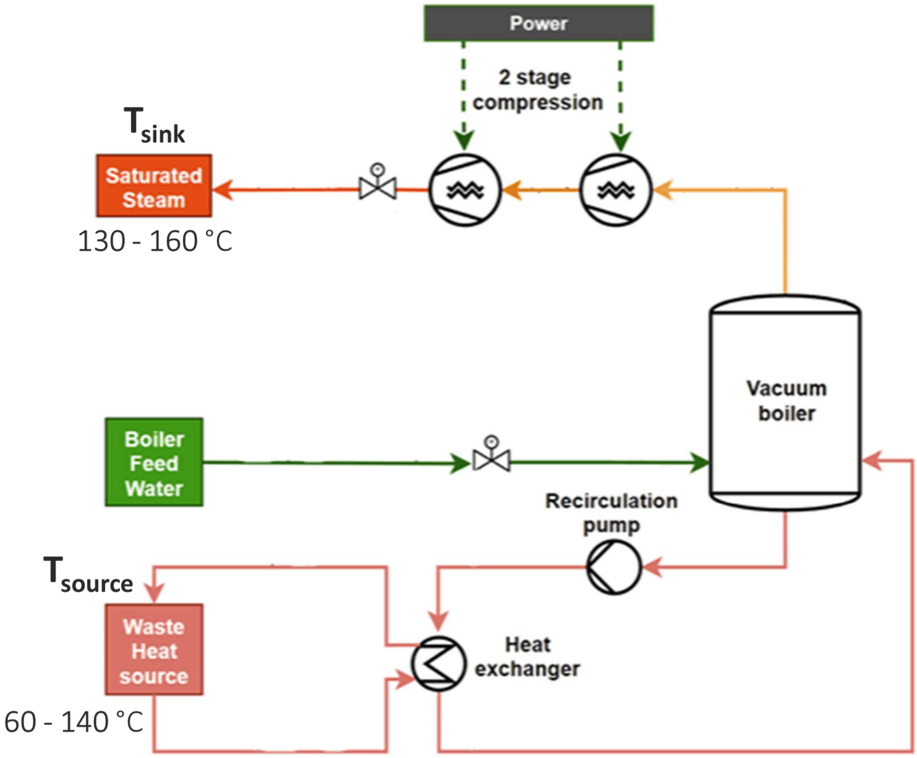

Figure 2.5. Simplified HP schematic highlighting the main components of the TNO and Standard Fasel prototype. Adapted from Ramirez et al. [8].

The COP of the HP is computed using Equation 2.9.

$$COP = 5.57 - 0.046\Delta T_{\mathrm{HP}}, \tag{2.9}$$

where ΔT_{HP} is the temperature lift of the HP, defined as the difference between the source T_{source} and the sink T_{sink} temperatures of the HP. This linear relation is derived from Ramirez et al. [8] and presented in Figure 2.6. This figure presents two HP characteristics, the bottom line (yellow) characterizes the measured performance of the prototype, while the red line represents the theoretical potential of the design in the absence of preventable thermal and mechanical losses. This thesis utilizes COP characteristics of the upper-bound COP curve, which is a realistic benchmark for the HP as it approaches maturity. The figure additionally compares the COP characteristics from Ramirez et al. against the theoretical limit, COP_{carnot} (blue), as defined in Equation 1.1. The performance of HPs in literature is often evaluated using the Carnot efficiency, defined as the ratio of the HPs COP to the corresponding COP_{carnot}. The maximum Carnot efficiency of the presented HP is 39%, at a temperature lift of 60 °C. This falls within the range of Carnot efficiencies reported for high temperature HPs according to Arpagaus et al. [47].

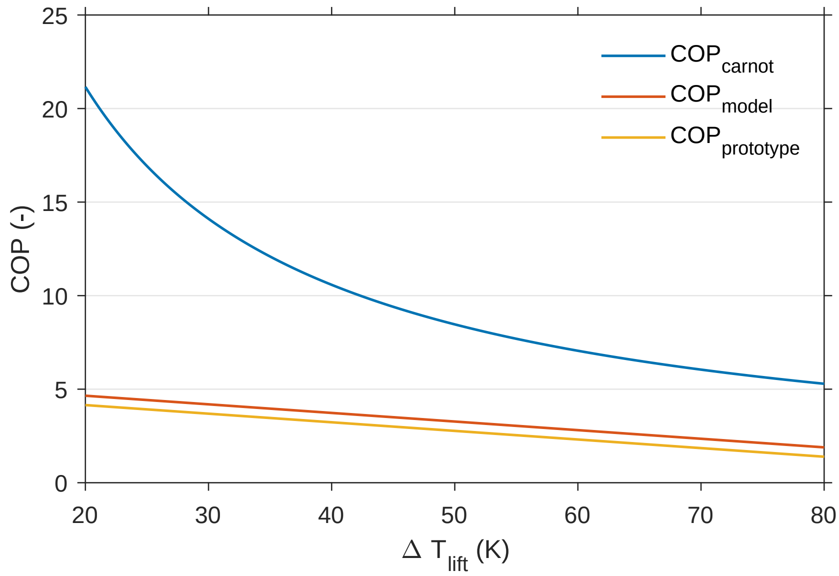

Figure 2.6. The COP characteristics of the numerical HP model (orange) are compared against the COP_{carnot} characteristics (blue). The actual prototype performance (yellow).

Although the HP prototype is designed and tested with source temperatures between 60 to 80 °C [8], the numerical model extends this range to higher source temperatures up to 140 °C. This extension is physically justified since the steam compression HPs can operate at higher source temperatures when increasing the vacuum boiler pressure. The extended source temperature range enable the system to be more effective when combined with variable ST heat generation and HT-ATES. This is attributable to higher achievable COP values when operating at higher vacuum boiler temperatures, due to a reduction in required steam compression power. Furthermore, the effective temperature range of the ATES is increased, reducing the required storage volume. The minimum source temperature is constrained to 60 °C and sink steam temperature is limited to 130–160 °C, consistent with the achievable range of the prototype.

2.3.1. Coolprop

The model employs the CoolProp library [85] to retrieve fluid properties of water for the HP. This is necessary since the temperature of the water ranges between 80 and 160 °C within the HP. This results in a significant variation in the boiling pressure, viscosity, and density of water. CoolProp is integrated into the MATLAB code, allowing for hourly updates of fluid properties in the system based on temperature and pressure. This ensures accurate results for a range of operating conditions of the HP. CoolProp has been previously employed in the PVMD toolbox to validate the performance of low temperature HPs.

2.4. Heat exchangers - newly developed model

The heat exchangers in the system are modeled in two different ways, depending on the specific use. Both heat exchangers are coupled to the vacuum boiler.

The first heat exchanger couples the vacuum boiler with the buffer storage. This heat exchanger is fully submerged within the thermal buffer storage tank. Therefore, the heat exchanger only requires fluid circulation on the HP side. This simplifies the heat exchanger modeling substantially because the water temperatures coming out of the heat exchanger do not have to be tracked. The performance of these heat exchangers is taken into account in the COP characteristics of the HP. This performance includes the pumping power required to pump the water through the heat exchanger. Since the pumping power and thermal losses associated with these heat exchangers are already embedded in the COP characteristics of the HP, it is not necessary to determine the electrical energy required to pump water through the heat exchanger. The heat exchanger can be simply modeled by extracting the required heat from the buffer tank. The corresponding heat exchanger equations are discussed in Section 3.2.

The second heat exchanger is used in combination with the HT-ATES. This heat exchanger requires a different heat transfer model because water flows on both sides of the exchanger and the outflow temperatures have to be tracked to be used in the ATES model. The heat exchanger connected to the ATES system is a shell-and-tube heat exchanger which are commonly employed in industry due to their high heat transfer rate, compact space requirements, and the ability to handle high pressure [86]. A temperature difference of 5 K is assumed at the heat exchanger outlet, referred to as the pinch point temperature (T_{pinch}). This lies on the lower end of typical pinch temperatures which range from 5 K to 30 K, depending on the trade-off between energy efficiency and heat transfer area [87]. This assumption is considered reasonable since both working fluids are water and the heat exchange involves condensation and boiling, which are associated with significantly higher heat transfer coefficients than single-phase convection [88]. However, it should be noted that such a low pinch temperature may require a larger heat transfer area and therefore represents an optimistic performance oriented design choice.

Figure 2.7 presents the temperature profiles of water on both sides of the heat exchanger for two operating scenarios. The profiles shown are illustrative examples for specific ATES temperatures and shift accordingly as the aquifer temperature varies throughout the year. The x-axis represents the position along the heat exchanger from inlet to outlet, and the y-axis shows the fluid temperature. Each figure presents two temperatures, the HP side (T_{HP}) and the ATES water side (T_{ATES}) with the dashed line indicating ATES temperature as a reference.

During surplus operation (Figure 2.7a) the ATES functions as the heat sink of the HP. Steam at 160 °C is generated by the HP, which condenses in the heat exchanger, transferring heat to cold well water. Since the HP side undergoes condensation, its temperature remains constant at 160 °C along the full heat exchanger length. The cold well water is heated from 90 °C to 155 °C along the heat exchanger before being pumped into the warm well.

During shortage operation (Figure 2.7b) the ATES functions as the heat source of the HP. Warm well water enters the heat exchanger at 140 °C and transfers heat to water from the vacuum boiler. The water from the vacuum boiler evaporates at a constant temperature controlled by the vacuum boiler pressure, leaving the heat exchanger as steam. The water on the ATES side is cooled down to 5 K above the steam temperature and inserted into the cold well. The heat exchangers are further discussed in Appendix A.2, where the required heat exchanger area is determined to assess technical feasibility.

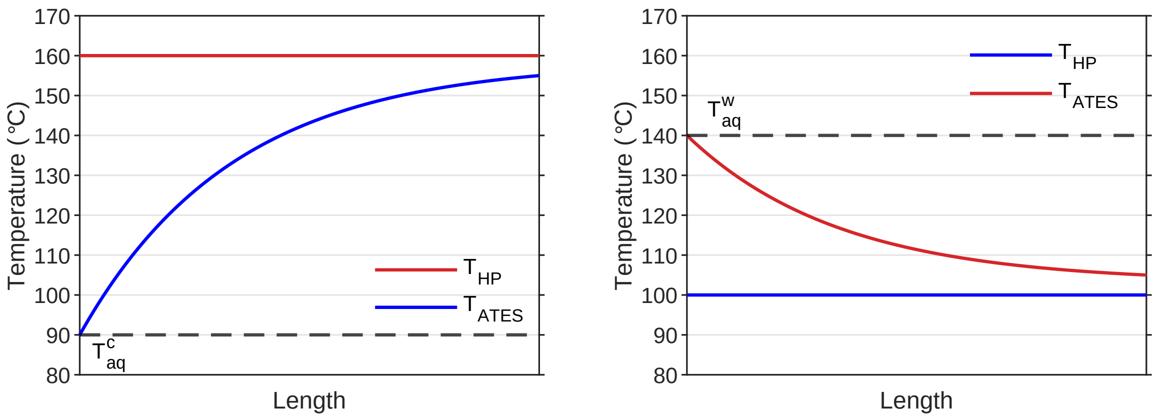

(a) Surplus operation **(b)** Shortage operation

Figure 2.7. Temperature of heat exchanger integrated with the ATES in two scenarios: Surplus operation where cold water is pumped from the cold to the warm well and heated through steam condensation and shortage operation where the ATES is delivering heat to the HP by pumping water from the warm to the cold well. The reference warm and cold well temperatures are also presented.

2.5. Aquifer thermal energy storage - existing

ATES systems employ underground aquifers to store heat by adding and extracting hot water. The numerical model in this thesis uses a two-well approach. The model is based on the work by Van Rossum [80] on low temperature ATES systems which is implemented in the PVMD toolbox. The parameters used in these equations can be found in table 2.2. ATES sizing, including determining the thermal radius R_{th}, follows the same approach as Van Rossum [80]. The work of Van Rossum et al. is based on ATES systems designed for domestic hot water supply and space heating demand. This requires significantly lower ATES temperatures between 10 and 30 °C compared to the industrial ATES system in this thesis, which operates between 40 and 150 °C, referring to the minimum temperature of the cold well and the maximum temperature of the warm well, respectively. The aquifer dynamics change significantly at higher temperatures as discussed in Section 1.4 and therefore the thermal efficiency approximation does not hold for these ATES systems.

2.5.1. Aquifer thermal energy storage - modified model

Before going into the ATES equations, Figure 2.8 presents some important parameters of the ATES model. The left figure presents the operation during summer when surplus heat is stored in the ATES. The figure on the right presents the ATES operation during winter when the solar collector system is not sufficient to meet all heat demand. The figure further highlights the temperature ranges of the two wells and the vacuum boiler. Finally, important parameters of the system are displayed such as the depth of the aquifer, the screen length H_a, and the thermal radius R_{th}.

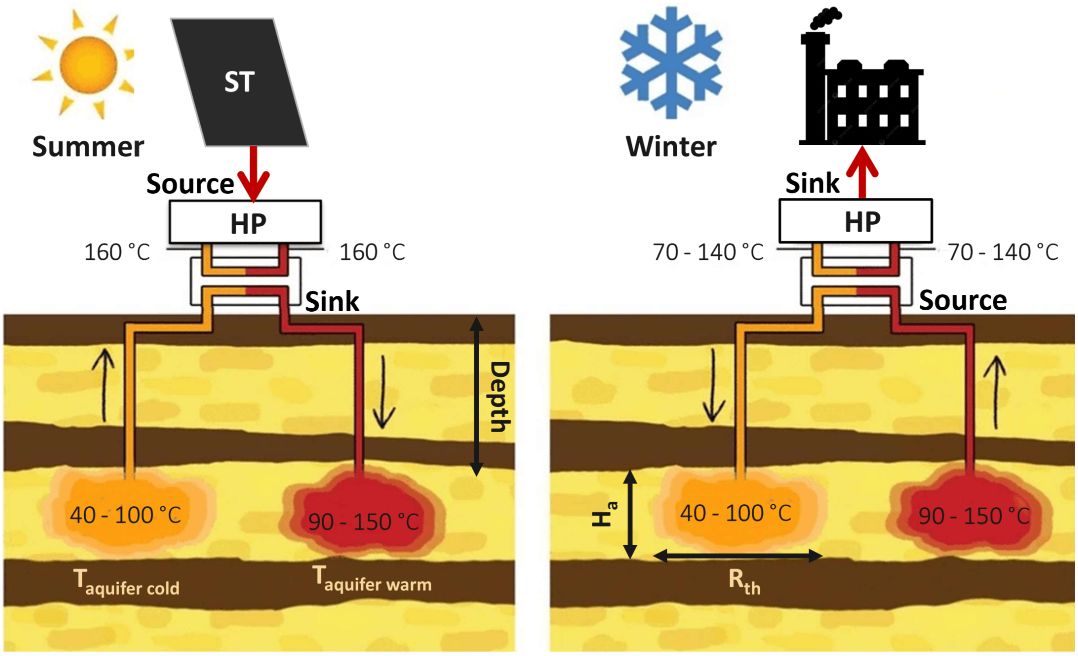

Figure 2.8. ATES operation in summer (left) and winter (right) showing the temperature ranges and important well parameters. Adapted from Bloemendal et al. [9].

The HT-ATES is modeled using a lumped energy balance approach, in which the aquifer is represented as a single well-mixed thermal node with a uniform temperature. Hydraulic mass flow balance is not explicitly enforced since this requires a numerical groundwater flow model beyond the scope of this study. Consequently, the model does not capture thermal fronts, spatial groundwater flow, and hydraulic pressure changes. Instead, the energy balance of the system is enforced through annual aquifer temperature stability. This ensures that the system can be used sustainably over multiple years. The ATES model uses CoolProp, discussed in Section 2.3.1, for hourly updates of the fluid properties of water. This is necessary because the thermophysical properties of water, such as density and viscosity, vary significantly with temperature and therefore change considerably as the ATES temperature fluctuates throughout the year.

Heat losses to the ground for the lumped energy balance are accounted for using the recovery efficiency, which is determined based on the approach developed by Schout et al. [89] and further validated for high temperature conditions by Sheldon et al. [55]. The approach takes into account heat loss due to buoyancy and density driven flow which are important heat loss mechanisms in high temperature ATES systems. Using this approach, an annual recovery factor for the ATES can be approximated based on local aquifer conditions, following Equation 2.10:

$$R = A_{ates} e^{B_{ates} Ra^*}, \tag{2.10}$$

where R is the annual recovery efficiency of the system and Ra^* is a modified Rayleigh number expressed in Equation 2.11. A_{ates} and B_{ates} are derived through curve fitting using detailed high temperature ATES simulations and are based on the screen length of the ATES H_a.

$$Ra^* = 1634 \frac{\rho_{\text{w}} H_a^{2.5} \sqrt{k_a^v k_a^h} \Delta T}{\mu \sqrt{V_{\text{in}}}}, \tag{2.11}$$

where ρ_{w} is the density of water, k_a^v and k_a^h are the vertical and horizontal permeability of the aquifer, ΔT is the difference between the injection temperature and the temperature of the ground surrounding the aquifer, μ is the viscosity of water and V_{in} is the injected volume of water in one year. The first variable found through the curve fitting A_{ates}, is calculated using Equation 2.12.

$$A_{ates} = 0.82 - \frac{1.70}{H_a^{1.2}} \tag{2.12}$$

To accurately determine B_{ates}, two different relations are required to describe aquifer dynamics. Equation 2.13 is valid when the screen length of the aquifer is within 10 to 60 m and Equation 2.14 is valid for screen lengths between 60 and 200 m.

$$B_{ates1} = -\frac{1.2}{H_a^{1.35}} + 2.2 \cdot 10^{-3} \tag{2.13}$$

$$B_{ates2} = \frac{2.7}{H_a^{1.7}} \tag{2.14}$$

The MATLAB model applies the recovery efficiency R at each timestep when heat is injected. This is a conservative assumption since it underestimates heat recovery for short storage cycles. Since the ATES system is predominantly used for seasonal storage, this simplification yields acceptable results. The temperature of the warm well is updated using Equation 2.17.

$$\Delta T_{\text{warm}} = \frac{RQ_{\text{in}} - Q_{\text{out}}}{C_{\text{ates}}}, \tag{2.15}$$

where Q_{in} is the energy which is added to the aquifer, Q_{out} is the extracted energy, and R is the recovery efficiency. The equations determining Q_{in} and Q_{out} are described in Section 3.2. The thermal capacity of the aquifer C_{ates} is described by Equation 2.16.

$$C_{\text{ates}} = nV_{\text{ates}}((C_{\text{w}}\rho_{\text{w}}\phi) + (C_r\rho_r(1-\phi))), \tag{2.16}$$

where n is the number of wells and V_{ates} is the volume of the ATES determined by the previously mentioned equations in van Rossum et al. [80]. The specific heat capacities of water and rock are given by C_w and C_r, the densities of water and rock are denoted by ρ_{w} and ρ_r, and ϕ is the porosity of the aquifer.

Subsequently, the temperature of the warm well is updated as shown below:

$$T_{\text{aq}}(i+1) = T_{\text{aq}}(i) + \Delta T_{warm} \tag{2.17}$$

The cold well temperature ranges between 40–100 °C, which is high when compared to conventional low temperature ATES systems, but represents the cold side within the high temperature context of this thesis. The cold well temperature is modeled as the mirror image of the warm well such that $\Delta T_{\text{warm}} = -\Delta T_{\text{cold}}$. While this simplification does not capture the independent thermal dynamics of the cold aquifer, its influence on total system performance is limited. The cold well temperature primarily affects the hydraulic pumping losses, which account for only a small fraction of total energy consumption. Accurately resolving cold well dynamics would require a full two-well distributed groundwater flow model, which is outside the scope of this thesis.

Most parameter values are based on the parameters used by Sheldon et al. [55]. Some parameter choices do require additional explanation to understand the way they have been determined. A screen length of 60 m is adopted, as longer screen lengths yield higher recovery efficiencies, particularly at large injection volumes. The industrial system considered in this thesis requires a large storage volume. To determine the aquifer recovery efficiency an injection volume of V_{ates} of 2×10^5 m^3 is considered. The aquifer is placed at a depth of 400 meters to avoid contamination of drinking water reserves. Deeper aquifer placements significantly increases the pumping power required to extract water from the ground.

Horizontal permeability is considered to be 10×10^{-12} m^2, which is on the low end of what is considered in most numerical modeling studies of high temperature ATES [55, 89]. Low permeability aquifers have higher recovery efficiencies, but extraction of water requires more pumping power. When permeability is low, heat transfer is dominated by conduction instead of convection. The anisotropy is determined to be 10 because this is a reasonable estimate for layered aquifers according to Bakker et al. [90]. High anisotropy is beneficial because losses through buoyancy effects are reduced.

The resulting recovery, based on these parameter values, is approximately 0.8 after five years of operation. However, recovery efficiency is very sensitive to local ground conditions and may differ significantly from the value assumed here. Favorable ATES conditions are assumed in this thesis in order to assess the technical potential of the broader system, including the solar collector array. To determine the site-specific system performance, local geological conditions must be inserted into the model. Finally, the aquifer temperatures are limited to the ranges presented in the table below. This is done to prevent physically unfeasible ATES operation. When these limits are reached, the aquifer system stops being used for surplus or shortage situations, depending on the limit reached.

Table 2.2. Aquifer thermal energy storage parameters

Parameter	**ATES**
Porosity ϕ (-)	0.25
Specific heat capacity aquifer C_r $(Jkg^{-1}K^{-1})$	800
Density rock ρ_r (kgm^{-3})	2650
Density water ρ_w (kgm^{-3})	943–975
Screen length H_a (m)	60
Depth (m) L_{ATES}	400
Horizontal permeability K_a^h (m^2)	$10 \cdot 10^{-12}$
Anisotropy (-) k_{ah}/k_{va}	10
Viscosity μ (Pa s)	0.0002825
ATES injection volume V_{ATES} (m^3)	$2 \cdot 10^5$
Cold aquifer max T (°C)	100
Cold aquifer min T (°C)	40
Warm aquifer max T (°C)	150
Warm aquifer min T (°C)	90

2.6. Hydraulic Pumps ATES - newly developed model

Extracting water from the ATES system requires hydraulic pumps capable of overcoming the hydrostatic pressure of the water column and frictional losses in the piping. Since minimizing electricity consumption from the grid is a primary objective of this thesis, it is crucial to account for the electricity demand of these pumps. The hydraulic pump model has been adapted from the work of Beijneveld [61] and Van Rossum [80].

First, the optimal diameter of the inner tube is determined using Equation 2.18, based on the design volumetric flow rate and the chosen design velocity. The total volumetric flow rate of the ATES system during peak loads is divided by the number of well pairs to obtain the flow rate per well.

$$D = \sqrt{\frac{4\dot{Q}}{\pi V}}, \tag{2.18}$$

where D is the optimal inner pipe diameter, Q represents the volumetric flow rate per well and V is the design water flow velocity. A design velocity of 1.5 m/s is adopted, consistent with standard practice to prevent excessive friction losses in well piping [91]. Additionally, high flow velocities can cause pipe erosion, while very low velocities can cause sedimentation within the piping [92].

The total power requirement of the pumps is expressed in Equation 2.19.

$$W_P = \dot{Q}\frac{(\Delta P_{\text{hydraulic}} + \Delta P_{\text{friction}})}{\eta_{\text{pump}}}, \tag{2.19}$$

where W_P is the total pumping power, $\dot{Q}$ is the total volumetric flow rate, η_{pump} is the pump efficiency, and $\Delta P_{\text{hydraulic}}$ and $\Delta P_{\text{friction}}$ are the hydraulic and frictional pressure contributions respectively. The hydraulic pump efficiency is assumed to be 75%, used by Boateng et al. [93] for a centrifugal pump system coupled to a borehore thermal energy storage system. Figure 2.9 illustrates these two contributions to pressure loss in the ATES piping: frictional losses, represented by the Darcy friction factor f_D and hydraulic losses due to gravity g. The figure shows a fully developed laminar flow through a pipe of length L, diameter D and surface roughness ϵ.

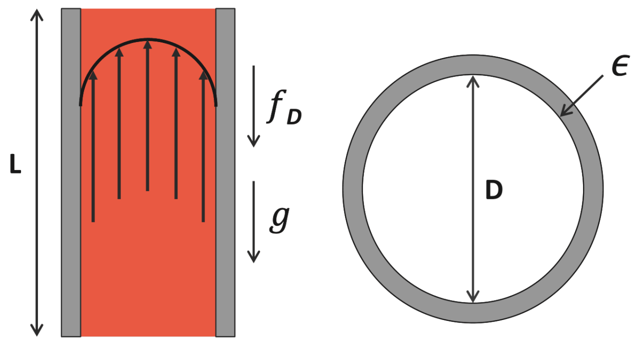

Figure 2.9. Illustration of water moving up through an ATES pipe on the left and a cross section of the pipe on the right.

The dominant pressure contribution is given by the hydraulic head of the water column given by Equation 2.20. When water is transported over large horizontal distances, the pressure drop by friction becomes increasingly more significant. Therefore, ATES systems have to be placed close to the industrial demand to prevent excessive losses. Appendix B.1 presents an analysis on the influence of distance from the industry to the ATES.

$$\Delta P_{\text{hydraulic}} = \rho_w g L_{\text{ates}}, \tag{2.20}$$

where ρ_w is the density of water at aquifer temperature. The gravitational constant g = 9.81 ms^{-2} is the gravitational acceleration and L_{ATES} is the depth of the aquifer.

The frictional pressure drop is computed using the Darcy-Weisbach equation. Firstly, the actual flow velocity through the pipe is determined based on the volume of water required and the inner diameter of the pipe 2.21.

$$V = \frac{4Q}{\pi D^2} \tag{2.21}$$

The Reynolds number dictates the flow regime of the water and is determined using Equation 2.22.

$$Re = \frac{\rho V D}{\mu}, \tag{2.22}$$

where μ is the dynamic viscosity of water at the temperature and pressure of the aquifer and V is flow velocity.

For laminar flow (Re < 2000) the Hagen-Poiseuille Equation 2.23 is used to determine the Darcy friction factor f_D. The Darcy friction factor is a dimensionless coefficient that quantifies the friction loss due to flow in a pipe.

$$f_D = \frac{64}{Re} \tag{2.23}$$

For transitional and turbulent flow (Re > 2000) the Darcy friction factor is approximated using the Swamee-Jain Equation 2.24.

$$f_D = \frac{0.25}{(log(\frac{\epsilon}{3.7D} + \frac{5.74}{Re^{0.9}}))^2}, \tag{2.24}$$

where ϵ is the roughness of the pipe wall. The Swamee-Jain equation is a good approximation for the Darcy friction factor in fully turbulent (Re > 5000) flow through a pipe. In the transitional flow regime (2000 < Re < 5000) the Swamee-Jain equation overestimates the friction factor compared to the iterative Colebrook-White equation. This results in a conservative overestimate of pumping power at partial load.

Finally, the frictional pressure drop over pipe length L is expressed using Equation 2.25.

$$\Delta P_{\text{friction}} = f_D \frac{L_{\text{ates}} \rho V^2}{2D} \tag{2.25}$$

Since the hydrostatic pressure of the water column exceeds the frictional resistance during injection, no additional pump is required on the injection side. Therefore the hydraulic pumping model is only applied on the extraction side.

2.7. Electrical battery - newly developed model

A simplified electric battery model is added to represent large-scale battery storage. The batteries have a charge and discharge efficiency of 95%. This corresponds to a round trip efficiency of approximately 90%, which is in line with modern lithium-ion batteries [94]. Self-discharge losses are neglected, as these are typically below 3% per month for lithium-ion batteries and are therefore negligible for typical cycling periods of 1–3 days in this thesis [95]. Excess electricity is stored in the batteries and discharged during periods of insufficient generation. The inclusion of battery storage improves system resilience and reduces dependence on grid electricity. The state of charge (SOC) is determined using Equations 2.26 and 2.27 .

$$\Delta SOC = \frac{\eta_{\text{bat}} E_{\text{in}} - \frac{E_{\text{out}}}{\eta_{\text{bat}}}}{C_{\text{bat}}}, \tag{2.26}$$

where E_{in} and E_{out} are the energy flows in and out of the batteries in joules, η_{bat} is the efficiency of charging and discharging the batteries, and C_{bat} is the total energy capacity of the battery storage in joules. The resulting difference in state of charge ΔSOC is used to update the battery SOC in Equation 2.27.

$$SOC(i+1) = SOC(i) + \Delta SOC. \tag{2.27}$$

2.8. Conclusion

This chapter has presented the developed and adapted numerical models for the individual system components required for a high temperature heating system, including thermal energy storage, a heat pump, and solar collectors (Objective 1). The models range from existing PVMD toolbox components to newly developed models for high temperature applications, including the PVT collector, high temperature HP, and the modified high temperature ATES. The newly developed models are incorporated into the PVMD toolbox and are specifically aimed at industrial heating applications. Figure 2.10 provides an overview of how the individual components described in this chapter are integrated. This integrated system and the interactions between the individual components are further described in Chapter 3.

Although the individual component models are based on established methods from literature, several simplifying assumptions have been made, including neglect of thermal and hydraulic pumping losses for the ST/PVT piping, the lumped energy approach for both the buffer storage and ATES, and the extrapolation of heat pump COP characteristics beyond experimentally validated source temperatures. These simplifications create a good balance between accuracy and complexity of the model but have to be considered when evaluating the results in Chapter 4.

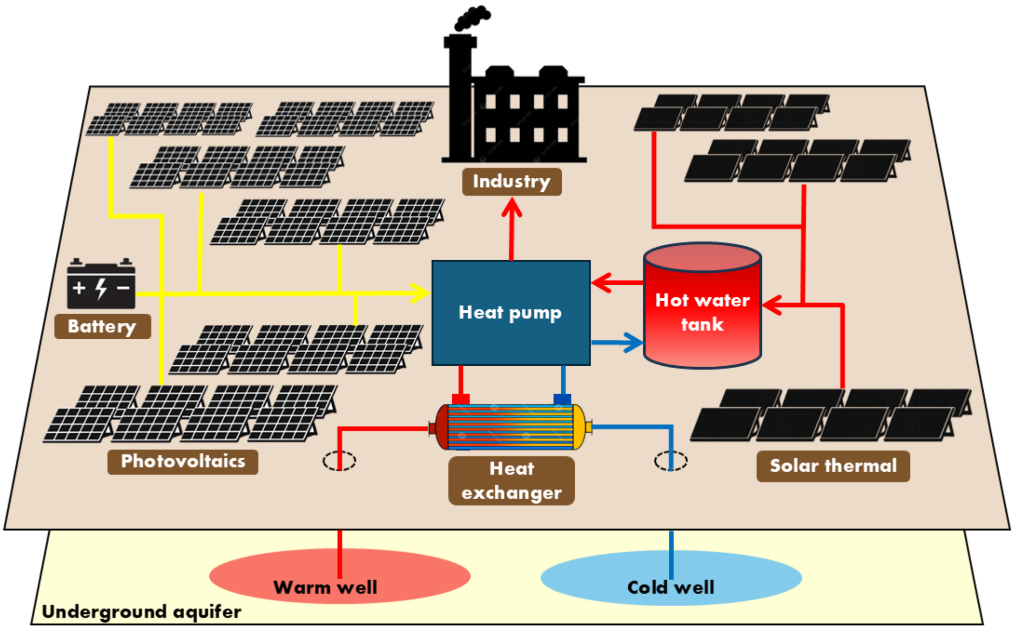

Figure 2.10. Illustration of the individual components into an integrated industrial system.

Chapter 3

Integrated system

This chapter presents the development of an integrated energy model that combines the high-temperature components described in Chapter 2 into a complete industrial process heat supply system, with multiple operational modes, and system configurations (Objective 2). Thereby, enabling the simulation of solar-powered industrial heat supply under varying conditions. A schematic diagram of the industrial heating system is shown in Figure 3.1. It should be noted that the distinction between warm and cold water in the legend is determined by the relative enthalpy of the water instead of the temperature.

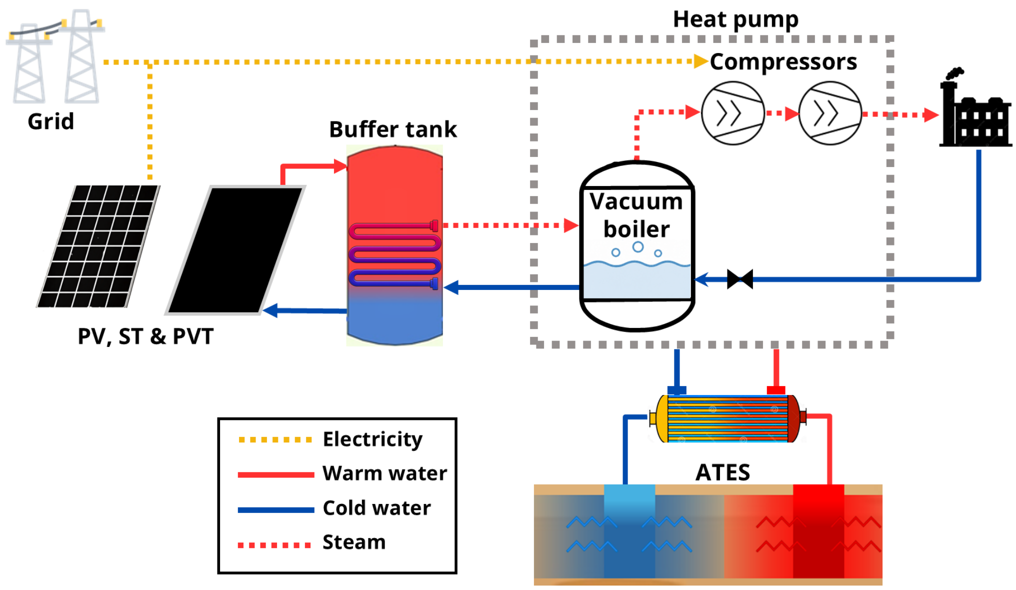

Figure 3.1. Schematic diagram of an industrial heating system comprising out of solar collectors (ST, PVT, and PV), an ATES system, heat exchangers, a buffer storage tank, and a HP

The chapter is structured as follows. Section 3.1 introduces the six system configurations considered in this thesis, outlining the key differences between them. Section 3.2 then describes the operational modes of the energy system, including the governing equations used to describe the energy flows within each mode and the control strategy used to select between them. The system inputs are discussed in Section 3.3, covering both the industrial heat demand profiles and the weather data used to operate the model. Finally, Section 3.4 presents a brief validation of the integrated energy system model.

3.1. System configurations

This section outlines the six system configurations compared in this thesis. The system configurations are divided into five primary system configurations and one additional system configuration. The five primary system configurations are built up from a simple system to a more complex system by incrementally adding components, allowing the individual contribution of each component to be assessed. In addition to the primary system configurations, configuration 6 is introduced which replaces the ST and PV with PVT collectors. The different configuration are summed up below.

- Configuration 1 (reference): Resistive heater heat generation
- Configuration 2 (reference): ST heat generation with HP
- Configuration 3 (reference): ATES seasonal storage
- Configuration 4 (reference): PV electricity generation
- Configuration 5 (main): Battery energy storage system
- Configuration 6 (main): PVT heat and electricity generation

Configuration 1 (Resistive heater heat generation) is depicted in Figure 3.2 and serves as the baseline configuration. In this configuration, a resistive heater supplies 100% of the heating demand. The resistive heater is assumed to operate at 100% efficiency. This configuration serves as a reference scenario, representing a system fully dependent on grid electricity. Figure 3.3 shows Configuration 2 (ST heat generation with HP), in which ST collectors are used to generate thermal energy that is subsequently stored in a thermal buffer storage tank. The buffer storage tank is not sized for seasonal thermal energy storage and only covers short thermal energy shortages of three to four days. This buffer storage is coupled to a HP to supply steam for industrial process heating. The HP draws its electrical power from the grid.

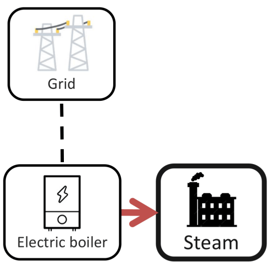

Figure 3.2. Configuration 1 (reference): Resistive heater heat generation.

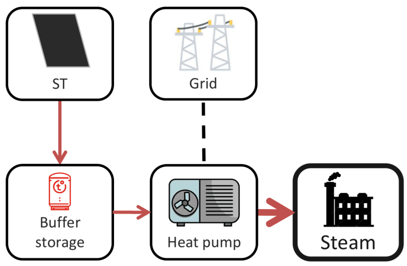

Figure 3.3. Configuration 2 (reference): ST heat generation with HP.

Configuration 3 (ATES seasonal storage) extends the previous system by integrating an ATES for seasonal thermal energy storage, as shown in Figure 3.4. The ATES is coupled to the HP and provides thermal energy during longer shortages not covered by the buffer. Consequently, mitigating the negative effects of seasonal solar irradiance variation on system performance. Figure 3.5 presents Configuration 4 (PV electricity generation), in which PV modules are added to provide electricity to the system. The electricity is used to power the HP and hydraulic pumps for the ATES, potentially enabling the system to function completely independently of the grid.

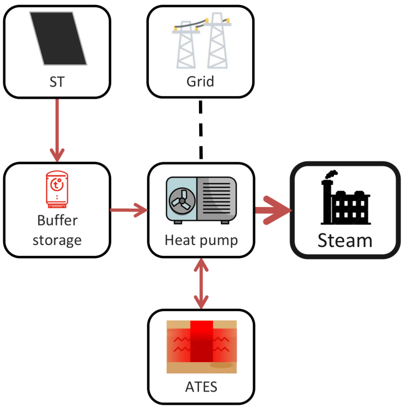

Figure 3.4. Configuration 3 (reference): ATES seasonal storage.

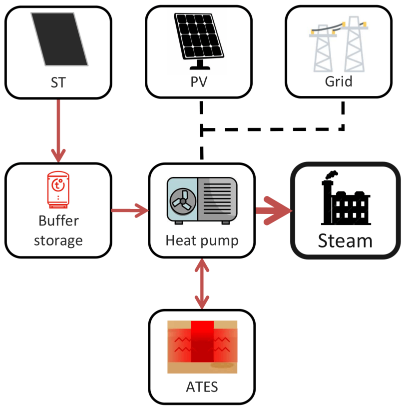

Figure 3.5. Configuration 4 (reference): PV electricity generation.

Finally, Configurations 5 and 6 are shown in Figures 3.6 and 3.7. Configuration 5 (Battery energy storage system) incorporates a battery energy storage system, as shown in Figure 3.6, increasing the self-sufficiency of the system by reducing electrical power shortages. In Configuration 6 (PVT heat and electricity generation) the separate ST and PV arrays are replaced by PVT collectors, which simultaneously generate thermal and electrical energy. This system configuration is illustrated in Figure 3.7. The aim of this configuration is to assess whether PVT collectors can reduce the total collector area required relative to separate ST and PV installations. Configuration 5 and 6 largely follow the same operational mode logic as Configuration 4 discussed in Section 3.2. Configuration 5 adds the battery charging and discharging logic discussed in Section 2.7 to the electrical energy Section 3.2.5 and Configuration 6 is adapted by replacing the PV and ST models with the PVT model discussed in 2.2.4.

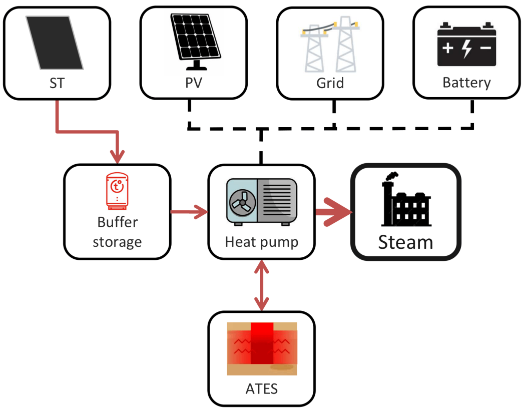

Figure 3.6. Configuration 5 (main): Battery energy storage system.

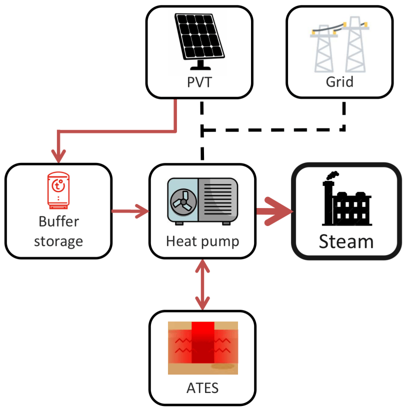

Figure 3.7. Configuration 6 (main): PVT heat and electricity generation.

3.2. Operational modes

This section describes the different operational modes of Configuration 4 and 5 (Figure 3.5 and 3.6). The governing equations of Configuration 1, 2 and 3 are described accordingly, since the thermal governing equations of Configuration 4 and 5 are built up incrementally from those configurations. When replacing ST generation by PVT heat generation the governing equations can also be applied to Configuration 6. The modes are divided into 3 main modes: Mode I (Balanced operation), Mode II (Surplus), and Mode III (Shortage). The surplus and shortage modes are divided into two sub-modes A and B. Each mode is illustrated with a figure, accompanied by its governing equations. Subsequently, the optimal temperature lift of the heat pump is discussed in Section 3.2.4. The description of the modes focuses exclusively on the thermal energy flows and does not take into account electrical energy consumption or generation. Electrical energy flows are discussed in Section 3.2.5. The section concludes with a control flow chart (Figure 3.16) showing which mode is selected based on the conditions in the system.

Before describing the individual modes, several variables, and equations that appear throughout this section are defined here to avoid repetition. The first step is to determine the difference between the generation and consumption of heat during each time step with Equation 3.1.

$$\Delta Q = Q_{\mathrm{ST}} - Q_{HP}, \tag{3.1}$$

where ΔQ is the difference between generation and consumption, Q_{ST} is the energy generated by the ST collectors described by Equation 3.2, and Q_{HP} is the thermal energy extracted from the heat pump source .

$$Q_{\mathrm{ST}} = G\eta_{\mathrm{th}} N_{\mathrm{ST}} A_{\mathrm{c}} dt, \tag{3.2}$$

where G is the plane of array irradiance in $\mathrm{W\,m^{-2}}$, η_{th} is the thermal efficiency of the ST collectors, N_{ST} is the number of collectors, A_c is the aperture area of a single collector, and dt is the number of seconds of one time step. The thermal energy consumed by the heat pump, Q_{HP}, depends on the COP reached during operation. The COP is determined through Equation 2.9 and depends on the temperature lift ΔT_{HP}. The temperature lift varies by mode and is defined in each section. The thermal energy that the HP must extract from its heat source to satisfy the industrial process demand Q_{D} is:

$$Q_{\mathrm{HP}} = Q_{\mathrm{D}} \frac{COP - 1}{COP} \tag{3.3}$$

The HP in this system consists of a vacuum boiler coupled to a two-stage compression cycle. The water in the vacuum boiler evaporates at a temperature slightly below the source temperature by operating at reduced pressure. This reduces the required compressor work and improves the COP. The COP is evaluated at the source temperature rather than the vacuum boiler evaporation temperature, conforming to the method of Ramirez et al. [8]. The evaporated steam is separated from the residual liquid and compressed until it reaches the industrial demand temperature T_{D}. Condensate returning from the process re-enters the vacuum boiler at approximately 70 °C, consistent with process steam condensate temperatures found in literature [96][16]. This operating principle applies in all modes and is not repeated in the individual subsections.

3.2.1. Mode I: Balanced operation

Mode I represents normal system operation, during which ST collectors charge the buffer storage while the HP simultaneously extracts heat from the buffer to meet industrial demand. In this mode the total heat capacity of buffer storage is able to cover mismatches between heat consumption and generation. No ATES interaction occurs. The main components of this system are the ST collectors, the thermal buffer storage, and the HP consisting of a vacuum boiler and a two-stage compression cycle as shown in Figure 3.8

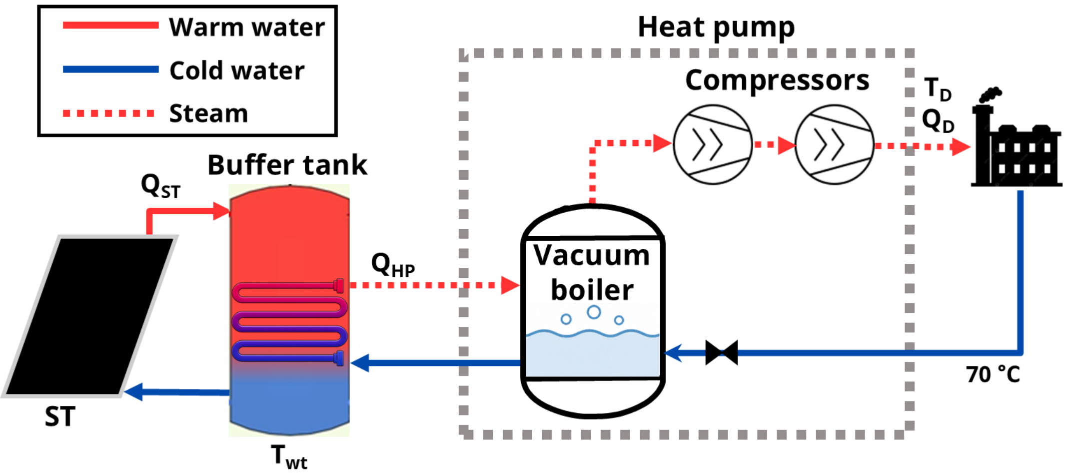

Figure 3.8. Illustration of operational Mode I: Balanced operation. System relies on buffer storage tank to supply heat and no surplus generation takes place, with buffers storage operating temperatures constrained by $80 \leq T_{\text{wt}} \leq 120\ ^\circ\text{C}, \quad \text{while } T_{\text{D}} \in \{130, 150\}\ ^\circ\text{C}.$

The ST collectors generate heat Q_{ST} according to Equation 3.2, which is added to the buffer storage. Simultaneously, the HP extracts source heat from the buffer to meet the process heating demand. The temperature lift required from the HP depends on the industrial demand temperature (T_D) and the temperature of the buffer tank (T_{wt}), as expressed in Equation 3.4.

$$\Delta T_{\text{HP}} = T_{\text{D}} - T_{\text{wt}} \tag{3.4}$$

The temperature lift ΔT_{HP} is used to determine the COP of the system with Equation 2.9. A lower temperature lift results in a higher COP since the required compressor work is reduced. Subsequently, the source heat demand of the HP is determined using Equation 3.3. The buffer storage temperature is then updated using Equation 2.8, where $Q_{\text{out}} = Q_{\text{HP}}$ and $Q_{\text{in}} = Q_{\text{ST}}$.

3.2.2. Mode II: Surplus

Mode II is activated when the ST collectors generate more thermal energy than can be consumed by the HP or stored in the buffer tank. Depending on the temperature of the ATES wells, this surplus is stored seasonally in Mode IIA or curtailed in Mode IIB.

- **Mode IIA: Charging of ATES**

Mode IIA is activated when the buffer storage has reached its maximum temperature (120 °C). Excess ST thermal energy generation is stored within the ATES system, which functions as the HP sink. The surplus thermal energy is upgraded to high temperature steam at 160 °C using the HP and used to charge the ATES via a heat exchanger. This represents the maximum temperature that can be reached by the HP, allowing seasonal thermal energy storage over a larger temperature range. Figure 3.9 illustrates the heat flows of this mode.

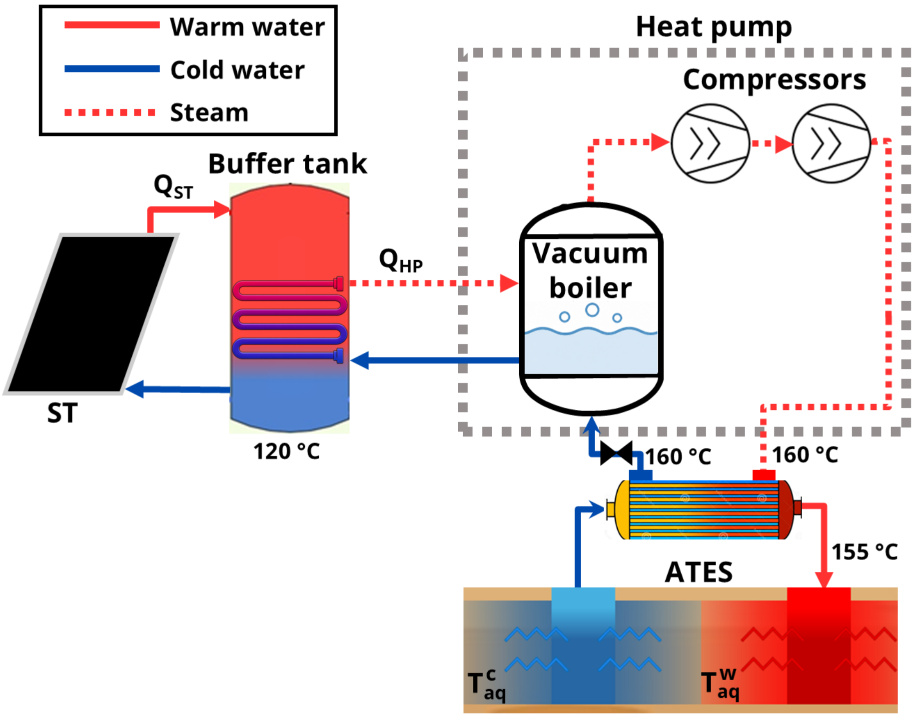

Figure 3.9. Illustration of operational Mode IIA: Charging of ATES. Surplus heat from the ST collectors is used to charge the ATES, with ATES operating temperatures constrained by $90 \leq T^{\mathrm{w}}_{\mathrm{aq}} \leq 150$ °C, $\quad 40 \leq T^{\mathrm{c}}_{\mathrm{aq}} \leq 100$ °C.

The ATES is charged using the portion of Q_{ST} that exceeds the buffer storage capacity. Since the maximum HP output temperature (160 °C) and maximum buffer temperature $T_{\mathrm{wt,max}}$ (120 °C) are fixed, the temperature lift is fixed at 40 °C:

$$\Delta T_{\mathrm{HP}} = 160 - T_{\mathrm{wt,max}} \tag{3.5}$$

The COP is then computed based on Equation 2.9 using the fixed ΔT_{HP} found in Equation 3.5. The electrical work required by the HP compressors W_{HP} is then determined using the surplus generation and the COP:

$$W_{\mathrm{surplus}} = \frac{Q_{\mathrm{HP}}}{COP - 1} \tag{3.6}$$

The surplus heat is transferred to the ATES system via condensation in a heat exchanger. The thermal energy transfer from the buffer storage to the HP and from the HP to the ATES are both fully driven by a phase change. Therefore, both are equal to the product of the produced steam mass M_{steam} and its latent heat of vaporization L_w. This relation between the thermal energy surplus Q_{ST} and heat added to the ATES Q_{in} is presented in Equation 3.7

$$Q_{\mathrm{in}} = M_{\mathrm{steam}} L_w = Q_{\mathrm{surplus}} \tag{3.7}$$

The temperature of the ATES can be updated by inserting Q_{in} into Equation 2.15. The mass flow rate of water pumped from the cold well to the warm well, M_{ATES}, is determined using Equation 3.8.

$$M_{\mathrm{ATES}} = \frac{Q_{\mathrm{in}}}{\Delta T_{\mathrm{hex}} C^{\mathrm{c}}_{\mathrm{p}}}, \tag{3.8}$$

where C_p^c is the specific heat capacity of the cold well water. The temperature increase of the cold well water ΔT_{hex} inside the heat exchanger is given in Equation 3.9.

$$\Delta T_{\text{hex}} = 160 - T_{\text{aq}}^{\text{c}} - T_{\text{pinch}}, \tag{3.9}$$

with $T_{\text{pinch}} = 5$ °C, as defined in Section 2.4 and T_{aq}^{c} is the temperature of the cold well.

After condensing, the water leaves the heat exchanger at a temperature of approximately 160 °C and a pressure of 6.18 bar. This water is passed through a pressure relief valve, where the pressure is reduced to the pressure of the vacuum boiler. As a result, a fraction of the water flashes into steam. Equation 3.10 shows how the mass percentage of flashed water x_{evap} is determined.

$$x_{\text{evap}} = \frac{h_{\text{hex}} - h_{\text{HP}}}{L_w}, \tag{3.10}$$

where h_{hex} is the enthalpy of the water leaving the heat exchanger and h_{HP} is the enthalpy of the water in the vacuum boiler. The flashed steam is separated from the liquid water in the vacuum boiler and fed into the two-stage compression system. Thereby, reducing the heat demand on the buffer storage in the subsequent timestep.

$$Q_{\text{red}} = Q_{\text{HP}} - x_{\text{evap}} L_w. \tag{3.11}$$

- **Mode IIB: Curtailment ST**

Mode IIB is used when both buffer storage and ATES storage have reached their maximum storage capacity. The ST generation is curtailed to prevent storage temperatures from exceeding the system limits. Curtailment is achieved by stopping the fluid flow through the ST collectors. No governing equations beyond those in Mode I apply, since the HP continues operating to deliver the process heating demand while the ST surplus is discarded. This mode is depicted in Figure 3.10.

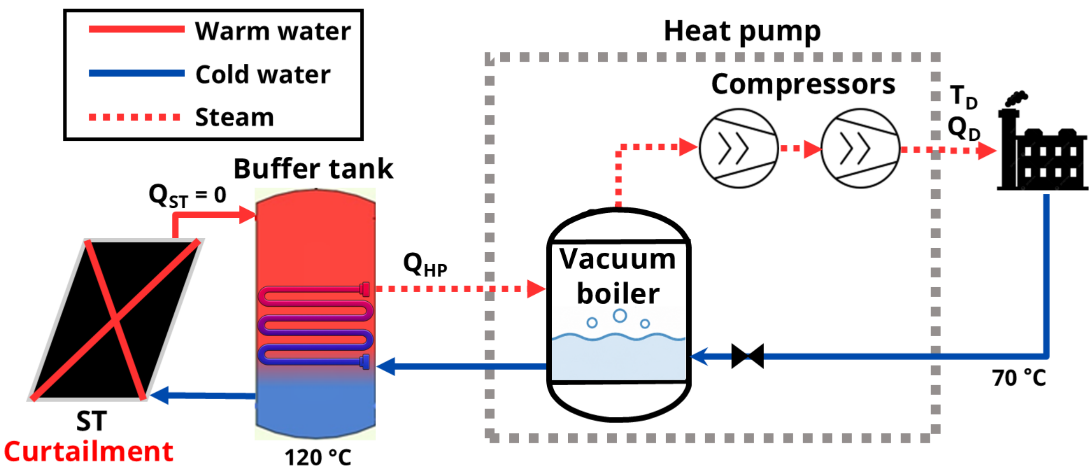

Figure 3.10. Illustration of operational Mode IIB: Curtailment ST. Excess heat generation in the ST collectors is curtailed, where $T_D \in \{130, 150\}$ °C.

3.2.3. Mode III: Shortage

Mode III is activated when the thermal buffer storage reaches its minimum operating limit ($T_{\text{wt}} = 80$ °C) and cannot satisfy the industrial heat demand. In this scenario, heat is extracted from the warm ATES well in Mode IIIA, or a backup resistive heater is activated in Mode IIIB.

• **Mode IIIA: Discharge ATES**
When the buffer storage cannot fully satisfy the process heating demand and the ATES wells have not reached their operational limits, Mode IIIA is activated. During which heat from the warm well is extracted and used to evaporate water from the vacuum boiler via a heat exchanger. This is done by pumping warm water from the ATES through a heat exchanger that is coupled to the vacuum boiler. The ATES heat cannot be directly be used in industry since ATES temperatures are frequently below those required in industry. Furthermore, the industry requires high temperature compressed steam which can be effectively generated using the steam compression HP used within this thesis. The different components and thermal energy flows of Mode IIIA are shown in Figure 3.11.

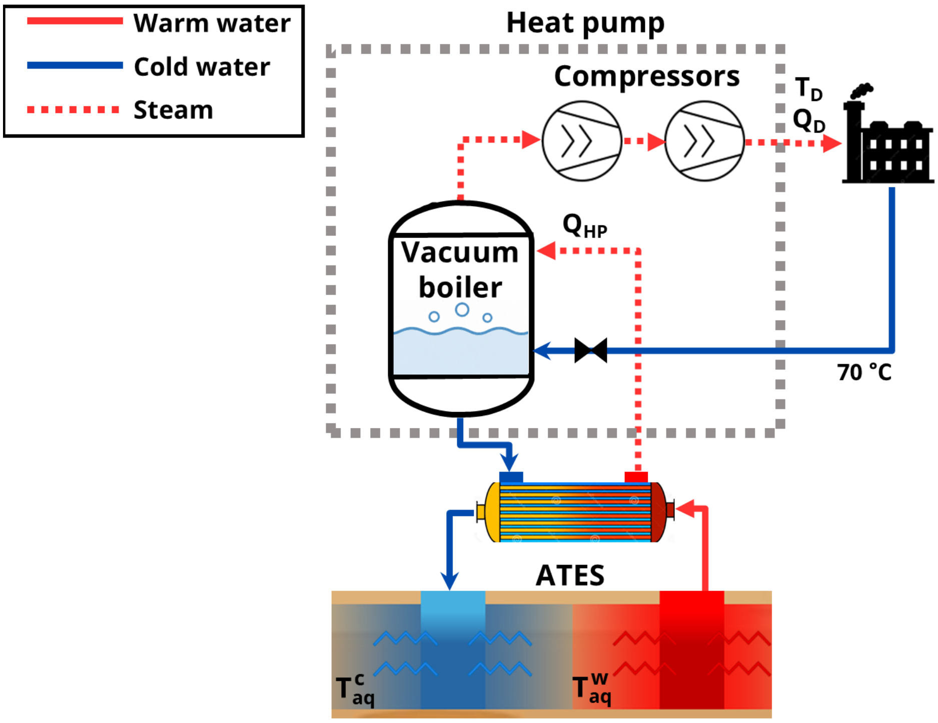

Figure 3.11. Illustration of operational Mode IIIA: Discharge ATES. The ATES warm well supplies heat to the HP, with ATES operating temperatures constrained by $90 \leq T^{\mathrm{w}}_{\mathrm{aq}} \leq 150$ °C, $40 \leq T^{\mathrm{c}}_{\mathrm{aq}} \leq 100$ °C, while $T_D \in \{130, 150\}$ °C.

For Mode IIIA, finding an optimal temperature lift ΔT_{HP} is more complex compared to for the other modes I and IIA. This complexity stems from the competing influence of ΔT_{HP} on both the COP and the pumping power required to extract water from the ATES. The derivation of the optimal ΔT_{HP} that minimizes electrical consumption for varying warm well temperatures is presented in Section 3.2.4 and summarized in Equation 3.12.

$$\Delta T_{HP} = D + 0.8(T^{\mathrm{w}}_{\mathrm{aq,max}} - T^{\mathrm{w}}_{\mathrm{aq}}), \tag{3.12}$$

where D is a constant dependent on the industrial demand temperature T_{D}, as defined in Section 3.2.4. $T^{\mathrm{w}}_{\mathrm{aq,max}}$ is the maximum temperature of the warm well in the ATES system and $T^{\mathrm{w}}_{\mathrm{aq}}$ is the current warm well temperature. Subsequently, the COP is determined using ΔT_{HP} in Equation 2.9 and the heat extracted from the warm well follows from Equation 3.3. This extracted water cools down with ΔT_{hex} across the heat exchanger before injection into the cold well. This temperature difference can be expressed as follows:

$$\Delta T_{\mathrm{hex}} = T^{\mathrm{w}}_{\mathrm{aq}} + \Delta T_{\mathrm{HP}} - T_{\mathrm{pinch}} - T_{\mathrm{D}}, \tag{3.13}$$

where $T_{\mathrm{aq}}^{\mathrm{w}}$ is the current temperature of the warm well and T_{pinch} is 5 °C as defined in Section 2.4. The corresponding mass flow rate M_{ates} of the aquifer water is then given by Equation 3.14.

$$M_{\mathrm{ates}} = \frac{Q_{HP}}{\Delta T_{hex} C_{p,warm}}, \tag{3.14}$$

where C_p^{w} is the specific heat capacity of the warm well water. The ATES temperature is subsequently adjusted using Equation 2.17 where $Q_{\mathrm{out}} = Q_{\mathrm{HP}}$.

• **Mode IIIB: Backup electrical boiler**
Mode IIIB is utilized when both buffer storage and ATES have reached their minimum temperature limits. To meet industrial heat demand, an electrical backup resistance heater is used to supply heat directly to the vacuum boiler. This system is comparable to Configuration 1 discussed in Section 3.1 and is depicted in Figure 3.12.

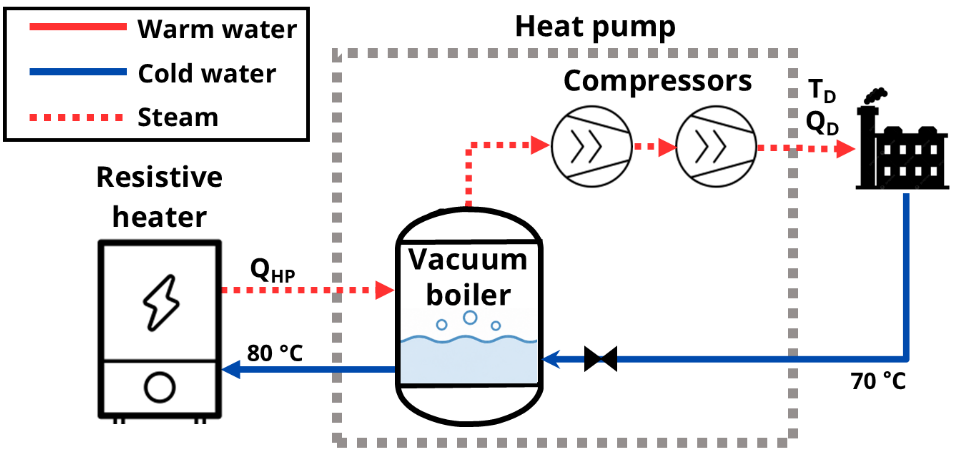

Figure 3.12. Illustration of operational Mode IIIB: Backup electrical boiler. Shortage of heat requires a backup electrical boiler to be used for heat generation, where $T_{\mathrm{D}} \in \{130, 150\}$ °C.

During this operational mode the thermal and mechanical losses in the resistive heater and HP are assumed to be negligible. This results in an underestimation of the required electrical energy. However, since this mode is only activated sparingly in properly sized systems, the impact on the overall results is limited. Under this assumption, the electrical work supplied by the backup boiler W_{backup} is equal to the industrial heat demand Q_{D}, as expressed in Equation 3.15.

$$W_{\mathrm{backup}} = Q_{\mathrm{D}}. \tag{3.15}$$

3.2.4. Heat exchanger temperature

When the system operates in Mode IIIA water is pumped out of the warm ATES well through a heat exchanger which acts as the HP source. The total electrical power consumption in this mode has two competing contributions.

1. **Hydraulic pumping power** (W_{pump}): The pumping power increases proportional to the volume of water extracted from the ATES. A larger temperature drop across the heat exchanger (ΔT_{hex}) means more heat is extracted per kilogram of water, reducing the required flow rate and therefore the pumping power. From a pumping power perspective, a lower evaporation temperature in the vacuum boiler is preferable.

2. **Heat pump compressor power** (W_{HP}): The compressor power required by the HP decreases with decreasing temperature lift ΔT_{HP}. A higher evaporation temperature in the vacuum boiler reduces the temperature lift and is therefore preferable from compressor power perspective. However, a higher evaporation temperature also reduces the temperature drop across the heat exchanger, limiting the heat that can be extracted per kilogram of ATES water.

These two effects act in opposite directions, as illustrated in Figure 3.13. Increasing ΔT_{HP} reduces pumping power but increases compressor power. This section derives the optimum HP temperature lift at which $W_{\text{total}} = W_{\text{pump}} + W_{\text{HP}}$ is minimized.

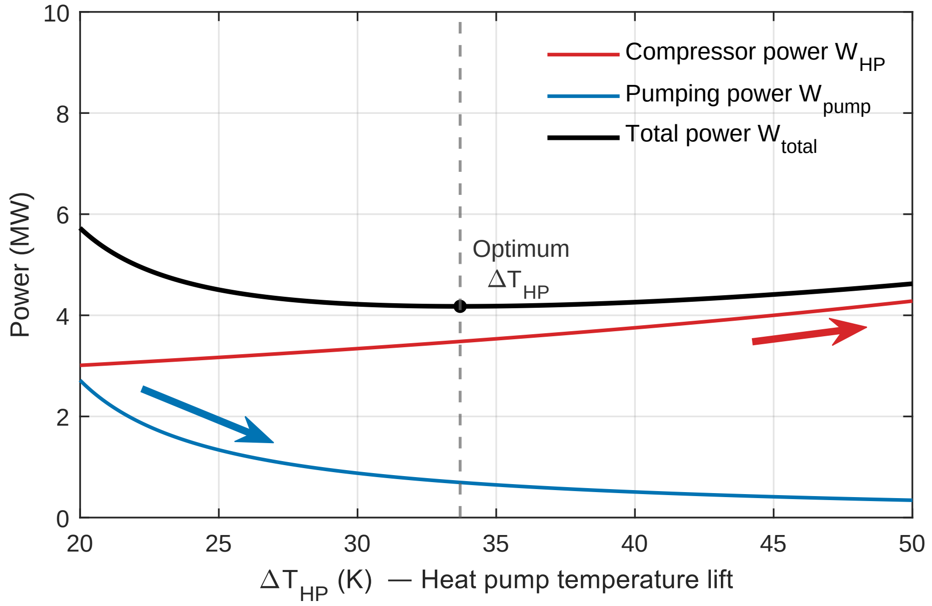

Figure 3.13. Illustrative example of HP compressor and hydraulic pump power consumption during Mode IIIA operation for $T_{\text{ATES}} = 120$ °C and $T_{\text{D}} = 130$ °C. The compressor power increases and the pumping power decreases with increased HP temperature lift.

To find the optimum ΔT_{HP}, an expression must be derived that accounts for both the HP COP and the ATES pumping power. The ΔT_{hex} of the warm water in the heat exchanger is defined by Equation 3.13. The heat transferred per unit mass of ATES water Q_{source} is calculated as:

$$Q_{\text{source}} = C_{\text{w}} \Delta T_{\text{hex}}, \tag{3.16}$$

where Q_{source} is the specific heat transfer in Jkg^{-1}, C_{w} is the specific heat capacity $Jkg^{-1}K^{-1}$ and ΔT_{hex} is the temperature drop of the warm-side fluid in the heat exchanger. The specific heat capacity C_{w} is evaluated at 130 °C, representing a typical mean ATES operating temperature. The work done by the HP can be expressed by equation as:

$$W_{\text{HP}} = \frac{Q_{\text{source}}}{(COP - 1)}, \tag{3.17}$$

where W_{HP} is the work done by the HP expressed in Jkg^{-1} of water pumped up from the warm well. The COP is determined using equation 2.9. Using W_{HP} and Q_{source}, the total thermal energy delivered $Q_{\text{delivered}}$, per kg of ATES water, can be determined by the following equation.

$$Q_{\text{Delivered}} = Q_{\text{source}} + W_{\text{HP}}, \tag{3.18}$$

where $Q_{\text{delivered}}$, Q_{source}, and W_{HP} are all expressed in Jkg^{-1} of water pumped up from the warm well. To determine the pumping power of the hydraulic pumps per unit mass of water, the total pressure drop is determined using the equations described in Section 2.6. Using these equations, the hydraulic and frictional pressure contributions are determined to find the total pressure drop in the pipes. The water is assumed to move at the design velocity of 1.5 ms^{-1}. The pumping power per kg of water is determined using Equation 3.19.

$$W_{pump} = \frac{\Delta P_{total}}{\rho_w \eta_{pump}}, \tag{3.19}$$

where ΔP_{total} is the sum of the hydraulic and frictional pressure contributions in Jm^{-3}, ρ_{w} is the density of water at 130 °C in kgm^{-3}, and η_{pump} is the pump efficiency defined in Section 2.6. Finally, a new COP can be defined describing the system performance by combining $Q_{\text{delivered}}$, W_{pump}, and W_{HP} in Equation 3.20.

$$COP_{\text{system}} = \frac{Q_{\text{delivered}}}{W_{\text{pump}} + W_{\text{HP}}} \tag{3.20}$$

Using this equation, an optimum ΔT_{HP} can be found for each warm well ATES temperature. Figures 3.14 and 3.15 show the COP_{sys} plotted against ΔT_{HP} for six different warm well temperatures. Figure 3.14 shows the COP_{sys} for an industrial heating system requiring 130 °C process heating.

As ΔT_{HP} increases, the relative pumping power contribution is reduced, causing the COP_{sys} curves to approach the dotted line representing COP without pumping losses. However, increasing ΔT_{HP} simultaneously increases the compressor power consumption of the HP, resulting in a clear optimum where total electrical power consumption is minimized. These optimums are depicted using dots, accompanied by their respective ΔT_{HP} values.

The optimal temperature lift of the heat pump decreases as the temperature of the warm well increases. This is because a lower warm well temperature reduces the ΔT_{hex} within the heat exchanger ($\Delta T_{\text{hex}} = T^{\text{w}}_{\text{aq}} - T_{\text{evap}} - \Delta T_{\text{pinch}}$), thereby increasing the required pumping power. To compensate for the increased pumping power, the vacuum boiler pressure is reduced to decrease the evaporation temperature. This results in an increase of ΔT_{hex} and a reduction the required mass flow rate.

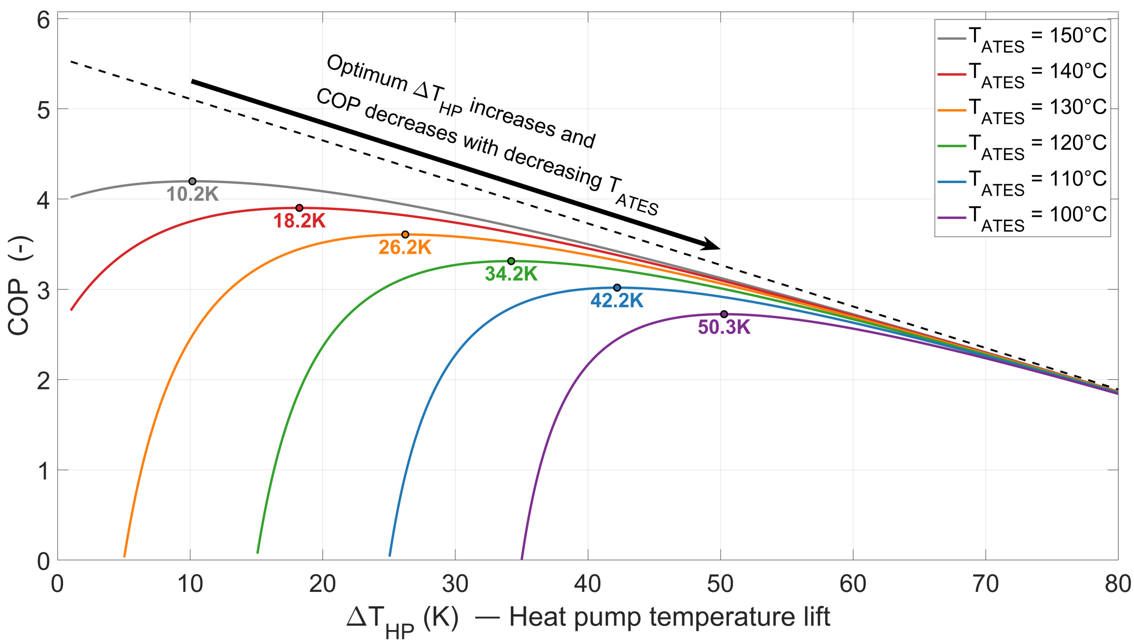

Figure 3.14. COP of a heat pump including hydraulic pumping power from the ATES. The dotted line shows the COP without hydraulic pumping power. $T_{\text{D}} = 130$ °C, depth = 400 m. Optimum temperature lifts for varying ATES temperatures are included.

Figure 3.15 presents the COP_{sys} for an industrial heating system requiring 150 °C process heating. The figure shows a similar trends to Figure 3.14, with system performance decreasing with decreasing aquifer temperature. Compared to the 130 °C scenario, the optimal ΔT_{HP} values are higher and COP values are lower, indicating a reduced overall system performance. This is a direct consequence of the larger required temperature lift due to a higher demand temperature of 150 °C.

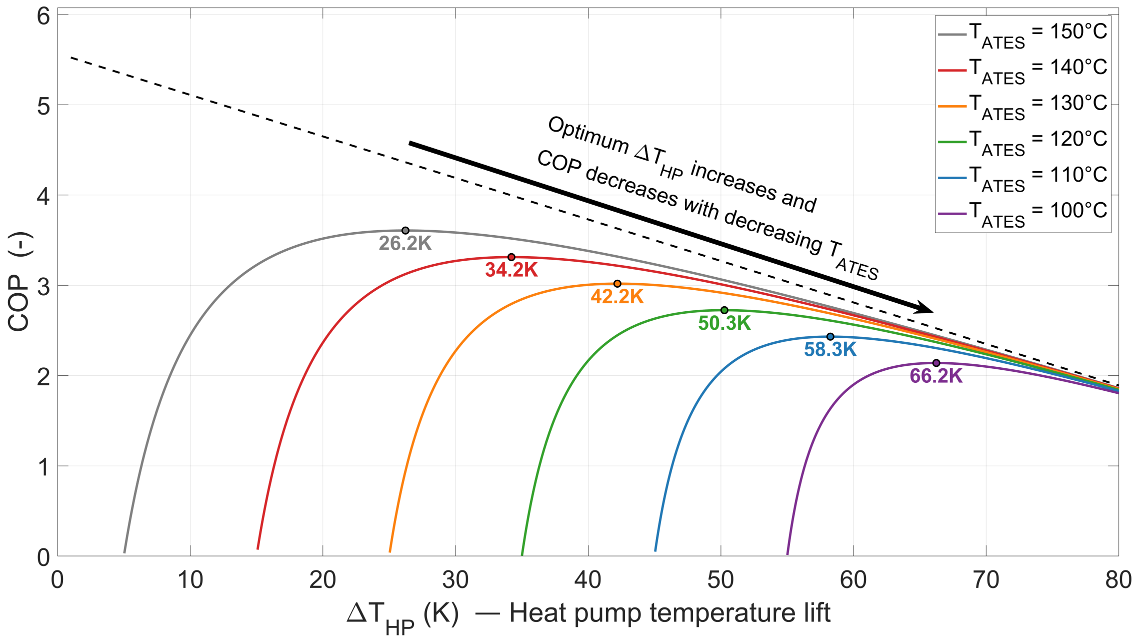

Figure 3.15. COP of a heat pump including hydraulic pumping power from the ATES. The dotted line shows the COP without hydraulic pumping power. T_{D} = 150 °C, depth = 400 m. Optimum temperature lifts for varying ATES temperatures are included.

A linear relationship between the optimal ΔT_{HP} and the warm well temperature (T_{ATES}) is identified and expressed in Equation 3.12. The coefficient D depends on the required steam temperature T_{D}, as expressed in Equation 3.21.

$$D(T_D) = \begin{cases} 10.2 & \text{if } T_D = 130\ ^\circ\text{C} \\ 26.2 & \text{if } T_D = 150\ ^\circ\text{C} \end{cases} \tag{3.21}$$

Only demand temperatures of 130 and 150 °C are considered, consistent with the industrial heating scenarios defined in Section 3.3.1. For other demand temperatures or system conditions, the above procedure must be repeated to find the relationship between the warm well temperature and the optimal ΔT_{HP}. Appendix B.1 presents a similar optimal COP analysis for ATES systems located far from industrial demand, as a solution to locally unfavorable geological conditions.

3.2.5. Electrical energy

In addition to thermal energy flows, the system requires electrical energy to operate. The two-stage compression of the HP and the hydraulic pumps of the ATES represent the dominant electrical consumers. Therefore these are the only electrical loads considered in this study. The electrical loads W are expressed in joules. The electrical work done by the two-stage compressors W_{HP} can be described by the following equation.

$$W_{\text{HP}} = \frac{Q_{\text{D}}}{COP} \tag{3.22}$$

The electrical work done by the hydraulic pumps of the seasonal storage W_{P} is described by Equation 2.19 and subsequent equations in Section 2.6. This equation is adapted so that the mass flow rates M_{ates}, determined in Equations 3.8 and 3.14, are used as inputs. The mass flow rates are divided by the local water density to obtain the volumetric flow rate Q. The total electrical power demand W_{el} is obtained by summing the hydraulic pump power W_{P} consumption, and the two stage compressor power W_{HP} consumption, as expressed in Equation 3.23.

$$W_{\mathrm{el}} = W_{\mathrm{P}} + W_{\mathrm{HP}} \tag{3.23}$$

Configuration 4 also uses PV collectors to generate electrical energy to power the system. This reduces the system's dependence on grid electricity. The net consumption of electricity from the grid W_{grid} is expressed as:

$$W_{\mathrm{grid}} = W_{\mathrm{el}} - W_{\mathrm{PV}}, \tag{3.24}$$

where W_{PV} is the total electricity generation from the PV collectors which is determined using the equations in Section 2.2.1. When W_{PV} exceeds W_{el}, W_{grid} becomes negative, indicating a surplus of electricity that must be fed back to the grid or curtailed. For Configuration 5 and 6 which include electrical batteries surplus electricity can be stored in the batteries which can be recovered during shortages.

3.2.6. Control strategy

The operational mode is selected at each timestep according to a predefined control strategy, summarized in the flow chart in Figure 3.16. In the flow chart, a clear distinction is made between the default, shortage, and surplus modes. All decision diamonds in the chart apply AND logic, meaning both conditions must be satisfied simultaneously. Furthermore, the system is controlled on an hourly basis, with all inputs representing hourly values.

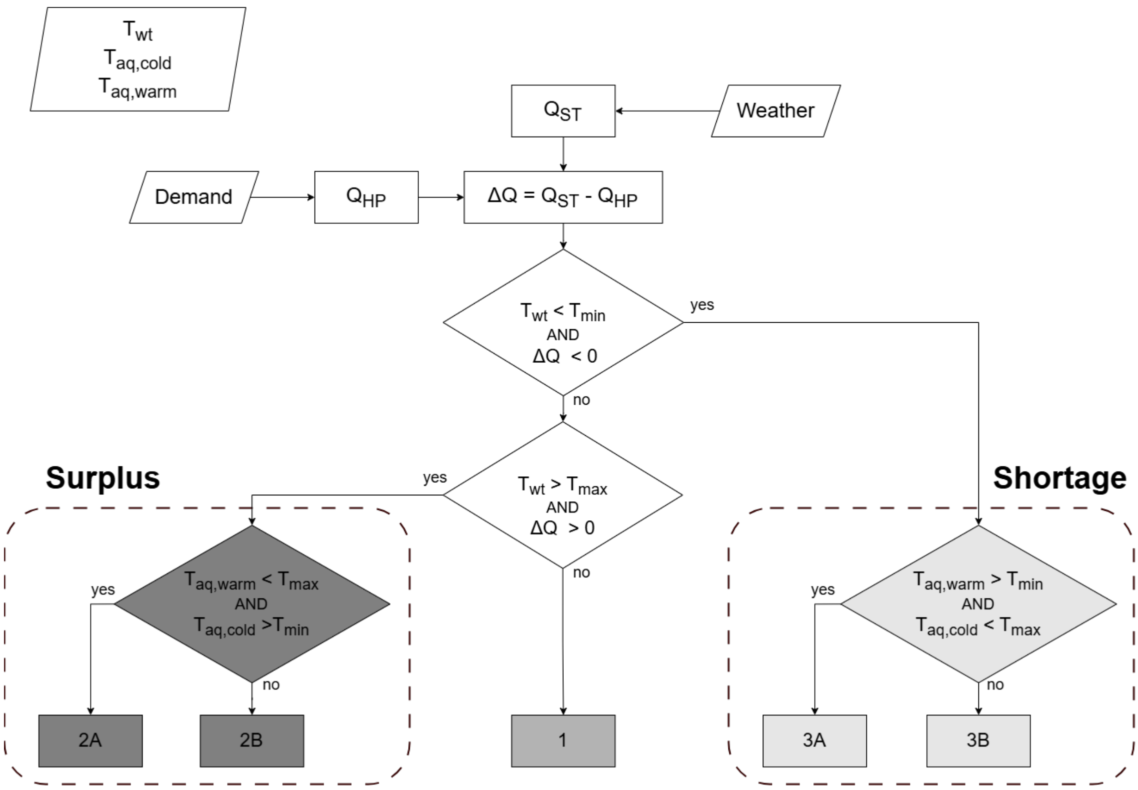

Figure 3.16. Flow chart depicting the control strategy used in this thesis. A clear distinction is made between the default, surplus, and shortage modes.

Using weather data, the thermal output of the ST collectors (Q_{ST}) is determined. The heat influx required by the HP (Q_{HP}) is determined from the hourly industrial process heat demand. The difference between these two quantities defines the hourly net thermal energy balance ΔQ. Additionally, the temperatures of the buffer storage and the ATES wells are used to determine the selected operational mode. The two white decision diamonds determine whether the system operates in surplus, shortage or default mode. When the temperature of the buffer storage is below the minimum buffer storage temperature ($T_{\mathrm{wt}} = 80$ °C) and ΔQ is negative, the system selects the shortage mode. When the buffer storage temperature is above the maximum buffer temperature (120 °C) and there is a net positive heat flow into the buffer, the surplus mode is used. When neither condition is met, the system operates in Mode I, during which the buffer storage is charged or discharged depending on the sign of ΔQ.

The dark gray diamond in the surplus mode determines whether the system operates in Mode IIA or IIB. When the temperature of the warm well is below its defined maximum (150 °C) and the temperature of the cold well is above its defined minimum (40 °C), the system operates in Mode IIA. When neither condition is met, meaning that both storage systems have reached their capacity limits, the system operates in Mode IIB and ST generation is curtailed. The light gray diamond in the shortage mode decides whether the system operates in Mode IIIA or IIIB. When the warm well temperature is above its minimum limit (90 °C) and the cold well temperature remains below its maximum limit (100 °C), the system operates in Mode IIIA. Alternatively, when these conditions are not met, the system operates in Mode IIIB and rely on an electric backup boiler. The modes can work in tandem in some situations where, for example, only a portion of the thermal energy demand can be met by the ST buffer tank. In such cases, the buffer tank and ATES operate simultaneously to collectively meet the heat demand. The use of the buffer tank is always prioritized over the ATES since the heat is not stored deep underground and therefore energy losses are lower. The equations are run sequentially within one time step, where heat extracted from the ATES is determined based on how much Q_{HP} is left over when the buffer storage has reached its limits.

3.3. Model inputs

This section describes the hourly model inputs used in this thesis. First, the industry heating demand is discussed in Section 3.3.1. This section describes the industrial sectors considered and their respective thermal energy demands. Subsequently, the weather inputs for two different locations are discussed in Section 3.3.2.

3.3.1. Industry demand

As illustrated in Figure 1.1 in Chapter 1, a substantial share of European industrial heat demand in the 100–200 °C range is attributed to the Food & Beverage sector, and the Paper, Pulp & Print industry. These sectors are therefore the primary focus of this thesis. To align with conventions used in the literature and available datasets, the sector definition of the Paper, Pulp & Print is referred to as the Paper & Pulp industry throughout the remainder of this thesis. The energy consumption of the considered factories is approximately 440 TJ, equal to the annual thermal and electrical energy demand of 11,000 Dutch households [97].

The Paper & Pulp sector is modeled as a continuous energy consumer, operating uniformly throughout the year rather than in batch or periodic cycles. Continuous operation is standard practice in paper processing, as it ensures consistent product quality [98]. According to Solar Heat Europe, an average Paper & Pulp plant requires 20 tonnes of steam per hour at temperatures around 150 °C [73]. Resulting in a annual energy consumption of approximately 449 TJ. These temperatures correspond to the requirements for drying and boiling processes in the Paper & Pulp industry [47].

The Food & Beverage sector is characterized by a daily peak in energy consumption as reported by Bedocchi et al.[99]. The steam consumption used in the model peaks between 9:00 and 15:00 and is nearly zero throughout the night. This represents a 2-hour shift relative to the demand profile reported by Bedocchi et al. [99], introduced to better align with peak solar irradiance hours. The energy consumption in the study above is averaged over multiple factories and processes. Many Food & Beverage processes use batch operations that can vary in time between seconds and hours [100].

Since the model works with hourly time steps, batch processing with varying durations is difficult to integrate. Therefore, the hourly averaged demand profile presented by Bedocchi et al. is used. This demand pattern broadly aligns with the daily solar irradiance cycle, reducing the need for short-term daily storage and potentially reducing grid electricity consumption through PV generation during peak load hours. One of the most common Food & Beverage processes is sterilization. This process typically operates at temperatures between 120 and 140°C [101]. In this thesis, the steam supplied to the Food & Beverage sector is modeled at a temperature of 130 °C. The demand profile is scaled so that the total annual steam consumption of the Food & Beverage sector equals that of the Paper & Pulp sector, resulting in a total energy consumption of 440 TJ. The demand curves of the two sectors are shown in Figure 3.17. The figure shows three days of operation and this pattern repeats throughout the year.

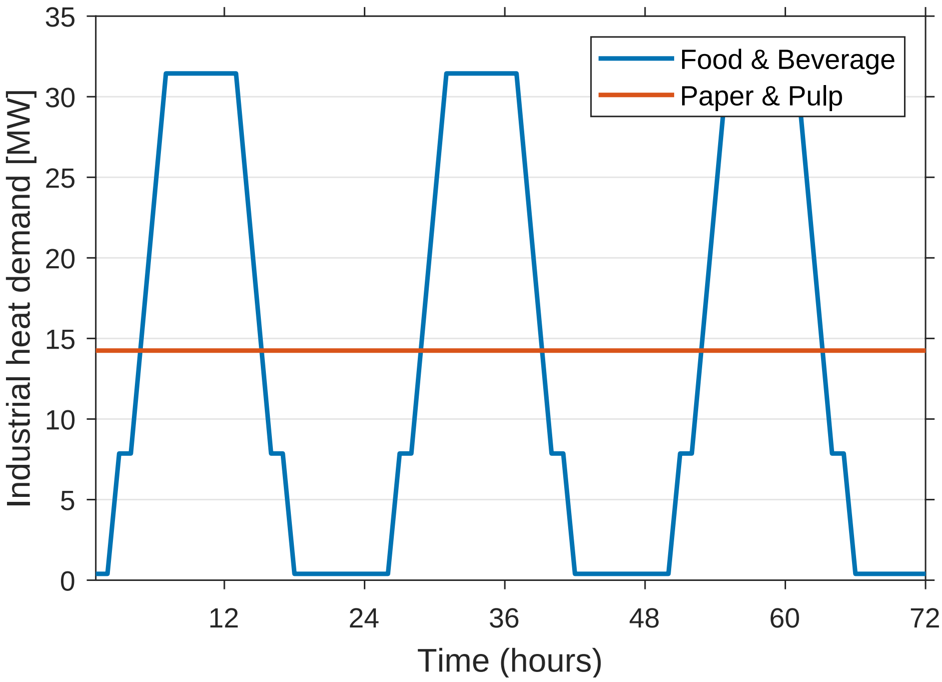

Figure 3.17. The steam demand for the paper & pulp, and food & beverage industries for three days

3.3.2. Weather data

The performance of solar energy systems is strongly dependent on the total received irradiance and its seasonal variation. To assess the viability of the proposed system across different climatic conditions, two locations are considered in this thesis: Delft (the Netherlands) and Seville (Spain). These locations provide contrasting climatic conditions in northwestern and southern Europe respectively, offering a broad basis to compare system performance. Hourly weather data, including the plane of array irradiance and ambient temperature, are obtained from Renewables.ninja [102] [103], which uses the CM-SAF SARAH data record. This dataset is produced by the EUMETSAT Climate Monitoring Satellite Application Facility (CM SAF) and consists of hourly high-resolution surface irradiance values derived from satellite observations [104]. The CM-SAF SARAH dataset has been validated by numerous studies, demonstrating consistently high accuracy across a wide range of climatic conditions [105–108].

Figures 3.18 and 3.19 present the mean monthly irradiance and the monthly average temperature for Delft and Seville respectively. Two distinct trends can be observed. First, Seville receives considerably more annual plane of array irradiation than Delft, 2148 and 1243 kWh/m^2 respectively.

Secondly, Delft exhibits a much greater seasonal imbalance: summer irradiation is 6.6 times higher than in winter, compared to a factor of 2.0 for Seville. A pronounced seasonal imbalance necessitates either a very large solar collector area or a form of seasonal thermal storage to meet year-round demand.

Comparing these two locations therefore provides insight into how collector sizing, storage capacity and grid dependence vary with climate.

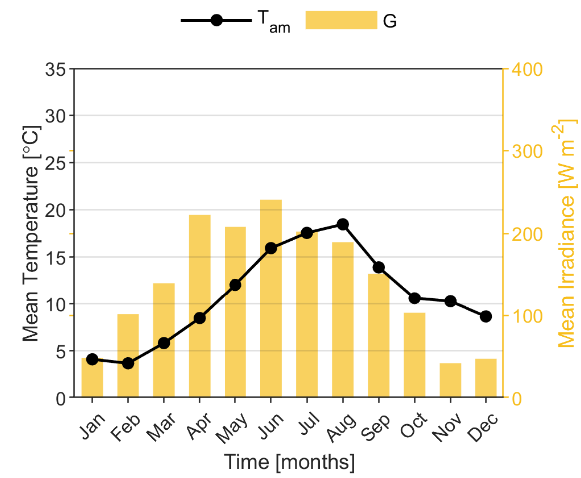

Figure 3.18. Monthly weather data Delft.

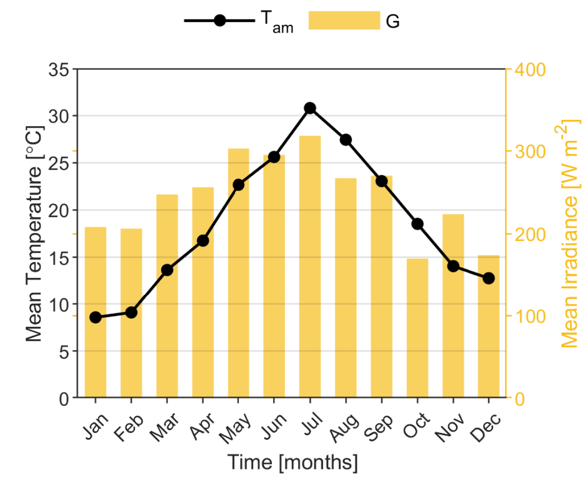

Figure 3.19. Monthly weather data Seville.

The hourly weather data for three distinct weeks throughout the year are presented in Figure 3.20 and Figure 3.21. The weeks presented in these figures coincide with the weekly results presented in Chapter 4. Delft shows a strong seasonal dependence on irradiance and temperature. For Seville irradiance has a less pronounced seasonal pattern but ambient temperature still varies significantly between different seasons.

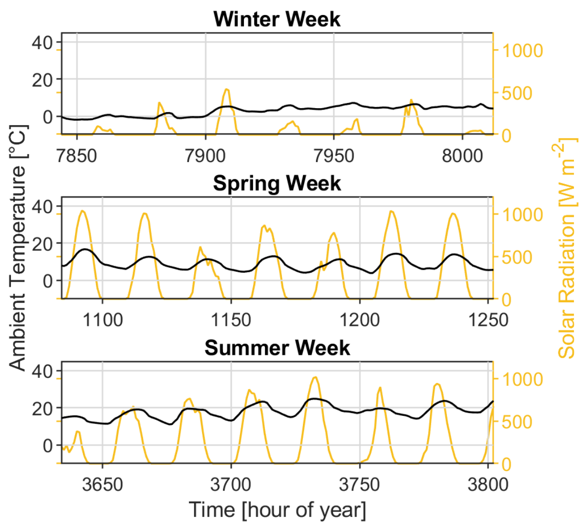

Figure 3.20. Hourly weather data Delft for three weeks.

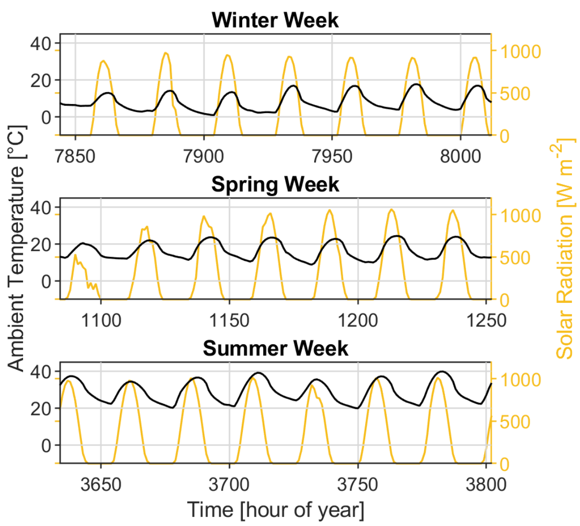

Figure 3.21. Hourly weather data Seville for three weeks.

3.4. Validation of the model

The industrial process heating system developed in this thesis represents a novel combination of components that has not been realized in practice. As a result, no experimental data exists for this integrated system, and direct validation of the integrated model is not possible. Instead, the individual component models are validated separately against experimental data and results from literature. Following the validation of the individual components, the numerical model can be applied with confidence to generate results in Chapter 4. Firstly, the PV, ST, and PVT collectors are validated by comparing outputs to values from literature in Section 3.4.1. This is followed by a validation of the ATES in Section 3.4.2, in which the long-term stability of the ATES is assessed. Finally, the output of the integrated system is validated in Section 3.4.3, where energy balances in the HP system are evaluated.

3.4.1. Solar collector validation

Accurate modeling of the thermal and electrical energy output of the solar collectors is critical to the overall performance of the industrial energy system. The PV yield was validated against long-term average data from the Solargis database [109], which has been validated against ground measurements across various climate zones [110]. The Solargis output incorporates 11% system losses, which must be taken into account when comparing the modeled PV yield against these reference values.

The modeled PV energy yield for Delft shows good agreement with the Solargis reference data. The Solargis data approximates the long-term average PV yield to be 1000 to 1100 $\text{kWh}\,\text{kWp}^{-1}$ in Delft. When excluding system losses, this range increases towards 1123 to 1235 $\text{kWh}\,\text{kWp}^{-1}$. A PV module generates 538 kWh/year in Delft with a peak power of 460 W. This results in an energy yield of 1169 $\text{kWh}\,\text{kWp}^{-1}$, which is within the Solargis range. For Seville, the long-term average PV yield is approximated to be around 1650 to 1750 $\text{kWh}\,\text{kWp}^{-1}$. When excluding system losses, this range increases towards 1854 to 1966 $\text{kWh}\,\text{kWp}^{-1}$. A PV module in Seville generates 910 kWh/year with a peak power of 460 W. This results in an energy yield of 1978 $\text{kWh}\,\text{kWp}^{-1}$ which is slightly above the long-term average range, but is reasonable for a year with above average irradiation. The results of this comparison are depicted in Figure 3.22.

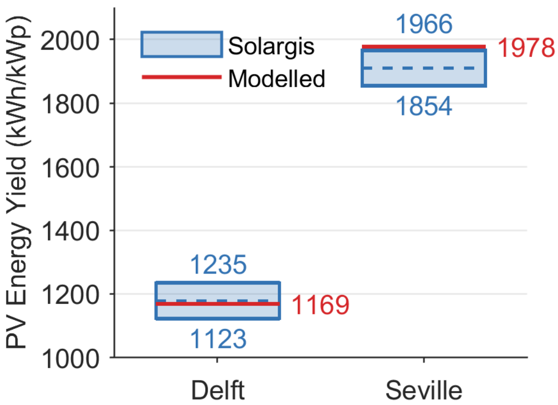

Figure 3.22. PV yield simulation results compared against Solargis data.

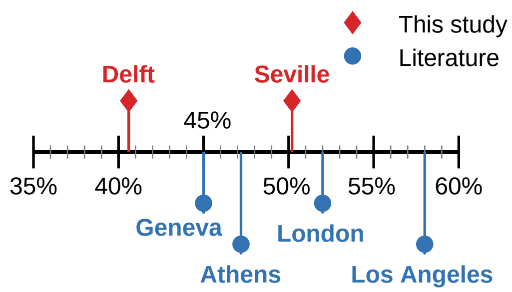

Figure 3.23. Annual ST collector efficiency results compared against literature.

The evacuated flat plate ST collector model is validated against literature data for evacuated flat plate solar collectors operating at similar temperatures (≈ 100 °C) [111–113]. Since reported collector efficiency curves vary between manufacturers and studies, even within the same collector category, this comparison should be understood as an exploration of whether the modeled output is physically realistic rather than a formal validation against a specific reference system. The ST collectors in Delft and Seville generate 999 and 2142 $\text{kWhm}^{-2}\text{year}^{-1}$ respectively. The average efficiencies of collectors in Delft and Seville are 40% and 50% respectively, as illustrated in Figure 3.23. The higher average efficiency in Seville compared to Delft reflects the higher ambient temperatures and irradiance levels in Seville, increasing ST output. These average efficiencies are consistent with a broad range of values (45% to 58%) reported in the literature, such as those of Bellos et al. [111], who reported a measured average annual thermal efficiency of 47.2% for evacuated flat plate collectors in Athens at an operating temperature of 125°C, which is within 3 percentage points of the modeled Seville value of 50.2%. Duret et all [112] report a measured annual thermal efficiency of 45% for evacuated flat plate collectors in Geneva operating between 80 to 95 °C. This is in line with values reported in the model considering the slightly lower operating temperatures than this work. Gao et al. [113] reported annual average thermal efficiencies ranging from 52 to 58% across four different climates at an operating temperature of 100 °C. The comparatively high thermal efficiencies presented by Gao et al. [113] can be attributed to the high zero loss efficiency in the numerical model, in combination with somewhat lower temperature operation compared to this work. It can be concluded that the ST collectors as modeled in this work, show closer agreement with experimentally validated ST systems than with the optimized numerical model of Gao et al. [113]. This suggests the model parameters are representative of currently available collectors. The lower average efficiency found in Delft reflects the higher reduced temperatures that are reached in northern European climates.

The monthly thermal and electrical efficiency of high vacuum flat plate PVT collectors in Delft and Seville are shown in Figures 3.24 and 3.25 respectively. The profiles show good agreement with results reported by De Luca et al [114] for similar high vacuum flat plate PVT collectors operating at comparable locations and inlet temperatures of 100 °C. Both studies show higher thermal efficiency in summer months and a consistent electrical efficiency across seasons. Quantitatively, the average annual thermal efficiencies of the model (26% Delft, 34% Seville) are both 14 percentage points lower than the reference values from Amsterdam and Naples respectively. Conversely the electrical efficiency is approximately 6 percentage points higher than both reference locations. The primary explanation for both differences is the higher electrical efficiency under standard test conditions of the modeled PVT cells (23%) than the reference PVT collector (15%). Through the thermal-electrical coupling of Equation 2.7, the higher electrical efficiency directly reduces the thermal efficiency by approximately 6 percentage points. The remaining difference can be attributed to the difference in inlet temperature of the PVT modules between both studies and differences in the optical and thermal properties between the PVT collectors. The seasonal profile agreement is considered sufficient validation for energy system simulation purposes.

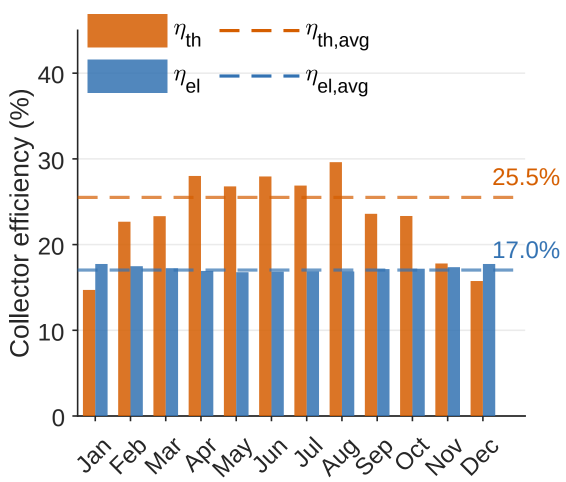

Figure 3.24. Thermal and electrical efficiency of the PVT collectors for Delft.

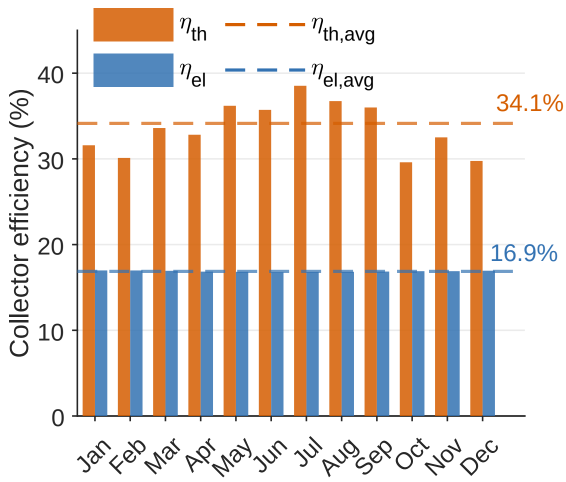

Figure 3.25. Thermal and electrical efficiency of the PVT collectors for Seville.

3.4.2. ATES validation

Experimental validation of the high-temperature ATES model is challenging, as there are currently no operational systems in the temperature range considered in this thesis. Therefore, this section validates the ATES through the long-term stability of the system and the shape of the annual ATES curve.

The temperature progression of the warm ATES well during a period of five years is shown in Figure 3.26. These simulations use the Food & Beverage heat demand profile, the weather data for Delft, and two ATES well pairs designed for an injection volume of $2 \cdot 10^5 m^3$ per well. The same annual weather dataset is applied repeatedly across all simulated years. The upper and lower temperature limits of the warm well are indicated to illustrate the permissible operating range. Three scenarios are considered to illustrate the sensitivity of the warm well temperature to collector array size. The orange line represents the warm well temperature for a collector array of 100,000 ST modules, which maintains long-term ATES temperature stability. The blue line depicts a scenario with 80,000 ST modules, representing conditions of insufficient thermal energy generation. The yellow line represents a scenario with excess thermal energy generation using 140,000 ST modules.

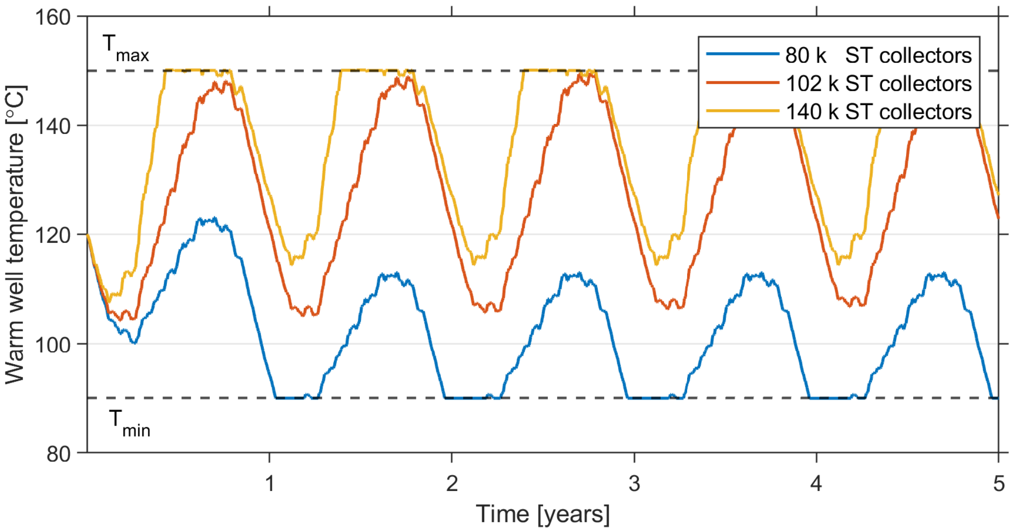

Figure 3.26. Development of ATES temperatures for three ST collector quantities over a five year period.

As shown in Figure 3.26, each scenario converges to a stable periodic equilibrium that is repeated annually. This demonstrates that the model remains within ATES temperature boundaries, even under large yearly surplus and shortage heat generation.

The modeled ATES temperature curve differs somewhat from studies in which spatial groundwater flow and thermal fronts are explicitly simulated, such as Sheldon et al. [55] and Beernink et al. [52]. In those studies, the temperature rises sharply to the injection temperature during charging periods, plateaus for a while, and then declines rapidly as the thermal front reaches the measurement node during discharge. This difference is attributable to the lumped energy balance approach adopted in this thesis, which does not consider groundwater flow and spatial thermal fronts. The gradual temperature development, periodicity and stability of the ATES model is consistent with other lumped energy balance ATES models, including those of Beijneveld [61] and Van Rossum [80].

Overall, the ATES model demonstrates consistent long-term behavior and produces results comparable to established lumped energy balance approaches in the literature, providing sufficient confidence for its application in this thesis.

3.4.3. HP system validation

To validate the HP, COP values are compared to literature to verify that the modeled HP performance is consistent with existing industrial heat pump technology. In addition, the internal energy balances of the system are verified to ensure consistency between thermal and electrical energy flows.

Figure 3.27 presents the COP distribution for the 100,000 ST module scenario described in Section 3.4.2, using the Paper & Pulp heating demand, and the weather data for Delft. The COP of the HP varies between 2.3 and 4.2, both achieved during Mode I operation when the buffer storage is at minimum and maximum capacity, respectively. When the Food & Beverage demand input is used the COP increases to a minimum of 3.3 and maximum of 5.1. This can be attributed to the lower demand temperatures, which decrease the required ΔT_{HP}. The figure illustrates that the mean COP is higher in summer than in winter. Additionally, the whiskers of the box-and-whisker plot indicate that each month contains hours in which the COP deviates significantly from the monthly mean. This can be attributed to short term weather patterns that deviate from the mean monthly weather.

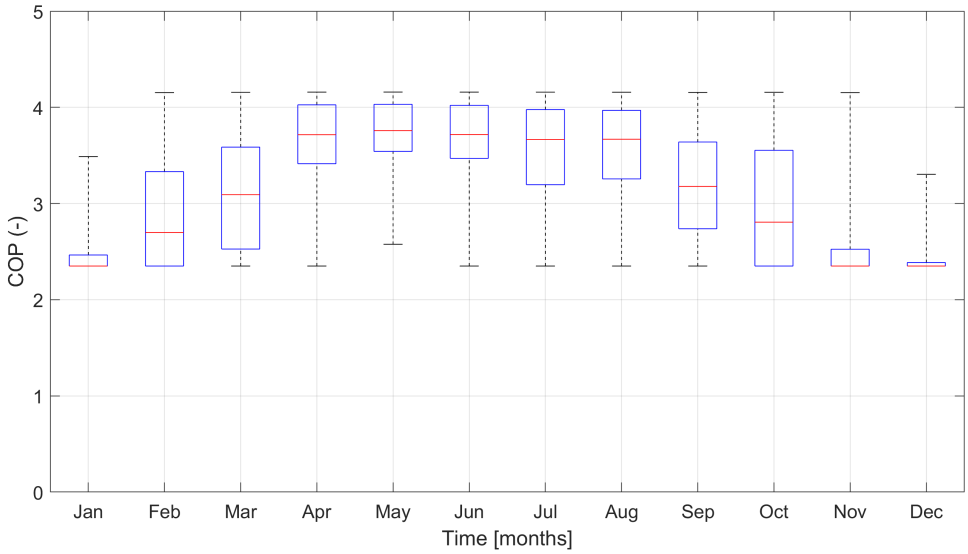

Figure 3.27. Monthly COP distribution of the HP for the 100,000 ST module scenario using the Paper & Pulp heating demand profile, and Delft weather data.

The COP range that is utilized in this thesis shows good agreement with industrial heat pump COPs in literature. Arpagaus et al. [47] provide a market overview of high temperature industrial heat pumps with heat sink temperatures between 90 and 160 °C. The COPs range from 2.4 to 5.8 for these industrial heat pumps at temperature lifts between 40 and 95 K. This corresponds well with the performance of the heat pump in this thesis. Additionally, Marina et al. [16] performed an estimation of the European market potential for industrial heat pumps operating at sink temperatures between 100 and 200 °C, in which most heat pumps function at a COP between 2 and 6. These studies confirm that the HP performance modeled in this thesis falls within the range reported for existing high-temperature industrial heat pump technology. The design of this system uses a steam compression heat pump, which uses a different type of thermodynamic cycle than the closed-loop heat pumps referenced in this validation. Nevertheless, the COP ranges reported in the literature provide a reliable benchmark for achievable industrial HPs performance, which show good agreement with the results of this HP model.

Finally, internal energy balance checks are performed to verify the consistency of the energy accounting within the model. These checks are applied to the 95,000 ST module scenario described in Section 3.4.2. Firstly, the total energy added to and extracted from the buffer storage are both equal to 343 TJ, confirming the conservation of energy within the storage component. Furthermore, the total industrial heat demand is equal to the sum of heat extracted from the buffer storage and ATES combined with the electrical energy consumed by the HP compressors. Both sides of this balance sum up to 449 TJ of which 229 TJ is directly extracted from the buffer, 89 TJ is extracted from the ATES system and 131 TJ is consumed by the HP compressors. These energy balance verifications confirm the internal consistency of the numerical model.

3.5. Conclusion

This chapter has described the development of an integrated energy model that combines the high-temperature components described in Chapter 2 into a complete industrial process heat supply system, with multiple operational modes and system configurations (Objective 2). First, six different system configurations are presented. Subsequently, the five operational sub modes of Configuration 4 and 5 are described. The operational modes are illustrated alongside their governing equations that describe the energy flows within the system. A control flow chart is also presented, that summarizes the mode selection logic. Together, these elements provide a comprehensive description of the integrated numerical model.

The weather and demand inputs have been described in Section 3.3. The selection of the Food & Beverage, and Paper & Pulp sectors, as well as the choice of Delft and Seville as representative locations, are justified based on their relevance to European industrial heat demand and their contrasting climatic profiles. This is followed by a validation of the individual components and the integrated model. The modeled solar collector output demonstrates good agreement with values reported in the literature. Additionally, the seasonal storage is shown to be stable for multiple years, the COP output of the heat pump model falls within the range common for industrial heat pumps at similar source and sink temperatures and the internal energy balances of the system are verified, confirming the consistency of the energy accounting. These validation results provide a solid foundation for interpreting the simulation results presented in Chapter 4.

Chapter 4

Results and Discussion

This chapter presents the simulation results of the integrated model under varying operating conditions to examine to what extent medium temperature (130–150 °C) industrial heat demand can be covered by solar energy generation, using high temperature solar thermal (HT-ST), high temperature photovoltaic-thermal (HT-PVT), and photovoltaic (PV) modules in combination with thermal energy storage comprising a thermal buffer storage and a seasonal aquifer thermal energy storage (ATES) system (Objective 3). Additionally, the system size is optimized and an economic analysis is performed on the developed industrial heating energy system, assessing the economic viability of the system under varying climate conditions (Objective 4).

The chapter is divided into three sections. The performance of the integrated system is analyzed in Section 4.1. This section examines the performance of the different configurations introduced in Section 3.1 and highlights the operational performance of Configuration 5 (ST + PV + ATES + batteries) across a range of scenarios. The results for Configuration 6 are presented in Appendix C.1 and results of reference Configurations 1–4 can be found in the thesis repository. Section 4.2 aims to optimize the energy system through varying the individual component quantity. Following this, an economic analysis is performed in Section 4.3. This analysis aims to determine the economic viability of the designed industrial energy system compared to a reference natural gas benchmark.

4.1. System performance

This section explores the performance of the integrated energy system. First, the performance results of the different configurations are analyzed in Section 4.1.1. Subsequently, Section 4.1.2 discusses the detailed results of Configuration 5 (Figure 3.6) for two distinct locations (Delft and Seville) and two industries (Food & Beverage, and Paper & Pulp). The simulation results are visualized in weekly and annual figures highlighting key model outputs including the COP, storage temperature, solar collector efficiency, power consumption and mode activation. Finally, the section is concluded by presenting the most important takeaways in Section 4.1.3.

4.1.1. Configurations 1 to 6 comparison

This section aims to find the optimal system configuration based on the total and peak annual electricity consumption from the grid. The total grid electricity consumption is an important metric for self-sufficiency of the system. However, the peak energy consumption from the grid is the most important parameter to secure a grid connection in a congested network. Consequently, peak load reduction is the primary metric determining the technical feasibility.

In order to compare the configurations, the system size is kept the same across all scenarios evaluated in Section 4.1. Configuration 6 uses as many PVT modules (190,000) as the PV collectors and ST modules combined in Configuration 5. This results in some scenarios using sub-optimal system sizes, such as the Seville scenarios which use an oversized collector field. System sizing input parameters are presented in Table 4.1. As can be observed in the table, the start date of the simulations is the 1st of March and the initial warm well temperature is close to the minimum temperature of 90 °C. This is done to prevent result distortion due to the depletion of the ATES during a year, essentially providing a free energy buffer. March is the first month of the year in which the ST modules yield enough thermal energy to meet industry demand in properly sized systems. The ATES system can still be charged to a higher final temperature (above 95 °C) after one year, which can distort consumption results compared to balanced ATES operation. This however, has a smaller influence on the main results including the peak grid load compared to the opposite scenario where free energy is extracted from the ground.

Table 4.1. System performance study parameters

Parameter	Value	Electrical capacity	Thermal capacity
ST modules	100,000	-	120,000 kWp
PV modules	90,000	41,000 kWp	-
PVT modules	190,000	65,000 kWp	168,000 kWp
ATES well pairs	2	-	61,000 MWh
Initial warm well temperature	95 °C	-	-
Buffer storage volume	10,000 m^3	-	450 MWh
Number of batteries	10	100 MWh	-
Start date	1st of March	-	-

The performance of the different system configurations is depicted in Figures 4.1 and 4.2. The required electricity demand from the grid decreases substantially when additional components are introduced, as illustrated in Figure 4.1. Configurations 5 (ST + ATES + PV + batteries) and 6 (PVT) yield the best performance, as they integrate an ATES system, batteries, and either ST collectors alongside PV modules or PVT modules, respectively. The simulation results of Configuration 5 are discussed in Section 4.1. The simulation results for Configuration 6 using PVT are presented in Appendix C.1 to refine the focus of this chapter. Figures 4.1 and 4.2 show that Configuration 6 is able to slightly outperform Configuration 5. This shows the technical potential of PVT collectors for high temperature applications. Furthermore, the Seville results are better than those in Delft, which is attributable to the higher annual irradiance in Seville compared to Delft.

Another notable result is the slight increase in grid consumption in Configuration 3 in Seville, which is caused by the ATES being charged to 140 °C at the end of the year. This phenomenon is further discussed in Section 4.1.2. Furthermore, Seville achieves near zero grid energy consumption for both industry types, demonstrating the systems potential to operate fully independently of the grid in Seville.

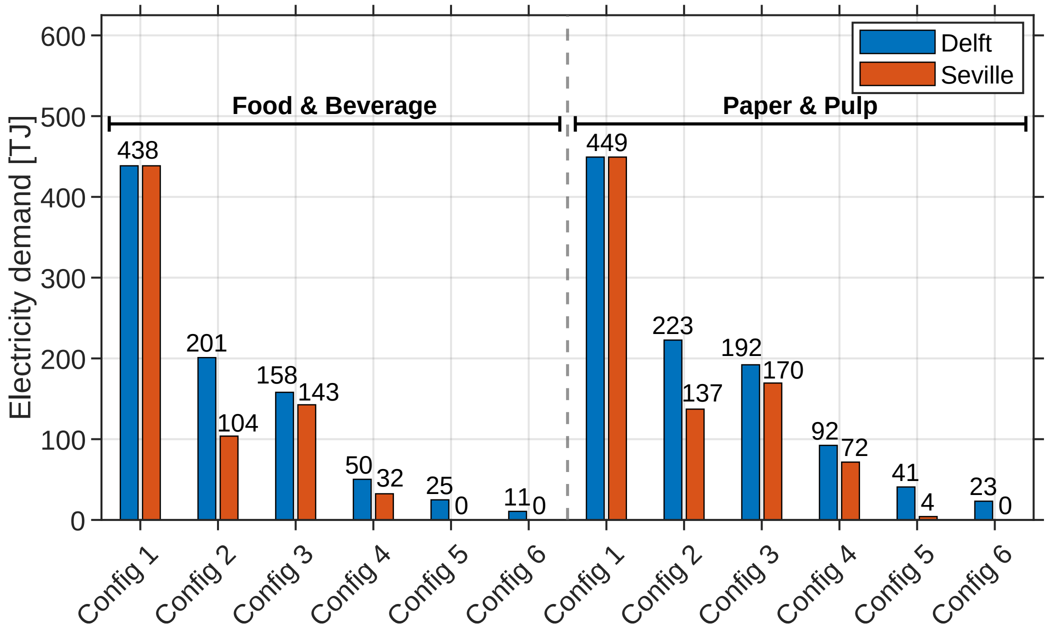

Figure 4.1. Annual grid electricity consumption for different system configurations. Config. 1: Resistive heater, Config. 2: ST with HP, Config. 3: ATES, Config. 4: PV. Config. 5: Battery, Config. 6: PVT.

Configuration 5 and 6 generally show the highest reduction in peak grid electricity demand, as depicted in Figure 4.2. With Configuration 6 again showing a slightly better performance. Peak load reductions are relatively smaller than reduction in total grid consumption in all configurations. This is most evident in Configuration 5 for the Seville Paper & Pulp scenario where total energy consumption decreases by 99% but peak load only by 57%. This can be attributed to the fact that individual hourly peaks have a disproportionate influence on the peak load metric while contributing negligibly to the total annual consumption. The aforementioned mechanism causes peak load reduction to be more challenging compared to a reduction of total annual electricity consumption.

Additionally, reference Configuration 3 sees a very large increase in peak load for all scenarios. This is caused by large surplus thermal energy generation in Mode II during peak irradiance. This surplus thermal energy is converted into steam using the HP before the heat is transferred to the ATES causing high electricity peaks. When PV modules are added in the correct ratio relative to ST modules, the PV generation can offset these electricity demand peaks, which explains the reduction in peak load observed in reference Configuration 4. The results of Configuration 4 in the Seville Paper & Pulp scenario show what happens when the ST and PV modules are not in the right ratio. In this scenario there are not enough PV modules to cover the surplus electricity demand, resulting in high grid consumption during surplus thermal generation for Seville compared to Delft.

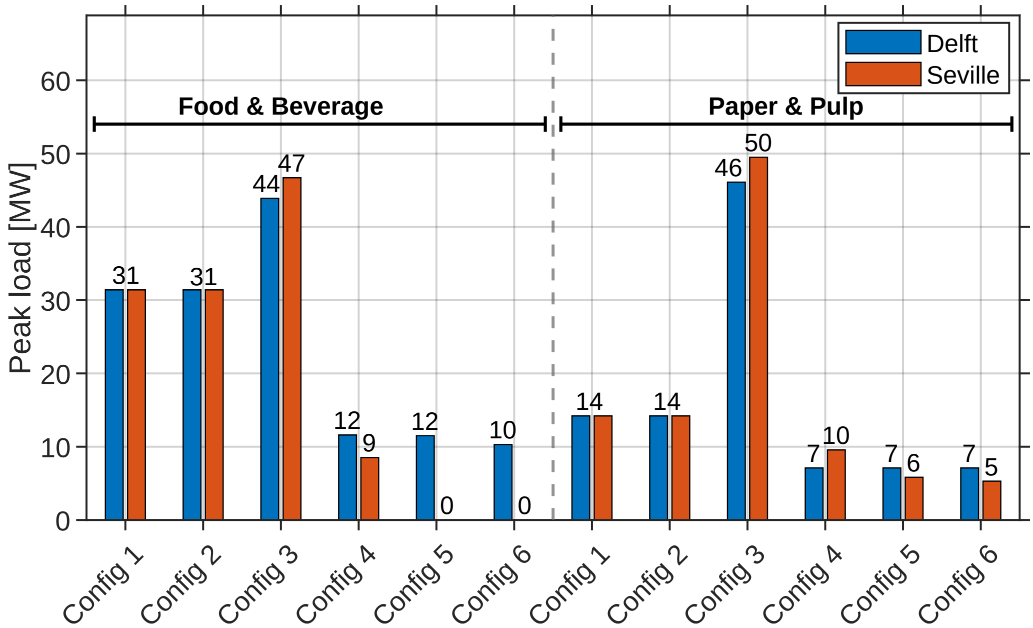

Figure 4.2. Annual peak grid electricity consumption for different system configurations. Config. 1: Resistive heater, Config. 2: ST with HP, Config. 3: ATES, Config. 4: PV. Config. 5: Battery, Config. 6: PVT.

4.1.2. Simulation highlights

This section presents the weekly and annual operation of the energy system of Configuration 5 (ST + ATES + PV + batteries). The simulation results of Configuration 6 (PVT) are depicted in Appendix C.1. The simulation highlights of reference Configurations 1–4 are not presented within the report but are included in the thesis repository. First, the results of the Delft Food & Beverage scenario are discussed. These are presented through a collection of figures showing the energy flows, operating temperatures, module efficiency, and COP. Following this, simulation results for the other three scenarios are presented, highlighting the results that deviate from the Delft Food & Beverage scenario. Simulation results of Configuration 5, not presented in this chapter are also available in the thesis repository.

• Food & Beverage Delft

The Food & Beverage industry is characterized by a demand profile with daily peaks (see Figure 3.17) and a demand temperature of 130 °C. There is a large seasonal imbalance in irradiance in Delft, where average summer months receive 6.6 times as much irradiation. The thermal efficiency of the ST collectors (purple) and electrical efficiency of the PV modules (yellow) are presented in Figure 4.3. Figure 4.3a presents hourly efficiency values for three seasonally distinct weeks, for which the hourly weather data is presented in Figure 3.20. The weekly average efficiencies over a full year are presented in Figure 4.3b. Other figures presented in this section follow the same approach, presenting three weeks throughout the year on the left and annual daily/weekly averages on the right. The weekly average efficiency presented in the annual figure is irradiance weighted to avoid over representation of low irradiance hours. The PV efficiency remains stable around 21–22% throughout the year, resulting in a total annual electrical yield of 269 kWh/m^2. The electrical efficiency exhibits only minor fluctuations as a result of varying ambient temperature and incoming irradiance. In contrast, the ST efficiency exhibits large seasonal fluctuations, averaging 40–50% in summer and 15–40% in winter. Such behavior can be attributed to rapid increases in reduced temperature, for the ST collectors with high operating temperatures under low irradiance conditions. This high sensitivity to irradiance is also visible in the daily curves where the thermal efficiency remains zero during the first and last hour of sunlight while the PV modules generate electricity. At these hours the reduced temperature is too high to extract heat from the ST collectors and water circulation from the buffer storage to the collectors is stopped. For some winter days the irradiance is too low to extract any heat at all. However, due to high efficiency during spring and summer months the total annual thermal yield totals 500 kWh/m^2.

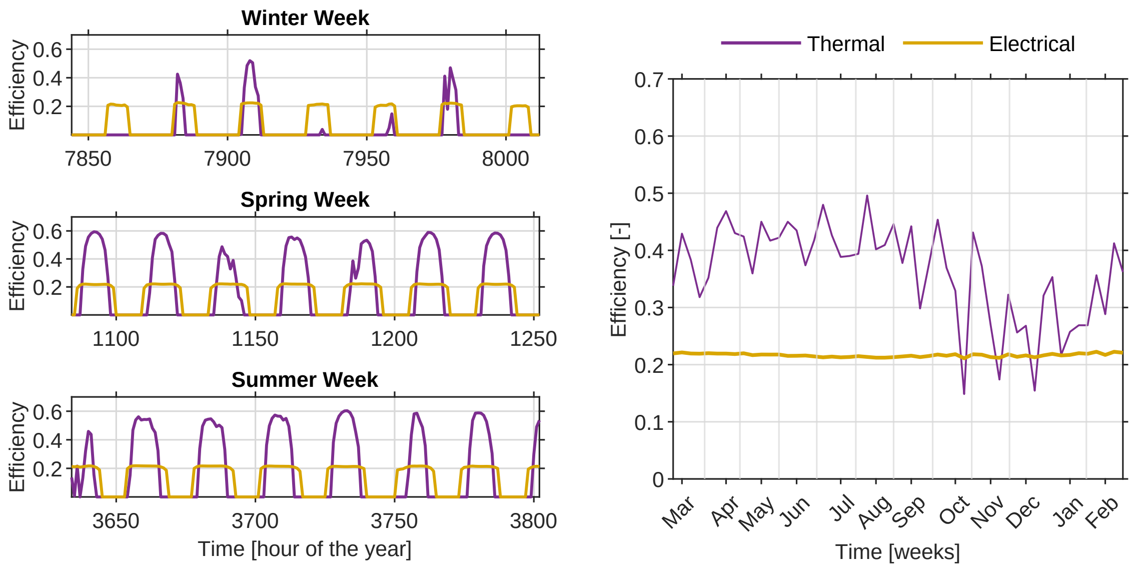

(a) Simulation results for three weeks

(b) Annual simulation results

Figure 4.3. Thermal and electrical efficiency of ST and PV respectively for the Delft Food & Beverage scenario.

Figure 4.4 illustrates the activation of operational modes throughout the year. Mode I (Balanced) dominates system operation with 6663 annual hours, during which industrial heat demand is met from the buffer storage. Mode IIIA (discharging - 2343 hours) is activated predominantly in winter when solar irradiance is insufficient to meet industry demand. Conversely, Mode IIA (charging - 714 hours) operates during summer when surplus ST generation is available for ATES charging. The absence of Mode IIB (ST curtailment) and Mode IIIB (backup resistive heater) activation confirms that the system is appropriately sized for this scenario, since usage of these modes should be minimized for optimal system performance.

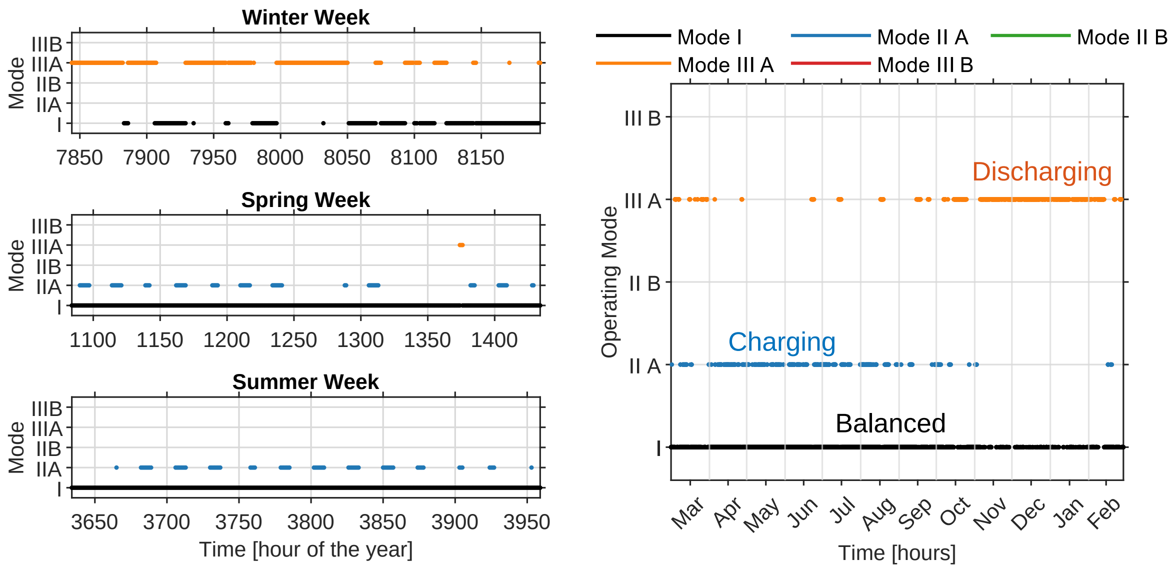

(a) Simulation results for three weeks

(b) Annual simulation results

Figure 4.4. Activation of operational modes for the Delft Food & Beverage scenario.

Figure 4.5 presents the storage temperature of the thermal buffer storage (red) and the warm ATES wells (black). During winter weeks the buffer storage temperature is consistently at or slightly above the minimum temperature limit of 80 °C (see Figure C.3a). The buffer storage temperature in spring and summer remains close to its maximum of 120 °C. However, during these months larger temperature fluctuations are observed, corresponding to sunny and cloudy days (see Figure 4.5b). The HT-ATES temperature is considerably more stable only changing slowly throughout the year. The ATES is charged from 95 to 138 °C from April to August and depleted from 138 °C back to its initial temperature from October to February. The ATES is cycled through a large fraction of its total allowable temperature range from 90 to 150 °C.

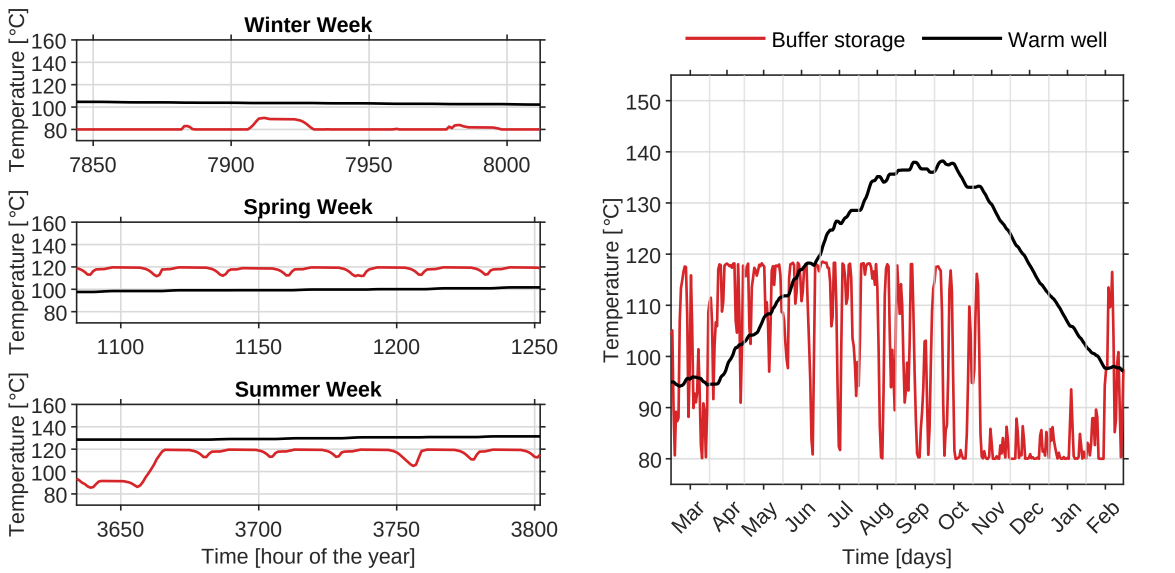

(a) Simulation results for three weeks

(b) Annual simulation results

Figure 4.5. Temperature of the buffer storage and warm ATES well for the Delft Food & Beverage scenario.

System COP (green) is depicted in Figure 4.6, defined as heat delivered to industry or ATES divided by the combined electricity consumption of the HP and hydraulic pumps. The annual average COP is 4, with significant hourly and seasonal fluctuations. These are strongly correlated with the storage temperatures presented in Figure 4.5. During summer, the COP corresponds closely to the buffer storage temperature while in winter the COP follows the downward trend of the warm well storage temperature. The steep decrease in COP from 5 to 3 visible in the spring and summer week (see Figure 4.6a), result from surplus generation. During which, the HP switches to 160 °C steam generation to charge the ATES, instead of the 130 °C steam required by the Food & Beverage industry. The resulting increase in temperature lift of the HP leads to a significant decrease in the COP.

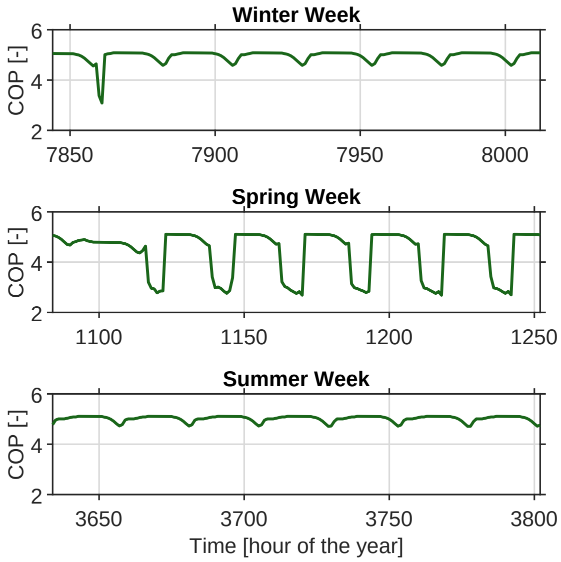

(a) Simulation results for three weeks

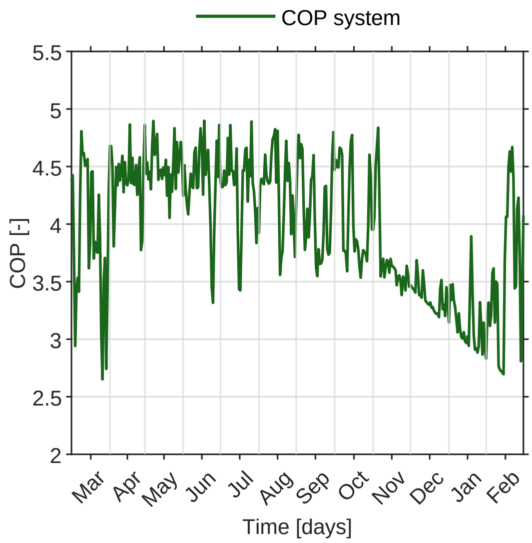

(b) Annual simulation results

Figure 4.6. System COP for the Delft Food & Beverage scenario.

Power consumption during different modes is depicted in Figure 4.7. The total power consumption of Mode I (balanced) and III (discharging) show a negative correlation where Mode I is mainly used during summer and Mode III is mainly used during winter (see Figure 4.8b). The highest energy consumption (40 MW) takes place during surplus operation of Mode II (charging), significantly more than the 14 MW maximum required for industrial heat supply (see Figure 4.8a). This poses a challenge for HP and heat exchanger sizing which could possibly be resolved by spreading surplus generation over the day to reduce the high peaks. Over the course of a year the ATES is charged by 119 TJ from which 89 TJ is recovered (Mode IIIA). The gap between injected and recovered heat is 29 TJ, corresponding to the heat loss to the ground.

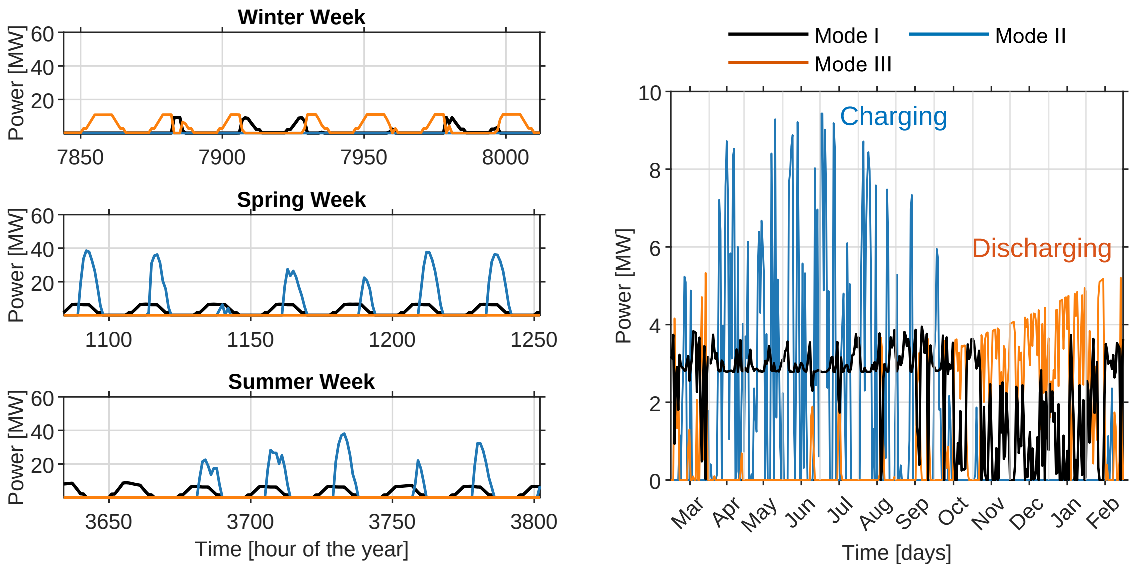

(a) Simulation results for three weeks

(b) Annual simulation results

Figure 4.7. Electricity consumption of Mode I, Mode II, and Mode III for the Delft Food & Beverage scenario.

The total electricity demand across all modes presented in Figure 4.7 is 157 TJ. This encompasses the HP consumption and the electricity required by the hydraulic pumps. Figure 4.8 shows the weekly and annual electricity demand (purple), PV generation (yellow), and grid consumption (blue). There are high electricity demand peaks in demand (40 MW) during the summer, when the ATES is charged by excess generation of the ST due to high irradiance (see Figure 4.7a). Since the surplus ST generation coincides with high PV generation these peaks can be covered and no grid consumption is required in summer. The grid consumption in this scenario takes place in winter when the PV generation is low (see Figure 4.8b) and decreasing storage temperatures result in higher electricity demand through COP. Annual PV generation yields 174 TJ, exceeding total demand by 17 TJ. However, due to a seasonal mismatch not all generated electricity can be used, resulting in a total grid electricity consumption of 25 TJ and a peak load of 12 MW.

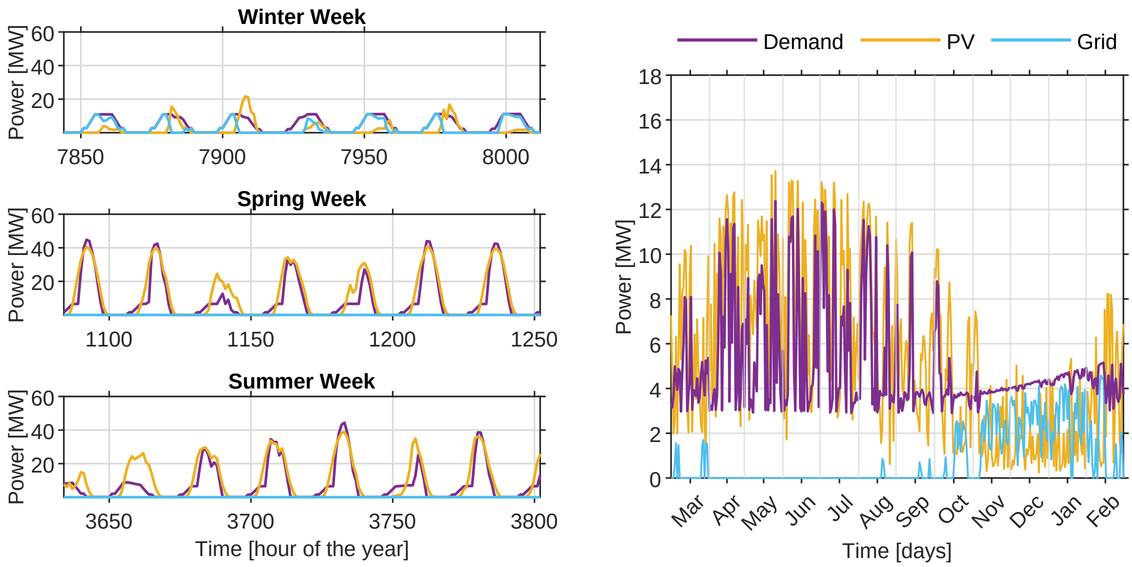

(a) Simulation results for three weeks

(b) Annual simulation results

Figure 4.8. Electricity demand, generation and grid consumption in the Delft Food & Beverage scenario.

• **Paper & Pulp Delft**
Next the Paper & Pulp industry results are presented, characterized by a continuous demand of 150 °C (see Figure 3.17). The ST and PV efficiencies of the Delft Paper & Pulp scenario deviate less than 1% compared to the Delft Food & Beverage scenario, since weather conditions and buffer storage temperatures are comparable. Therefore Figure 4.3 presents an accurate indication of solar collector efficiencies in this scenario. The operational modes follow a similar pattern to the Food & Beverage industry, where the ATES is charged (Mode IIA) during the summer and discharged in winter (Mode IIIA).

Figure 4.9 presents the storage temperatures of the buffer storage and ATES for the Paper & Pulp industry. A sawtooth pattern can be recognized in the weekly buffer storage temperature. This pattern is a result of the continuous energy demand in this scenario, depleting the buffer storage from 120 to 105 °C during the night of spring and summer weeks (see Figure 4.9a). Figure 4.9b shows that the warm well temperature at the end of the year is 105 °C which is 10 °C higher than the initial temperature at the start of the year. This can be attributed to higher demand temperature of the Paper & Pulp industry, resulting in a lower system COP. Consequently the fraction of heat extracted from the buffer storage and ATES per unit of heat delivered to industry is reduced. This results in an imbalance of thermal generation and consumption throughout the year, since ST generation remains similar.

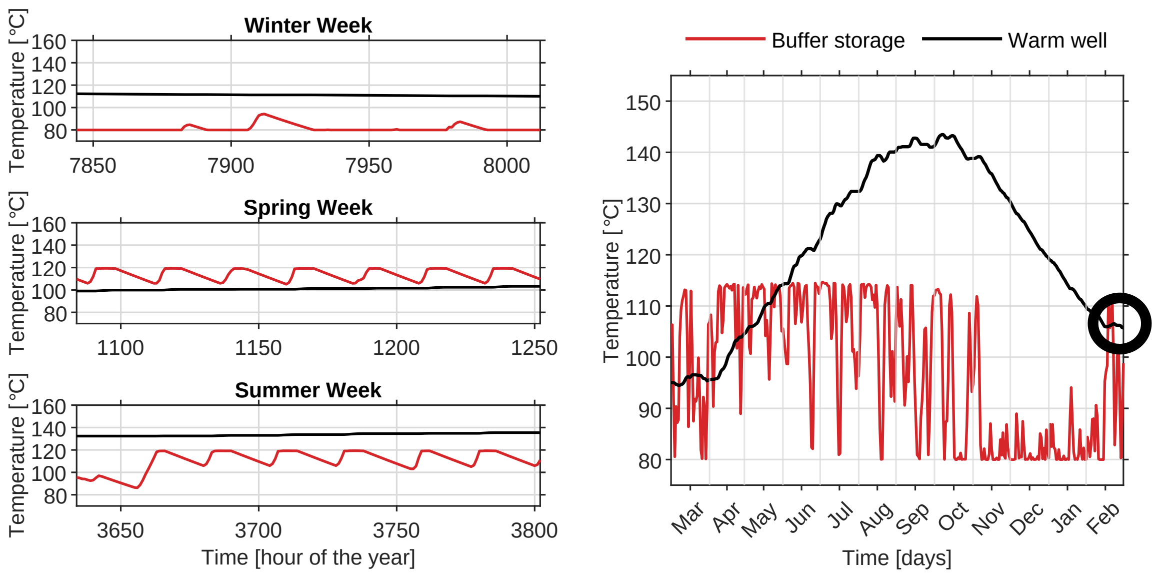

(a) Simulation results for three weeks

(b) Annual simulation results

Figure 4.9. Temperature of the buffer storage and warm ATES well for the Delft Paper & Pulp scenario.

The lower COP achieved by the Paper & Pulp industry as a result of the higher demand temperature of 150 °C, is illustrated in Figure 4.10. The average COP decreases from an annual average of 4 in the Food & Beverage scenario to an average of 3.2 in the Paper & Pulp scenario, as presented in Figure 4.10b. Consequently, the HP electricity consumption for this industry is significantly increased to 192 TJ, compared to 157 TJ for the Food & Beverage industry. During winter operation with an almost empty buffer storage COP approaches 2, whereas the minimum COP for the Food & Beverage industry was 2.6.

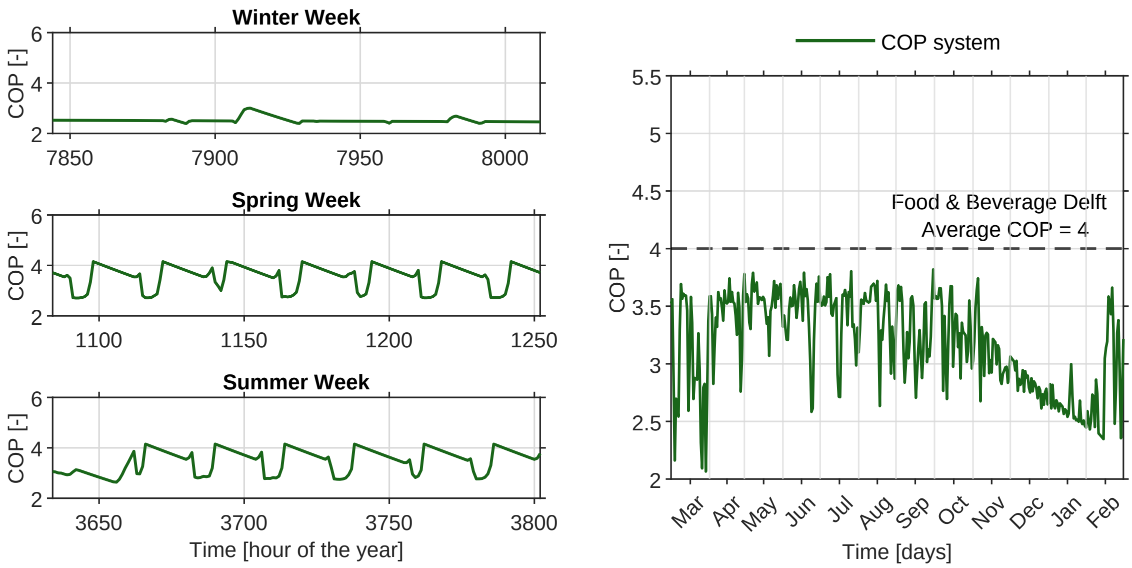

(a) Simulation results for three weeks

(b) Annual simulation results

Figure 4.10. System COP for the Delft Paper & Pulp scenario.

Total electricity consumption of Mode I (balanced), Mode IIA (charging), and Mode IIIA (discharging) follow a similar pattern to the Food & Beverage scenario. The summer consumption is characterized by high Mode IIA electricity loads while most Mode IIIA consumption is concentrated in winter when irradiance is low. The total electricity demand of these three modes adds up to 192 TJ (152 TJ for Food & Beverage) and is presented in Figure 4.11 by the purple line. This is 18 TJ more than the annual PV electricity generation of 174 TJ. Figure 4.11a shows that demand peaks exceed PV generation in spring and summer and that PV generation regularly falls short of demand in winter. This results in a total grid electricity consumption of 41 TJ, 64% higher than that for the Food & Beverage industry. However, maximum peak load (7 MW) is 50% lower than the resistive heater reference and 42% lower than that of the Food & Beverage industry. The lower peak load is caused by continuous demand spreading grid electrical energy consumption over a larger number of hours. In this scenario there is occasional grid consumption during summer months (see Figure 4.11b), these coincide with the highest irradiance hours when PV cannot cover all Mode IIA (charging) consumption. The total grid consumption during summer months is 1.8 TJ during summer months, while the Food & Beverage operated independently of the grid during the summer.

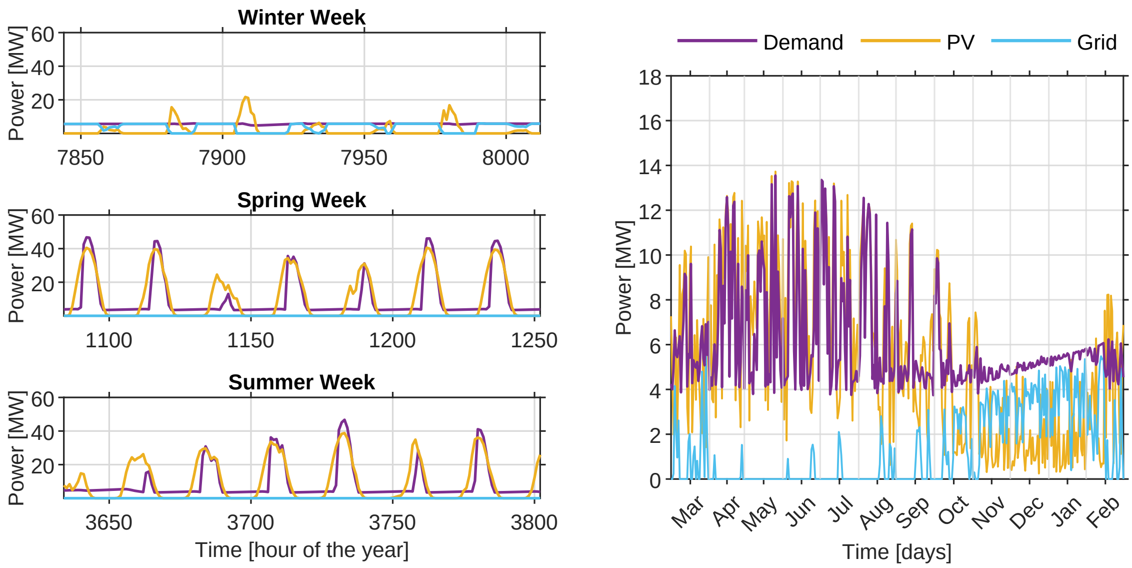

(a) Simulation results for three weeks

(b) Annual simulation results

Figure 4.11. Electricity demand, generation and grid consumption in the Delft Paper & Pulp scenario.

• **Food & Beverage Seville**

The weather conditions in Seville are characterized by a high annual irradiation of 2148 kWh/m^2 (compared to 1243 kWh/m^2 in Delft), low seasonal variation in irradiation (2 times as much irradiation in summer compared to winter compared to 6.6 for Delft), and a high average ambient temperature of 19 °C (compared to 11 °C in Delft). The thermal and electrical efficiency of the ST collectors and PV modules in Seville are presented in Figure 4.12. The corresponding weather data for the weeks presented in Figure 4.12a can be found in Figure 3.21. The PV efficiency remains stable at 20–22% throughout the year (see figure 4.12a), with a slight dip during summer attributable to higher module temperatures. The annual PV module yield is 455 kWh/m^2, a 69% increase compared to Delft as a result of the 73% higher annual irradiation. However, the ST collector output of 1071 kWh/m^2 is disproportionally large (114% higher compared to Delft). This is because the higher irradiance allows the ST collectors to operate at a higher efficiency. The average annual irradiance weighted thermal efficiency is 50% in Seville, significantly higher than the 40% in Delft (see Figure 4.12b). Furthermore, seasonal efficiency trends are less pronounced with the highest weekly average being 54% in summer and the lowest being 40% during winter. The ST collectors demonstrate peak hourly efficiency up to 60%, even during a winter week. This demonstrates the technical advantage of ST collectors for low latitude locations with high year-round irradiance.

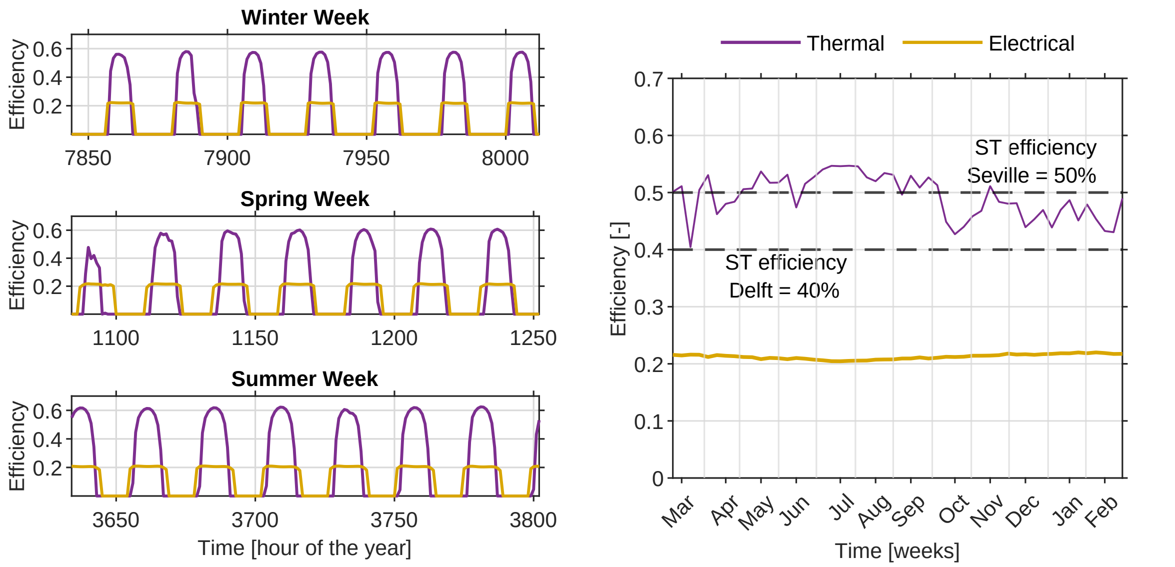

(a) Simulation results for three weeks **(b)** Annual simulation results

Figure 4.12. Thermal and electrical efficiency of ST and PV respectively for the Seville Food & Beverage scenario.

Comparatively high annual irradiance in Seville results in large surplus generation and eventually curtailment, as depicted in Figure 4.13. Throughout the year, Mode IIA (curtailment) is active for a total of 2363 hours, corresponding to 297 TJ of curtailed ST energy. Even in winter weeks with comparatively low irradiance, ST curtailment takes place daily (see Figure 4.13a), suggesting the system is significantly oversized. In contrast, Mode IIIA (discharging) is used only sparingly (37 hours), during weeks with exceptionally low irradiance. This indicates a minimal reliance on seasonal storage in this climate. The ATES is charged for a total of 623 hours before reaching full capacity in May, after which further surplus ST generation is curtailed.

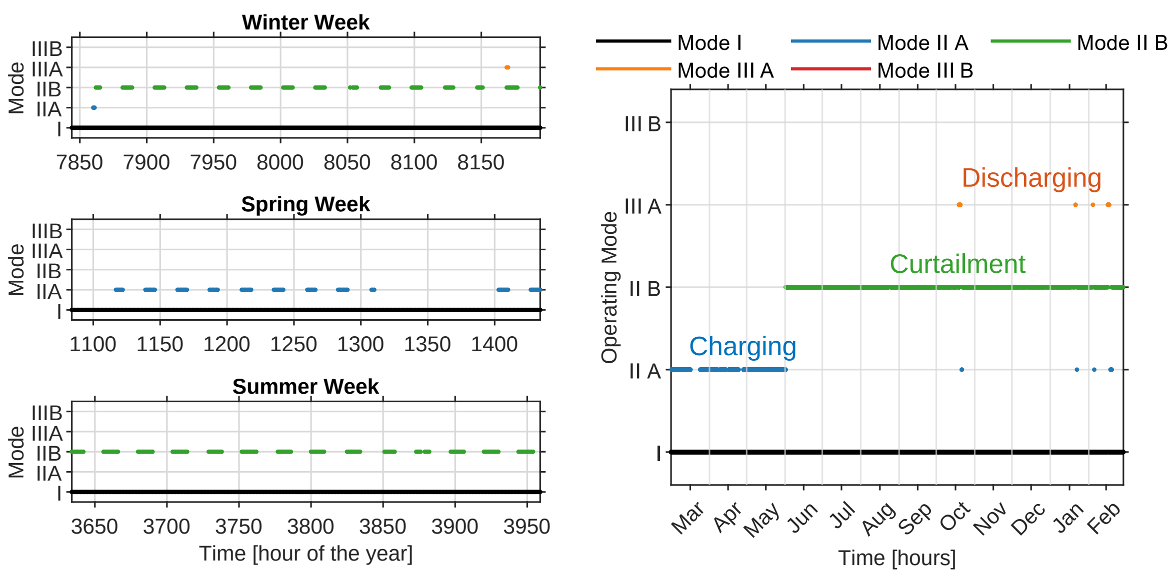

(a) Simulation results for three weeks **(b)** Annual simulation results

Figure 4.13. Activation of operational modes for the Seville Food & Beverage scenario.

Figure 4.14 depicts the temperatures of the thermal energy storage in the buffer and warm well. The buffer storage has an average annual temperature of 115 °C (17 °C higher than Delft) and consistently remains close to its maximum temperature of 120 °C during winter, spring, and summer (see Figure 4.14a). During winter the buffer storage experiences occasional temperature dips during periods with lower irradiance, as can be seen by the dips in average daily storage temperatures in Figure 4.14b. A significant rise in warm well temperature is visible during the first four months until the ATES temperature reaches 150 °C maximum.

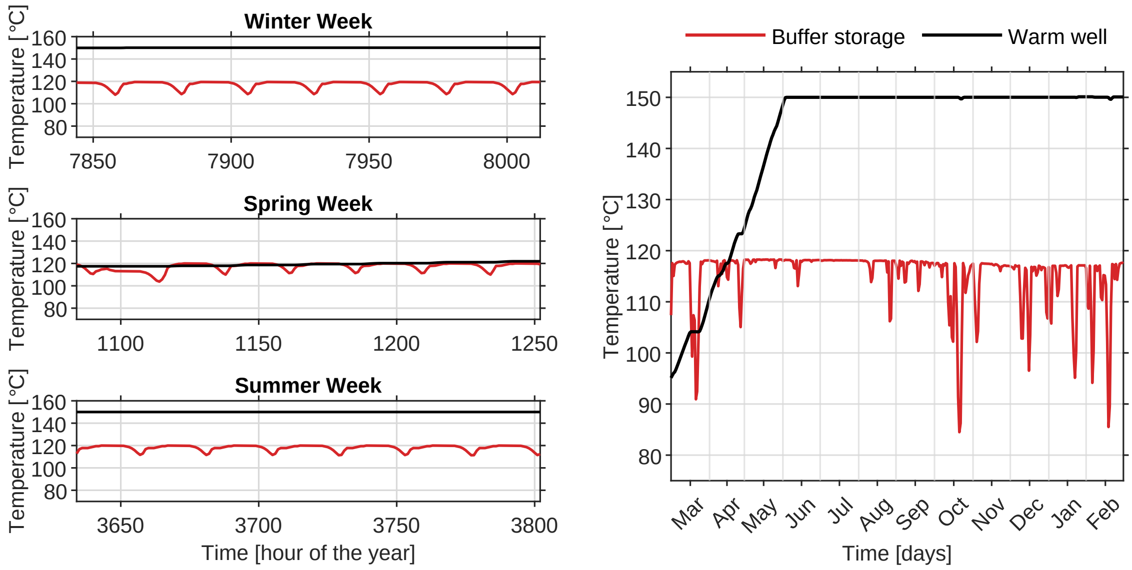

(a) Simulation results for three weeks

(b) Annual simulation results

Figure 4.14. Temperature of the buffer storage and warm ATES well for the Seville Food & Beverage scenario.

Due to an oversized ST array the average storage temperatures of the buffer and ATES are high. These elevated storage temperatures decrease the temperature lifts in the HP and consequently result in high COP values. During the first few months the COP fluctuates between 2.9 and 5 (see Figure 4.15a), resulting in an average daily COP of approximately 4.3 for the months in which the ATES is charging. After this the system operates with a COP of approximately 5 for most of the year resulting in an annual average COP of 4.7. Exceptions are visible when the buffer storage temperature decreases during low irradiance periods in winter and autumn. The lowest daily average COP is 3.6 and can be found in October during a period with relatively low irradiation.

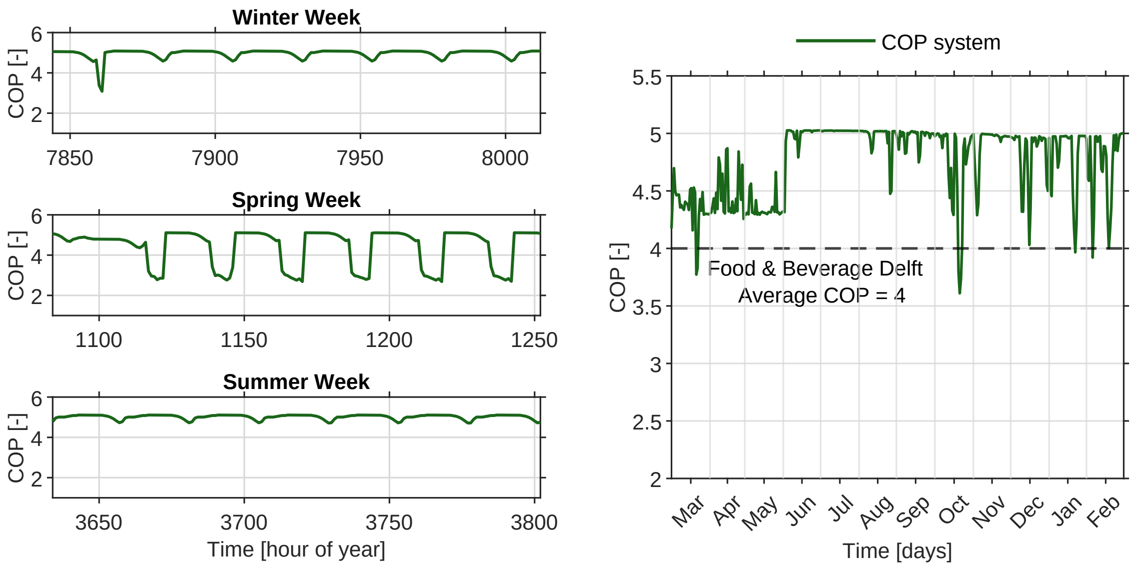

(a) Simulation results for three weeks

(b) Annual simulation results

Figure 4.15. System COP for the Seville Food & Beverage scenario.

Figure 4.16 shows the electricity consumption of the different operational modes. The curtailment of ST generation is not depicted since it does not require electrical energy consumption. Mode I (balanced) maintains a stable average power consumption of 3 MW of electricity throughout the year, since Mode IIIA (discharging) is used sparingly (see Figure 4.16a). Mode IIA operation consumes 50 TJ of electrical energy during the first 4 months of the year to charge the ATES. Resulting in a total 181 TJ of heat being injected into the ATES, while only 1.6 TJ is extracted, resulting in the significant annual increase from 95 to 150 °C of the warm well temperature. The very low extraction of 1.6 TJ suggests that ATES deployment might not be strictly necessary in southern European climates. The total contributions of HP and hydraulic pump performance result in an annual electricity demand of 141 TJ, 16 TJ less than the Delft Food & Beverage scenario.

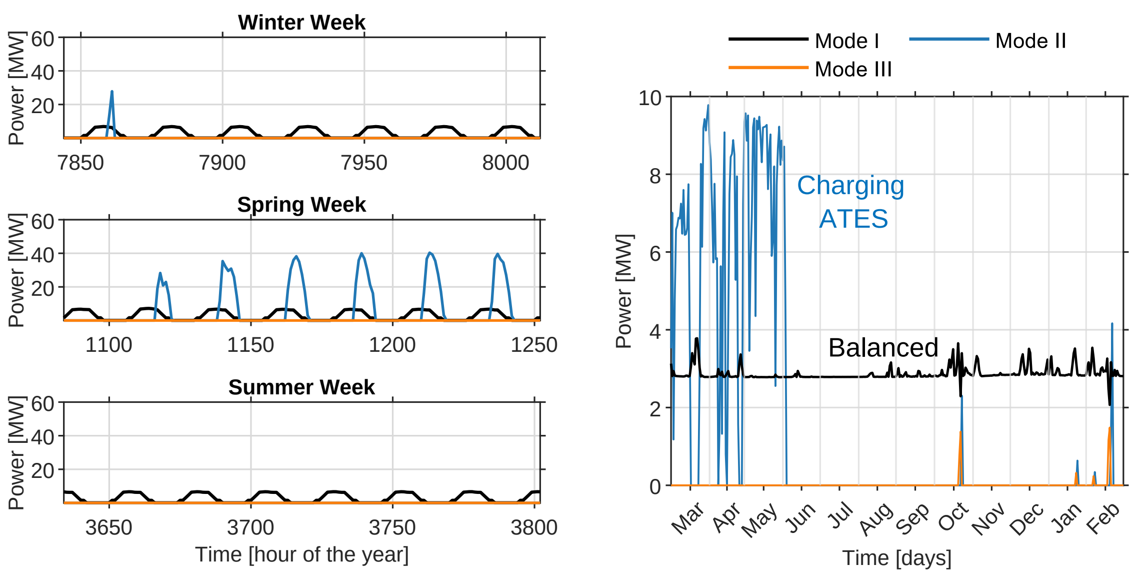

(a) Simulation results for three weeks

(b) Annual simulation results

Figure 4.16. Electricity consumption of Mode I, Mode IIA, and Mode IIIA for the Seville Food & Beverage scenario.

The total electricity demand of the Food & Beverage in Seville is 142 TJ of which half (71 TJ) is consumed during the first 3 months. After these first three months the ATES is fully charged and the daily electricity demand averages around 3 MW. In Seville the total PV generation is 295 TJ, more than twice the annual electricity demand. This results in the Seville Food & Beverage system operating completely independently from the electricity grid, as illustrated by the blue line (grid consumption) in Figure 4.17a and 4.17b. The high difference in annual PV generation to electricity consumption, and significant ST curtailment of 297 TJ suggest that the system is oversized and the number of solar collectors could be reduced.

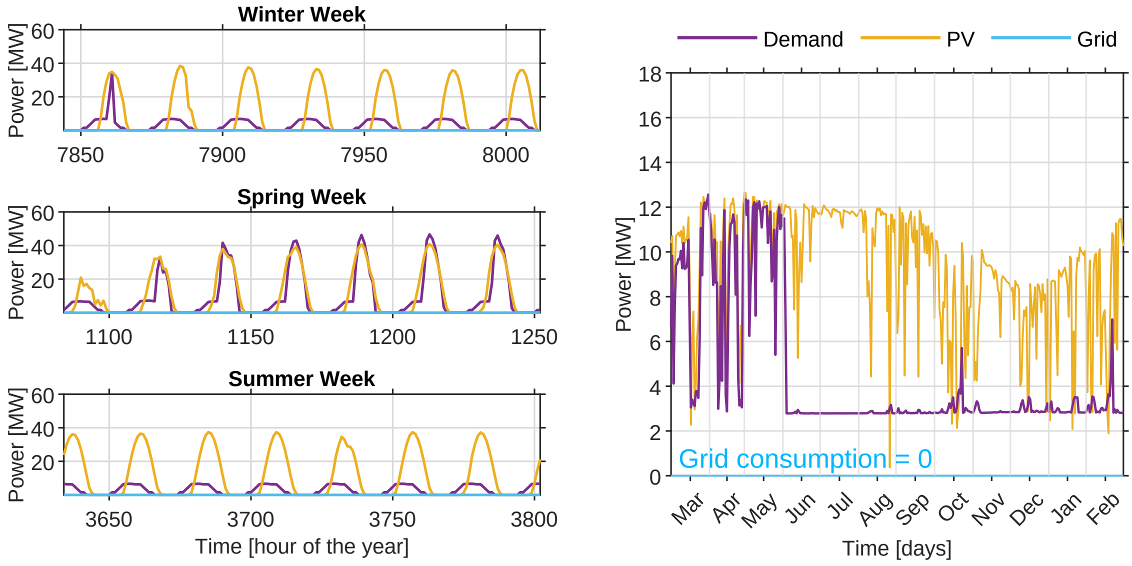

(a) Simulation results for three weeks

(b) Annual simulation results

Figure 4.17. Electricity demand, generation and grid consumption in the Seville Food & Beverage scenario.

• Paper & Pulp Seville

The Paper & Pulp industry in Seville is characterized by the same continuous (150 °C) steam demand as the Paper & Pulp industry in Delft. Furthermore, the weather data is the same as for the Seville Food & Beverage scenario, resulting in average electrical and thermal efficiencies of the solar collectors to be accurate within 1% to those displayed in Figure 4.12. This scenario also experiences significant Mode IIB (curtailment) operation, totaling 2427 hours starting at the end of May. The total Mode IIIA operation is 43 hours, comparable to the 37 hours in the Food & Beverage industry. Figure 4.13 gives a good approximation of the mode utilization of this scenario. The average daily storage temperatures in Figure 4.14b give a good approximation for the storage temperatures in this scenario. The only change is that the daily averages of the buffer storage are slightly lower due to nightly depletion, comparable the pattern in Figure 4.9a. This is a result of the continuous demand profile of the Paper & Pulp industry.

The system COP of this scenario is similar in shape to the one seen in the Food & Beverage industry in Seville. Due to nightly reduction in buffer storage temperature, a sawtooth pattern can be recognized in winter and summer weeks (see Figure 4.18a). During these weeks COP is reduced from 4 during the day to 3.5 during the night. The highlighted spring week COP shows a different pattern, where nightly depletion is followed by a sharp increase and then a significant decrease to 2.8. These results are cause by the switch from Mode I (balanced) to Mode IIA (charging) operation, since charging the ATES requires 160 °C steam. Furthermore, the average COP decreased from 4.7 in the Food & Beverage industry in Seville to 3.7 in this scenario. However, this is significantly higher than that of Delft Paper & Pulp scenario, averaging a COP of 3.2 (see Figure 4.18b).

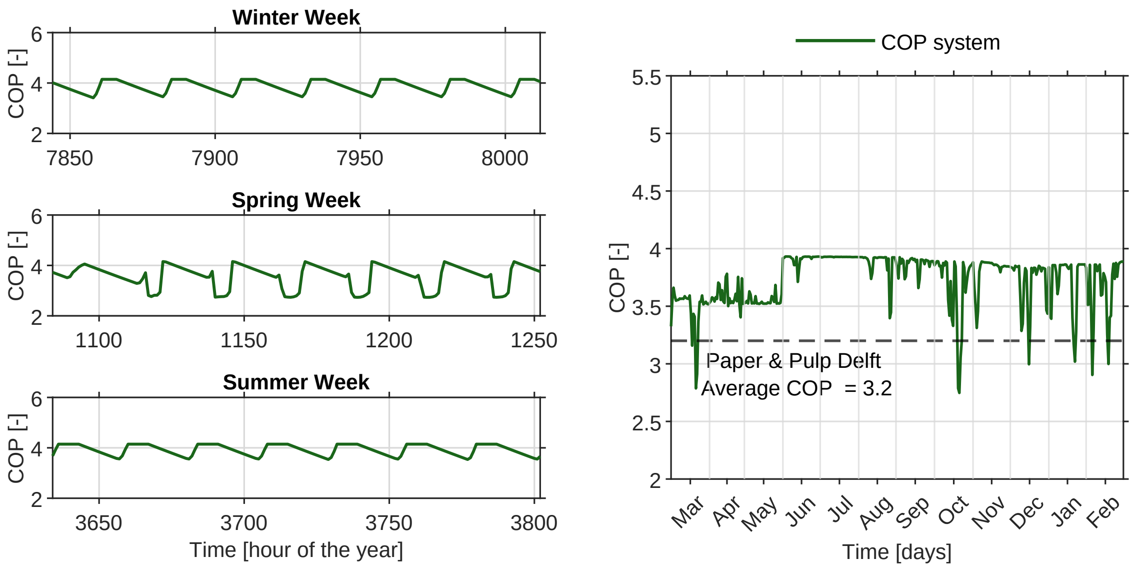

(a) Simulation results for three weeks

(b) Annual simulation results

Figure 4.18. System COP for the Seville Paper & Pulp scenario.

The electrical power consumption is close to that seen the Food & Beverage industry in Figure 4.16. The main two exceptions are the daily power consumption, which follows a continuous demand profile instead of the daily peaks depicted in Figure 4.16a, and the higher daily average Mode I (balanced) consumption (3.8 MW compared to 3.0 MW) as a result of the lower COP.

The total electricity demand when combining all modes is 169 TJ, while total electricity generation by the PV modules totals 295 TJ. Although the electricity generation far outweighs the demand, grid consumption takes place during 332 hours. During spring weeks, demand regularly exceeds PV generation (see Figure 4.19a) due to high surplus ST generation. Additionally, grid consumption is present during a few days from August to February, as illustrated in Figure 4.19b. These days coincide with periods of relatively low irradiance, during which both PV generation and the buffer storage temperature are low. This results in a higher electrical demand through the lower COP which cannot be covered by PV generation. Throughout the whole year grid consumption only adds up to 4 TJ, a 99% reduction compared to the resistive heater reference. However, peak load is only reduced by 59% from 14 MW to 6 MW. The relatively high reduction in total consumption compared to peak load can be attributed to a small amount of consumption hours throughout the year. It should be noted that full grid independence can be achieved with a modest increase in system size through additions of 10,000 PV modules and ten batteries. Alternatively, the system can function fully grid independent if 3% of industry demand is curtailed.

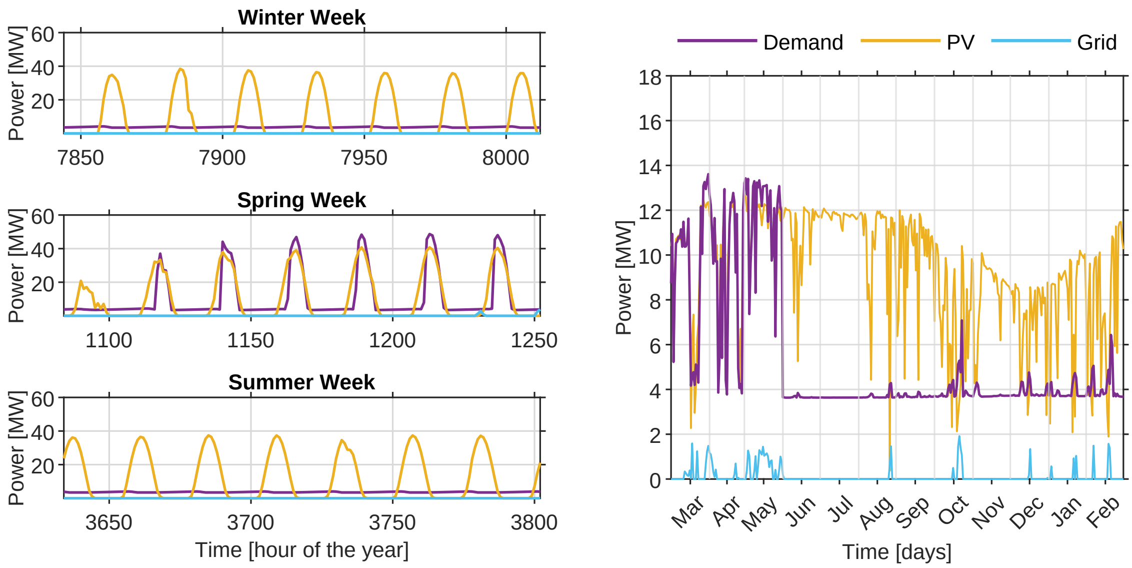

(a) Simulation results for three weeks

(b) Annual simulation results

Figure 4.19. Electricity demand, generation and grid consumption in the Seville Paper & Pulp scenario.

4.1.3. Main takeaways system performance

The simulation results show that Configuration 5 (ST + PV + ATES + battery) and Configuration 6 (PVT + ATES + battery) outperform other configurations in both the total grid consumption and peak load reduction. Configuration 6 slightly outperforms Configuration 5, demonstrating technical potential of HT-PVT collectors. Detailed simulation results for Configuration 6 can be found in Appendix C.1. Furthermore, the results show that the Paper & Pulp industry presents a larger challenge to decarbonize than the Food & Beverage sector. This can be attributed to the higher steam temperature that is required, reducing the COP. Additionally, the continuous demand of the Paper & Pulp industry results in heat demand during the night when no sunlight is available. This provides an additional challenge for the system to supply the industrial heating demand. Seville consistently outperforms Delft due to higher annual irradiance and reduced seasonal irradiance fluctuation. Configuration 3 (ST + ATES, no PV) demonstrates higher peak load consumption compared to system Configuration 2 (ST only). This is attributable to uncompensated electricity spikes during surplus operation.

The most important simulation highlights can be summarized as follows:

- Delft Food & Beverage: Grid consumption of 25 TJ is concentrated in winter when PV generation is low. The ATES is charged to 138 °C during April to August and depleted during October to February in a stable annual cycle returning to its initial temperature of 95 °C. The electrical efficiency of the PV modules remains stable around 21–22% year round. The thermal efficiency of the ST collectors averages 40–50% daily in summer and 15–40% daily in winter, yielding 500 kWh/m^2 annually.
- Delft Paper & Pulp: Higher demand temperature of 150 °C reduces average COP from 4 in the Food & Beverage industry to 3.2, thereby increasing electrical demand from 157 to 192 TJ. The reduction in thermal extraction from storage results in a net annual heat surplus in the ATES, with the warm well temperature finishing at 10 °C above its initial temperature. The peak load of 7 MW is 42% lower than that of the Food & Beverage industry due to the continuous demand profile. However, total electricity grid consumption is 64% higher.
- Seville Food & Beverage: The system operates fully independent of the grid, with total PV generation of 295 TJ against a total electricity demand of 142 TJ. The ATES reaches its maximum temperature after four months, after which a surplus thermal energy generation is curtailed for 2363 hours annually. This indicates that the system is oversized for a Seville Climate. Due to the higher irradiance and ambient temperatures the average annual ST thermal efficiency is 50%,

yielding 1071 kWh/m^2, compared to 500 kWh/m^2 in Delft.

- Seville Paper & Pulp: The system is close to full grid independence with grid consumption of 4 TJ, a reduction of 99.1% compared to the resistive heater reference. Grid consumption is concentrated in 332 hours annually during periods of comparatively low irradiance for a Seville climate. Through modest additions of 10,000 PV modules, ten batteries or minimal demand curtailment of 3%, full grid independence can be achieved. The average COP is 3.7, compared to 3.2 for the Delft Paper & Pulp scenario.

Overall, the proposed energy system provides a technically feasible avenue to reduce total grid consumption and peak grid load consumption. Thereby creating opportunities for energy intensive industries to decarbonize without exacerbating grid congestion issues. The results demonstrate a strong influence of climate conditions on the system performance, and the need for individual system sizing based on location and industry.

4.2. Optimization

This section aims to find the optimum system sizing for Configuration 5 under different scenarios. Results of Configuration 4 are implicitly presented through results of configurations without batteries. The results are evaluated based on the solar fraction and the reduced peak load. If the goal is to minimize CO2 emissions, the solar fraction is the most relevant metric. However, if the goal is an electricity grid connection in a congested network peak load reduction is most relevant.

The solar fraction is defined as the total reduction in grid consumption compared to Configuration 1 (Resistive heater) over the total electricity demand of Configuration 1. Where a solar fraction of 1 indicates that the system is fully grid independent and a solar fraction of 0 indicates no reduction of grid electricity consumption compared to the resistive heater reference. This is also the case for the reduced peak load reduction where 1 means that the there is no grid consumption and 0 means that no reduction in peak load is achieved compared to the reference. Negative values mean that the system requires a higher peak load than the reference Configuration 1. Peak load reduction is more challenging as this requires (stored) solar energy to be available for every hour of the year. For full grid independence, both the solar fraction and peak load reduction are equal to 1.

First, the optimal ratio of ST to PV is determined in Section 4.2.1. Subsequently, the performance sensitivity to individual component quantities is discussed in Section 4.2.2. Finally, a four-dimensional parameter heatmap is presented in Section 4.2.3 to identify the optimal system configuration. Additionally, an optimization for Configuration 6 is presented in Appendix C.2. This analysis examines if the total surface area of the solar collectors can be reduced when replacing the ST and PV arrays with PVT collectors.

4.2.1. Optimal ST/PV ratio

One of the most important parameters in the system is the ratio between ST collectors to PV modules in the system. Due to varying weather conditions and industrial demand requirements, the optimal ratio varies significantly between scenarios. Figure 4.20 presents the reduced consumption and peak power consumption of a range of ST fractions. For these simulations a total of 190,000 combined ST collectors (1200 kWp) and PV modules (460 kWp) is used. The Food & Beverage industry requires a slightly higher ST fraction since its lower operating temperature (130 °C compared to 150 °C) yields a higher COP. A higher COP means a larger fraction of the total heat delivered to industry originates from the thermal source rather than from electrical work, increasing the relative demand for thermal generation from the ST collectors. The Seville scenarios perform better at lower ST fractions due to the high irradiance and temperatures throughout the year, resulting in a higher ST collector efficiency. These decrease the reduced temperature and therefore increase thermal output while the electric output of the PV is not affected much. The optimum ST fraction is: 0.55 for Food & Beverage Delft (blue line), 0.50 for Paper & Pulp Delft (red line), 0.40 for Food & Beverage Seville (yellow line), and 0.30 for Paper & Pulp Seville (purple line). It should be noted that the optimal ST fraction may increase slightly for smaller total collector quantities, where the impact of additional ST collectors is more significant.

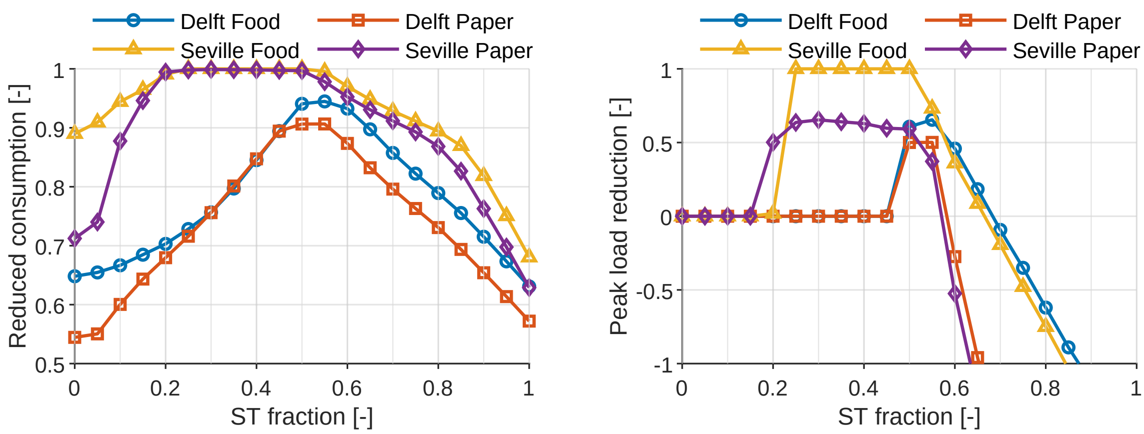

(a) Influence ST fraction on solar fraction.

(b) Influence ST fraction on peak load.

Figure 4.20. Optimal performing ST fraction for different scenarios.

4.2.2. Component quantity optimization

The following figures present the system performance for varying individual component quantities to identify the optimal system sizing. First, Figure 4.21 illustrates the system performance for a varying quantity of ST collectors (1200 kWp) and PV modules (460 kWp). The different scenarios use different ST fractions corresponding to the optima that have been determined in Section 4.2.1. Beyond 80,000 and 180,000 solar collectors, for the Seville (yellow and purple lines) and Delft (blue and red lines) scenarios respectively, the solar fraction demonstrates only marginal improvements (see Figure 4.21a). To achieve a peak load reduction a larger amount of modules is required for the Seville industries, as shown in Figure 4.21b. The Paper & Pulp industry requires 130,000 modules to achieve a 50% peak load reduction and full grid independence is only approached at 250,000 modules. For both Delft industries significant peak load reductions (60% for Food & Beverage, and 50% for Paper & Pulp) are achieved from 180,000 solar collectors onward, but only marginal additional peak load reductions are achieved when increasing the collector count to 250,000.

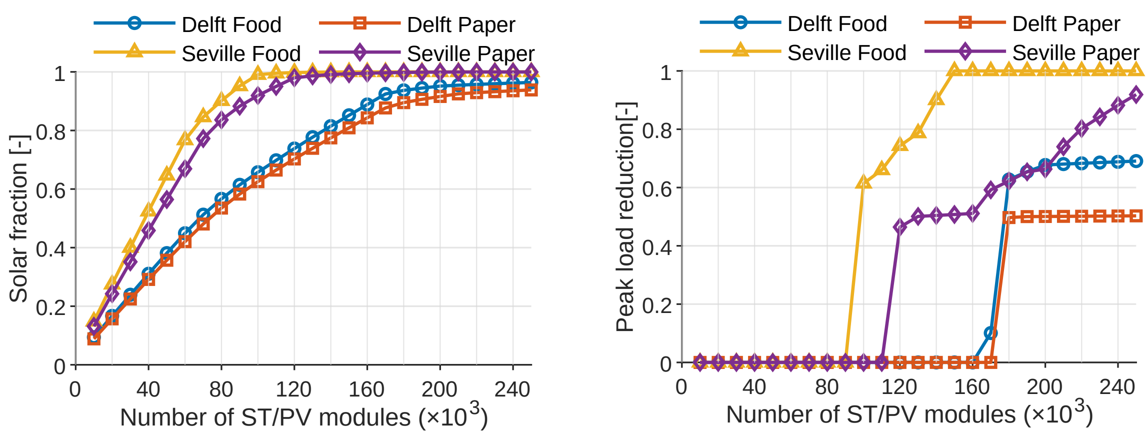

(a) Solar fraction for varying collector quantities.

(b) Peak load reduction for varying collector quantities.

Figure 4.21. System performance for varying collector quantities and scenarios.

Figure 4.22 presents the performance of the different configuration at different well pair quantities. Each additional ATES well provides a seasonal storage capacity of 55 TJ when cycled through its full temperature range, which is 12.5% of the total industrial heating demand. For the Delft scenarios, 180,000 modules are used with a ST fraction corresponding to each specific scenarios optimum (see Section 4.2.1). This collector count is the minimum collector quantity to achieve a 50% peak load reduction for both industries in Delft. The Delft scenarios (blue and red lines) achieve a large increase in solar fraction (≈0.75 to ≈0.9) with the addition of one well pair, as shown in Figure 4.22a. However, for peak load reduction 2 well pairs are required (see Figure 4.22b). Adding additional well pairs slightly reduces system performance since the additional capacity is not utilized, resulting in lower average warm well temperatures.

For Seville 130,000 collectors are used with the optimal ST fraction for each scenario. This is the minimum number of modules required to reach 50% peak reduction for both Seville scenarios. For the Seville scenarios (yellow and purple line) the optimum number of well pairs is one. However, the achieved solar fraction is high even when employing zero well pairs (no ATES), as shown in Figure 4.22a. This suggests that modest increases in buffer storage size, number of batteries or number of solar collectors may be sufficient to reach significant peak load reductions. Alternatively, modest demand curtailment could be employed in Seville to reduce peak load for smaller system sizes. These alternatives are especially critical when local geological conditions do not favor ATES employment in southern European locations.

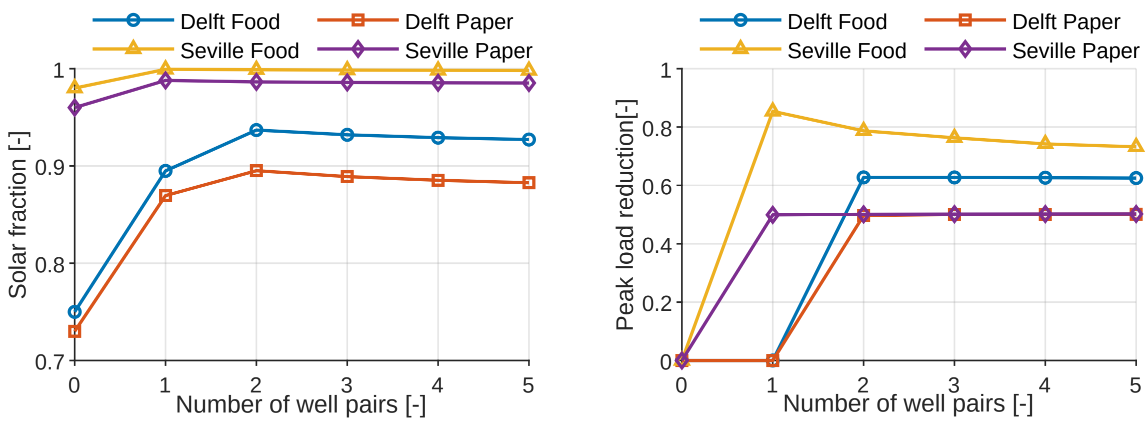

(a) Solar fraction for varying ATES well pair quantities. **(b)** Peak load reduction for varying well pair quantities.

Figure 4.22. System performance for varying ATES well pair quantities and scenarios.

Figure 4.23 shows the sensitivity to an increasing number of batteries (10 MWh per battery). In terms of total reduced consumption the first ten batteries are most impactful for all scenarios. The sensitivity of the reduced peak load depends strongly on the scenario. Whereas the Delft scenarios (blue and red lines) show no meaningful peak load reduction when employing up to 40 batteries, the Seville scenarios show a large decrease in peak load with increasing battery capacity (see Figure 4.23b). Increasing the number of batteries to 15 enables the Seville Food & Beverage scenario (yellow line) to achieve full grid independence. The Seville Paper & Pulp scenario (purple line) requires 35 batteries to become fully grid independent. These relatively modest battery quantities are sufficient to bridge short periods of low irradiance that occur even in southern climates. In contrast, the Delft scenarios would require a considerably larger number of batteries (in excess of 40) to bridge the substantially longer and more severe winter shortage period. This suggests batteries are an effective tool in Seville to achieve full grid independence but are insufficient for grid independence in northern European climates. However, to reduce total grid consumption a relatively small amount of batteries (up to 10) can make a significant impact in both climates (see Figure 4.23a).

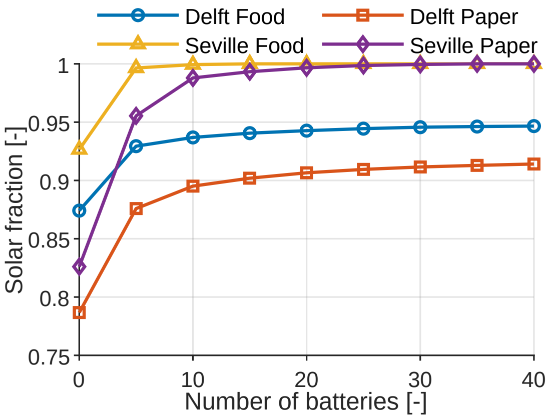

(a) Solar fraction for varying battery quantities.

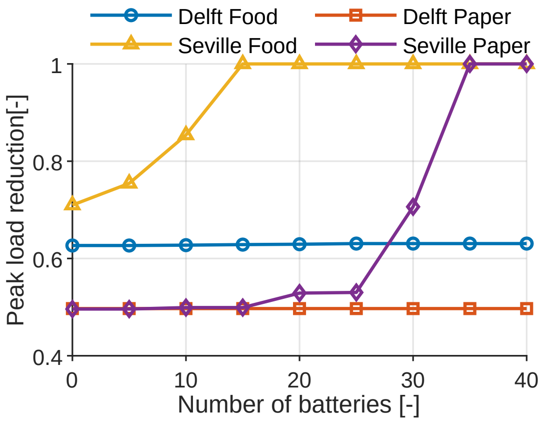

(b) Peak load reduction for varying battery quantities.

Figure 4.23. System performance for varying battery quantities and scenarios.

4.2.3. System size heatmap

This section provides a four-dimensional heatmap illustrating the performance of the energy system using different system sizes. The heatmap presents varying system size combinations for a range of solar collector (ST and PV), battery, and ATES well pair quantities. The quantities presented in the heatmap are based upon the results of the one-dimensional analysis in Section 4.2.2. For each scenario the ST and PV ranges are scaled according to the optimal ST fraction. The heatmaps include zero, one and two well pairs, corresponding to the range of wells that resulted in performance improvements in the one-dimensional optimization. The heatmap also uses zero, ten, and thirty batteries, capturing the range with the most performance improvements, as depicted in Figure 4.23. The heatmaps for the Paper & Pulp industry scenarios are presented in the repository.

The four-dimensional heatmap depicting the solar fraction of the Delft Food & Beverage scenario based on system size is depicted in Figure 4.24. The heatmap shows that the number of ST collectors and ATES well pairs have the largest influence on system performance. As expected there is a general positive solar fraction trend as a result of larger system sizes. Furthermore, the impact of going from zero to ten batteries (Capacity = 100 MWh) and going from zero to one well pair (capacity = 55 TJ) is much larger than additional increases after. This illustrates that small energy storage solutions can have a disproportionately large impact on the solar fraction. The solar fraction is not significantly affected when going from 100,000 to 125,000 ST collectors. This suggests that increasing the ST collector quantity yields diminishing returns beyond 100,000 collectors (120,000 kWp). Furthermore, the marginal impact of additional PV modules is larger for larger ST collector fields. This illustrates the synergy of ST and PV which works optimally when both are available in this system.

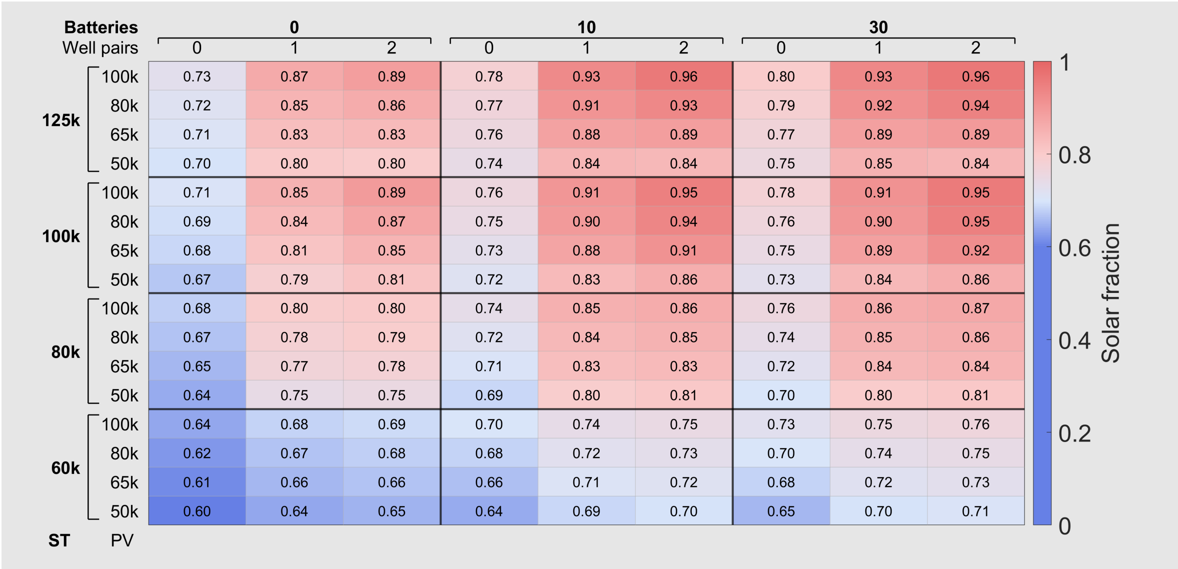

Figure 4.24. Heatmap Delft Food & Beverage total consumption.

The peak load reduction for the Delft Food & Beverage scenario is depicted in Figure 4.25. Peak load reduction is only achieved for a select few scenarios and is significantly more difficult to achieve than reducing total grid consumption. Only systems with more than 100,000 ST collectors and two ATES well pairs realize peak load reduction. When fewer ST collectors or well pairs are used the system is not able to provide thermal energy year round and Mode III B (Resistive heater) has to be activated. When enough ST collectors and well pairs are available the number of PV modules is very important for the system performance. When the ratio of PV modules to ST collectors is too small, not enough electricity is generated during surplus operation. This results in high peak loads that are not covered by self generated electricity. This effect is especially pronounced when 125,000 ST collectors are employed. The peak grid load increases when more ST collectors are added. Combining 125,000 ST collectors and 50,000 PV modules actually increases peak loads compared to Configuration 1 (Resistive heater). To some extent these issues can be mitigated through a more complex control strategy, limiting the ST thermal output generation based on available electrical energy from the PV modules and the batteries. The number of batteries has a comparatively small influence on the peak load reduction. Achieving full grid independence in the Delft Food & Beverage scenarios requires impractically large system size. To become fully grid independent the system requires 100,000 ST collectors, 250,000 PV modules, two well pairs and 50 large batteries. Such a system size is considered impractical and is therefore not included in optimization and economic analysis.

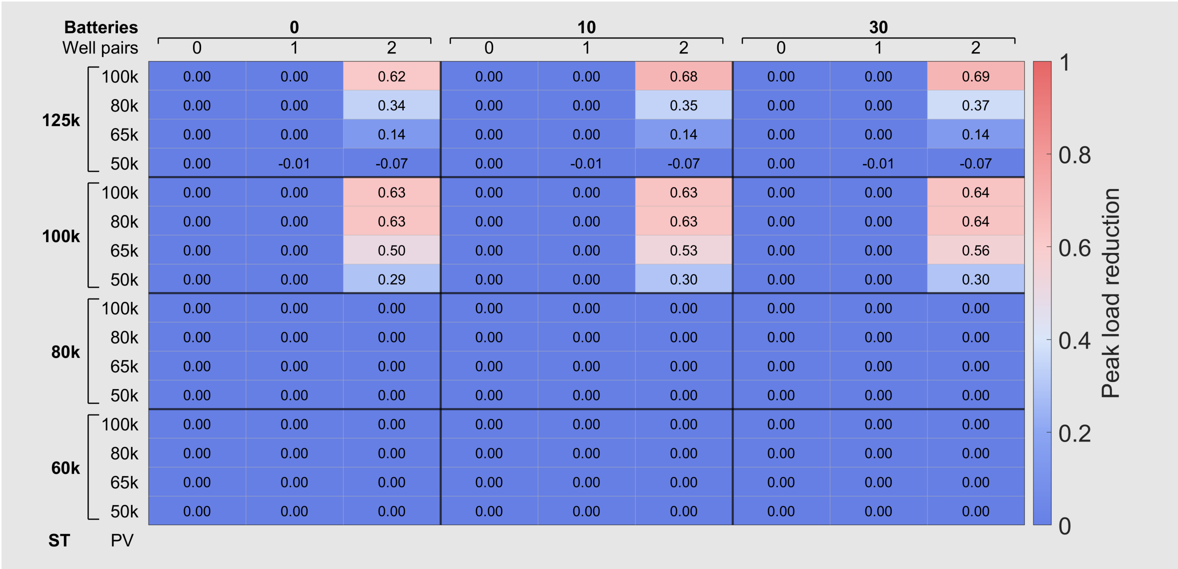

Figure 4.25. Heatmap Delft Food & Beverage peak load.

A heatmap of the solar fraction for different component quantities in the Seville Food & Beverage scenario is presented in Figure 4.26. The heatmap depicts much higher solar fractions than those of the Delft Food & Beverage scenario despite the lower solar collectors quantities. The number of well pairs has a negligible impact on the total grid consumption of the system. Conversely, solar fraction decreases in some scenarios when additional well pairs are introduced, due to an increased electrical demand as a result of excessive ATES charging. The system is more sensitive to battery quantity compared to the Delft Food & Beverage scenario. In particular, increasing the number of batteries from zero to ten yields a large increase in solar fraction. High solar fraction can already be achieved with relatively low quantities of PV and ST of 30,000 and 45,000 respectively. The heatmap also shows many combinations that have a 100% solar fraction. Due to the higher irradiation and smaller seasonal differences the system achieves grid independence for much smaller system sizes compared to the Delft scenario.

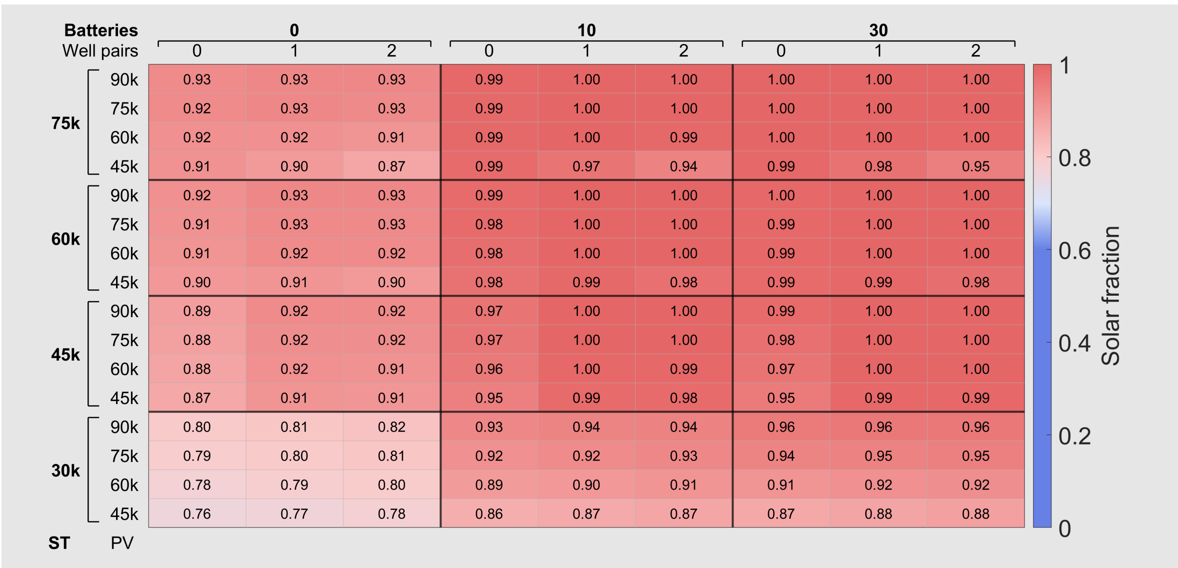

Figure 4.26. Heatmap Seville Food & Beverage total consumption.

Figure 4.27 shows a heatmap of the peak load reduction in the Seville Food & Beverage scenario. A peak load reduction is demonstrated from 45,000 ST collectors (54,000 kWp) and higher and for most configurations one well pair is required to see significant peak load reductions. The number of PV modules has a moderate influence on the peak load reduction. However, significant gains can be found when increasing PV modules from 45,000 to 60,000. In this scenario, the number of batteries has a large influence on peak load reduction. With many combinations being able to function fully independent of the grid when 30 industrial size batteries (300 MWh) are employed. Using large-scale battery storage also enables the system to reduce peak load consumption without requiring an ATES system in some scenarios when large numbers of solar collectors are employed. This is a promising result for southern European locations for which the geological conditions are not suitable for ATES implementation.

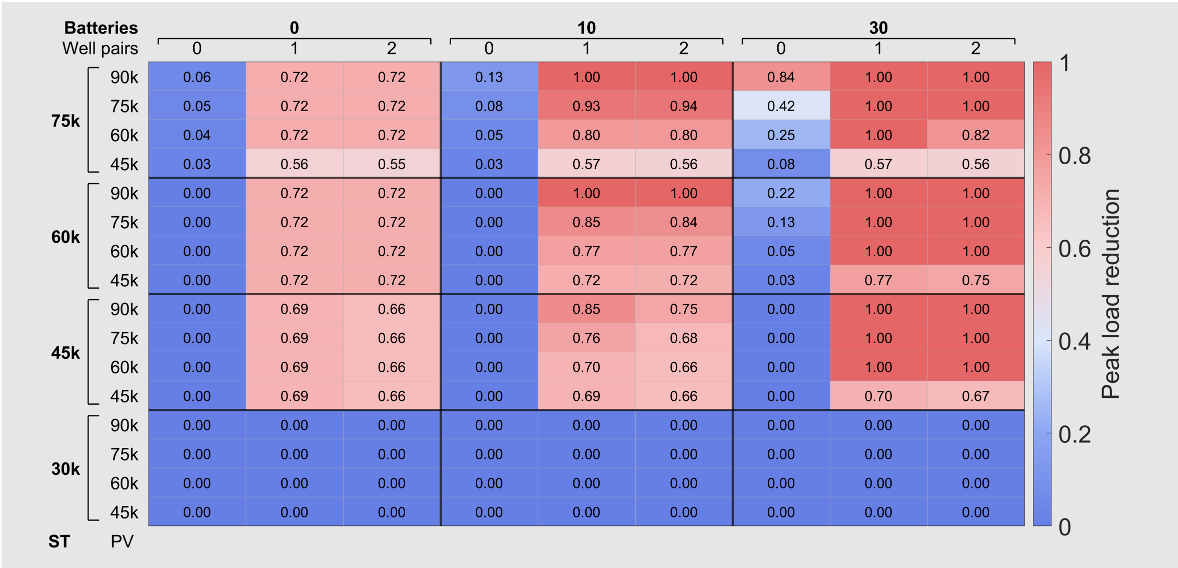

Figure 4.27. Heatmap Seville Food & Beverage peak load.

4.2.4. Main takeaways optimization

The optimization study demonstrates the importance of system sizing in achieving a high grid fraction and in particular for reducing peak grid loads. The most important takeaways are summarized as follows:

ST/PV ratio
The optimal ST fraction varies by scenario: 0.55 for Delft Food & Beverage, 0.50 for Delft Paper & Pulp, 0.40 for Seville Food & Beverage and 0.30 for Seville Paper & Pulp. These differences can be attributed to two factors, the weather conditions and the demanded steam temperature. The Seville climate requires fewer ST collectors relative to PV modules since the average thermal efficiency of the ST collectors in Seville is higher. The average PV electrical efficiency is slightly lower due to higher ambient temperatures. These factors cause a shift in the optimal ST fraction.

Higher industrial demand temperatures decrease the COP of the system. As a result the electrical energy demand of the HP increases and the thermal extraction from the storage decreases. Consequently, the optimal ST fraction is lower for the Paper & Pulp industry than for the Food & Beverage industry. More PV modules are required and fewer ST collectors.

At high ST fractions the peak load reduction can become negative due to high surplus heat generation during summer which is not compensated by PV electricity generation. This issue could be mitigated through a more advanced control strategy, for example by limiting surplus HP operation to periods of sufficient PV generation or by distributing ATES charging across a wider window of daily hours rather than concentrating it during peak irradiance.

Number of solar collectors
System performance improves with increasing solar collector quantities but shows diminishing returns

beyond a certain number of solar collectors. Beyond 45,000 and 100,000 ST collectors for the Seville and Delft scenarios respectively, no significant increase is found in system performance. Up to this point the ST collector quantity has a larger influence on system performance than the number of PV modules. This is especially noticeable in the solar fraction of the system. To see a meaningful reduction of the peak load, PV module quantity is essential. Significant improvements in peak load reduction are demonstrated from 45,000 and 65,000 PV modules in the Seville and Delft scenarios respectively.

ATES well pairs
The simulation results show that the optimum number of well pairs is two for Delft and one for Seville. Adding well pairs beyond the optimum reduces system performance since the higher thermal storage capacity prevents the ATES to be utilized through its full temperature range. Moreover, for large ST collector fields the wells do not return to their initial temperature after a seasonal cycle, causing additional unnecessary surplus operation when more wells are used. Introducing ATES wells enables seasonal storage which is essential for peak load reduction. When no seasonal storage is employed the peak load is not reduced in any of the scenarios. Introducing one well pair produces a substantial improvement on the achieved grid fraction of the Delft scenarios. For the Seville scenarios, introducing a single well pair only increases the solar fraction slightly because without seasonal storage the solar fraction already exceeds 95%. This suggests that seasonal storage may not be necessary for Seville scenarios when considering a large enough system size or when employing slight demand curtailment. This finding is particularly relevant for southern European locations with high year-round irradiance but unsuitable subsurface conditions for ATES implementation.

Number of batteries
The first five batteries deliver the largest gain in solar fraction, and beyond ten batteries the solar fraction improvements diminish. For peak load reductions higher battery quantities are required. In Seville adding batteries is highly effective for reducing the peak load, potentially allowing for full grid independence. In contrast, additional batteries in the Delft scenarios have a negligible effect on peak load since storage periods are too long to cover using reasonably sized battery systems.

Overall technical feasibility
The simulation results of the proposed energy system have shown that it can effectively reduce total grid consumption and peak load consumption from the grid. Full grid independence is not practically feasible in Delft, requiring an excessively large system. However, full grid independence in Seville can be achieved with reasonable collector counts of 45,000 ST collectors and 60,000 PV modules. A 50% reduction in peak load can be achieved in Delft with 100,000 ST collectors and 65,000 PV collectors. This 50% reduction in peak load may be sufficient to secure a grid connection in a congested distribution network.

In locations without suitable ATES geology, large battery storage combined with high collector counts can achieve peak load reduction in southern climates. In northern climates with large seasonal irradiance fluctuations, this is deemed infeasible. A study on the required number of PVT modules to decrease peak load is presented in Appendix C.2. This study demonstrates that the PVT collectors can effectively replace the ST and PV arrays, while also requiring a slightly smaller collector area to see meaningful peak load reductions.

4.3. Economic analysis

The previous sections have demonstrated the technical feasibility of reducing total and peak grid consumption through the proposed solar-assisted process heating energy system. This section aims to examine the economic viability of the designed energy system. Achieving 100% self-sufficiency requires impractical size requirements for some of the scenarios. Therefore, a minimum peak load reduction of 50% is adopted for the viability criterion for the economic assessment. A 50% reduced peak load is considered sufficient to facilitate grid connection in congested distribution networks.

The systems are judged based on the levelized cost of heat (LCOH). The LCOH quantifies the average cost of delivering thermal energy for any system by combining the capital, operational, and maintenance costs during the lifetime of the system. The LCOH is calculated using a net present value based levelized cost methodology commonly used in industrial heating systems [75, 115]:

$$\mathrm{LCOH} = \frac{\mathrm{CAPEX} + \mathrm{OPEX}}{\mathrm{E_{heat}}}, \tag{4.1}$$

where the capital expenditure (CAPEX) is determined by summing the investment costs for all components in Table 4.2. The investment cost of auxiliary components such as hydraulic pumps and pipes for the ST collectors, and cabling and inverters for the PV modules are included in the presented capital cost values. The total heat delivered to industry is $\mathrm{E_{heat}}$ and is described in Equation 4.3. The operational expenditure (operational expenditure (OPEX)) represents the discounted sum of operation and maintenance costs throughout the system lifetime and is described as follows:

$$\mathrm{OPEX} = \sum_{n=1}^{N} \frac{r_{\mathrm{O\&M}}\mathrm{CAPEX}}{(1+DR)^n} + P_{\mathrm{elec}} \sum_{n=1}^{N} \frac{E_{\mathrm{grid}}}{(1+DR)^n}, \tag{4.2}$$

where N is the lifetime of the energy system, $r_{\mathrm{O\&M}}$ is the annual operation and maintenance cost as a fraction of CAPEX, DR is the discount rate, E_{grid} is the annual grid electricity consumption in MWh, and P_{elec} is the industrial electricity price in €/MWh. The discounted total heat to industry, taking into account degradation of the solar collectors is expressed as:

$$\mathrm{E_{heat}} = \sum_{n=1}^{N} \frac{Q_{\mathrm{industry}}(1-SD)^n}{(1+DR)^n}, \tag{4.3}$$

where Q_{industry} is the heat delivered to industry during the first year of operation and SD is the degradation rate of technologies. An annual degradation rate of 0.5% is applied, consistent with values for ST and PV collector degradation in literature [116, 117]. Degradation of the ATES system and HT-HP is not included in this analysis. The parameters used in the economic LCOH analysis are listed in Table 4.2.

Table 4.2. Economic parameters used in the LCOH assessment.

Parameter	**Value**	**Unit**	**Source**
Capital costs			
ST collectors	~400	€/m^2	[118]
PV modules	640	€/kW_p	[119]
Heat pump	400	€/kW_{th}	[120]
HT-ATES	205	€/MWh_{th}	[60]
Hot water buffer storage	1.35	€/kWh_{th}	[50, 121]
Battery storage	125	€/kWh_{el}	[122]
Operational costs			
O&M cost (annual, % of CAPEX) ($r_{\mathrm{O\&M}}$)	2	%/yr	[115]
Industrial electricity price	110	€/MWh	[123]
Reference system (gas boiler)			
Gas boiler (reference system)	70	€/kW_{th}	[124]
Industrial natural gas price (current, 2026)	16.7	€/GJ	[14]
Industrial natural gas price (peak, 2022)	25	€/GJ	[14]
Gas boiler efficiency	95	%	[125]
CO_2 emission factor	0.055	tonne/GJ	[126]
EU ETS carbon price	70	€/tonne CO_2	[127]
Financial and degradation parameters			
Discount rate (DR)	6	%	[128]
System lifetime (N)	25	years	[119]
PV annual degradation rate	0.5	%/yr	[117]
ST annual degradation rate	0.5	%/yr	[116]

4.3.1. Optimal configuration economically

The following section identifies the system configuration which minimizes the LCOH for the Delft and Seville Food & Beverage industry. This is achieved by combining the heatmaps in Section 4.2.3 with the LCOH methodology described above. All results with a peak load reduction below 50% are excluded, since these systems are not able to secure a connection in a congested electricity grid. Systems with a LCOH below 80 €/MWh are depicted in green. These systems are economically competitive to a gas heated industrial boiler when including Emissions Trading System (ETS) carbon emission credits, as calculated using Equation 4.1. When applying the average European non-household price of natural gas during the 2022 peak, following the Russian invasion of Ukraine, the LCOH of gas increases to 120 €/MWh. When the LCOH surpasses 120 €/MWh, the system is considered to be currently economically infeasible and is depicted in red.

Figure 4.28 presents the LCOH for a range of system sizing of the Delft Food & Beverage scenario. The figure demonstrates that the cheapest system LCOH is comparable to the gas boiler reference value under peak natural gas price conditions observed during 2022.

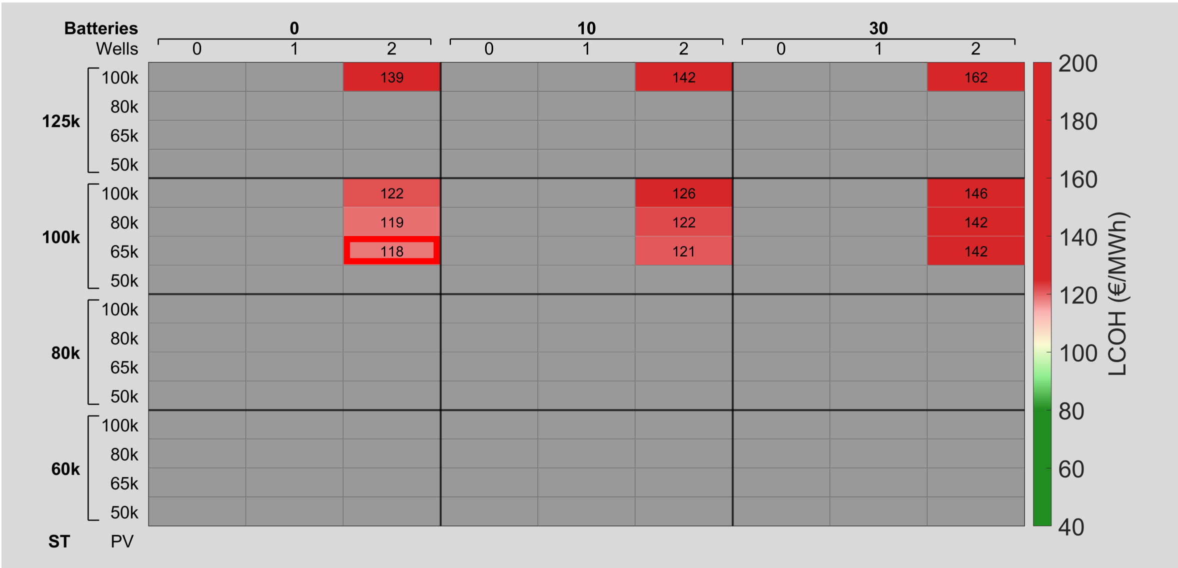

Figure 4.28. Heatmap presenting the LCOH of the Delft Food & Beverage scenario for varying system sizes.

The CAPEX distribution of the cheapest scenario is depicted in Figure 4.29. This scenario employs 100,000 ST modules, 65,000 PV modules and two ATES well pairs. The cheapest scenario does not employ batteries even though battery energy storage can increase the solar fraction significantly. This can be attributed to the high costs of such a large battery system. Through smart charging and discharging to the grid the battery economic impact could be improved.

Figure 4.29 illustrates that the ST collectors are responsible for more than half of initial investment costs. The water tank buffer storage is not included in the pie chart since it accounts for less than 0.5% of initial investment costs but is included in the total CAPEX number. The cost of ST collectors is expected to decrease as large-scale industrial deployment drives learning curve effects. Figure 4.30 depicts the sensitivity of the LCOH to varying collector prices and discount rates, since these are the most influential parameters on system cost. The graph shows that solar-assisted steam generation can compete with gas boiler heating under current gas prices if ST prices fall to 200 €/m^2 and a discount rate of 5% is assumed. For current conditions of 400 €/m^2 ST collector cost and a discount rate of 6% the LCOH already falls below the 120 €/MWh threshold. This threshold may be considered acceptable for industrial implementation, especially considering the independence from volatile gas prices and low grid electricity consumption. Furthermore, policy instruments such as subsidies and a higher ETS carbon price could make the system even more economically competitive.

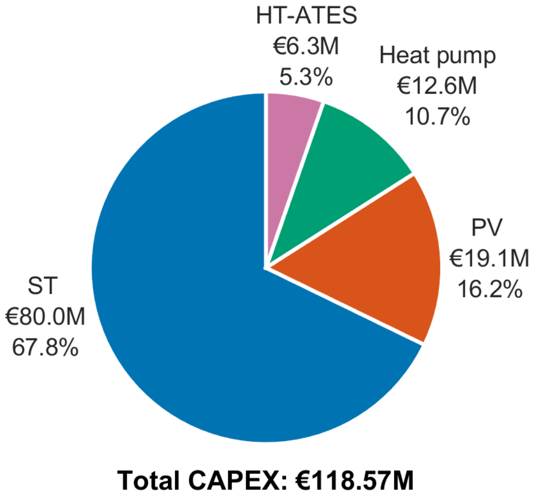

Figure 4.29. CAPEX Delft Food & Beverage scenario.

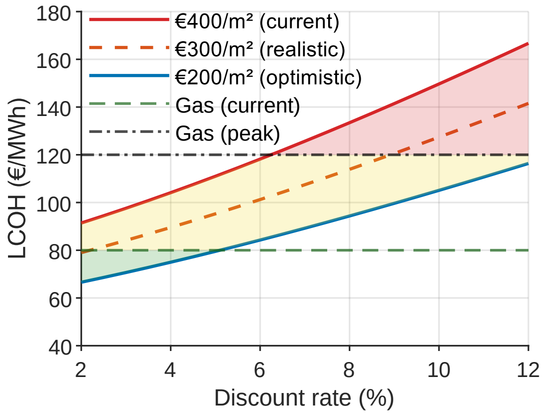

Figure 4.30. LCOH as function of discount rate for the Delft Food & Beverage scenario.

The Seville Food & Beverage scenario yields considerably more favourable results with LCOH values below 80 €/MWh for a large range of system sizes, as illustrated in Figure 4.31. The scenario using 45,000 ST collectors, 45,000 PV modules and one ATES well pair has the lowest LCOH of 66 €/MWh. The proposed system is therefore already financially competitive with gas boilers in southern European climates.

For scenarios with 100% grid independence the configuration using 60,000 ST collectors, 90,000 PV modules, one ATES well pair and ten batteries has the lowest LCOH of 88 €/MWh. Although this exceeds the current gas boiler reference, full grid independence offers significant advantages such as reduced exposure to volatile energy markets and flexibility in terms of location.

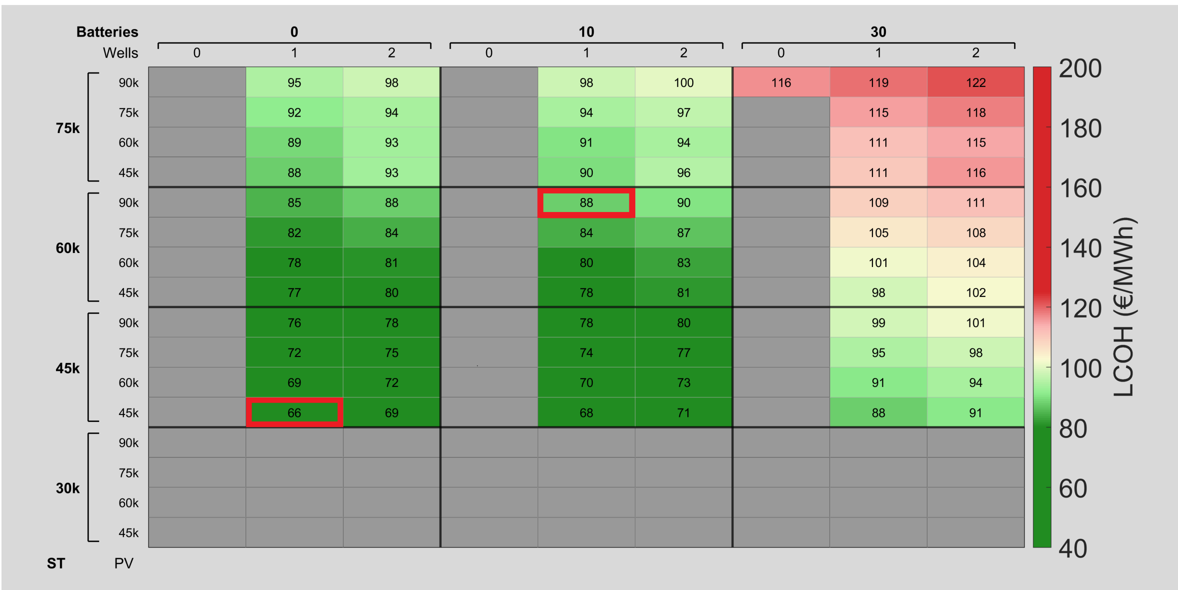

Figure 4.31. Heatmap presenting the LCOH of the Seville Food & Beverage scenario for varying system sizes.

Figure 4.32 shows that the ST collector fraction of total CAPEX is considerably smaller in the Seville scenario. The overall costs are also close to half of the costs required for the Delft Food & Beverage scenario. Figure 4.33 demonstrates that the LCOH of this Seville energy system is below current gas boiler LCOH for most discount rates and ST collector prices. This is a promising result for solar-assisted steam generation in low latitude locations. Further ST collector cost decrease is expected through learning curve effects, reinforcing the economic viability of the proposed energy system for southern European climates.

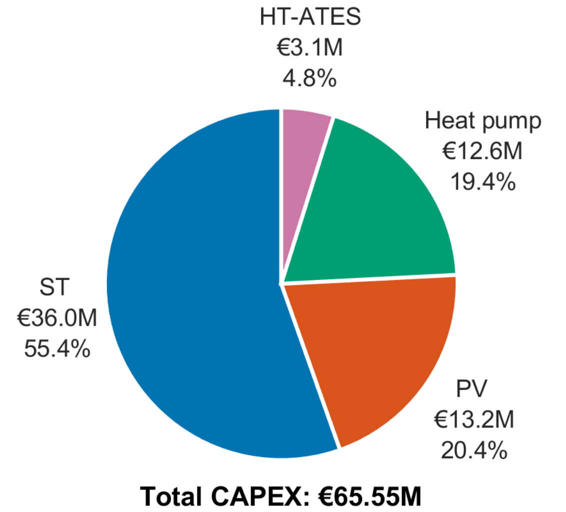

Figure 4.32. CAPEX Seville Food & Beverage scenario.

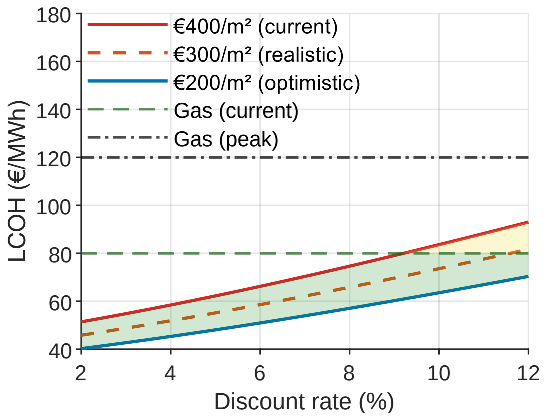

Figure 4.33. LCOH as function of discount rate for the Seville Food & Beverage scenario.

Figure 4.34 depicts the CAPEX of the cheapest configuration to reach 100% grid independence in Seville. The total CAPEX of the fully self-reliant system is €103 million, considerably higher than the €66 million required for a 50% peak load reduction. As shown in Figure 4.35, when using a lower discount rate or reduced ST collector costs, the LCOH falls below the current gas reference of 80 €/MWh. For most discount rates and ST collector prices the system is cheaper than gas boiler prices under high natural gas prices.

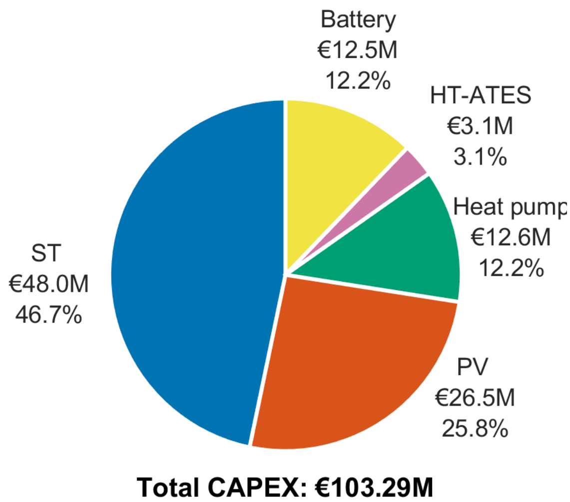

Figure 4.34. CAPEX Seville Food & Beverage scenario 100% grid independence.

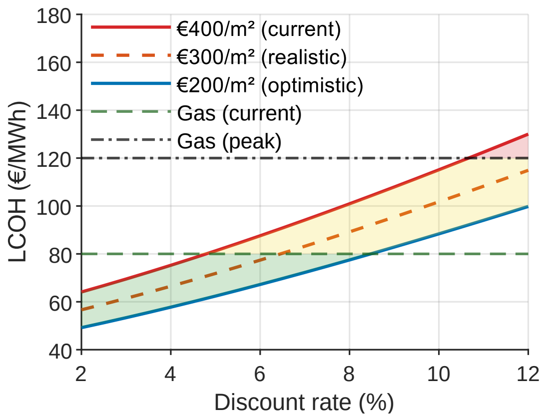

Figure 4.35. LCOH as function of discount rate for the Seville Food & Beverage scenario 100% independence.

The economic results of all three considered scenarios are presented in Table 4.3. The LCOH values of the different scenarios (119 €/MWh for Delft and 66–88 €/MWh for Seville) are relatively high compared to the values presented in Table 1.1 (38–70 €/MWh for southern Europe and 80–116 €/MWh for western Europe) in the literature review. This can be attributed to the grid congestion constraints imposed in this study. Due to these constraints, a much higher solar fraction is required in order to bring down peak load throughout the year. Consequently, large-scale thermal energy storage and increased solar collector quantities have to be used, raising system costs.

Table 4.3. LCOH and CAPEX contributions for three different scenarios.

Parameter	Delft	Seville	Seville grid independent
LCOH (€/MWh)	118.2	66.2	87.6
CAPEX (M€)	118.6	65.6	103.3
PV modules (M€)	19.1	13.3	26.5
ST collectors (M€)	80.0	36.0	48.0
Water tank (M€)	0.6	0.6	0.6
HP (M€)	12.6	12.6	12.6
ATES (M€)	6.3	3.1	3.1
Batteries (M€)	0	0	12.5

4.3.2. Main takeaways economic analysis

The economic analysis contextualizes the simulation results within a broader financial context going further than just technical feasibility. For large-scale implementation of a technology the financial competitiveness is necessary. The main takeaways of the analysis are listed below:

LCOH methodology
The economic assessment employs a net present value based LCOH formulation, accounting for discounted electricity costs, operation and maintenance costs, and degradation adjusted heat delivery over a 25 year lifetime. The results are compared against a gas boiler reference with a LCOH of 80 €/MWh at current natural gas prices and 120 €/MWh at the elevated gas prices observed during the 2022 European energy crisis.

Delft Food & Beverage
The cheapest configuration achieves a LCOH of 119 €/MWh, which is not competitive under current gas prices but is comparable to the high LCOH benchmark of 120 €/MWh. The optimal configuration uses 100,000 ST collectors, 65,000 PV modules and two ATES well pairs. The cheapest configuration does not employ batteries, even though they show promising technical benefits. For the considered energy system, capital costs of the batteries outweigh the energy savings. More than half of the capital costs are attributable to the ST collectors. If the costs of ST collectors drop below 200 €/m^2 and an optimistic discount rate of 5% is assumed the system can be competitive with a gas boiler under current natural gas prices.

Seville Food & Beverage
The cheapest configuration that achieves 50% peak load reduction uses 45,000 ST collectors, 45,000 PV modules and one ATES well pair, achieving a LCOH of 66 €/MWh. The total investment costs are roughly half of those of the Delft scenario. At 66 €/MWh, the system is already considerably cheaper than a natural gas boiler at current gas prices at 80 €/MWh.

For full grid independence a considerably larger system is required with investment costs of € 103 million and a LCOH of 88 €/MWh. This is slightly above the current gas price reference but far below the high gas price threshold. Utilizing cheaper collectors or a lower discount rate results in a LCOH below 80 €/MWh and therefore provides an economically competitive alternative to a natural gas boiler.

Overarching conclusions
The proposed solar-assisted industrial steam generation energy system including seasonal storage is a financially viable alternative to gas boilers in southern European climates. In northern European climates, the energy system is not financially competitive under current gas prices but approaches viability under high gas price conditions. Significant reductions in LCOH can be achieved through

price reduction of the ST collectors in combination with a favourable discount rate. This reduction can be expected through learning curve effects and large-scale deployment. The relative economic position of the solar-assisted heating system can also be improved through natural gas price increases and government support such as subsidies. By switching away from imported energy carriers such as natural gas the system also aligns with current European incentives to reduce dependency on external energy suppliers and enhance energy security.

4.4. Conclusion

This chapter presents the results of simulating the integrated model under varying operating conditions to examine to what extent medium temperature (130–150 °C) industrial heat demand can be covered by solar energy generation, using high temperature solar thermal and photovoltaic collectors in combination with thermal energy storage comprising a thermal buffer storage and a seasonal HT-ATES system (Objective 3). Furthermore, the system size is optimized and an economic analysis on the developed industrial energy system is performed, assessing the economic viability of the system under varying climate conditions (Objective 4).

Section 4.1 demonstrates that the system is technically capable of reducing grid electricity consumption substantially for both industry types and locations. The system is able to reach complete grid independence in Seville and a significant reduction in peak grid electricity consumption of more than 60% and 50% for the Food & Beverage and Paper & Pulp scenarios in Delft respectively. The simulation results highlight the influence of the demanded process temperature which affects the COP and thereby the ratio of thermal to electrical energy demand throughout the year. Reducing peak load is more difficult compared to total grid consumption and requires careful system size optimization.

The optimization analysis in Section 4.2 identifies the ST/PV ratio, ST collector quantity, and number of ATES well pairs as the dominant design variables. The optimal ST fractions are 0.55, 0.50, 0.40, and 0.30 for Delft Food & Beverage, Delft Paper & Pulp, Seville Food & Beverage, and Seville Paper & Pulp scenarios respectively. Additional solar collectors show diminishing returns beyond 80,000 and 180,000 solar collectors for the Seville and Delft scenarios respectively. The first ATES well pair and the first five batteries yield disproportionately large performance gains relative to subsequent additions. Full grid independence under the Delft climate requires an impractically large system, whereas it is achievable at reasonable scale in Seville.

The economic analysis in Section 4.3 demonstrates that the system is already competitive with gas-fired boilers in southern European climates, achieving a minimum LCOH of 66 €/MWh compared to the 80 €/MWh gas boiler reference. Full grid independence in Seville is achievable at 88 €/MWh. In northern European climates, the system achieves a minimum LCOH of 119 €/MWh and is therefore competitive with gas boilers under high gas prices of 120 €/MWh. The LCOH falls below the current gas reference when ST collector costs reach 200 €/m^2 and a 5% discount rate is applied. Future cost reductions through large-scale deployment alongside policy instruments such as subsidies or a higher EU CO_2 ETS price would further improve the economic viability.

Together, these findings demonstrate that the proposed system is a technically feasible solution for industrial decarbonization in locations with grid congestion. The system is currently economically competitive for southern European climates and can approach economic viability in northern European climates under certain conditions.

Chapter 5

Conclusion

This thesis presents an innovative solar-assisted steam generation design to provide industrial process heat at temperatures of 130–150 °C. The designed system includes evacuated flat plate ST collectors for high temperature heat generation, PV modules, a novel steam compression HP, a cutting-edge high temperature ATES system, water tank thermal energy storage and large electrical batteries. The primary objective of this thesis was to answer the question: "To what extent can solar-assisted industrial process heating in combination with thermal energy storage reduce grid congestion problems in Europe?". To achieve this goal several objectives have been addressed:

- **Objective 1:** Numerical models for the individual system components required for a high temperature heating system were developed and adapted, including thermal energy storage, a heat pump, and solar collectors. (Chapter 2)
- **Objective 2:** An integrated energy model was developed that combines the high-temperature components described in Chapter 2 into a complete industrial process heat supply system, with multiple operational modes and system configurations. (Chapter 3)
- **Objective 3:** The integrated model was used under different operating conditions to explore to what extent medium temperature (130–150 °C) industrial heat demand can be covered by solar energy generation using HT-ST and PV collectors in combination with thermal energy storage using a thermal buffer storage and a seasonal HT-ATES system. (Chapter 4)
- **Objective 4:** The system size was optimized and an economic analysis was performed on the developed industrial energy system, assessing the economic viability of the system under varying climate conditions. (Chapter 4)

5.1. Summary of key findings

Technical feasibility
The integrated energy system is technically capable of substantially reducing total and peak grid electricity consumption in all evaluated scenarios. In general, peak load reduction is considerably more difficult to achieve than total consumption reduction, but to secure a grid connection a peak load reduction is essential. The Seville scenarios can achieve full grid independence within reasonable system sizes. For the Delft scenarios a 50% reduction in peak grid consumption is more feasible. In Delft, at least 100,000 ST collectors and two ATES well pairs are required for a substantial peak load reduction. Seville requires a much smaller system size of 45,000 ST modules and one ATES well pair.

Role of ATES
The ATES system is crucial for seasonal energy shifting, especially for northern European climates where the mismatch between winter solar energy generation and consumption is most present. Without the HT-ATES peak load reduction is not achievable in Delft. In Seville one ATES well pair is sufficient and the need for an ATES can even be eliminated using a larger system size with 75,000 ST collectors, 90,000 PV modules, and 30 batteries. When properly sized, the ATES operates stably between its design temperature range of 90 to 150 °C, returning to its initial starting value after one year. These results

demonstrate the theoretical viability of HT-ATES for industrial process heat applications. Due to the novelty of ATES systems operating at these temperatures the practical viability is not yet confirmed.

System sizing and optimization
The optimization analysis highlights the importance of a well balanced ST and PV ratio which varies by location and industry: 0.55 for Delft Food & Beverage, 0.50 for Delft Paper & Pulp, 0.40 for Seville Food & Beverage, and 0.30 for Seville Paper & Pulp respectively. The largest performance increase is made by the first 5 batteries, the first well pair and the first 45,000 and 100,000 ST collectors, for the Delft and Seville scenarios respectively. Increasing system size beyond these quantities provides diminishing performance improvements. System sizing is strongly dependent on climate conditions and specific industrial demand, especially when significant peak load reductions need to be achieved.

Economic analysis
The LCOH is strongly dependent on climate conditions. In Seville the system achieves a LCOH of 66 €/MWh when aiming for a 50% reduction in peak grid consumption. This is already below the 80 €/MWh benchmark of a natural gas boiler including EU ETS carbon costs. The system is therefore economically competitive today in southern European climates without requiring future cost reductions or subsidies. For a fully grid independent energy system in Seville the LCOH increases to 88 €/MWh. This is slightly higher than the current gas reference but well below the 120 €/MWh LCOH threshold corresponding to 2022 gas prices.

In Delft the system is not yet economically competitive at current gas prices with the cheapest configurations costing around 120 €/MWh. This shows that the system would be competitive under a scenario with very high gas prices. In the future the system can become competitive with current gas prices if ST collector costs fall to 200 €/m^2 and a discount rate of 5% is applied. The ST collector costs account for the largest capital investment in all scenarios due to the currently high price for these collectors. This makes ST collector cost reduction through large-scale deployment the most important pathway to economic competitiveness in northern Europe.

5.2. Final conclusion

The answer to the research question is strongly climate dependent. In southern European climates, the system can reduce peak grid load by more than 50%, at a cost that is currently competitive with a gas-fired boiler alternative. The system is able to achieve complete grid independence for medium temperature industrial steam demand at a LCOH comparable to that of gas-fired boilers. When aiming for a 50% reduction in peak load from the grid LCOH can be reduced to 66 €/MWh, substantially below the LCOH of currently operating gas-fired boilers.

In northern European climates, the designed system can reduce peak grid consumption by more than 50%, often sufficient for a grid connection in congested networks. However, the system is not able to reach full grid independence within practical system sizes and is currently not yet financially competitive with fossil fuel alternatives. The system approaches economic viability when compared against gas-fired boilers under high natural gas prices such as in 2022. Furthermore, the system can potentially compete economically under current prices if ST collector costs decline or through policy instruments such as subsidies or higher EU ETS carbon prices.

The designed system therefore represents a technically sound and economically feasible solution for industrial process heating in locations with congested electricity networks. This in combination with the system's independence from volatile gas markets, makes solar-assisted steam generation with high temperature ATES seasonal storage a credible pathway toward decarbonized industrial heating in Europe. The system is currently economically competitive in southern climates and within reach of economic viability in northern regions under foreseeable market and policy conditions.

Chapter 6

Recommendations

The findings of this thesis highlight the potential of solar heating for industrial processes including seasonal storage to avoid grid congestion problems associated with electrification of industry. Even though the designed energy system shows promising technical and economic results, there are system-level improvements that could potentially increase system performance and economic viability. Furthermore, additional research is required to fill in research gaps for some components such as the high temperature ATES and HT-ST/PVT. This chapter outlines recommendations for future work, to cover aspects outside the scope of this thesis.

- **Advanced control system:** The system currently follows a simple control system choosing between five modes based on storage temperatures and net energy generation. A more advanced control strategy could limit surplus ATES charging to available electrical energy, distribute surplus energy over the day to reduce peak loads, use grid energy to charge batteries during periods with low electricity costs, and incorporate weather forecast based control. Additionally, industrial demand curtailment during a small number of hours responsible for peak grid consumption could be explored. These improvements could meaningfully reduce the required system size.
- **Advanced high temperature PVT collector:** Further research can focus on developing a heat transfer model that simulates the performance of an evacuated high temperature PVT collector. This model can be used to derive coefficients for an improved reduced temperature PVT model, which can be used in combination with the developed integrated system model.
- **Concentrated ST collectors:** Future work can assess the viability of using concentrated ST collectors for heat generation. In this thesis only evacuated ST and PVT collectors are considered but concentrated collectors provide some specific advantages including high efficiency operation during high temperature operation. Evaluation of these types of collectors for a range of climate conditions can provide valuable additional insights into solar-assisted industrial heating.
- **ATES groundwater flow model:** The current ATES model uses a lumped thermal capacity approach which does not capture groundwater flow within the aquifers. A more advanced simulation tool can be developed to capture spatial temperature gradients and groundwater flow. This would improve the accuracy of recovery efficiency predictions and yield different results for ATES extraction temperatures compared to a lumped thermal capacity model. This is especially interesting for novel ATES systems with a high temperature operating range of 90 to 150 °C where buoyancy driven flow becomes significant.
- **High temperature ATES feasibility:** High temperature ATES with an operating range of 90 to 150 °C is currently not employed due to a knowledge gap, additional challenges compared to lower temperature operation, and jurisdictional restrictions. Further research is required to fully assess the risks and challenges associated with ATES operation in these temperature ranges. Additionally, extensive ground condition monitoring is required to find which locations in Europe have suitable geological formations to employ these ATES systems. Alternatively, the performance of the system for a lower ATES operating range could be studied to determine viability when ATES operation at temperatures above 100 °C is not technically, economically or legally feasible.

Bibliography

[1] G. Kosmadakis, "Estimating the potential of industrial (high-temperature) heat pumps for exploiting waste heat in eu industries," *Applied Thermal Engineering*, vol. 156, pp. 287–298, 2019. [Online]. Available: https://www.sciencedirect.com/science/article/pii/S1359431118376087

[2] B. Norton, "Anatomy of a solar collector: Developments in materials, components and efficiency improvements in solar thermal collector systems," *Refocus*, vol. 7, pp. 32–35, 5 2006. [Online]. Available: https://www.sciencedirect.com/science/article/pii/S1471084606705704

[3] S. Cebotari, "Romanian electricity market in the light of fast development of renewable energies: General presentation and critical assessment," in *Perspectives of Renewable Energy in the Danube Region*, 03 2015.

[4] S. H. Bandaru, V. Becerra, S. Khanna, J. Radulovic, D. Hutchinson, and R. Khusainov, "A review of photovoltaic thermal (pvt) technology for residential applications: Performance indicators, progress, and opportunities," 7 2021.

[5] Cielo, "Ductless heat pumps: the only in-depth guide you need," 5 2025. [Online]. Available: https://cielowigle.com/blog/ductless-heat-pumps/

[6] L. Kumar, M. Hasanuzzaman, N. A. Rahim, and M. M. Islam, "Modeling, simulation and outdoor experimental performance analysis of a solar-assisted process heating system for industrial process heat," *Renewable Energy*, vol. 164, pp. 656–673, 2 2021. [Online]. Available: https://www.sciencedirect.com/science/article/pii/S0960148120314877

[7] Z. Ul-Abdin, O. Isabella, and R. Santbergen, "Performance evaluation of solar heat systems integrated with seasonal heat storage across varied operating modes for building applications: The case of netherlands," *Solar Energy*, vol. 299, p. 113772, 10 2025. [Online]. Available: https://www.sciencedirect.com/science/article/pii/S0038092X25005353#b11

[8] M. Ramirez, G. Otero-Rodriguez, D. Scheepens, G. V. D. Weijer, and S. Spoelstra, "Development and testing of a steam compression heat pump for low-grade waste heat recovery," *16th IIR Gustav Lorentzen Conference on Natural Refrigerants*, 2024.

[9] M. Bloemendal, M. Jaxa-Rozen, and T. Olsthoorn, "Methods for planning of ates systems," *Applied Energy*, vol. 216, pp. 534–557, 4 2018. [Online]. Available: https://www.sciencedirect.com/science/article/pii/S0306261918301958?via%3Dihub

[10] A. Sevault, J. Soibam, N. E. L. Haugen, and Øyvind Skreiberg, "Thermal energy storage in a stovepipe using phase change material: a numerical study," 8 2018. [Online]. Available: http://www.preprints.org/manuscript/201808.0076/v1

[11] "2030 climate targets." [Online]. Available: https://climate.ec.europa.eu/eu-action/climate-strategies-targets/2030-climate-targets_en#:~:text=In%202023%2C%20the%20EU%20adopted,climate%2Dneutral%20continent%20by%202050.

[12] Eurostat, "Final energy consumption in industry – detailed statistics," https://ec.europa.eu/eurostat/statistics-explained/index.php?title=Final_energy_consumption_in_industry_-_detailed_statistics, 2025, accessed: 2025-12-01.

[13] International Energy Agency, "Clean and efficient heat for industry," https://www.iea.org/commentaries/clean-and-efficient-heat-for-industry, IEA, Paris, 2018.

[14] Eurostat, "Natural gas price statistics," 2025, dataset code: NRG_PC_203. [Online]. Available: https://ec.europa.eu/eurostat/statistics-explained/index.php?title=Natural_gas_price_statistics

[15] European Commission, "REPowerEU: Affordable, secure and sustainable energy for europe," 2022, accessed: 2026-06-14. [Online]. Available: https://commission.europa.eu/topics/energy/repowereu_en

[16] A. Marina, S. Spoelstra, H. A. Zondag, and A. K. Wemmers, "An estimation of the european industrial heat pump market potential," *Renewable and Sustainable Energy Reviews*, vol. 139, p. 110545, 4 2021, potential of heat pumps in EU is discussed. Also some good sources for model possibly on efficiency of heat pump.Also interesting info on waste heat which might be useful to look at. Might be a bit lower than I have seen in other studies.Definitely very useful overview of heat pump viability in different industry sectors. [Online]. Available: https://www.sciencedirect.com/science/article/pii/S1364032120308297

[17] S. Bobbo, G. Lombardo, D. Menegazzo, L. Vallese, and L. Fedele, "A technological update on heat pumps for industrial applications," 10 2024.

[18] L. Kumar, M. Hasanuzzaman, and N. A. Rahim, "Global advancement of solar thermal energy technologies for industrial process heat and its future prospects: A review," *Energy Conversion and Management*, vol. 195, pp. 885–908, 9 2019. [Online]. Available: https://www.sciencedirect.com/science/article/pii/S0196890419306363

[19] J. Goop, M. Odenberger, and F. Johnsson, "The effect of high levels of solar generation on congestion in the european electricity transmission grid," *Applied Energy*, vol. 205, pp. 1128–1140, 2017. [Online]. Available: https://www.sciencedirect.com/science/article/pii/S0306261917311601

[20] International Energy Agency, "Grid congestion is posing challenges for energy security and transitions," https://www.iea.org/commentaries/grid-congestion-is-posing-challenges-for-energy-security-and-transitions, 2025, licence: CC BY 4.0.

[21] L. Sens, U. Neuling, and M. Kaltschmitt, "Capital expenditure and levelized cost of electricity of photovoltaic plants and wind turbines – development by 2050," *Renewable Energy*, vol. 185, pp. 525–537, 2 2022. [Online]. Available: https://www.sciencedirect.com/science/article/pii/S0960148121017626?casa_token=YmuN41Ce3lcAAAAA:HgBcJ2-A9qN9A9g29_J0-W8MxTfBZhuCyfxFKLFMBhejdNvX0L5vCtvAV8C7rn_W1RcLXIKVCdM

[22] S. A. Kalogirou and Y. Tripanagnostopoulos, "Industrial application of pv/t solar energy systems," *Applied Thermal Engineering*, vol. 27, pp. 1259–1270, 6 2007. [Online]. Available: https://www.sciencedirect.com/science/article/pii/S1359431106004029

[23] P. Mayer, M. Heer, D. Y. Shu, N. Zielonka, L. Leenders, F. J. Baader, and A. Bardow, "Flexibility from industrial demand-side management in net-zero sector-coupled national energy systems," *Frontiers in Energy Research*, vol. 12, 2024.

[24] C. Ballif, F. J. Haug, M. Boccard, P. J. Verlinden, and G. Hahn, "Status and perspectives of crystalline silicon photovoltaics in research and industry," pp. 597–616, 8 2022.

[25] A. Mdallal, A. Yasin, M. Mahmoud, M. A. Abdelkareem, A. H. Alami, and A. G. Olabi, "A comprehensive review on solar photovoltaics: Navigating generational shifts, innovations, and sustainability," *Sustainable Horizons*, vol. 13, p. 100137, 3 2025. [Online]. Available: https://www.sciencedirect.com/science/article/pii/S2772737825000070?utm_source=chatgpt.com

[26] V. Benda and L. Cerna, "A note on limits and trends in pv cells and modules," *Applied Sciences*, vol. 12, no. 7, 2022. [Online]. Available: https://www.mdpi.com/2076-3417/12/7/3363

[27] “Silicon heterojunction solar cells: Techno-economic assessment and opportunities,” pp. 514–542, 3 2022.

[28] L. Kumar, J. Ahmed, M. E. H. Assad, and M. Hasanuzzaman, “Prospects and challenges of solar thermal for process heating: A comprehensive review,” 11 2022, different types of PV T, also providing some temperatures they can work with.

[29] Z. Han, K. Liu, G. Li, X. Zhao, and S. Shittu, “Electrical and thermal performance comparison between pvt-st and pv-st systems,” *Energy*, vol. 237, p. 121589, 12 2021. [Online]. Available: https://www.sciencedirect.com/science/article/pii/S0360544221018375

[30] P. Obstawski, T. Bakoń, and D. Czekalski, “Comparison of solar collector testing methods—theory and practice,” *Processes*, vol. 8, pp. 1–29, 11 2020.

[31] TVP Solar, “Technology,” https://www.tvpsolar.com/technology/, 2024, accessed: 31 March 2026.

[32] V. Shemelin and T. Matuška, “Quantitative review on recent developments of flat-plate solar collector design. part 1: Front-side heat loss reduction,” *Energy Reports*, vol. 9, pp. 64–69, 11 2023. [Online]. Available: https://www.sciencedirect.com/science/article/pii/S2352484723013884?utm_source=chatgpt.com

[33] A. Kumar, Z. Said, and E. Bellos, “An up-to-date review on evacuated tube solar collectors,” pp. 2873–2889, 9 2021.

[34] V. Prakash and A. K. Srivastava, “Experimental analysis of an evacuated tube solar collector using different phase change materials,” *Sadhana*, vol. 49, no. 4, 11 2024. [Online]. Available: http://dx.doi.org/10.1007/s12046-024-02644-3

[35] R. Santbergen, C. C. Rindt, H. A. Zondag, and R. J. van Zolingen, “Detailed analysis of the energy yield of systems with covered sheet-and-tube pvt collectors,” *Solar Energy*, vol. 84, pp. 867–878, 5 2010. [Online]. Available: https://www.sciencedirect.com/science/article/pii/S0038092X10001015

[36] Z. U. Abdin and A. Rachid, “A survey on applications of hybrid pv/t panels,” 2 2021.

[37] A. Kumar, P. Baredar, and U. Qureshi, “Historical and recent development of photovoltaic thermal (pvt) technologies,” *Renewable and Sustainable Energy Reviews*, vol. 42, pp. 1428–1436, 2 2015. [Online]. Available: https://www.sciencedirect.com/science/article/pii/S1364032114009757

[38] A. Kazemian, A. Taheri, A. Sardarabadi, T. Ma, M. Passandideh-Fard, and J. Peng, “Energy, exergy and environmental analysis of glazed and unglazed pvt system integrated with phase change material: An experimental approach,” *Solar Energy*, vol. 201, pp. 178–189, 5 2020. [Online]. Available: https://www.sciencedirect.com/science/article/pii/S0038092X20302267?utm_source=chatgpt.com

[39] C. Lamnatou, R. Vaillon, S. Parola, and D. Chemisana, “Photovoltaic/thermal systems based on concentrating and non-concentrating technologies: Working fluids at low, medium and high temperatures,” *Renewable and Sustainable Energy Reviews*, vol. 137, p. 110625, 3 2021. [Online]. Available: https://www.sciencedirect.com/science/article/pii/S1364032120309096

[40] M. Lämmle, A. Oliva, M. Hermann, K. Kramer, and W. Kramer, “Pvt collector technologies in solar thermal systems: A systematic assessment of electrical and thermal yields with the novel characteristic temperature approach,” *Solar Energy*, vol. 155, pp. 867–879, 10 2017. [Online]. Available: https://www.sciencedirect.com/science/article/pii/S0038092X17305881

[41] M. K. Sharma and J. Bhattacharya, “Deciding between concentrated and non-concentrated photovoltaic systems via direct comparison of experiment with opto-thermal computation,” *Renewable Energy*, vol. 178, pp. 1084–1096, 11 2021. [Online]. Available: https://www.sciencedirect.com/science/article/pii/S0960148121009940

[42] W. B. Mol, W. H. Knap, and C. C. van Heerwaarden, "Ten years of 1 hz solar irradiance observations at cabauw, the netherlands, with cloud observations, variability classifications, and statistics," *Earth System Science Data*, vol. 15, no. 5, pp. 2139–2151, 2023. [Online]. Available: https://essd.copernicus.org/articles/15/2139/2023/

[43] H. Willem, Y. Lin, and A. Lekov, "Review of energy efficiency and system performance of residential heat pump water heaters," *Energy and Buildings*, vol. 143, pp. 191–201, 5 2017. [Online]. Available: https://www.sciencedirect.com/science/article/pii/S0378778817304760

[44] M. Sadeghi, T. Petersen, Z. Yang, B. Zühlsdorf, and K. S. Madsen, "Thermal and economic performance assessment of different high temperature heat pump layouts for upgrading district heating to process heating of steam production at 160°c," *Energy*, vol. 313, p. 133832, 12 2024. [Online]. Available: https://www.sciencedirect.com/science/article/pii/S0360544224036107

[45] C. Höges, L. Wissing, C. Vering, and D. Müller, "Choosing the optimal refrigerant in heat pumps: Influence of the ecologic evaluation method," *Applied Thermal Engineering*, vol. 263, p. 125313, 3 2025. [Online]. Available: https://www.sciencedirect.com/science/article/pii/S1359431124029818?utm_source=chatgpt.com

[46] K. Hamid, U. Sajjad, M. U. Ahrens, S. Ren, P. Ganesan, I. Tolstorebrov, A. Arshad, Z. Said, A. Hafner, C. C. Wang, R. Wang, and T. M. Eikevik, "Potential evaluation of integrated high temperature heat pumps: A review of recent advances," *Applied Thermal Engineering*, vol. 230, p. 120720, 7 2023. [Online]. Available: https://www.sciencedirect.com/science/article/pii/S1359431123007494

[47] C. Arpagaus, F. Bless, M. Uhlmann, J. Schiffmann, and S. S. Bertsch, "High temperature heat pumps: Market overview, state of the art, research status, refrigerants, and application potentials," *Energy*, vol. 152, pp. 985–1010, 6 2018. [Online]. Available: https://www.sciencedirect.com/science/article/pii/S0360544218305759

[48] D. Bogdanov, R. Satymov, and C. Breyer, "Impact of temperature dependent coefficient of performance of heat pumps on heating systems in national and regional energy systems modelling," *Applied Energy*, vol. 371, p. 123647, 10 2024. [Online]. Available: https://www.sciencedirect.com/science/article/pii/S0306261924010304

[49] P. Diaz, "Analysis and comparison of different types of thermal energy storage systems: A review," *Journal of Advances in Mechanical Engineering and Science*, vol. 2, pp. 33–46, 2 2016. [Online]. Available: http://access.portico.org/stable?au=phx7d5q8wm0

[50] H. Kauko, A. Sevault, S. Vasta, H. Zondag, A. Beck, G. Drexler-Schmid, N. R. García Polanco, Z. Ma, and T. Roskilly, "Industrial thermal energy storage: Supporting the transition to decarbonise industry," European Energy Research Alliance (EERA), Joint Programme Energy Efficiency in Industrial Processes, White Paper, 2022. [Online]. Available: https://www.eera-set.eu/

[51] T. Yang, W. Liu, G. J. Kramer, and Q. Sun, "Seasonal thermal energy storage: A techno-economic literature review," *Renewable and Sustainable Energy Reviews*, vol. 139, p. 110732, 4 2021, extensive overview different TES technologies. Also looking at costs and pheasability. [Online]. Available: https://www.sciencedirect.com/science/article/pii/S1364032121000290

[52] S. Beernink, N. Hartog, P. J. Vardon, and M. Bloemendal, "Heat losses in ates systems: The impact of processes, storage geometry and temperature," *Geothermics*, vol. 117, p. 102889, 2 2024. [Online]. Available: https://www.sciencedirect.com/science/article/pii/S0375650523002444

[53] M. Bloemendal and N. Hartog, "Analysis of the impact of storage conditions on the thermal recovery efficiency of low-temperature ates systems," *Geothermics*, vol. 71, pp. 306–319, 1 2018. [Online]. Available: https://www.sciencedirect.com/science/article/pii/S0375650517302067?via%3Dihub

[54] P. Vardon, M. van der Schans, A. Koulidis, T. Grubben, S. Beernink, and M. Bloemendal, “High-temperature aquifer thermal energy storage (HT-ATES) system for research development and demonstration on the TU Delft campus,” in *EGU General Assembly 2024*, Vienna, Austria, Apr. 2024, eGU24-14989. [Online]. Available: https://doi.org/10.5194/egusphere-egu24-14989

[55] H. A. Sheldon, A. Wilkins, and C. P. Green, “Recovery efficiency in high-temperature aquifer thermal energy storage systems,” *Geothermics*, vol. 96, p. 102173, 11 2021, on the thermal recovery efficiency of high-temperature (90 - 300 C) ATES systems. Conlusion is that from a thermal recovery perspective very high temperature ATES systems can be viable. Although the thermal recovery efficiency will vary for annual ATES use. Mainly depending on the horizontal hydraulic conductivity which can’t be too high. [Online]. Available: https://www.sciencedirect.com/science/article/pii/S0375650521001334

[56] D. Geerts, A. Daniilidis, G. J. Kramer, M. Bloemendal, and W. Liu, “Analytically estimating the efficiency of high temperature aquifer thermal energy storage,” *Geothermal Energy*, vol. 13, 12 2025, might be useful when looking modelling efficiency of ATES system in different regions in the word. Includes formulas and experimental data.

[57] P. Fleuchaus, S. Schüppler, M. Bloemendal, L. Guglielmetti, O. Opel, and P. Blum, “Risk analysis of high-temperature aquifer thermal energy storage (ht-ates),” *Renewable and Sustainable Energy Reviews*, vol. 133, p. 110153, 11 2020, hT-ATES potential risk factorsAlso HT-ATES systems above 100 degrees celcius. [Online]. Available: https://www.sciencedirect.com/science/article/pii/S1364032120304445

[58] I. Sarbu and A. Dorca, “Review on heat transfer analysis in thermal energy storage using latent heat storage systems and phase change materials,” pp. 29–64, 1 2019.

[59] Y. I. Baeuerle, C. Arpagaus, and M. Y. Haller, “A review of seasonal energy storage for net-zero industrial heat: Thermal and power-to-x storage including the novel concept of renewable metal energy carriers,” 5 2025, review of different TES technologies. HT-ATES limitations are charing and discharging rates and face regulatory problems because of the high temperatures which are put into the ground. Can be done above 100 C but might have limitations.

[60] M. Herrmann, P. Fleuchaus, B. Godschalk, M. Verbiest, S. N. Sørensen, and P. Blum, “Capital costs of aquifer thermal energy storage (ates): a review,” *Renewable and Sustainable Energy Reviews*, vol. 226, p. 116202, 1 2026. [Online]. Available: https://www.sciencedirect.com/science/article/pii/S1364032125008755

[61] T. Beijneveld, J. Alpízar-Castillo, and L. Ramírez-Elizondo, “Photovoltaic thermal system design including aquifer thermal energy storage in a fifth generation district heating network in hilversum,” *Case Studies in Thermal Engineering*, vol. 68, 4 2025, this is the research paper that has been made with the thesis of Ties beijneveld.

[62] X. Xu, T. Ma, X. Feng, S. Weng, S. Li, and J. Peng, “Simulation and optimal configuration of a combined photovoltaic-thermal and heat pump system with a hybrid energy storage,” *Energy Conversion and Management*, vol. 317, p. 118851, 10 2024. [Online]. Available: https://www.sciencedirect.com/science/article/pii/S0196890424007921

[63] K. Kubiński and Łukasz Szabłowski, “Dynamic model of solar heating plant with seasonal thermal energy storage,” *Renewable Energy*, vol. 145, pp. 2025–2033, 1 2020. [Online]. Available: https://www.sciencedirect.com/science/article/pii/S0960148119311401

[64] K. Thinsurat, H. Bao, Z. Ma, and A. P. Roskilly, “Performance study of solar photovoltaic-thermal collector for domestic hot water use and thermochemical sorption seasonal storage,” *Energy Conversion and Management*, vol. 180, pp. 1068–1084, 1 2019. [Online]. Available: https://www.sciencedirect.com/science/article/pii/S0196890418312998

[65] N. Bianco, A. Fragnito, M. Iasiello, and G. M. Mauro, “Multiscale analysis of a seasonal latent thermal energy storage with solar collectors for a single-family building,” *Thermal Science and Engineering Progress*, vol. 50, p. 102538, 5 2024. [Online]. Available: https://www.sciencedirect.com/science/article/pii/S2451904924001562

[66] P. Kumar, K. K. Sinha, B. Đurin, M. K. Gupta, N. Saxena, M. K. Banerjee, N. Kranjčić, S. K. Singh, and S. Kanga, "Economics of implementing solar thermal heating systems in the textile industry," *Energies*, vol. 15, 6 2022.

[67] R. Silva, M. Pérez, and A. Fernández-Garcia, "Modeling and co-simulation of a parabolic trough solar plant for industrial process heat," *Applied Energy*, vol. 106, pp. 287–300, 6 2013. [Online]. Available: https://www.sciencedirect.com/science/article/pii/S0306261913000809

[68] O. M. B. Mousa and R. A. Taylor, "A broad comparison of solar photovoltaic and thermal technologies for industrial heating applications," *Journal of Solar Energy Engineering, Transactions of the ASME*, vol. 141, 2 2019.

[69] O. B. Mousa, R. A. Taylor, and A. Shirazi, "Multi-objective optimization of solar photovoltaic and solar thermal collectors for industrial rooftop applications," *Energy Conversion and Management*, vol. 195, pp. 392–408, 9 2019. [Online]. Available: https://www.sciencedirect.com/science/article/pii/S019689041930559X

[70] A. Allouhi, Y. Agrouaz, M. Benzakour Amine, S. Rehman, M. Buker, T. Kousksou, A. Jamil, and A. Benbassou, "Design optimization of a multi-temperature solar thermal heating system for an industrial process," *Applied Energy*, vol. 206, pp. 382–392, 11 2017. [Online]. Available: https://www.sciencedirect.com/science/article/pii/S0306261917312217

[71] W. Gruber-Glatzl, P. Nitz, J. Pfleger, R. Baumann, W. Braumann, S. Moser, P. Kurup, V. Rodin, G. Muja, and F. Pag, "Update on SHIP technology costs and SHIP business and financing models," IEA Solar Heating and Cooling Technology Collaboration Programme, Task Report D.E2 and D.E3, Jun. 2024, IEA SHC Task 64 / IEA SolarPACES Task IV: Solar Process Heat, Subtask E: Guideline to Market. [Online]. Available: https://task64.iea-shc.org/Data/Sites/1/publications/IEA-SHC-Task64-SubtaskE-D.E2-D.E3.pdf

[72] European Solar Thermal Technology Panel (ESTTP) and European Technology and Innovation Platform on Renewable Heating & Cooling (RHC-ETIP), "Strategic research & innovation agenda for solar thermal technologies," European Technology and Innovation Platform on Renewable Heating & Cooling (RHC-ETIP), Brussels, Belgium, Tech. Rep., May 2022. [Online]. Available: https://www.rhc-platform.org/content/uploads/2022/07/RHC_Strategic_Agenda_single_pages_final.pdf

[73] Solar Heat Europe, "Solar heat integration: Solutions for the decarbonisation of the pulp and paper industry," 2024, factsheet.

[74] J. Jiang, L. Liu, J. Song, B. Hu, Y. Bi, S. Jiang, Y. Dai, and R. Wang, "Solar-assisted high-temperature heat pumps to achieve off-grid zero-carbon heating in industrial parks," *Renewable and Sustainable Energy Reviews*, vol. 226, p. 116412, 1 2026. [Online]. Available: https://www.sciencedirect.com/science/article/pii/S1364032125010858

[75] G. ram Lee, B. J. Lim, S. H. Cho, M. Farooq, H. Tanaka, and C. D. Park, "Performance and economic analysis of solar-heat pump system for process steam supply in industrial sector," *Energy Conversion and Management*, vol. 328, p. 119596, 3 2025. [Online]. Available: https://www.sciencedirect.com/science/article/pii/S0196890425001190

[76] G. Martínez-Rodríguez, J. C. Baltazar, and A. L. Fuentes-Silva, "Heat and electric power production using heat pumps assisted with solar thermal energy for industrial applications," *Energy*, vol. 282, p. 128379, 11 2023. [Online]. Available: https://www.sciencedirect.com/science/article/pii/S0360544223017735

[77] J. Hirvonen, H. ur Rehman, and K. Sirén, "Techno-economic optimization and analysis of a high latitude solar district heating system with seasonal storage, considering different community sizes," *Solar Energy*, vol. 162, pp. 472–488, 3 2018. [Online]. Available: https://www.sciencedirect.com/science/article/pii/S0038092X18300732

[78] M. R. Vogt, C. R. Tobon, A. Alcañiz, P. Procel, Y. Blom, A. N. E. Din, T. Stark, Z. Wang, E. G. Goma, J. G. Etxebarria, H. Ziar, M. Zeman, R. Santbergen, and O. Isabella, "Introducing a comprehensive physics-based modelling framework for tandem and other pv systems," *Solar Energy Materials and Solar Cells*, vol. 247, p. 111944, 10 2022. [Online]. Available: https://www.sciencedirect.com/science/article/pii/S0927024822003622?via%3Dihub

[79] Z. Ul-Abdin, M. Zeman, O. Isabella, and R. Santbergen, "Investigating the annual performance of air-based collectors and novel bi-fluid based pv-thermal system," *Solar Energy*, vol. 276, p. 112687, 7 2024. [Online]. Available: https://www.sciencedirect.com/science/article/pii/S0038092X24003827?via%3Dihub

[80] A. van Rossum, "Developing and implementing toolbox integrations for storing excess heat generated by a PVT system," Master's Thesis, Delft University of Technology, Delft, The Netherlands, February 2024, faculty of Electrical Engineering, Mathematics and Computer Science. [Online]. Available: https://resolver.tudelft.nl/uuid:b4066b14-7087-4ab7-8628-e7a2af4a2b83

[81] D. N. Kanawala, "Optimization of heating and cooling systems consisting of pvt collectors, seasonal storage and heat pumps," Master's Thesis, Delft University of Technology, Delft, The Netherlands, August 2024, faculty of Electrical Engineering, Mathematics and Computer Science.

[82] D. E. M. Aguilera, "Integration and optimization of a solar collector heat pump system model for households in the netherlands," Master's Thesis, Delft University of Technology, Delft, The Netherlands, July 2024, faculty of Electrical Engineering, Mathematics and Computer Science. [Online]. Available: https://repository.tudelft.nl/record/uuid:d1cb5f99-7fff-45a3-92a9-14f29540ec76

[83] J. Remund, S. Müller, M. Schmutz, and P. Graf, "Meteonorm version 8, meteotest. 2020, www," *Meteotest, Com*, 2020.

[84] V. Sun, A. Asanakham, T. Deethayat, and T. Kiatsiriroat, "Evaluation of nominal operating cell temperature (noct) of glazed photovoltaic thermal module," *Case Studies in Thermal Engineering*, vol. 28, p. 101361, 12 2021. [Online]. Available: https://doi.org/10.1080/01430750.2018.1443500

[85] I. H. Bell, J. Wronski, S. Quoilin, and V. Lemort, "Pure and pseudo-pure fluid thermophysical property evaluation and the open-source thermophysical property library coolprop," *Industrial & Engineering Chemistry Research*, vol. 53, no. 6, pp. 2498–2508, 2014. [Online]. Available: http://pubs.acs.org/doi/abs/10.1021/ie4033999

[86] S. K. Gupta, H. Verma, and N. Yadav, "A review on recent development of nanofluid utilization in shell and tube heat exchanger for saving of energy," *Materials Today: Proceedings*, vol. 54, pp. 579–589, 1 2022. [Online]. Available: https://www.sciencedirect.com/science/article/pii/S2214785321063719

[87] G. P. Towler and R. K. Sinnott, *Chemical engineering design : principles, practice and economics of plant and process design.* Butterworth-Heinemann is an imprint of Elsevier, 2022.

[88] Engineering ToolBox, "Heat exchangers overall heat transfer coefficients," https://www.engineeringtoolbox.com/heat-transfer-coefficients-exchangers-d_450.html, 2003, accessed: 23-04-2026.

[89] G. Schout, B. Drijver, M. Gutierrez-Neri, and R. Schotting, "Analysis of recovery efficiency in high-temperature aquifer thermal energy storage: A rayleigh-based method," *Hydrogeology Journal*, vol. 22, pp. 281–291, 2014.

[90] M. Bakker and B. Bot, "The effective vertical anisotropy of layered aquifers," *Groundwater*, vol. 63, pp. 68–75, 1 2025.

[91] G. J. Houben, "Revue: Hydraulique des puits—pertes de charge des différents composants," *Hydrogeology Journal*, vol. 23, pp. 1659–1675, 12 2015.

[92] C. Tong, *Advanced Materials Enable Renewable Geothermal Energy Capture and Generation*. Cham: Springer International Publishing, 2019, pp. 321–377. [Online]. Available: https://doi.org/10.1007/978-3-319-98002-7_5

[93] M. Osei-Boateng, L. Li, M. Minnick, H. Zhou, and Z. Ye, "Impact of borehole connections on thermal recovery and economic performance in borehole thermal energy storage systems," *Mathematical Geosciences*, 3 2026. [Online]. Available: https://link.springer.com/10.1007/s11004-026-10272-2

[94] K. Mongird, V. Viswanathan, J. Alam, C. Vartanian, V. Sprenkle, and R. Baxter, "2020 grid energy storage technology cost and performance assessment," *Energy*, 2020. [Online]. Available: https://www.pnnl.gov/main/publications/external/technical_reports/PNNL-28866.pdf

[95] S. D. Peeyush Phogat and M. Wan, "Powering the sustainable future: a review of emerging battery technologies and their environmental impact," pp. 3266–3306, 7 2025.

[96] S. Brückner, S. Liu, L. Miró, M. Radspieler, L. F. Cabeza, and E. Lävemann, "Industrial waste heat recovery technologies: An economic analysis of heat transformation technologies," *Applied Energy*, vol. 151, pp. 157–167, 8 2015. [Online]. Available: https://www.sciencedirect.com/science/article/pii/S0306261915004584

[97] CBS (Statistics Netherlands), "Energy consumption private dwellings; type of dwelling and regions," 2024, statLine database, accessed June 2026. [Online]. Available: https://www.cbs.nl/en-gb/figures/detail/81528ENG

[98] C. Wu, Y. Zhou, W. Gan, and J. Wu, "Robust scheduling of a pulp and paper mill considering flexibility provision from steam power generation," *Applied Energy*, vol. 377, p. 124595, 1 2025. [Online]. Available: https://doi.org/10.1049/enc2.12059

[99] C. Bedocchi and G. Cassetti, "Electrification of industrial heat: The key to a sustainable and competitive industry report march 2025," 2025.

[100] S. Attri and G. Goel, "Sterilization in bioprocesses," *Basic Biotechniques for Bioprocess and Bioentrepreneurship*, vol. 229, pp. 329–339, 1 2023. [Online]. Available: https://doi.org/10.1177/1755738020964525

[101] A. Karim, A. Rehman, Z. Lianfu, A. Noreen, S. Ahmad, M. Usman, and S. M. Jafari, "Introduction to thermal food processes by steam and hot water," *Thermal Processing of Food Products by Steam and Hot Water: Unit Operations and Processing Equipment in the Food Industry*, pp. 3–26, 1 2023. [Online]. Available: https://doi.org/10.1007/0-387-31129-7_1

[102] S. Pfenninger and I. Staffell, "Long-term patterns of european pv output using 30 years of validated hourly reanalysis and satellite data," *Energy*, vol. 114, pp. 1251–1265, 2016.

[103] I. Staffell and S. Pfenninger, "Using bias-corrected reanalysis to simulate current and future wind power output," *Energy*, vol. 114, pp. 1224–1239, 2016.

[104] U. Pfeifroth, S. Kothe, J. Drücke, J. Trentmann, M. Schröder, N. Selbach, and R. Hollmann, "Surface radiation data set - heliosat (sarah) - edition 3," 2023. [Online]. Available: https://wui.cmsaf.eu/safira/action/viewDoiDetails?acronym=SARAH_V003

[105] U. Pfeifroth, J. Drücke, S. Kothe, J. Trentmann, M. Schröder, and R. Hollmann, "Sarah-3 – satellite-based climate data records of surface solar radiation," *Earth System Science Data*, vol. 16, no. 11, pp. 5243–5265, 2024. [Online]. Available: https://essd.copernicus.org/articles/16/5243/2024/

[106] B. Babar, R. Graversen, and T. Boström, "Solar radiation estimation at high latitudes: Assessment of the cmsaf databases, asr and era5," *Solar Energy*, vol. 182, pp. 397–411, 4 2019. [Online]. Available: https://www.sciencedirect.com/science/article/pii/S0038092X19301847

[107] Y. Wang, J. Trentmann, W. Yuan, and M. Wild, "Validation of cm saf clara-a2 and sarah-e surface solar radiation datasets over china," *Remote Sensing*, vol. 10, no. 12, 2018. [Online]. Available: https://www.mdpi.com/2072-4292/10/12/1977

[108] L. Sander, C. Jung, A. Matzarakis, and D. Schindler, "Global assessment of availability, reliability, and spatiotemporal variability in ground-based solar radiation measurements," *Solar Energy*, vol. 309, p. 114458, 2 2026. [Online]. Available: https://www.sciencedirect.com/science/article/pii/S0038092X26001465

[109] Solargis, "Solar resource maps of Europe," 2021, accessed: 20-04-2026. [Online]. Available: https://solargis.com/resources/free-maps-and-gis-data?locality=europe

[110] ——, "Solargis solar resource database: Validation of satellite-based solar radiation model," Solargis, Tech. Rep. 170-18/2024, 2024. [Online]. Available: https://solargis2-web-v2-assets.s3.eu-west-1.amazonaws.com/public/doc/Solargis_Solar-Model-Validation-2024-09.pdf

[111] E. Bellos and C. Tzivanidis, "A detailed investigation of an evacuated flat plate solar collector," *Applied Thermal Engineering*, vol. 234, p. 121334, 11 2023. [Online]. Available: https://www.sciencedirect.com/science/article/pii/S1359431123013637

[112] A. Duret, X. Jobard, S. Pauletta, and G. Demonchy, "Performance monitoring of an 800m2 solar thermal plant with evacuated flat plate collectors coupled to a dhn," in *Eurosun2022*. International Solar Energy Society (ISES), 1 2024, pp. 1–10.

[113] D. Gao, G. Gao, J. Cao, S. Zhong, X. Ren, Y. N. Dabwan, M. Hu, D. Jiao, T. H. Kwan, and G. Pei, "Experimental and numerical analysis of an efficiently optimized evacuated flat plate solar collector under medium temperature," *Applied Energy*, vol. 269, p. 115129, 7 2020. [Online]. Available: https://www.sciencedirect.com/science/article/pii/S0306261920306413

[114] D. D. Luca, P. Strazzullo, E. D. Gennaro, A. Caldarelli, E. Gaudino, M. Musto, and R. Russo, "High vacuum flat plate photovoltaic-thermal (hv pv-t) collectors: Efficiency analysis," *Applied Energy*, vol. 352, p. 121895, 12 2023. [Online]. Available: https://www.sciencedirect.com/science/article/pii/S030626192301259X

[115] P. Saini, M. Ghasemi, C. Arpagaus, F. Bless, S. Bertsch, and X. Zhang, "Techno-economic comparative analysis of solar thermal collectors and high-temperature heat pumps for industrial steam generation," *Energy Conversion and Management*, vol. 277, p. 116623, 2 2023. [Online]. Available: https://www.sciencedirect.com/science/article/pii/S0196890422014017

[116] S. Meyers, B. Schmitt, and K. Vajen, "Techno-economic comparison of solar thermal and PV for heat generation in industrial processes," in *Proceedings of the ISES Solar World Congress*, 2015. [Online]. Available: https://proceedings.ises.org/conference/swc2015/papers/swc2015-0134-Meyers.pdf

[117] D. C. Jordan, S. R. Kurtz, K. VanSant, and J. Newmiller, "Compendium of photovoltaic degradation rates," *Progress in Photovoltaics: Research and Applications*, vol. 24, no. 7, pp. 978–989, 2016.

[118] A. Behzadi, A. Arabkoohsar, M. Sadi, and K. H. Chakravarty, "A novel hybrid solar-biomass design for green off-grid cold production, techno-economic analysis and optimization," *Solar Energy*, vol. 218, pp. 639–651, 4 2021. [Online]. Available: https://www.sciencedirect.com/science/article/pii/S0038092X21001791

[119] Fraunhofer ISE, "Photovoltaics report," Fraunhofer Institute for Solar Energy Systems ISE, Tech. Rep., 2024. [Online]. Available: https://www.ise.fraunhofer.de/content/dam/ise/de/documents/publications/studies/Photovoltaics-Report.pdf

[120] F. Schlosser, M. Jesper, J. Vogelsang, T. G. Walmsley, C. Arpagaus, and J. Hesselbach, "Large-scale heat pumps: Applications, performance, economic feasibility and industrial integration," *Renewable and Sustainable Energy Reviews*, vol. 133, p. 110219, 11 2020. [Online]. Available: https://www.sciencedirect.com/science/article/pii/S1364032120305086

[121] IRENA, "Innovation outlook: Thermal energy storage," International Renewable Energy Agency, Abu Dhabi, United Arab Emirates, Tech. Rep., 2020. [Online]. Available: https://www.irena.org/-/media/Files/IRENA/Agency/Publication/2020/Nov/IRENA_Innovation_Outlook_TES_2020.pdf

[122] ——, "Renewable power generation costs in 2024," International Renewable Energy Agency, Abu Dhabi, United Arab Emirates, Tech. Rep., 2025. [Online]. Available: https://www.irena.org/-/media/Files/IRENA/Agency/Publication/2025/Jul/IRENA_TEC_RPGC_in_2024_Summary_2025.pdf

[123] Eurostat, "Electricity prices for non-household consumers – bi-annual data (from 2007 onwards)," 2024, dataset code: NRG_PC_205. [Online]. Available: https://ec.europa.eu/eurostat/databrowser/view/nrg_pc_205/default/table?lang=en

[124] L. D. Tommasi, H. Ridouane, G. Giannakis, K. Katsigarakis, G. N. Lilis, and D. Rovas, "Model-based comparative evaluation of building and district control-oriented energy retrofit scenarios," *Buildings*, vol. 8, no. 7, 2018. [Online]. Available: https://www.mdpi.com/2075-5309/8/7/91

[125] E. K. Vakkilainen, "Boiler processes," *Steam Generation from Biomass*, pp. 57–86, 2017.

[126] P. Balcombe, N. P. Brandon, and A. D. Hawkes, "Characterising the distribution of methane and carbon dioxide emissions from the natural gas supply chain," *Journal of Cleaner Production*, vol. 172, pp. 2019–2032, 1 2018. [Online]. Available: https://www.sciencedirect.com/science/article/pii/S0959652617328962

[127] European Commission, Directorate-General for Economic and Financial Affairs, "Trends in carbon intensity and the macroeconomic role of the EU emissions trading system," European Commission, Special Issue, November 2025. [Online]. Available: https://economy-finance.ec.europa.eu/trends-carbon-intensity-and-macroeconomic-role-eu-emissions-trading-system_en

[128] B. Steffen, "Estimating the cost of capital for renewable energy projects," *Energy Economics*, vol. 88, p. 104783, 5 2020. [Online]. Available: https://www.sciencedirect.com/science/article/pii/S0140988320301237

[129] E. Tumilowicz, C. L. Chan, P. Li, and B. Xu, "An enthalpy formulation for thermocline with encapsulated pcm thermal storage and benchmark solution using the method of characteristics," *International Journal of Heat and Mass Transfer*, vol. 79, pp. 362–377, 12 2014. [Online]. Available: https://doi.org/10.1115/1.2905942

[130] V. R. Voller and C. Prakash, "A fixed grid numerical modelling methodology for convection-diffusion mushy region phase-change problems," *International Journal of Heat and Mass Transfer*, vol. 30, pp. 1709–1719, 8 1987. [Online]. Available: https://doi.org/10.1115/1.3246636

[131] P. Jančík, M. Schmirler, T. Hyhlík, A. Bláha, P. Sláma, J. Devera, and J. Kouba, "Experimental investigation and modelling of a laboratory-scale latent heat storage with cylindrical pcm capsules," *Scientific Reports*, vol. 11, 12 2021.

[132] Y. F. Kening Yan, Lin Qiu, "Erythritol/expanded graphite form-stable phase change materials with excellent thermophysical properties," *Journal of Energy Storage*, vol. 68, p. 107667, 9 2023. [Online]. Available: https://doi.org/10.1016/j.energy.2021.122191

[133] F. P. Incropera, D. P. DeWitt, T. L. Bergman, and A. S. Lavine, *Fundamentals of Heat and Mass Transfer*, 6th ed. John Wiley & Sons, 2007.

[134] Hexonic, *Industrial Heat Exchangers TEMA: Custom Solutions*, Hexonic, Poland, 2023, product brochure, version EN.ver.1.2022. [Online]. Available: https://sugein.com/sec_din/archivos/docs/1707905389HEXONIC_CUSTOM_EN_CMYK_2023-05-24.pdf

[135] V. Madan and I. Weidlich, "Investigation on relative heat losses and gains of heating and cooling networks," *Environmental and Climate Technologies*, vol. 25, no. 1, pp. 479–490, 2021. [Online]. Available: https://doi.org/10.2478/rtuect-2021-0035

Chapter A

Chapter 2

A.1. Phase change material storage

This Appendix presents the modeling approach as well the simulation results for a configuration in which the water tank buffer storage is replaced by a phase change material PCM buffer storage. The phase change material(PCM) buffer storage is modeled using a lumped enthalpy method that tracks the specific enthalpy of the buffer tank. The corresponding temperature of the buffer tank is determined through Equation A.1 [129], comprising three regimes: a fully solid zone, a mushy zone, and a fully liquid zone. Following the standard three-zone enthalpy method commonly employed in PCM modeling [130]. The mushy zone can be seen as a latent heat plateau in which temperature stays the same but the fraction of liquid to solid changes. The fully solid and liquid regions represent sensible heat changes. The buffer storage is modeled using a lumped heat storage model instead of a spatially resolved model, providing an accurate representation while computational complexity is significantly reduced [131]. The enthalpy is updated at each timestep according to the net heat flux from the ST/PVT collectors and the industrial heat demand.

$$T_{\text{buffer}} = \begin{cases} \dfrac{h}{C_{p,\text{solid}}} & \text{if } h < C_{p,\text{solid}} T_{\text{melt}} \quad \text{(fully solid)} \\ T_{\text{melt}} & \text{if } C_{p,\text{solid}} T_{\text{melt}} \leq h \leq C_{p,\text{solid}} T_{\text{melt}} + L_{pcm} \quad \text{(mushy zone)}, \\ \dfrac{h - L_{pcm} - C_{p,\text{solid}} T_{\text{melt}}}{C_{p,\text{liquid}}} + T_{\text{melt}} & \text{if } h > C_{p,\text{solid}} T_{\text{melt}} + L_{pcm} \quad \text{(fully liquid)} \end{cases} \tag{A.1}$$

where T_{buffer} is the temperature of the buffer storage and T_{melt} is the melting temperature of the PCM. The enthalpy of the system is denoted by h. The specific heat capacity is divided according to the thermodynamic phase of the material in $C_{p,\text{solid}}$ and $C_{p,\text{liquid}}$. Lastly, L_{pcm} represents the latent heat of fusion of the PCM.

The PCM storage in this thesis is based upon Erythritol, a sugar alcohol with advantageous properties for medium temperature thermal energy storage. It has a melting temperature of 117 °C and a high latent heat of fusion, making it ideal for the application in this thesis. The properties of Erythritol are presented in table A.1 and are taken from Sevault et al. [10]. The supercooling behavior of erythritol is detrimental to PCM heat storage performance, as it prevents heat recovery at the charging temperature of the thermal buffer [132]. To simplify the modeling approach, supercooling effects are not considered. Consequently, the actual thermal recovery performance of an Erythritol-based system may be lower than the values presented in this thesis.

Table A.1. Parameters for phase change material heat storage [10]

Parameter	Erythritol based PCM
Melting temperature (°C)	117
Latent heat of fusion L_{pcm} $(kJkg^{-1})$	340
Specific heat capacity solid $C_{p,\text{solid}}$ $(kJkg^{-1}K^{-1})$	1.38
Specific heat capacity liquid $C_{p,\text{liquid}}$ $(kJkg^{-1}K^{-1})$	2.76
Density Solid (kgm^{-3})	1480
Density fluid (kgm^{-3})	1300

A.1.1. Simulation results

This section analyses the system performance when PCM storage replaces the water tank buffer employed in the default configurations. The initial PCM storage was designed for a phase change temperature of 117 °C, since this yields a high COP. However, high buffer temperatures negatively affect the ST collector efficiency. For this reason, a phase change temperature of 83 °C is also considered.

For this comparison, the total thermal capacities of the two storage types are kept equal. The PCM buffer has a volumetric thermal capacity of 5.2e8 J/m^3, which is 3.1 times higher than that of the water tank buffer at 1.68e8 J/m^3. Consequently, the PCM buffer volume is smaller than that of the water tank, at 3 200 m^3 and 10 000 m^3 respectively.

Figure A.1 illustrates that no single buffer storage type consistently outperforms the others across all scenarios. In the Delft Food & Beverage scenario, the 83 °C PCM buffer achieves a slightly lower total electricity demand than the water tank, while the 117 °C PCM buffer has the highest consumption. In the Delft Paper & Pulp scenario, the water tank and 117°C PCM buffer perform comparably, with the 83°C PCM buffer showing the highest consumption. The Seville results differ from both Delft scenarios, with the 117 °C PCM buffer achieving the lowest consumption. These differences are further discussed in the detailed simulation highlights of the system in Section A.1.2.

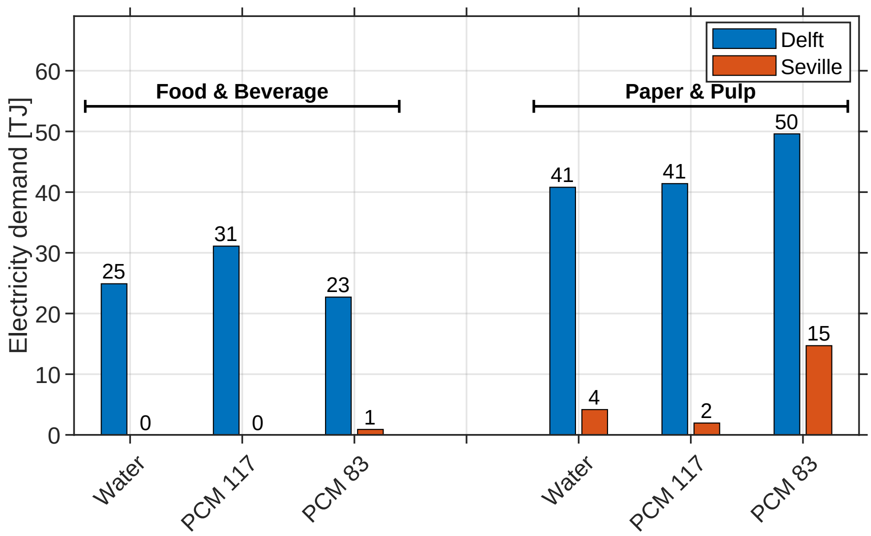

Figure A.1. Annual grid electricity consumption for water tank and PCM thermal buffer storage technologies.

Figure A.2 presents the peak grid consumption for the different buffer storage options. These results similarly show no consistently superior option across all scenarios. In the Delft Food & Beverage scenario, the water tank and 83 °C PCM buffer achieve equal peak loads, while the 117 °C PCM buffer has a significantly higher peak load. In the Seville Food & Beverage scenario, both the water tank and 117 °C PCM buffer achieve full grid independence, whereas the 83 °C PCM buffer has a high peak load. This high peak load can be attributed to only a small number of hours throughout the year, as reflected by the low total grid consumption of this scenario. The remaining scenarios show broadly similar performance across all three buffer technologies. The ambiguous results are a consequence of the complex influence of buffer storage temperature on system performance, acting through both the COP and the reduced temperature of the ST collectors.

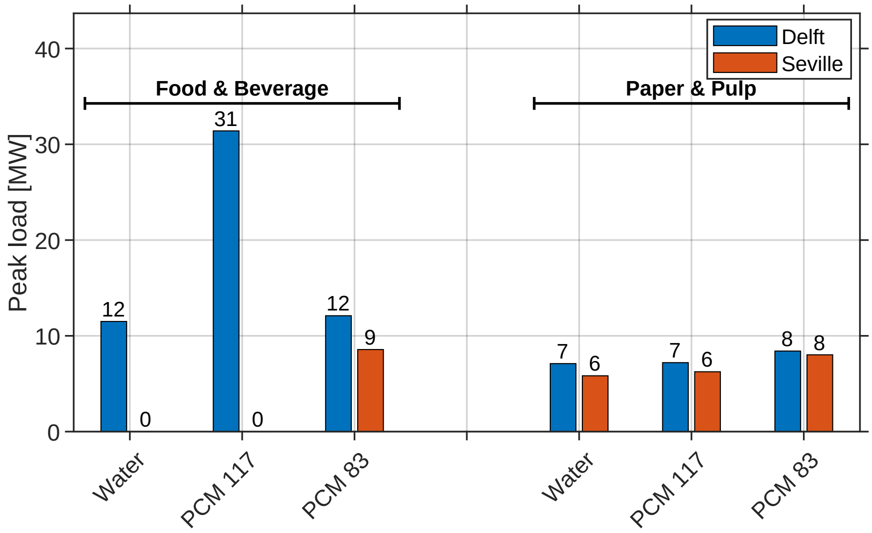

Figure A.2. Annual peak grid electricity consumption for water tank and PCM thermal buffer storage technologies.

A.1.2. Detailed simulation results

This section presents the results of the different PCM buffer storage options highlighting key operational differences. These differences mainly come down to the 83 °C PCM buffer yielding higher thermal energy generation and the 117 °C PCM buffer operating at a higher COP.

Food & Beverage Delft PCM

The storage temperatures of a system with the 83 °C and the 117 °C PCM material are presented in Figures A.3 and A.4 respectively. A clear difference in average operating temperature is evident between the two systems. The 83 °C system maintains a considerably lower buffer storage temperature, which results in a net annual heat surplus in the ATES, with the warm well temperature reaching approximately 110 °C by the end of the year. In contrast, the 117 °C system exhibits the opposite behavior. In this scenario, the warm well temperature declines to the minimum permissible limit of 90 °C, resulting in 237 hours of Mode IIIB (backup resistive heater) activation.

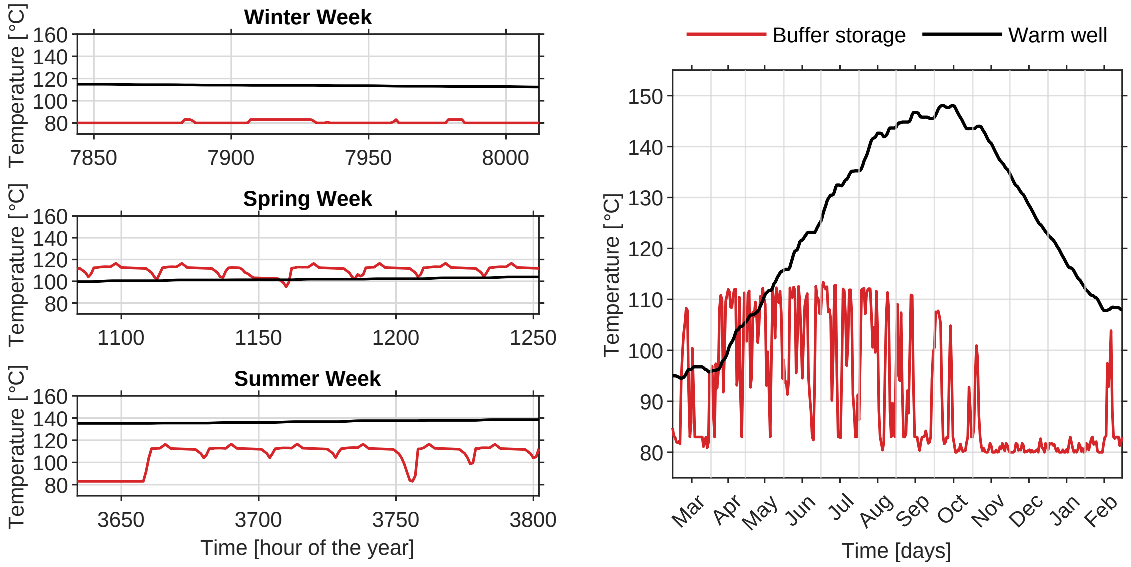

(a) Weekly storage temperatures **(b)** Annual storage temperatures

Figure A.3. Weekly and annual storage temperatures for the PCM buffer of 83 °C using the Delft Food & Beverage scenario.

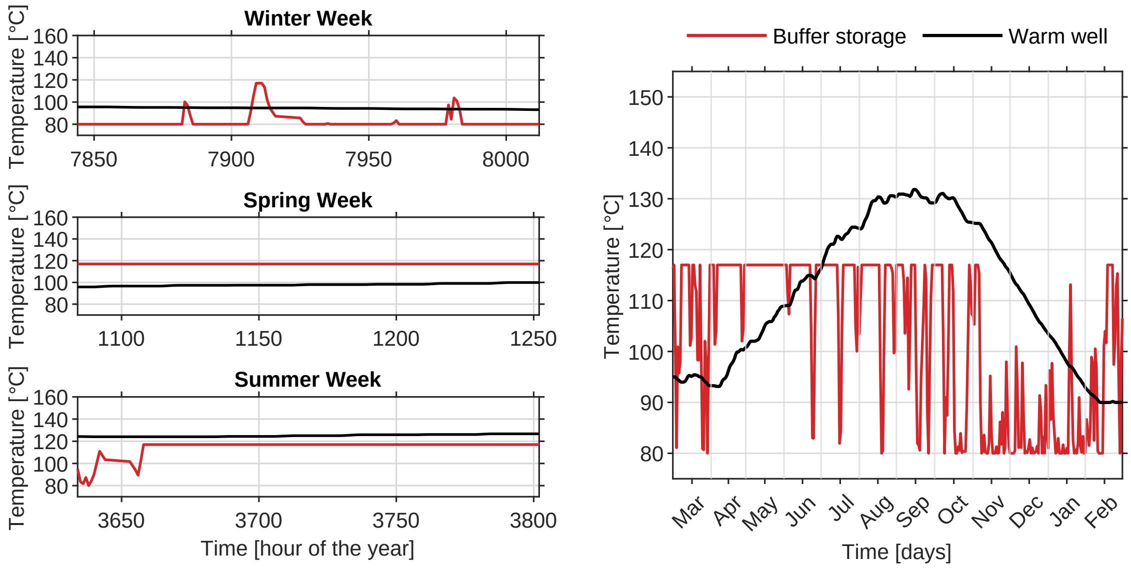

(a) Weekly storage temperatures **(b)** Annual storage temperatures

Figure A.4. Weekly and annual storage temperatures for the PCM buffer of 117 °C using the Delft Food & Beverage scenario.

Figure A.5 illustrates that the 117°C system operates at a slightly higher COP during the first part of the year. However, the COP declines rapidly in the latter part of the year as the ATES temperature decreases. During the final month the ATES is fully depleted and the COP of the 117 °C scenario is reduced to one. This is attributable to resistive heater usage during these shortage hours.

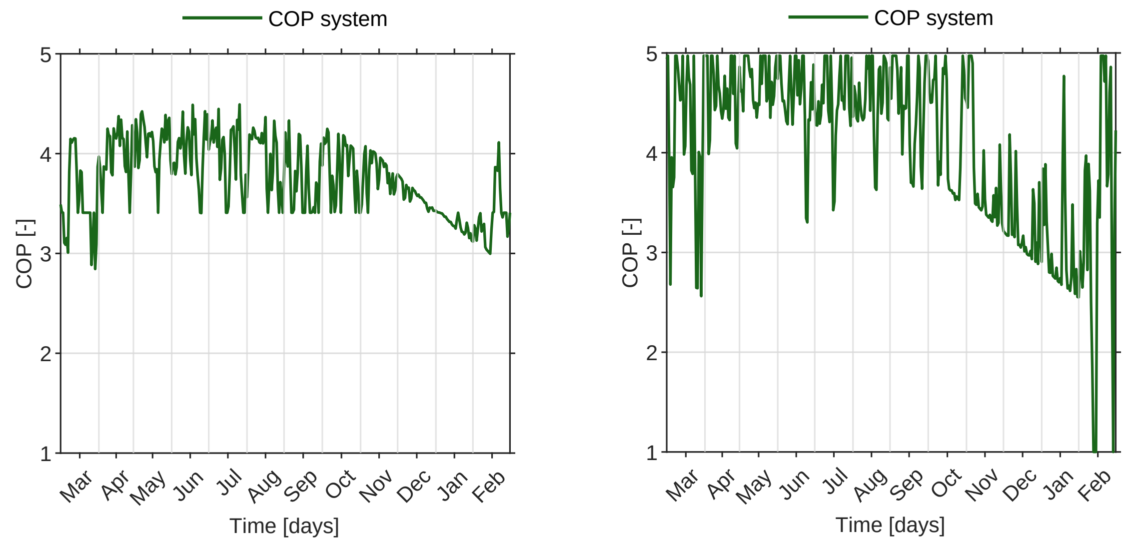

(a) 83 °C PCM

(b) 117 °C PCM

Figure A.5. Annual COP comparison for two PCM phase change temperatures using the Delft Food & Beverage scenario.

The total ST generation in the 83 °C PCM scenario adds up to 378 TJ, 35 TJ higher than the 117 °C PCM scenario. This can be attributed to higher thermal efficiencies that are reached for the PCM with a lower phase change temperature. The electrical requirement of Mode IIA has higher peaks for the 83 °C PCM scenario, as shown in Figure A.6. These results are attributable to the higher thermal efficiency of the ST collectors. In contrast, Mode I electricity consumption is significantly higher in the 83 °C scenario, peaking at 4 MW compared to 3 MW in the 117 °C scenario. This is attributable to the lower average buffer temperature, which increases the temperature lift, resulting in a lower COP and higher electricity consumption.

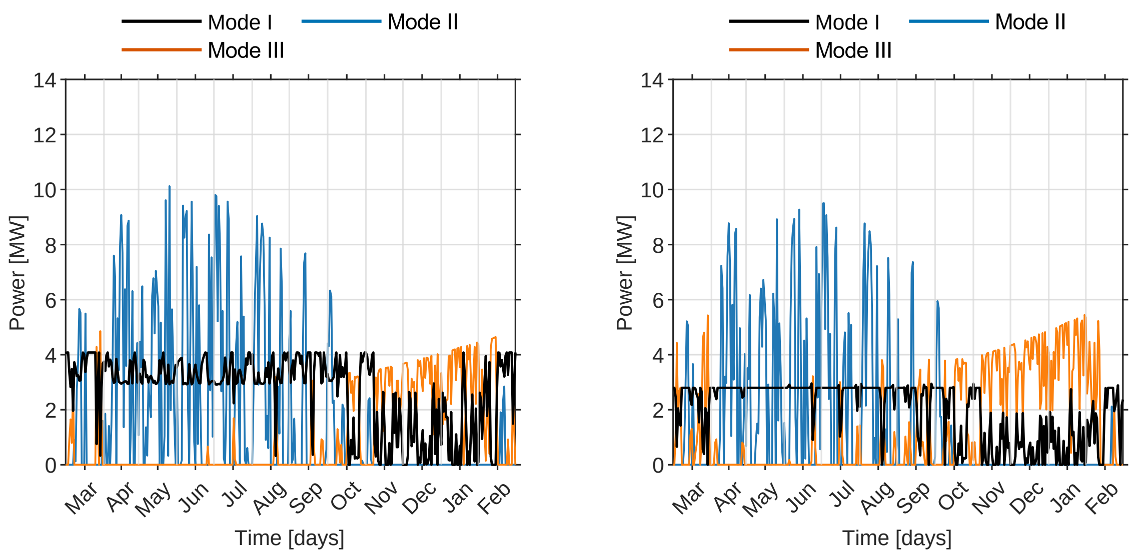

(a) 83 °C PCM

(b) 117 °C PCM

Figure A.6. Annual electrical power consumption comparison for two PCM phase change temperatures using the Delft Food & Beverage scenario.

Paper & Pulp Seville PCM

Figures A.7 and A.8 present the temperature development of the ATES and the buffer storage for the two different scenarios. The 83 °C buffer has an average temperature of 95 degrees, which is the result of the buffer being charged to 120 °C during the day and discharged to 83 °C during the night. The 117°C buffer storage maintains a steady temperature close to its phase change temperature throughout the year, with only brief deviations during periods of very low irradiance.

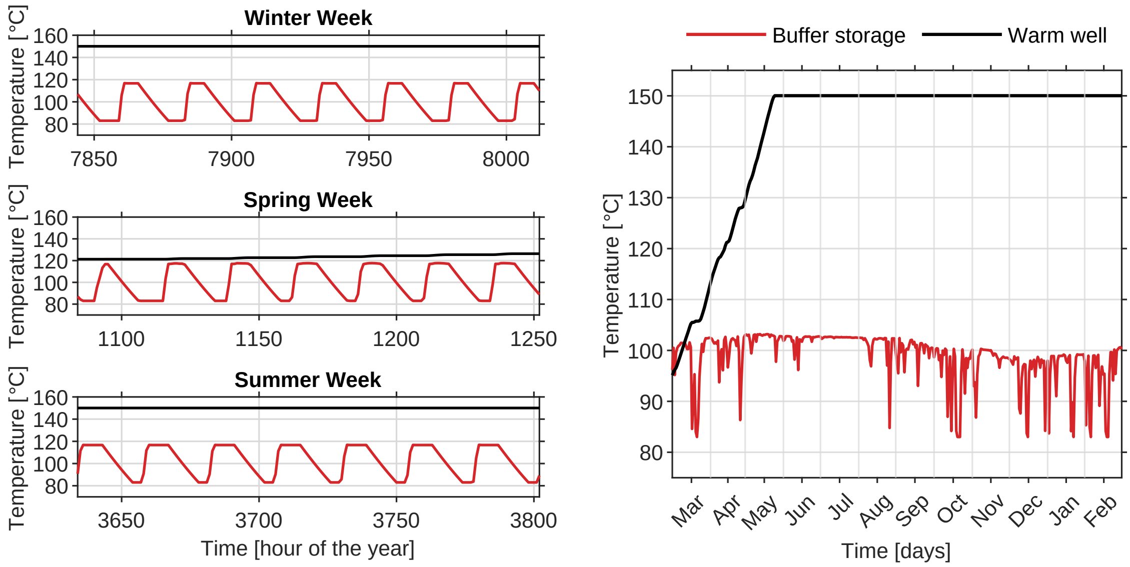

(a) Weekly storage temperatures **(b)** Annual storage temperatures

Figure A.7. Weekly and annual storage temperatures for the PCM buffer of 83 °C using the Seville Paper & Pulp scenario.

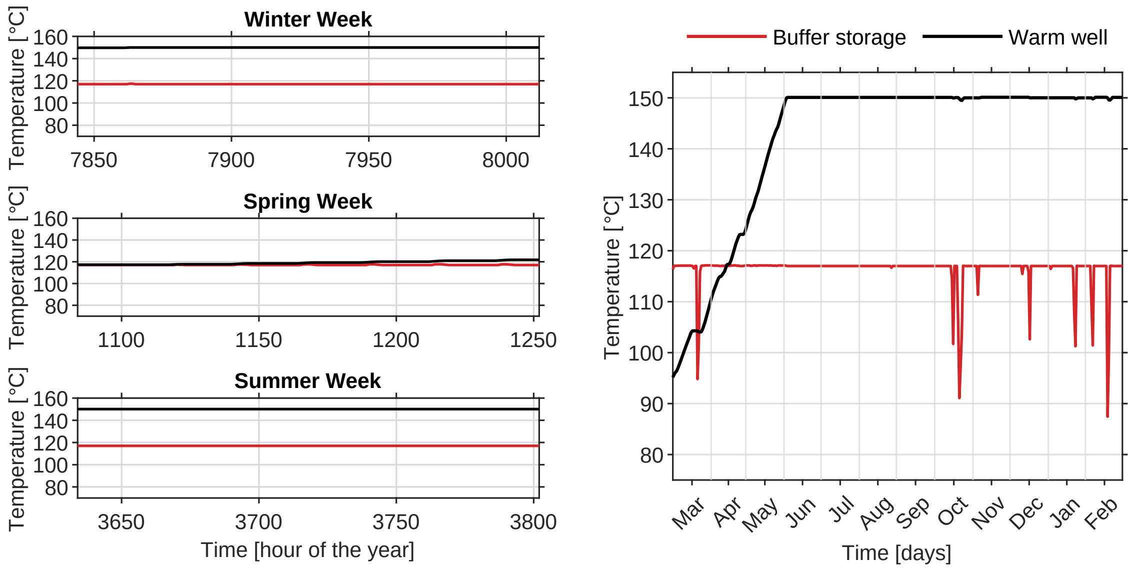

(a) Weekly storage temperatures **(b)** Annual storage temperatures

Figure A.8. Three week storage temperature comparison for two PCM phase change temperatures using the Seville Paper & Pulp scenario.

The influence of buffer storage temperature on system COP is clearly visible in Figure A.9. The 83 °C PCM system exhibits a sawtooth pattern in COP reflecting the cyclic charging and discharging of the buffer, while the 117 °C system maintains a stable COP throughout most of the year, with the exception of ATES charging periods which require an elevated steam temperature and therefore a higher temperature lift.

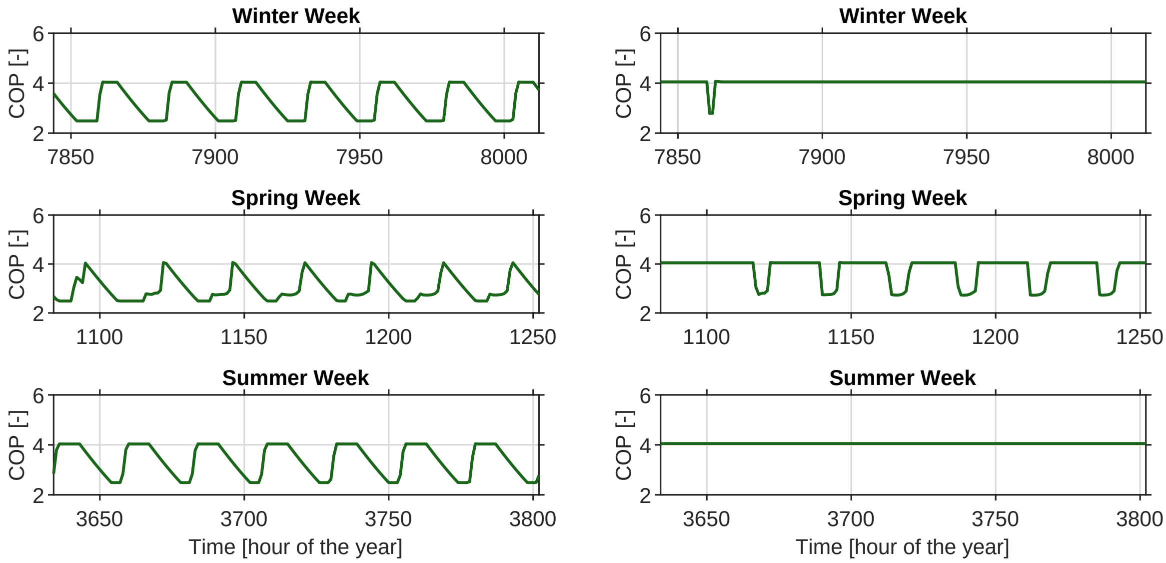

(a) 83 °C PCM **(b)** 117 °C PCM

Figure A.9. Three week COP comparison for two PCM phase change temperatures using the Delft Food & Beverage scenario.

Figure A.10 illustrates how the electrical demand of the 83 °C buffer storage is higher than that of the 117 °Cbuffer storage. This can be attributed to the relatively lower COP. The resulting increase in electricity demand exceeds the available PV generation more frequently, leading to higher grid consumption. In total, the 83 °C system draws 15 TJ from the grid, compared to only 2 TJ for the 117 °C system, which requires grid consumption during only a small number of peak hours.

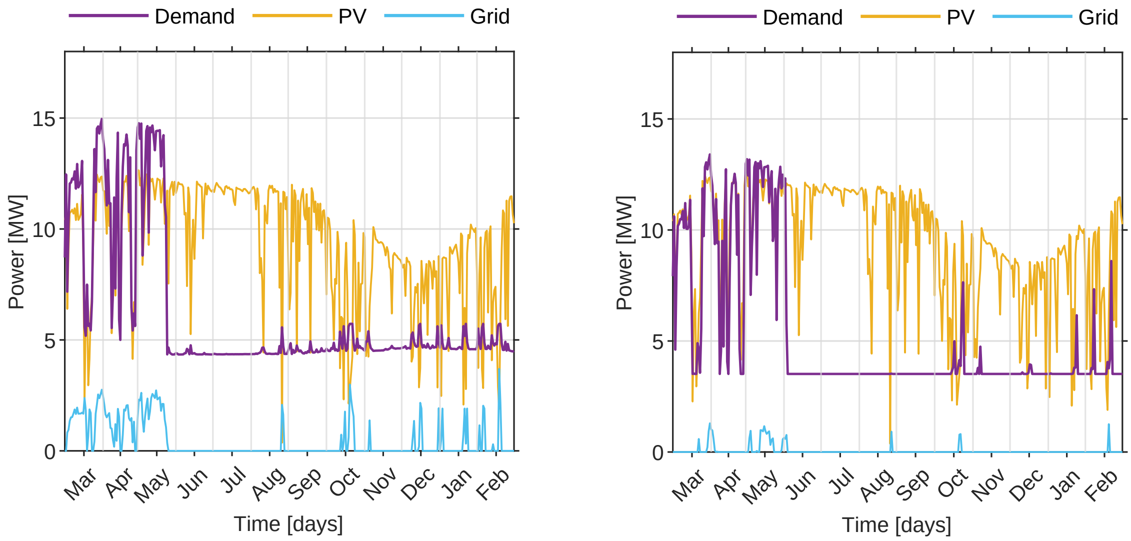

(a) 83 °C PCM　　**(b)** 117 °C PCM

Figure A.10. Annual comparison of electrical demand and grid consumption for two phase change temperatures.

The phase change temperature is a critical design parameter for the PCM buffer storage. A high phase change temperature results in lower ST generation as a result of the elevated reduced temperature of ST the collectors. The electrical consumption of a system with a high phase change temperature is higher due to a smaller required temperature lift resulting in a higher COP. These trends require careful consideration of system size for optimal system performance.

In most scenarios, the water tank based buffer storage outperforms both PCM options. The natural temperature variation of the buffer results in low temperature ST operation in low irradiance periods. This results in a lower reduced temperature and consequently higher thermal efficiency during winter. In contrast the system operates at low COP when producing excess heat for the ATES which reduces peak electrical demand. As a result, the water tank configuration is generally less reliant on grid electricity than either PCM alternative.

A.2. Heat Exchanger Area Estimation

This appendix covers a preliminary estimate of the required heat exchanger area that is required within the energy system. The analysis looks at two different heat exchangers in the system: The condensation heat exchanger charging the ATES warm well during surplus operation and the evaporation heat exchanger supplying the HP during shortage operation. The goal of this analysis is to determine whether the area required for these heat exchangers is realizable within conventional industrial heat exchanger sizes.

The Number of Transfer Units (NTU) method is applied [133]. This method is significantly simplified within this thesis, since both heat exchangers are driven by phase change on one side. This simplifies the capacity ratio $C^* = 0$ and the effectiveness of the heat exchanger reduces to:

$$\varepsilon = \frac{\dot{Q}}{\dot{Q}_{max}}, \qquad \varepsilon = 1 - \exp(-\mathrm{NTU}), \tag{A.2}$$

Subsequently, the heat exchanger area required can be determined using equation A.3

$$A = \frac{\mathrm{NTU} \cdot C_{\min}}{U} \tag{A.3}$$

The peak annual heat duty is used as the design point. General heat transfer coefficients are taken from tabulated ranges of shell-and-tube heat exchangers [88], resulting in a required area range depending on the transfer coefficient U. The results are summarized in Table A.2.

Table A.2. Estimated heat exchanger areas at peak design duty.

Configuration	$\dot{Q}_{\text{max}}$ (MW)	ε (–)	NTU (–)	U range (W/m²K)	A_{min} (m²)	A_{max} (m²)
Condensation (surplus)	100	0.944	2.90	1500–4000	1050	2800
Evaporation (shortage)	25	0.833	1.79	600–1700	1060	3010

The estimated areas fall in the range of 1050–3010 m^2, which is within the practical limits of industrial shell-and-tube heat exchangers. Single units of comparable area have been manufactured for applications in the power industry [134], confirming the physical viability of the required heat exchangers used in the model.

The results of this analysis are preemptive and should be worked out in more detail for advanced system design. Fouling of the heat exchanger is not considered, which can significantly decrease performance over time. In contrast, the heat exchangers are sized at peak annual heat transfer requirements, which is a conservative design point. Designing at a slightly lower design point such as the 95^{th} percentile peak could avoid oversizing for a small number of extreme hours. Furthermore, implementing a smart control system which spreads heat transfer over a larger number of hours could significantly reduce the required heat exchanger size. These factors are beyond the scope of this work but should be included when optimizing the proposed system.

Chapter B

Chapter 3

B.1. Heat Loss through horizontal transport

This appendix presents a simplified analytical assessment of the impact of transporting high-temperature ATES heat over horizontal distances on system COP and heat losses. The aim of the analysis is to study the technical feasibility of long distance horizontal heat transport, in case no suitable ATES geology is available nearby. The analysis uses the same approach as presented in Section 3.2.4 This appendix includes two additional mechanisms: thermal losses along the transport pipe and additional frictional pumping losses. The model only considers one way transport losses from ATES to industry. Losses during surplus operation are not considered since these coincide with high solar energy availability and are therefore less consequential for the system performance. However, for a more in depth analysis of horizontal transport losses these have to be considered and this analysis provides an optimistic scenario.

B.1.1. Heat Loss Model

The temperature drop along the supply pipe is modeled as:

$$\Delta T_{\text{loss}} = \frac{U \cdot L \cdot (T_{\text{aq}}^{\text{w}} - T_{\text{ground}})}{\dot{m} \cdot c_p} \tag{B.1}$$

where U is the linear heat loss coefficient ($\mathrm{W\,m^{-1}K^{-1}}$), L is the one-way pipe length (m), T_{aq}^{w} is the ATES warm well temperature, T_{ground} is the ground temperature along the pipe route (assumed 15 °C), $\dot{m}$ is the mass flow rate ($\mathrm{kg\,s^{-1}}$) and c_p is the specific heat capacity of water ($\mathrm{J\,kg^{-1}K^{-1}}$).

A heat loss coefficient range of 0.1–0.5 $\mathrm{Wm^{-1}K^{-1}}$ is evaluated, consistent with reported values for well-insulated district heating pipes operating at temperatures above 100 °C [135]. Figure B.1 presents the resulting temperature loss as a function of transport distance for an ATES source temperature of 120 °C. At 200 km and $U = 0.3$ $\mathrm{Wm^{-1}K^{-1}}$ the total temperature loss reaches approximately 6 K, within acceptable margins to operate the system. The 0.1 $\mathrm{Wm^{-1}K^{-1}}$ line presents the temperature loss of a very well insulated pipe, resulting in a reduction of only 2 K over 200 km of transport. These results suggest that when temperature reduction is the only metric, long distance transport of warm water is feasible.

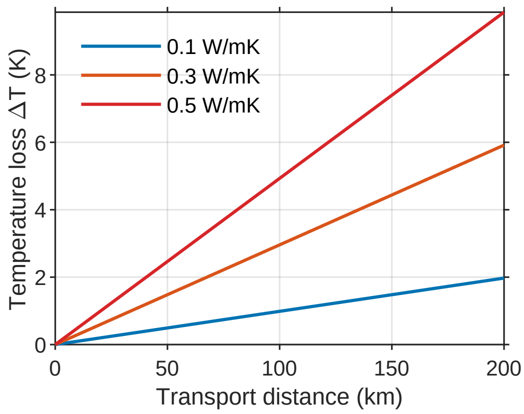

Figure B.1. Thermal losses due to horizontal transport of water through pipes.

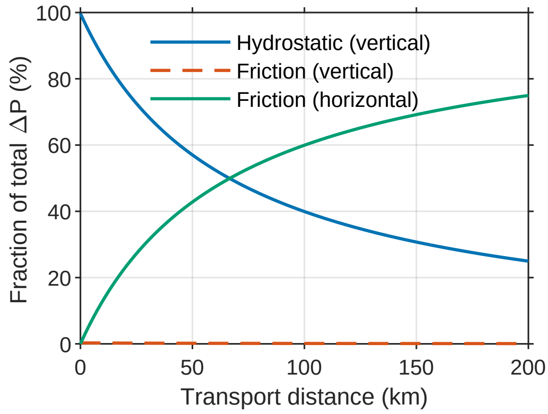

Figure B.2. Fraction of hydrostatic and friction pressure losses for horizontal transport through pipes.

B.1.2. Hydraulic Pressure Loss Model

The total pressure drop consists of three components: hydrostatic pressure from the vertical ATES well depth, vertical pipe friction, and horizontal pipe friction. The frictional pressure drop is calculated using the Darcy–Weisbach equation :

$$\Delta P_{\text{friction}} = f_D \frac{(L_{\text{hor}} + L_{\text{ver}})\rho V^2}{2D} \tag{B.2}$$

where f_D is the Darcy friction factor computed using the Swamee–Jain approximation, D is the inner pipe diameter (m), ρ is the fluid density ($\mathrm{kg\,m^{-3}}$), V is the flow velocity ($\mathrm{m\,s^{-1}}$), and L_{hor} and L_{ver} are the horizontal and vertical pipe length. The hydrostatic contribution from the vertical well of depth $L_{\text{ver}} = 400$ m is:

$$\Delta P_{\text{hydraulic}} = \rho_w g L_{\text{ver}} \tag{B.3}$$

Figure B.2 presents the relative contribution of each pressure component as a function of transport distance. The vertical friction contribution is negligible for all distances. At a transport distance of zero, the hydrostatic friction component dominates. Beyond approximately 65 km the horizontal friction becomes dominant, accounting more than 50% of the pressure drop.

B.1.3. Impact on System COP

The COP of the system is determined using a similar approach as presented in Section 3.2.4, where the delivered heat and the pressure loss over the pipe are determined per kg of transported water. The approach has been updated by increasing the transport length for the frictional pressure loss contribution as discussed in Section B.1.2 and including the reduced water temperature arriving at HP evaporator. The temperature arriving at the heat exchanger is determined as follows:

$$T^{\text{w}}_{\text{aq,eff}} = T^{\text{w}}_{\text{aq}} - \Delta T_{\text{loss}} \tag{B.4}$$

Since the HP evaporator temperature is determined by the incoming ATES water temperature, the effective temperature lift the HP must overcome increases from ΔT_{HP} to $\Delta T_{HP} + \Delta T_{loss}$. The system COP is therefore modeled using the augmented temperature lift:

$$COP_{\text{HP}} = 5.57 - 0.046 \cdot (\Delta T_{\text{HP}} + \Delta T_{\text{loss}}) \tag{B.5}$$

This approach captures both the reduction in available heat from the ATES heat exchanger since colder water arrives at the heat exchanger with increased transportation distance and the degradation of HP performance due to the lower source temperature. The temperature change over the heat exchanger is expressed in equation B.6 and the system COP is presented in equation B.7.

$$\Delta T_{\mathrm{HX}} = T^{\mathrm{w}}_{\mathrm{aq,eff}} - (T_{\mathrm{D}} - \Delta T_{\mathrm{HP}}) - \Delta T_{\mathrm{pinch}} \tag{B.6}$$

$$COP_{\mathrm{system}} = \frac{Q_{\mathrm{delivered}}}{W_{\mathrm{HP}} + W_{\mathrm{pump,total}}}, \tag{B.7}$$

where $W_{\mathrm{pump,total}}$ includes both the vertical ATES pumping work and the additional horizontal pipe friction losses.

Figures B.3 ($T_{\mathrm{D}} = 130$) and B.4 $T_{\mathrm{D}} = 150$) present the system COP as a function of HP temperature lift for transport distances of 0, 50, 100, 200 and 400 km at a fixed ATES warm well temperature of 120 °C. The results show that for short distance the COP does not see a major reduction. For distances further than 100 km the reduction in COP becomes very significant. COP decreases by approximately 0.15 for every 50 km of travel. Resulting in a decrease of 0.6 for a 200 km travel distance. In a system where margins are narrow this is a significant reduction, especially considering that the performance is worse when the ATES operates at a lower temperature.

In conclusion, these results suggest that when geological conditions are not favorable for ATES employment it is technically possible to transport warm water over long distances. However, transport over distances further than 100 km system results in a significant performance decrease. Furthermore, this analysis only includes losses in one transport direction and does not consider cost of such an extensive transport system. Therefore, a more in depth analysis is required to determine the economic viability of this system.

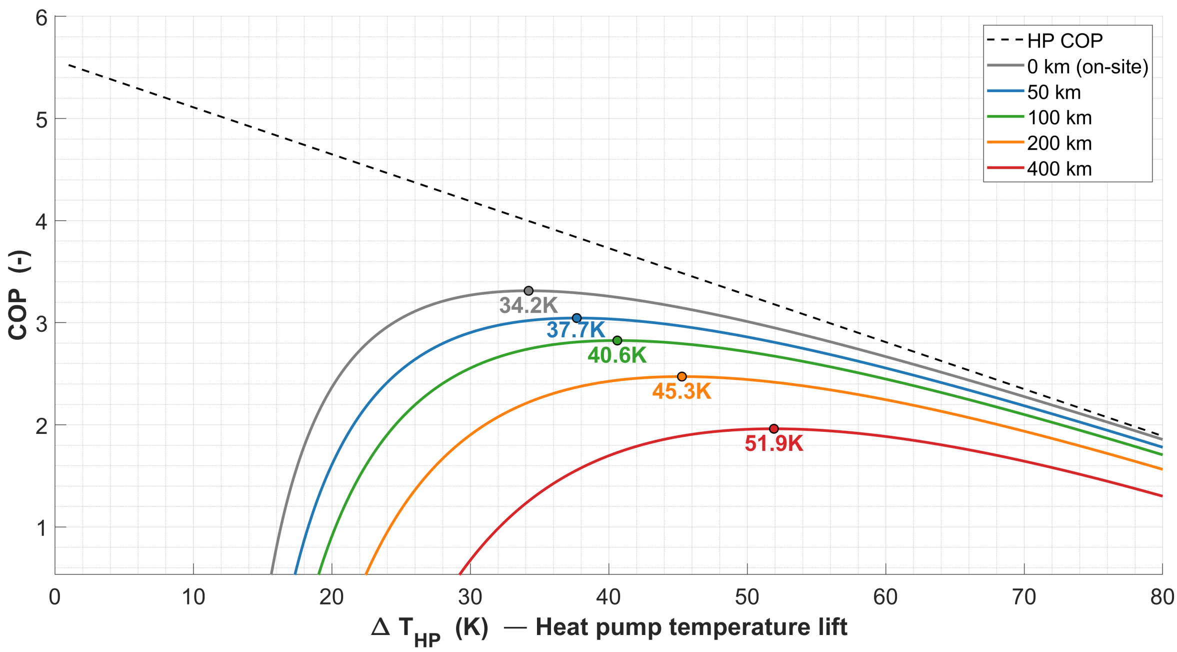

Figure B.3. COP of a heat pump including pumping losses and heat loss for long horizontal transport distances. The dotted line shows the COP without hydraulic pumping power. $T_{\mathrm{D}} = 130$ °C, depth = 400 m, $T^{\mathrm{w}}_{\mathrm{aq}} = 120$ °C

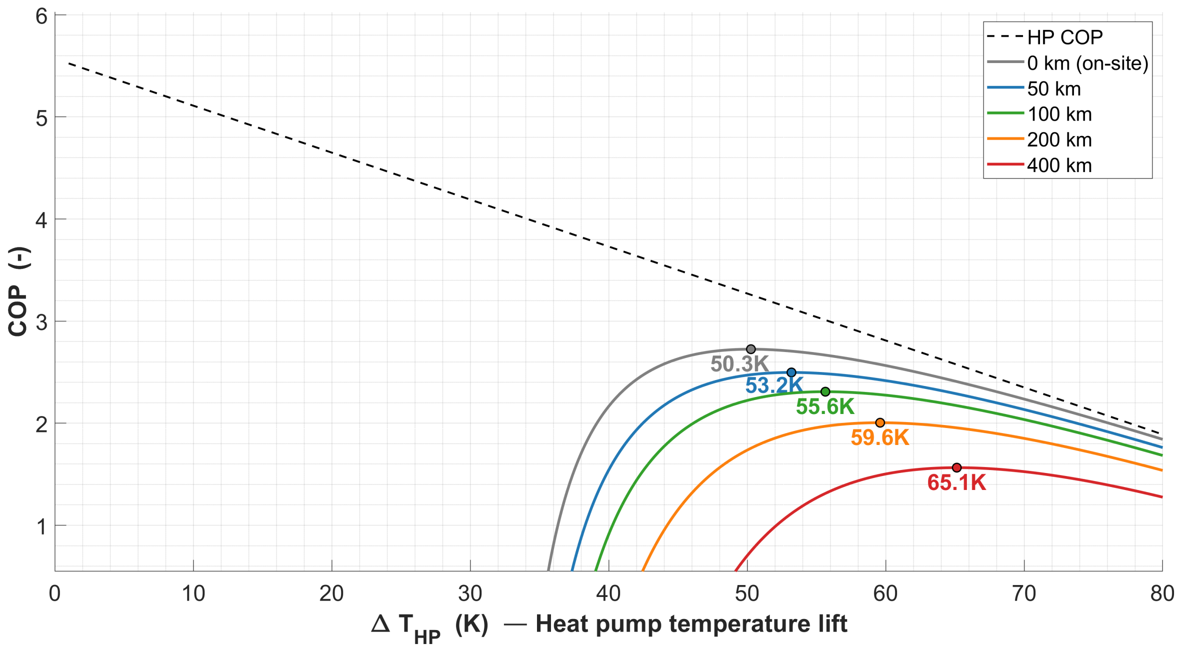

Figure B.4. COP of a heat pump including pumping losses and heat loss for long horizontal transport distances. The dotted line shows the COP without hydraulic pumping power. $T_{\mathrm{D}} = 150\ ^{\circ}\mathrm{C}$, depth = 400 m, , $T^{\mathrm{w}}_{\mathrm{aq}} = 120\ ^{\circ}\mathrm{C}$

Chapter C

Chapter 4

C.1. PVT performance

This appendix presents the weekly and annual operation of the energy system in Configuration 6. Since some graphs are comparable to the results found in Section 4.1, only a selection of results is shown highlighting key differences. The simulation results that are not covered in this chapter can be found in the thesis repository.

- **Food & Beverage Delft PVT**

The Delft Food & Beverage scenario with PVT has a total grid consumption of 11 TJ and a peak load of 10 MW. This is slightly lower compared to the Configuration 5 results. Figure C.1 presents the thermal (purple) and electrical (gold) efficiency of the PVT collectors. The average electrical efficiency is 17%, mainly depending on the temperature of the buffer storage tank, which directly influences the module temperature. This is 23% lower than the average efficiency of the PV collectors, reducing from an average of 22%. The thermal efficiency decreases even more between scenarios, 40% to 26% in Configuration 6.

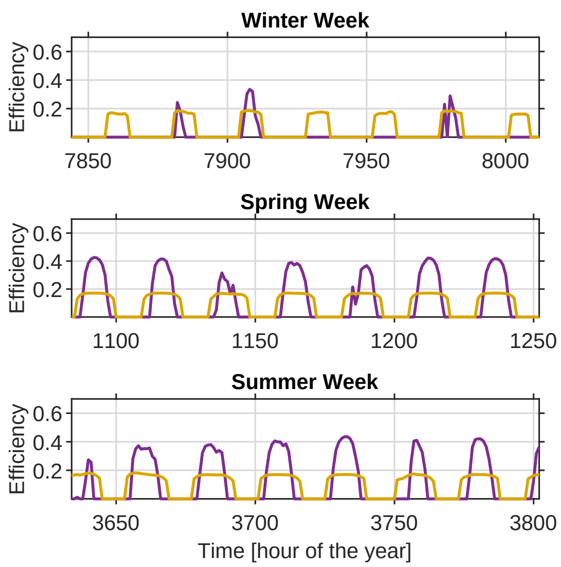

(a) Simulation results for three weeks

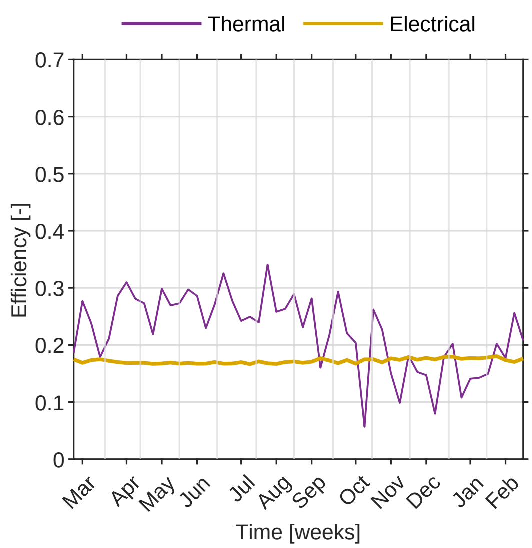

(b) Annual simulation results

Figure C.1. Thermal and electrical efficiency of PVT modules for the Delft Food & Beverage scenario.

The relatively large decrease in thermal efficiency compared to electrical efficiency can also be seen in Figure C.2. Where electricity demand and PV generation were somewhat balanced in Configuration

6, this graph shows a significant surplus in electrical generation. The electrical generation also reaches daily power generation averages of up to 22 MW, much higher than the 13 MW maximum in other scenarios A possible solution is to use PVT with additional ST modules to balance the thermal and electrical generation. This is explored in Section C.2.

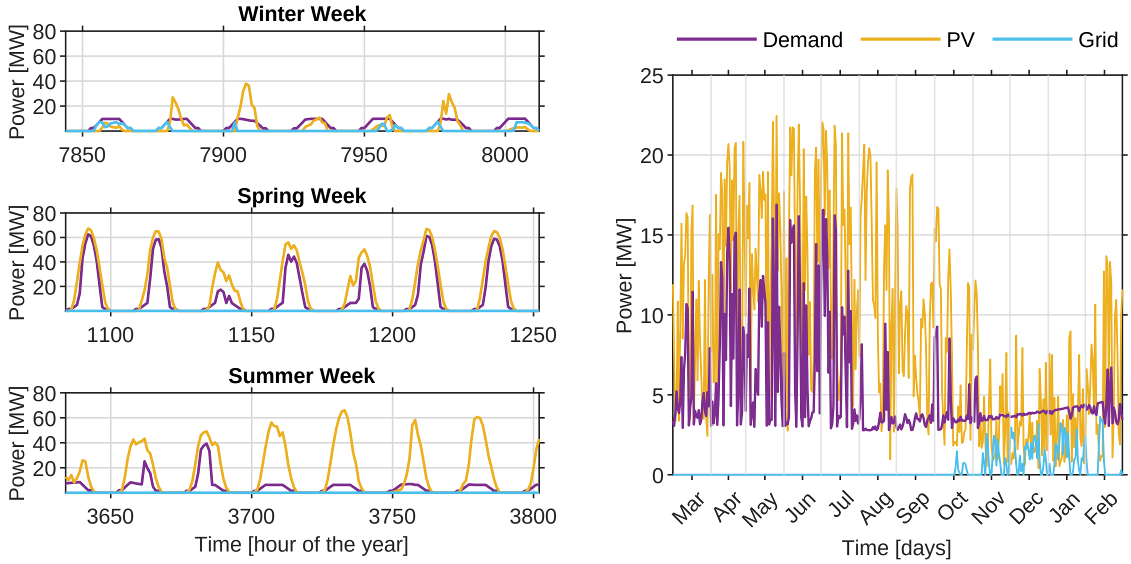

(a) Simulation results for three weeks

(b) Annual simulation results

Figure C.2. Electricity demand, generation and grid consumption in the Delft Food & Beverage scenario with PVT.

Figure C.3 shows how the storage shows comparable trends to the Configuration 5 results. Although, thermal efficiency is reduced when using PVT, the total thermal energy generation of the system is higher. This is caused by the larger number of PVT modules compared to the ST modules in Configuration 5. This results in the ATES reaching its maximum temperature of 150 °C and ending up at 110 °C at the end of the year. This is an increase in 15 °C compared to the starting temperature. These results suggest that the system is oversized and could function properly with a reduced number of PVT modules.

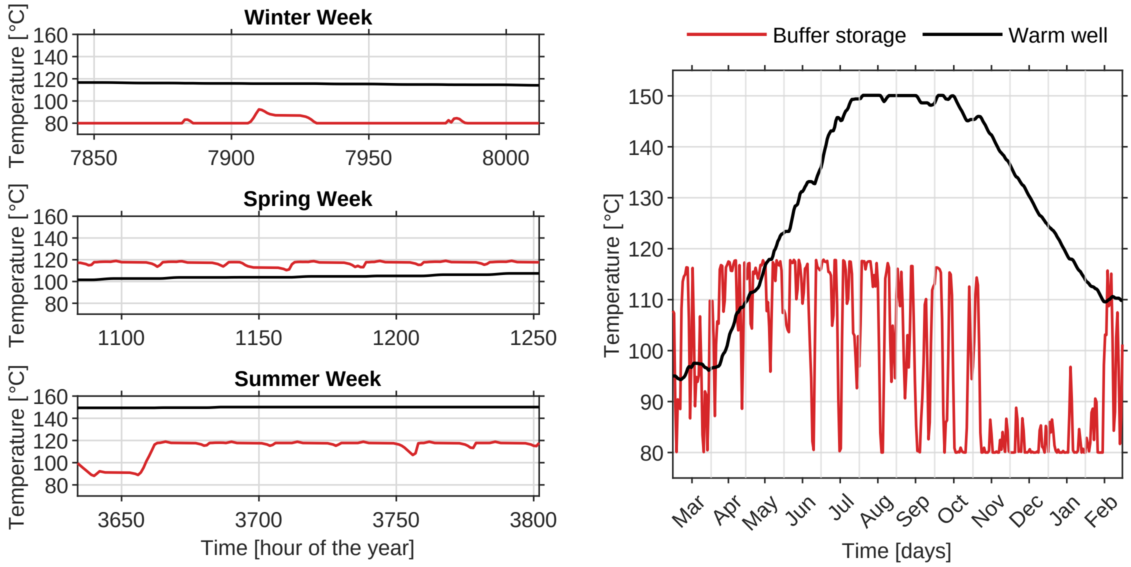

(a) Simulation results for three weeks

(b) Annual simulation results

Figure C.3. Temperature of the buffer storage and warm ATES well for the Delft Food & Beverage scenario with PVT.

- **Paper & Pulp Delft PVT**

The Delft Paper & Pulp scenario with PVT has a total electricity consumption from the grid of 23 TJ and a peak load of 7 MW. The grid consumption is slightly lower than Configuration 5 scenario but the peak load is the same. Figure C.4 illustrates the comparatively high demand as a result of the lower COP caused by the higher steam demand temperature.

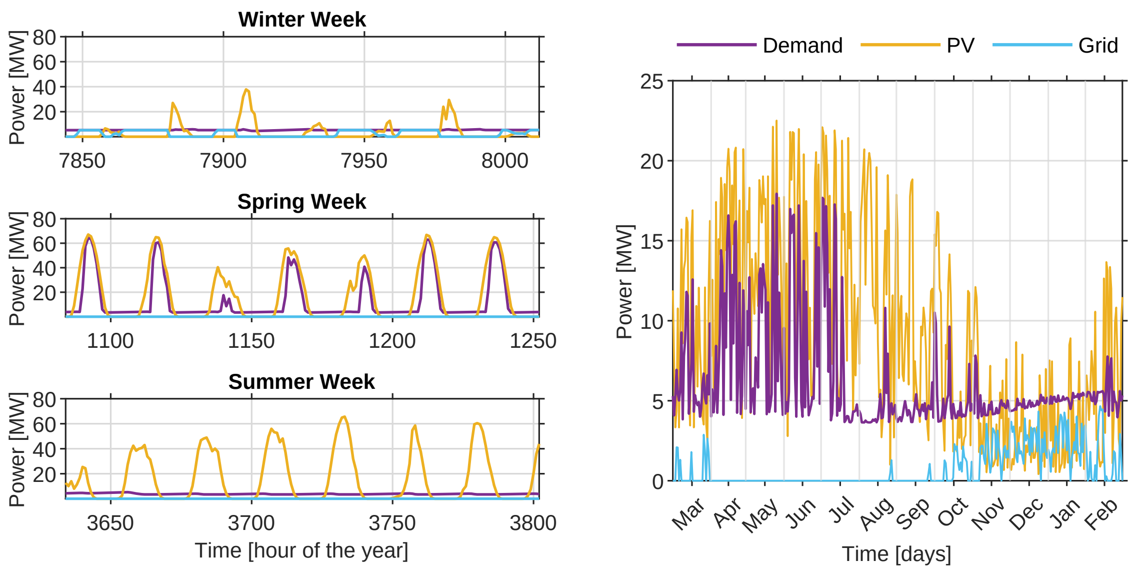

(a) Simulation results for three weeks

(b) Annual simulation results

Figure C.4. Electricity demand, generation and grid consumption in the Delft Paper & Pulp scenario with PVT.

The final ATES temperature is close to 115 °C as can be seen in Figure C.5. Similar to the Configuration 5 analysis this increase in final temperature after one year of operation is caused by lower COP in the Paper & Pulp section resulting in reduced thermal extraction from the storage.

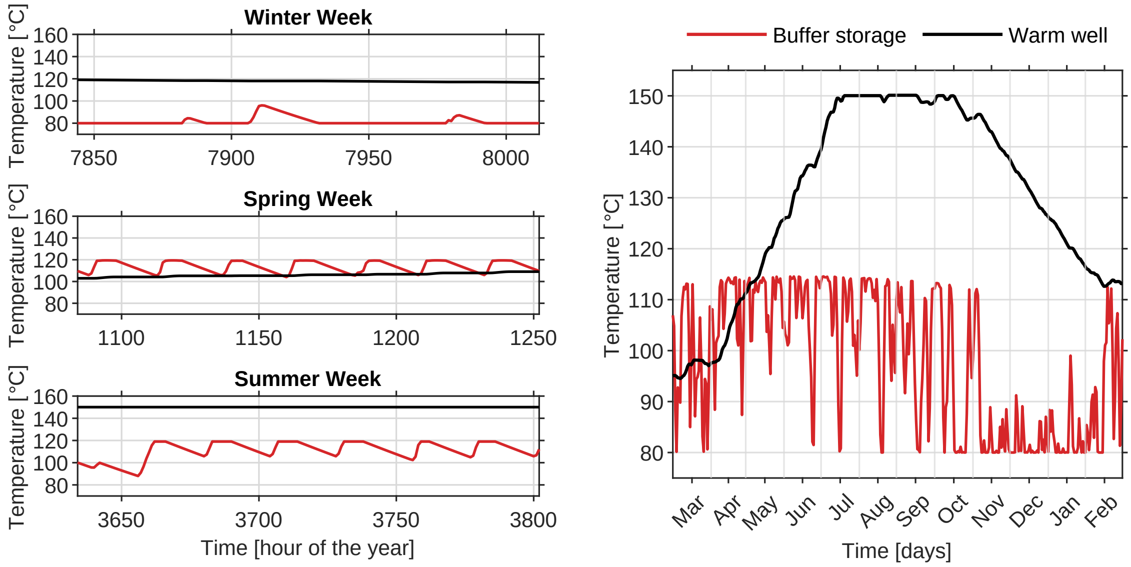

(a) Simulation results for three weeks

(b) Annual simulation results

Figure C.5. Temperature of the buffer storage and warm ATES well for the Delft Paper & Pulp scenario with PVT.

- **Food & Beverage Seville PVT**

The Seville Paper & Pulp scenario with PVT has a total electricity consumption of 0 TJ and a peak load of 0 MW. This is equivalent to the Configuration 5 scenario. The thermal and electrical efficiency of the PVT collectors is depicted in Figure C.6. The electrical efficiency is around 17% comparable to the efficiency seen in Delft. The average thermal efficiency is 34% during, significantly higher than the average efficiency in Delft but significantly lower than the 50% average efficiency of ST collectors in Seville.

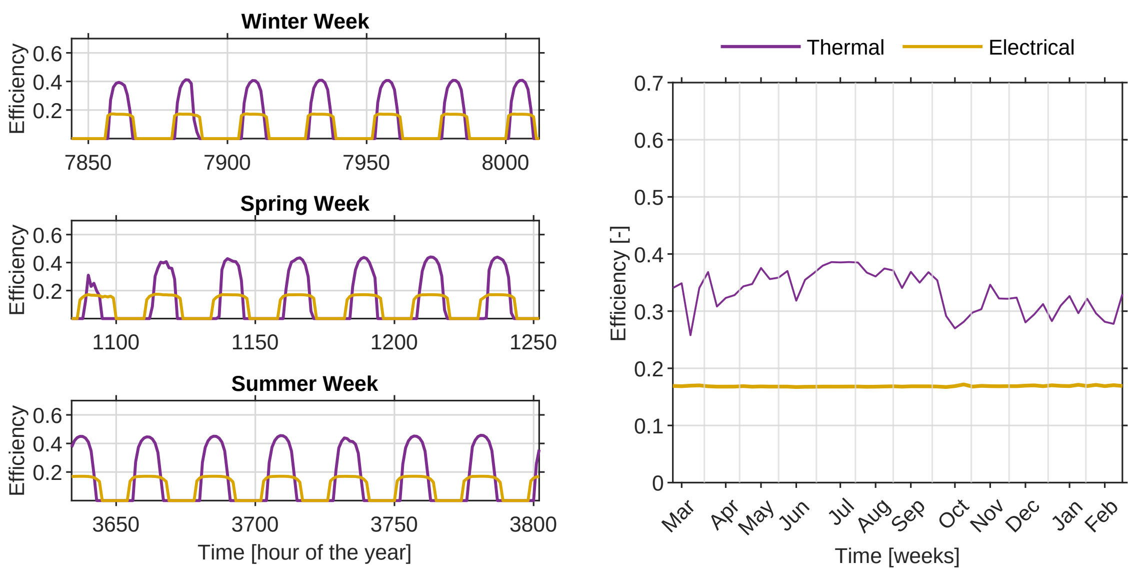

(a) Simulation results for three weeks

(b) Annual simulation results

Figure C.6. Thermal and electrical efficiency of PVT modules for the Seville Food & Beverage scenario.

Figure C.7 shows that the warm well reaches its maximum storage temperature at the start of may. Almost two months earlier compared to the Configuration 5 results. These results of the PVT collectors show that the average thermal and electrical yield of two PVT collectors is higher than the yield of one ST and one PVT module. Further illustrating the technical advantages of using PVT collectors.

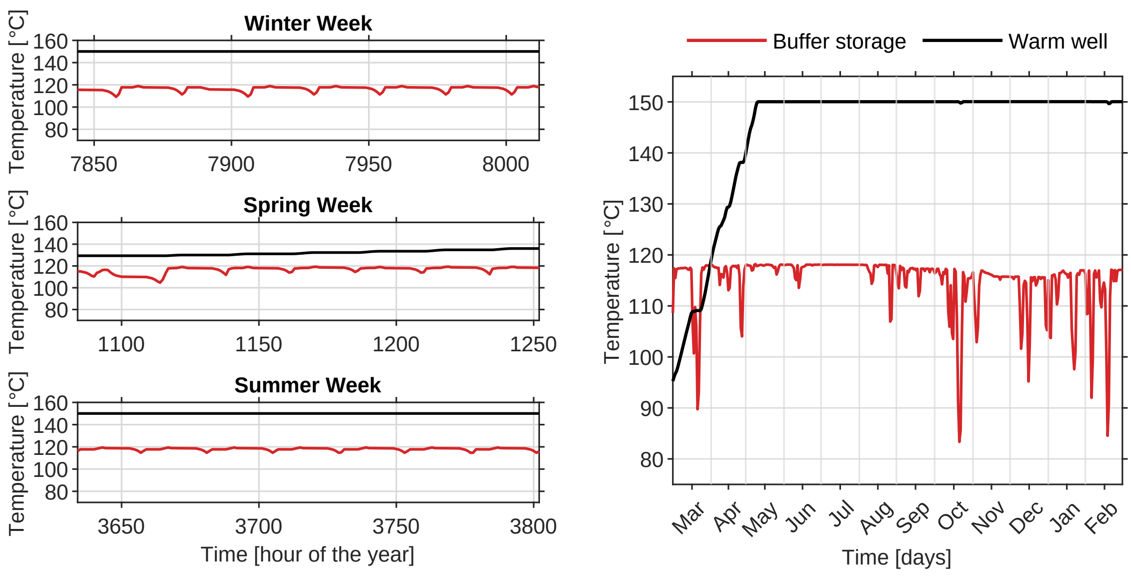

(a) Simulation results for three weeks

(b) Annual simulation results

Figure C.7. Temperature of the buffer storage and warm ATES well for the Seville Food & Beverage scenario with PVT.

• Paper & Pulp Seville PVT

The Seville Paper & Pulp scenario with PVT has a total electricity consumption from the grid of 0.2 TJ and a peak load of 5 MW. The total consumption of this scenario is lower than that of Configuration 5, even reaching full grid independence when rounding down the total consumption. The peak load is 5 MW, but grid consumption is only 10 hours annually concentrated in two days, as can be seen in Figure C.8. These few hours of consumption have a negligible effect on the total electricity consumption which is only 0.2 TJ and could be covered through implementing a slightly larger electrical storage capacity or slight demand curtailment.

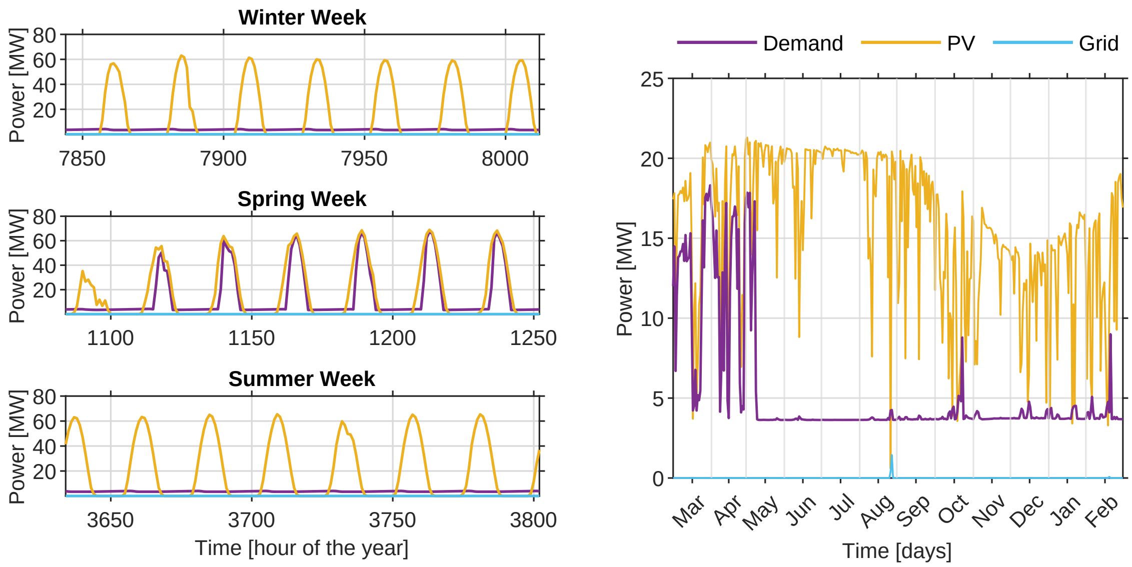

(a) Simulation results for three weeks

(b) Annual simulation results

Figure C.8. Electricity demand, generation and grid consumption in the Seville Paper & Pulp scenario with PVT.

C.2. PVT optimum

This section examines the system performance for varying quantities of PVT modules, with the aim of determining whether replacing separate ST and PV collectors with PVT modules affects the required system size. A pronounced difference in required collector quantity is observed between the Delft and Seville scenarios. In Seville, total grid consumption approaches zero at approximately 60 000 PVT modules, whereas in Delft this requires around 150 000 modules. Regarding peak load reduction, only the Seville Food & Beverage scenario achieves full grid independence. The Seville Paper & Pulp scenario can be considered practically grid-independent from 80,000 modules onward, where grid electricity consumption is reduced by more than 99%.

Compared to Configuration 5, Configuration 6 requires fewer modules to achieve a significant peak load reduction in the Delft scenarios. The Delft Food & Beverage scenario requires 150,000 PVT modules compared to 180,000 combined ST collectors and PV modules, while the Delft Paper & Pulp scenario sees the required quantity decrease from 180,000 to 140,000 modules. The Seville results are more promising, with significant peak load reductions achievable at 60,000 modules —considerably fewer than the 100,000 and 120 000 modules required for the Food & Beverage and Paper & Pulp scenarios respectively in Configuration 5, as shown in Figure 4.21.

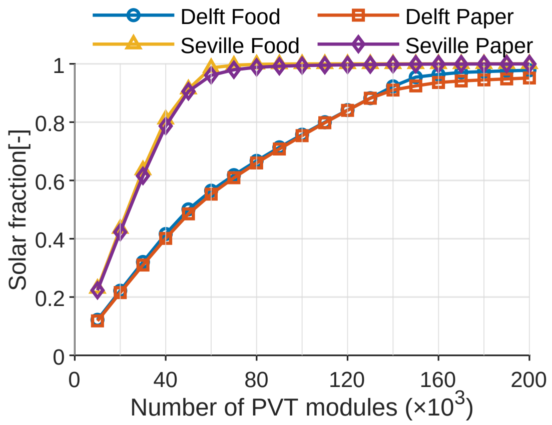

(a) Solar fraction for varying collector quantities

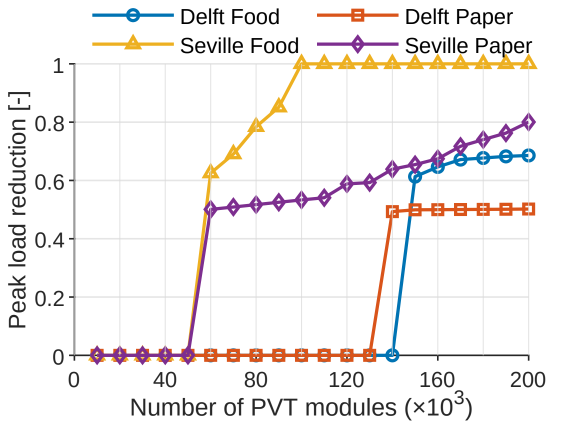

(b) Peak load reduction for varying collector quantities.

Figure C.9. System performance for varying PVT collector quantities.

Since the thermal efficiency of PVT modules is reduced proportionally more than the electrical efficiency compared to separate ST and PV collectors, a mixed collector field combining ST and PVT modules may yield better performance than a purely PVT system. Such a configuration could compensate for the thermal deficit of PVT collectors while retaining their combined electrical and thermal output advantage per unit area. Figure C.10 presents the system performance as a function of ST fraction within a combined ST and PVT collector field, showing to what extent the total required collector area can be reduced compared to a purely PVT or purely ST and PV configuration.

When employing 80000 PVT and 40000 ST collectors the peak load is reduced by 50%. Alternatively, for a 50% peak load reduction when combiningST collectors and PV modules a total of 180000 modules was required. This results in a 33% reduction in required module area when employing a combination of PVT and ST collectors.

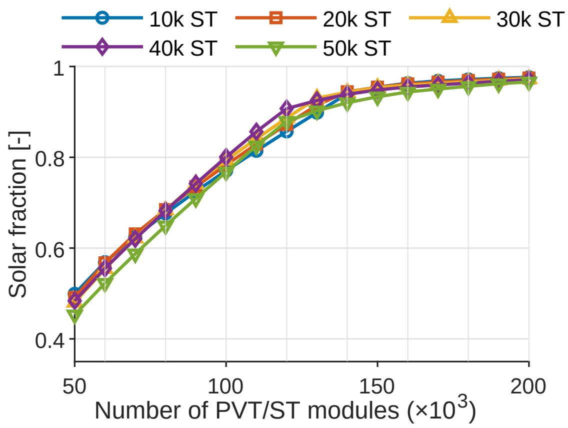

(a) Solar fraction for varying total collector quantities.

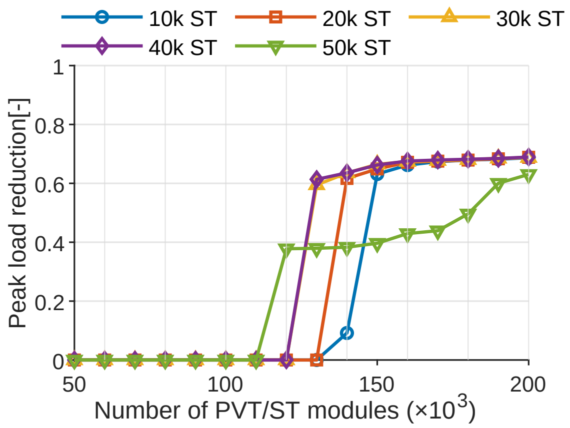

(b) Peak load reduction for varying total collector quantities.

Figure C.10. System performance for varying PVT and ST quantities and ratios.